Biomechanical Analysis and Modeling of the In Vivo Lumbar Spine

by

Ryan Byrne

BS in Mechanical Engineering, University of Pittsburgh, 2014

Submitted to the Graduate Faculty of the

Swanson School of Engineering in partial fulfillment

of the requirements for the degree of

Doctor of Philosophy

University of Pittsburgh

2019

UNIVERSITY OF PITTSBURGH

SWANSON SCHOOL OF ENGINEERING

This dissertation was presented

by

Ryan Byrne

It was defended on

November 4, 2019

and approved by

Xudong Zhang, Ph.D., Professor,
Department of Industrial & Systems Engineering, Texas A&M University

Jeffrey Vipperman, Ph.D., Professor,
Department of Mechanical Engineering and Materials Science

William Anderst, Ph.D., Assistant Professor,
Department of Orthopaedic Surgery

Ameet Aiyangar, Ph.D.,
Empa – Swiss Federal Laboratories for Materials Science and Technology

Dissertation Director: Patrick Smolinski, Ph.D., Associate Professor,
Department of Mechanical Engineering and Materials Science

Biomechanical Analysis and Modeling of the In Vivo Lumbar Spine

Ryan Byrne, PhD

University of Pittsburgh, 2019

Low back pain is the most prevalent musculoskeletal disorder in the United States and worldwide. To better understand the mechanical antecedents which exacerbate low back pain, further investigation of lumbar mechanics during functional activity is required. Advancements in medical imaging techniques have paved the way to address current knowledge gaps regarding in vivo lumbar mechanics, providing the capability of capturing motion of the lumbar spine with high accuracy during dynamic activities. The current work comprises three aims. The first aim was to accurately quantify in vivo deformation of the lumbar intervertebral discs in healthy subjects during dynamic lifting tasks. The second aim was to evaluate lumbar facet joint kinematics during the same lifting tasks. Utilizing directly measured subject-specific lumbar vertebral kinematics, the third aim was to investigate the potential for obtaining more accurate joint reaction and muscle force estimates. To accomplish this, in vivo data were incorporated within subject-specific musculoskeletal models, whereby the joint reaction and muscle force patterns of the lumbar spine during the lifting motion were estimated. The current study found uniquely different intervertebral disc morphometry, disc deformation, and facet join translational kinematics at the L5S1 disc during the lifting tasks. The incorporation of accurately measured lumbar vertebral kinematics within musculoskeletal models led to decreased joint reaction forces compared to those with generic, rhythm-based lumbar kinematic inputs. Lumbar kinematic input also displayed significant interaction with passive stiffness properties and the neutral state configuration defined at the lumbar joints of the musculoskeletal models. The results suggest that the mechanical behavior of

the L5S1 is distinctly different from the rest of the lumbar segments, and that approaches to restore normal, functional motion at the segment should differ from other joint levels. Furthermore, results indicate that inclusion of the accurate vertebral kinematics – including rotational as well as translational kinematics – within musculoskeletal models may lead to improved estimates of lumbar loading patterns. Such input datasets can also provide a better insight into the stabilizing role of deep intrinsic muscles such as the multifidus. On the other hand, it may also heighten the demand for accuracy of accompanying parameters.

Table of Contents

List of Tables

List of Figures

Preface

This work was supported by a research grant (R21OH00996) from the Centers for Disease Control and Prevention/National Institute for Occupational Safety and Health (CDC/NIOSH) and an Ambizione Career Grant Award (PZ00P2_154855/1) from the Swiss National Science Foundation (SNSF).

1.0 Introduction

1.1 Background

1.1.1 Low Back Pain

For nearly three decades, low back pain (LBP) has been identified as one of the three leading causes of non-fatal disease and the most significant cause – Level 3 – of global years lived with disability (YLD), with counts increasing from 2007 to 2017[1]. Global disability-adjusted life-years (DALYs) associated with LBP increased by more than 17% from 2007 to 2017, ranking LBP 5th among all non-communicable diseases and 1st among musculoskeletal disorders. LBP has several causes, some of which include disc herniation, low back muscular and ligament strains, and osteoarthiritis, among many others, stenosis, nerve root inflammation.

Studies investigating the etiology of low back disorders have established excessive or altered mechanical loading as a central factor leading to degenerative disc disease (DDD), a common disease of the intervertebral disc that can lead to further loss of structural integrity, and, more importantly, debilitating LBP[2,3]. Identifying the mechanical antecedents of DDD is a complex issue, however, as degenerative conditions in the intervertebral disc are often concomitant with facet joint osteoarthritis (degeneration of the facet joint) due to the interdependence of the motion and loading patterns between the two structural components. Furthermore, there is still much not known in understanding the basic science of low back mechanics during functional tasks.

1.1.2 In Vivo Lumbar Mechanics

1.1.2.1 In Vivo Measurements

The mechanics of the disc and facet joint have a strong influence on the structural stability of the lumbar spine and alterations in their mechanical properties and motion patterns during non-functional or static poses have often been associated with DDD[2,4-10]. What remains unclear, however, are the dynamic motion and loading patterns of these structures during the in vivo, functional activities that can exacerbate DDD. Identifying disc deformation and facet joint kinematics along with the corresponding loading patterns during a lifting task has the potential to improve our knowledge of the physiological demands inflicted on the structural components of the lumbar segments during functional activity. Furthermore, it can help establish a more concrete baseline of "normal" *in vivo* motion and loading patterns with which degenerative conditions can be compared against.

1.1.2.2 Simulation and Modeling Techniques

Due to the relative infeasibility of measuring the loading patterns of the mechanical structures in the lumbar spine *in vivo*, they are often estimated using biomechanical models. Many finite element (FE) models, musculoskeletal models, or hybrid FE-musculoskeletal models, have been developed to observe the functional mechanics of the lumbar spine[4,11-24]. However, validation of these models is a difficult task due to both the inevitable variability of physiological parameters among subjects and the absence of *in vivo* data in literature[14,15,25]. The results derived from these models are often validated against *in vitro* or *in vivo* data from previous studies. However, the kinematic and loading boundary conditions applied during *in vitro* studies do not guarantee the spine to function as it would *in vivo*, and while utilizing *in vivo* datasets are an improvement, they often have limited accuracy or are based on static or nonfunctional loading conditions.

The next three subsections will detail the knowledge and methodologies of previous studies regarding disc deformation, facet joint kinematics, and biomechanical modeling of the in vivo lumbar spine.

1.1.3 In Vivo Disc Height and Deformation

1.1.3.1 Significance

Intervertebral discs are critical structural components of the spine, comprising the softer, more compliant portion that transmits approximately 80% of its axial loads, while providing almost all the mobility[26-28]. Degenerative or trauma-related changes to the intervertebral discs in the lumbar spine can lead to loss of structural integrity and, more importantly, debilitating chronic low back pain LBP[29]. Given the unclear etiology of degeneration-related LBP and lack of an accepted disease model, comprehensive treatment remains elusive[30]. For example, currently available surgical interventions such as lumbar fusion or artificial disc replacement might successfully mitigate pain symptoms when conservative treatment fails, but may not fully restore joint motion or force transmission capabilities[31-35]. Furthermore, iatrogenic factors lead to altered mechanical responses resulting in sub-optimal long-term outcomes[36,37]. Tissue engineering-based repair or replacement solutions to restore structural *and* functional capabilities, while retaining the capacity to remodel in response to external stimuli[38], present a promising treatment approach[39]. However, a lack of well-defined biomechanical functional benchmarks or design parameters with respect to the *in vivo* load capacity as well as disc height and deformation patterns has hindered successful translation of these approaches into clinical reality[40].

Although a multi-factorial conundrum, changes in the *in vivo* mechanical environment and the ensuing changes in biochemical environment within the discs have been accepted as separate but inter-related contributing factors to disc degeneration. Consequently, there is a growing interest in clarifying the mechanobiological links between the mechanotransduction, biochemical environment, and overall *in vivo* mechanical environment[30,41]. While *aberrant* mechanical loading has been determined to affect intervertebral disc cellular response in *ex vivo* experiments[42-46], there is limited knowledge regarding the *in vivo* mechanical environment of the lumbar intervertebral disc – such as stress and strain patterns – during dynamic functional activities. Studies employing direct intra-discal measurement techniques have generated limited, precious data to allow characterization of the intra-discal pressure distribution in various static positions[47-49] and even estimation of spinal loads therefrom[49]. Though insightful, a major limitation of these studies has been the inability to measure shear stresses and strains[41], which are thought to drive the degenerative cascade in the intervertebral discs[8,50]. Moreover, highly invasive, needle-based disc puncture techniques are now discouraged[41] due to the risk of instigating disc degeneration[51], and our understanding of *in vivo* loading relies primarily on computational models employing inverse static and dynamic analyses[14,22,52-57].

1.1.3.2 Limitations of Disc Deformation Measurements

Although several studies have investigated the disc height and deformation of the lumbar intervertebral discs, only a few have observed them in vivo. Some studies have quantified such parameters in vitro[58-60], while others have developed finite-element models to simulate disc deformation by utilizing disc geometry and material property data found in literature[61-64]. However, due to the absence of *in vivo* measurements in these studies, the kinematic and loading patterns prescribed may not be indicative of *in vivo* conditions, therefore limiting their significance. Despite a number of studies having utilized imaging techniques to quantify *in vivo* lumbar intervertebral kinematics at certain static postures or movements, only a few studies have used such data to examine in detail the associated deformation patterns of the intervertebral disc.

To our knowledge, (Pearcy et al.) was the first group to investigate lumbar disc deformation in vivo[65]. In this study, disc deformation was defined as the change in height of the anterior and posterior edges of the annulus fibrosis analyzed by lateral X-rays at the flexed and extended posture. Despite the simplistic analysis and imaging methodology, this study set the foundation for future investigations on lumbar intervertebral disc deformation. Many more subsequent studies have explored changes in disc height at discrete locations by utilizing similar imaging techniques to capture the lumbar spine during static poses[66-69]. While a few measurements may be satisfactory when attempting to calculate a rough estimate of disc height at a segment in order to make comparisons between symptomatic and asymptomatic groups, analyzing the disc in such a perfunctory fashion provides only limited information on the *in vivo* mechanical deformation of the intervertebral disc as a whole.

In a study by (Kanayama et al.), the intervertebral discs were approximated as quadrilaterals by connecting points placed at the anterior and posterior “corners” of adjacent vertebra seen in a static radiograph[70]. Participants then flexed their trunk from the neutral to the fully-flexed position over a span of six seconds, then returned to their upright position at the same speed, while a cineradiographic system captured their lumbar motion at a frequency of 25 Hz. At every 10 frames of motion, the deformation of each disc was estimated by the displacement of each point from the neutral position. The deformation data were then utilized in a finite-element model consisting of nuclei pulposi, annuli fibrosi, and vertebral endplates to calculate the *in vivo* strains of the disc at each segment. Compressive strains were reported at the anterior and posterior edges and shear strains were reported at the top and bottom edges of the L3L4, L4L5, and L5S1 discs. While this study greatly improved knowledge of disc mechanics with a dynamic analysis, the intervertebral disc geometry lacked the detail necessary to provide an accurate estimation of disc deformation except for at the anterior and posterior discrete locations of the disc. Furthermore, the imaging technique captured only sagittal plane views of the lumbar spine and was therefore incapable of seeing out-of-plane deformation of the disc.

A study by (Li et al.) investigated *in vivo* disc deformation using a more sophisticated method[8,71]. The participants were first asked to complete an MR scan in the supine position from which a model of the lumbar spine was created. The disc height, or distance between the adjacent vertebral endplates, was then calculated at approximately 800 points per disc. Participants were then asked to stand in the upright posture while a dual fluoroscopic imaging system captured images of their lumbar spine. Vertebral models of the L2 to L5 derived from an MR scan were then matched to the fluoroscopic image with a minimum accuracy of 0.3 mm and 0.7° in position and orientation, respectively. Once the position and orientation of each vertebra was determined, the elongation of the point-to-point distances in the normal and shear direction during the weight-bearing kinematics were calculated to quantify the compressive and shear strains in the disc.

Deformation plots at each joint level were created and compressive and shear strain values at nine discrete locations were further analyzed. This sophisticated method of quantifying disc deformation showed the ability to utilize imaging techniques to obtain the subject-specific vertebral geometry and kinematics necessary to calculate *in vivo* disc deformation. However, the deformation was calculated only at a static standing position, providing no indication of how the disc deforms during a dynamic task. An additional limitation is that the deformation characteristics of their extremely detailed discs (~800 points each) were only compared between joint levels at nine different locations. A more complete analysis inclusive of the entire disc area would be preferred.

In another study by (Li et al.), the same general technique was applied to analyze the effects of DDD on the disc deformation at cephalic levels of the lumbar spine[8]. In this study, deformation was analyzed at six end-range of motion postures with respect to the standing position. The maximum tensile and shear deformations, along with the percentage of disc area experiencing less than 5% deformation, were determined at each posture and compared between disc levels and patient types. This study improved upon the previous study by reporting range of motion values of disc deformation, however the limitation of only capturing deformation at static poses remained. Furthermore, the deformation plots corresponding to several of the static postures went unreported, while differences in deformation between segment levels were not determined across the entire disc area.

(Martin et al., 2018) developed a framework for quantifying disc deformation in vivo and assessing durnial variations in lumbar disc shape[72]. While the MRI-based framework proved capable of detecting spatial changes in L5-S1 shape after daily activity, the changes in other lumbar segments were not studied, apart from serving as a sensitivity analysis of the methods. Further, the study was not designed to provide insight on the mechanical strains induced during normal functional activity, but only the resulting changes in disc height after activity.

One study investigating the effect of lumbar axial rotation on the distribution of intervertebral disc height performed a very detailed and structured analysis of changes across the entire disc area[73]. In addition to providing color maps of the disc height distribution at the supine position and supine + axially rotated position during CT scans, each disc was separated into five regions, where the differences in mean disc height of each region before and after lumbar rotation were determined. The effects of spinal level, disc degeneration, age, sex, and symptomatic low back pain were also analyzed using a Fisher post hoc test. The detailed analysis and description of the dataset showing areas of the disc that may be more affected by torsion and provides a strong, comprehensive benchmark with which future studies can verify their data against. However, despite the in-depth analysis, like many other studies this data does not reflect the functional and/or dynamic mechanics of the lumbar spine.

1.1.3.3 Disc Deformation Knowledge Gaps

Currently, some significant knowledge gaps surrounding the disc height and deformation patterns of the lumbar intervertebral discs continue to exist. First, a detailed description of the instantaneous intervertebral disc height and deformation patterns during dynamic motion is still missing. Second, quantification of disc deformation during more physically demanding functional activity, and how external loading and lumbar segment level affect the deformation patterns needs improvement. Third, there is still need for a more novel and comprehensive method of analyzing the deformation patterns throughout the entire disc area, while also establishing differences between segment levels of the lumbar spine.

1.1.4 In Vivo Facet Joint Kinematics

1.1.4.1 Significance

Lumbar facet joint (FJ) pain is a prevalent pathology shown to account for around 20% of cases of low-back pain (LBP)[74,75], but its biomechanical antecedents are less clear. Although changes in FJ mechanics, particularly kinematics, have been linked to tissue degeneration[76-78], quantification of their normal mechanics *in vivo* during functional activity is lacking. Such normative data are important, as studies have alluded to associations between deviations from "*normal*" facet mechanics and the overloading or damaging of surrounding spinal tissues, such as facet cartilage, capsular tissues, and intervertebral discs[5,6,76]. Additionally, excessive or *abnormal* motion between lumbar facet surfaces can stress the well-innervated cartilaginous tissues and capsular ligaments of the FJ, which have been shown to release pain receptors when put under significant stress[79-82].

From a clinical perspective, an accurate depiction of normal facet joint *translational kinematics* can help improve our understanding as well as diagnosis of degenerative diseases such as FJ osteoarthritis. For example, FJ gap is an important metric for evaluating the progression of osteoarthritis, as narrowing of the facet gap and subsequent articular cartilage thinning have been highly correlated with the onset of osteoarthritis[76,83,84]. Nevertheless, static CT imaging-based evaluations of facet gap[76] or facet contact area[85] may not discern the presence of different damage mechanisms based on differing movement patterns[86], and, as reiterated by (Simon et al., 2012), relationships between extent and location of facet degeneration and *in vivo* kinematics still require further clarification. Secondly, although FJ pain and associated osteoarthritic conditions are often preceded by degenerative disc disease, it has also been shown to occur without concomitant disc degeneration in about 20% of degenerated spines[87]. This implies FJ pathologies are not always directly attributable to pathologies arising within the intervertebral disc[87-90].

Quantifying dynamic *in vivo* lumbar FJ motion, however, can be quite challenging given the relatively small magnitudes of translation. At present, our understanding of FJ motion is based primarily on *in vitro* cadaveric studies[10,86] or CT and MRI imaging in static, non-functional positions[76,91,92]. Li and co-workers were the first — and to our knowledge the only to attempt — to demonstrate the use of biplane video-fluoroscopic imaging to quantify facet 3D angular and translational orientations in functional weight-bearing poses in healthy individuals[93]. While their study provided invaluable insight into FJ orientation in static poses, a dynamic dataset acquired during functional activities could offer more clarity normal physiological motion of the lumbar facet joints.

1.1.4.2 Progression of Facet Joint Kinematic Measurements

(Otsuka et al.) investigated the *in vivo* lumbar facet area in both asymptomatic and chronic LBP subjects[85]. Following a CT scan of the participant, an orthopedic surgeon traced the superior and inferior facet joint surfaces slice by slice, ultimately creating a polygon mesh of the entire facet surface. The area of each facet joint was determined by combining the surface area of the two adjacent facet surfaces, and differences between left and right location, symptomatic pain group, segment level, and age were analyzed. (Simon et al.) investigated lumbar facet joint space *in vivo* by analysis of CT scans from asymptomatic subjects[76]. First, the facet surfaces from L1 to S1 were separated into five separate anatomical zones. Using a least-distance method, the facet joint space width was calculated between adjacent facets at each point on the surfaces. Differences in spacing between the zones, segment levels, age, and pain symptoms were evaluated. These studies provides valuable, detailed information regarding facet joint parameters associated with mechanical loading and osteoarthritic conditions of the facet joint. Nevertheless, static CT imaging-based evaluations of facet gap or facet contact area may not discern the presence of different damage mechanisms based on differing movement patterns[86], and, as reiterated by (Simon et al., 2012), relationships between extent and location of facet degeneration and *in vivo* kinematics still require further clarification.

Li and co-workers were the first — and to our knowledge, the only group — to demonstrate the use of biplane video-fluoroscopic imaging to quantify lumbar facet 3D angular and translational orientations in static, functional weight-bearing poses in healthy individuals[93]. In this study, the same methodology as described by (Li et al., 2009) was utilized to examine the functional range of motion of the lumbar facet joints. Participants were asked to assume several different postures while a biplane fluoroscopy system captured static images of their lumbar spine. MR models of each vertebra were created and registered to the images to determined their respective 3D position and orientation in space during each posture. Facet joint ranges of motion were based on the overall difference in kinematics between the flexed and extended, left and right bending, and left and right axial rotation postures. Although range of motion data provides valuable insight on the overall motion the facet joint may experience, the degree of linearity of the kinematic pattern is undetectable due the absence of instantaneous facet joint kinematics during dynamic motion of the lumbar spine. It should also be noted that although the overall accuracy in determination of position and orientation of the vertebra are impressive (0.3 mm and 0.7°, respectively), the facet joints' translational and angular ranges of motion, primarily during twisting and bending, were nearly just as small. Therefore, even slight improvements in accuracy would lead to more dependable results. In two other studies by Li and co-workers, the effects of disc degeneration and degenerative spondylolisthesis on facet joint kinematics were determined using the same approach and consisted of the same limitations[5,94].

Similar to disc deformation, there are still a few aspects of facet joint kinematics that remain absent from literature. First, a dynamic description of *in vivo* facet joint kinematics, as opposed to static or range of motion values, is not yet available. Furthermore, the effect of a more physiological demanding functional activity on the dynamic *in vivo* motion of the facet joint has not yet been examined. Due to the relatively small values of facet joint translations, improvements in accuracy of the position and orientation of the lumbar vertebrae are necessary to adequately examine *in vivo* facet joint motion.

1.1.5 Biomechanical Models of the Lumbar Spine

1.1.5.1 Lumbar Spine Finite Element Models

Due to the relative infeasibility of measuring the loading patterns in the lumbar spine *in vivo*, they are often estimated using computational models. Several studies have developed or utilized finite element (FE) models to observe the functional mechanics of the lumbar spine[4,20,21,23,24,95-98]. A common limitation shared amongst these studies is that their models' lumbar motions are either prescribed according to, or validated against, *ex vivo* data or *in vivo* data with substantial limitations. These limitations include lack of dynamic characterization, lack of translational kinematics, and limited accuracy. While some of these models have proven capable of replicating kinematic and loading patterns within ranges of measured values from *ex vivo* studies[20,23,24,95], a study comparing eight previously validated and published FE models found that replicating *in vivo* flexion of the lumbar spine is a challenge[16]. When subjecting the models to the physiologically realistic compressive loads and flexion moments determined by (Rohlmann et al., 2009)[99], each model that was able to converge produced L2L3, L3L4, and L4L5 intervertebral rotations that substantially underestimated those measured *in vivo* by (Pearcy et al., 1984)[65]. As demonstrated by this study, a disadvantage of FE modeling is the difficulty of replicating the *in vivo* physiological environment of the lumbar spine.

1.1.5.2 Lumbar Spine Musculoskeletal Models

Another approach to analyze lumbar mechanics is rigid body modeling. While FE modeling offers the advantage of investigating the stress and strain distributions within deformable structures, FE models are typically best-suited for static analyses. On the other hand, rigid body modeling has often been used to determine generalized forces, moments, and muscle activity during dynamic motion. Some studies have taken the approach of combining rigid body and FE modeling to obtain both rigid body and soft tissue behavior of the lumbar and cervical spine[100,101]. While there are advantages of incorporating FE models of the intervertebral discs and ligaments within a dynamic RBM of the lumbar spine, their inclusion is not necessary to drive the proposed model. In our case, soft tissue properties – such as the intervertebral disc, facet joint capsules, and ligaments – will have no effect on the model's lumbar kinematics, as the intervertebral joint motion will be explicitly prescribed as an input based on the acquired measurements from DSX. However, the stiffness of the soft tissue *will* affect the magnitude of loads transferred to the joints during simulation. In an FE model, these loads would rely entirely on the material properties defined within the model, which unfortunately were not quantifiable *in vivo* and would have to be estimated based on data from previous studies. Although feasible, generating subject-specific FE models of the soft tissue at each segment level for every subject involved in the study would be an extremely time-consuming task. Given that the behavior of the FE components would be completely reliant on *estimated* material property values, the value added to the model may not justify the effort required. This decision was made with the realization that a more time-efficient solution was available.

Alternatively, rigid-body modeling software allows the stiffness of a joint to be defined by a "bushing element", described by a 6x6 matrix defining the force-displacement and moment-angle relationships at a joint. Like the material properties of intervertebral soft tissue, joint stiffness data based on *ex vivo* studies is also readily available from literature[102-104]. Implementing bushing elements at each joint will provide us with a more computationally efficient method to define intervertebral joint stiffness compared to generating FE models. Therefore, FE modeling will not be included within the main body of work in this study. However, to aid in defining the stiffness properties of the model's bushing elements, load-displacement curves of the lumbar joints quantified by a co-existing FE study will be utilized.

A number of RBMs have been developed to estimate muscle forces and joint reaction loads in the lumbar spine[11,12,17,19,22,54,105-111]. While dynamic models of the lumbar spine exist, a lack of comprehensive dynamic *in vivo* lumbar kinematics in literature compels these models to prescribe motion based on an average dataset from either individual or a combination of studies. In all but one of these studies, the lumbar intervertebral kinematics implemented within the models are prescribed using data from *ex vivo* or static *in vivo* datasets. To our knowledge, (Eskandari et al., 2017) is the only study that has used image-based subject-specific kinematics to drive the kinematics of an RBM model[109]. However, it should be noted that the translational motion, although acquired, did not appear to be included within the RBM model. Furthermore, only static postures were analyzed by the model for a single subject. An additional limitation of this study, which is commonplace among many of the existing RBMs[12-15,19,22,96,97,105,109,111], is the absence of passive elements such as ligaments or facet joints necessary to simulate the load-sharing capability of the lumbar spine. Without the incorporation of subject-specific vertebral kinematics, direct use of these models aren't necessarily suitable to evaluate subject-specific lumbar mechanics as differences in lumbar rhythms – for example, between an individual's lumbar rhythm and that of an average dataset – have been shown to affect the distribution of lumbar loads[11].

1.1.5.3 Improving Subject-Specific Musculoskeletal Models

Multi-body musculoskeletal modeling based on inverse dynamics is a commonly deployed approach for assessing mechanical loading within the lumbar spine. As with any modeling approach, the accuracy of resulting load predictions is sensitive to the quality of the input parameters. Fundamental to modeling is the validity of simplifying assumptions governing two key sets of input parameters and their interaction: joint kinematics and passive tissue [intervertebral discs (IVD) and ligaments] stiffness properties.

Under conventional assumptions, three rotational degrees of freedom (DOF) are sufficient for describing the kinematics of individual intervertebral joints (IVJ) comprising the lumbar spine; translational DOF are either non-existent, or, at best, small enough to only negligibly influence joint reaction force estimates. Second, individual IVJ rotations can be satisfactorily interpolated from the overall lumbar spinal rotations based on a fixed fractional distribution—lumbar spinal rhythm—throughout the entire range of a given movement[14,112-114]. Consequently, IVJ were routinely modelled in rigid body musculoskeletal spine models as 3-DOF spherical joints with their individual rotational contributions estimated based on a presumed lumbar rhythm. Over the last decade, however, new in vivo 6-DOF intervertebral kinematic data acquired using technologies such as dynamic X-ray imaging have challenged these assumptions[37,109,115-119].

The availability of in vivo subject-specific intervertebral kinematics data presents a dilemma for the modelers. On one hand, the 6-DOF kinematic datasets for individual IVJ based on direct vertebral motion measurements *theoretically* present the opportunity to obtain more accurate joint load estimates than was possible before. On the other hand, increased complexity of these input datasets can not only lead to higher computational cost, but also extract a more stringent penalty for any errors within these datasets, heightening the demand on the accuracy of these parameters. For example, a recent *Monte Carlo* simulation-based study reported that even small translation component errors (0.1 – 0.3mm) could induce large variations in IVD joint force estimates[120].

Passive stiffness properties of the intervertebral disc (IVD) and ligaments comprise the second key set of input parameters. Solving an inverse dynamics problem, as it pertains to the lumbar spine, requires an accounting of the contribution of active *(muscles) and* passive *(IVD and ligaments)* components supporting the lumbar joint to properly satisfy the joint's measured generalized displacements, velocities, and accelerations during a specific movement. Passive reaction moments arising from IVD and ligament deformations contribute to the total reaction moment, thus altering the net moment contribution from the musculature and, consequently, the distribution of forces across the involved muscles and the resultant joint reaction forces. Hence, assumptions regarding the representation of the IVD and ligaments could have significant effects on model simulation results. For instance, while the IVD and ligaments are inherently nonlinear, linear stiffness properties are often assumed[121-123]. Second, the corresponding *in vivo* initial or "neutral position" and, consequently, the magnitudes of inherent pre-strain within these structures are not always known, thus creating an additional source of variability.

1.2 Specific Aims and Significance

1.2.1 Specific Aim 1

Quantify subject-specific 3D lumbar intervertebral disc height and disc deformation patterns during a dynamic lifting task. Instantaneous measured of nominal compressive and shear strain across the entire disc area will be calculated with respect to disc height at the upright posture.

Hypothesis 1.2.1.1: Upright disc height, flexed disc height, and the dynamic nominal compressive, shear, and radial strain trends will vary with segment level.

Hypothesis 1.2.1.2: The magnitude of external load listed will affect the upright disc height, flexed disc height, and the dynamic nominal compressive and shear strain trends.

Hypothesis 1.2.1.3: Intervertebral disc height will influence the rotational kinematics of the corresponding joint level.

1.2.2 Specific Aim 2

Determine subject-specific 3D lumbar facet joint kinematics during the dynamic lifting task. Instantaneous measures of translational kinematics between adjacent facet surfaces will be calculated.

Hypothesis 1.2.2.1: Facet joint translational motion patterns will vary with segment level.

Hypothesis 1.2.2.2: The magnitude of external load lifted will affect facet joint translational motion patterns.

1.2.3 Specific Aim 3

Quantify subject-specific joint and muscle loading patterns in the lumbar spine during the dynamic lifting tasks. Study the effects of vertebral kinematic input and joint stiffness properties on joint reaction forces and force distribution among the components of the lumbar spine. A previously-existing lumbar model will be enhanced to include intervertebral soft tissue passive stiffness and 6-DOF subject-specific in vivo lumbar kinematics. Rhythm-based lumbar kinematics from literature and DSX-derived kinematics will be implemented within the model separately, as will linear and nonlinear stiffness properties of the soft tissues.

Hypothesis 1.2.3.1: The inclusion of DSX-derived vertebral kinematics, as opposed to an average, rhythm-based kinematic dataset, will affect joint reaction force magnitudes during the lifting task.

Hypothesis 1.2.3.2: Force distribution trends among lumbar muscles will be affected by the integration of DSX-derived vertebral kinematics.

Hypothesis 1.2.3.3: The inclusion of linear passive stiffness properties, nonlinear passive stiffness properties, or the exclusion of passive stiffness will result in uniquely different lumbar muscle force distribution and joint reaction forces throughout the lifting motion.

Hypothesis 1.2.3.4: Compressive and shear deformation trends (from Aim 1) will linearly correlate with the compressive and shear joint reaction forces estimated by the model simulations.

1.2.4 Clinical Significance

Despite the valuable insights provided by previous studies investigating the lumbar spine, knowledge of *in vivo* lumbar mechanics remains incomplete. Disc deformation and facet joint kinematics have been quantified by previous studies but are limited by their lack of dynamic characterization, particularly during functional activity. The loading patterns of lumbar components estimated by MS models also remain limited due to either assumptions regarding lumbar vertebral kinematics, absence of dynamic analysis, inability to quantify load distribution, and limited sample size. The current work will fill the knowledge gap first by utilizing previously measured vertebral kinematics to quantify *in vivo* disc deformation and facet joint kinematics during a functional lifting task. Subsequently, subject-specific DSX-derived vertebral kinematics will be incorporated within a full-body musculoskeletal model – consisting of an enhanced lumbar spine – to estimate loading patterns in the intervertebral discs, facet joints, ligaments, and muscles of the lumbar spine. The sensitivity of the simulation's results will be thoroughly assessed to observe the influence of model parameters, such as input kinematics, joint configuration, and stiffness properties

Potential applications of the work resulting from this proposal are widespread. As previously emphasized, studies investigating the kinematic or loading patterns of the lumbar spine often look to *ex vivo* or static *in vivo* datasets to validate their results. Although appropriate for some studies, the limited availability of dynamic *in vivo* datasets hinders the ability of those investigating dynamic lumbar mechanics to properly evaluate their data. The characterization of disc deformation, facet joint kinematics, and load distribution between lumbar structures determined in this work can provide dynamic, functional benchmarks that previous studies were unable to provide. Furthermore, the data could serve as a reference for healthy lumbar mechanics to assist studies with identifying aberrations in the mechanics of the dysfunctional lumbar spine, such as patients suffering from DDD for facet joint osteoarthritis.

These benchmarks, aside from validation, can be utilized for other purposes as well. From a clinical perspective, accurate characterization of *in vivo* lumbar mechanics during a functional activity is critical to the design of orthopaedic interventions. For example, the current "gold standard" treatment for DDD is lumbar fusion, where the two adjacent vertebrae surrounding the injured disc are fused together to prevent the pain-inducing segmental motion. Although this procedure has achieved moderate success in relieving symptomatic pain, studies have found that lumbar fusion may have long-term adverse effects on the health of adjacent segments[31,124]. Ideally, in the case of DDD and also other musculoskeletal disorders, spinal interventions would effectively restore the motion and loading patterns of a healthy intervertebral disc and facet joint to effectively eliminate abnormal loading of adjacent segments. An example is the total disc replacement (TDR), an alternative treatment to the lumbar fusion that inserts an artificial disc between adjacent vertebrae to relieve pain while maintaining flexibility at the joint. However, a systematic review on TDR for patients with symptomatic lumbar degenerative disease found no sufficient evidence of long-term benefits compared to lumbar fusion. Furthermore, cohort studies have reported a wide range of post-TDR complication rates due to many factors, including implant failure or displacement[125]. Successful translation of these approaches into clinical implementation may be hindered by the lack of well-defined functional benchmarks or design parameters with respect to load capacity as well as motion patterns of the intervertebral disc[40]. Advancing our knowledge on disc deformation, facet joint kinematics, and joint loads during a dynamic lifting task can provide insight on the physiological mechanics that orthopaedic interventions should account for. Furthermore, knowledge of how the mechanics vary across intervertebral levels may indicate the need for segment-specific implants or intervention techniques.

2.0 Research Design and Methods

2.1 Previous Data Acquisition

2.1.1 Participant Recruitment

Data utilized in the current work was acquired during an Institutional Review Board (IRB)-approved study in which 14 healthy participants (8 male, 6 female, aged 19-30, 54-92 kg) were recruited to perform upright standing and functional load-lifting tasks while their lumbar spine motions were recorded using dynamic stereo-radiography (DSX)[116]. Participants reported having no issues of low back pain or lumbar spine deformities. All participants provided informed consent, and IRB guidelines and regulations were appropriately followed.

2.1.2 Data Collection and Data Processing

The study involved DSX imaging of a participant's lumbar region during several static standing and dynamic straight-legged lifting tasks while holding various weights of external load (4.5 kg, 9.1 kg, 13.6 kg). Simultaneously, surface marker-based motion and ground reaction forces (GRF) were captured to obtain full-body kinetics and external loads of the participants. Afterwards, the participants completed a CT scan in the supine position. Using a previously validated methodology, vertebral bone models derived from the CT data were co-registered to the two DSX radiographs using a volumetric model-based tracking process to determine the 3D bone positions and orientations in space with sub-millimeter accuracy (≤ 0.5°; 0.3mm). This was done during each timeframe of the static standing and dynamic lifting tasks[116,126].

2.2 Disc Height and Deformation

2.2.1 Approximation of Intervertebral Disc

On each endplate of the vertebra from L2 to L5, four points were manually picked; two at the furthest anterior and posterior locations along the *approximate* anterior-posterior (AP) axis, and two at furthest left and right locations along the *approximate* medial-lateral (ML) axis. Based on the eight endplate markers, a right-handed orthogonal coordinate system was created at the center of the vertebral body.

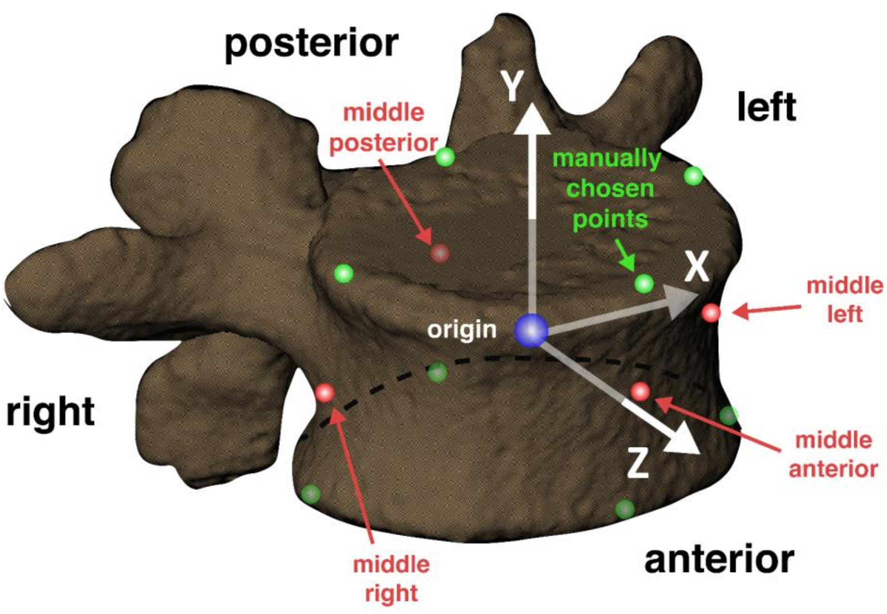

Figure 1: Manually picked points and anatomical coordinate system of vertebra.

The anatomical origin of the vertebral body was defined as the average of the eight points (Figure 1), while the vertebra's X-axis extended from origin parallel to the vector connecting the middle right point to the middle left point. The Y-axis was defined as the cross-product of the vector connecting the middle posterior point to the middle anterior point and the X-axis. Finally, the Z-axis was then defined as the cross product of the X- and Y- axes. Due to its difference in geometry, the coordinate system of the S1 was dependent only on four points picked on the superior surface (Figure 2).

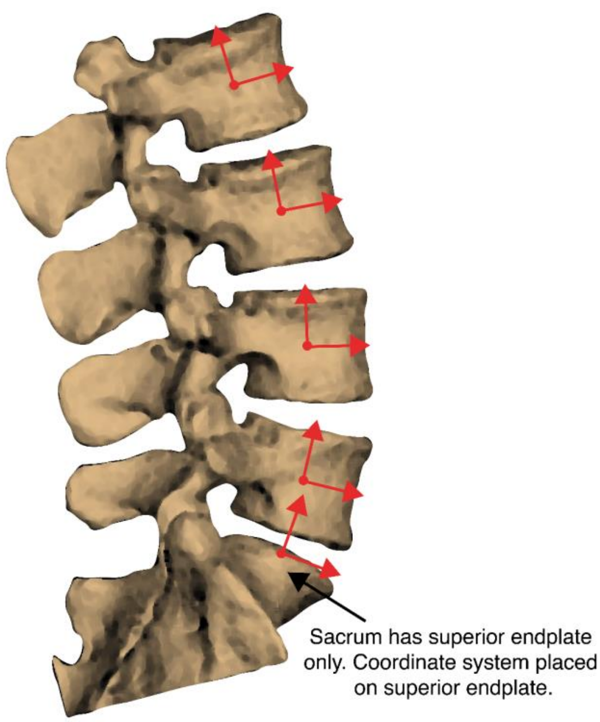

Figure 2: Difference in coordinate system definition for sacrum

The origin of the S1 was defined as the average location of the four points, while the X-axis was defined as the vector connecting the superior right marker to the superior left marker. The Y-axis was defined as the cross product of the vector connecting the superior posterior point to the superior anterior point and the X-axis, and the Z-axis was defined as the cross product of the X- and Y- axes. The vertebrae's X-, Y-, and Z- axes corresponded to the ML, superior-inferior (SI), and AP directions, respectively. The CT-acquired surfaces of the vertebral bone models were represented as triangular meshes sampled with a 0.8 mm spacing.

The location of all triangular element vertices and centroids in the defined anatomical coordinate system were imported into MATLAB (R2016b, Mathworks Inc., Natick, MA) as point clouds.

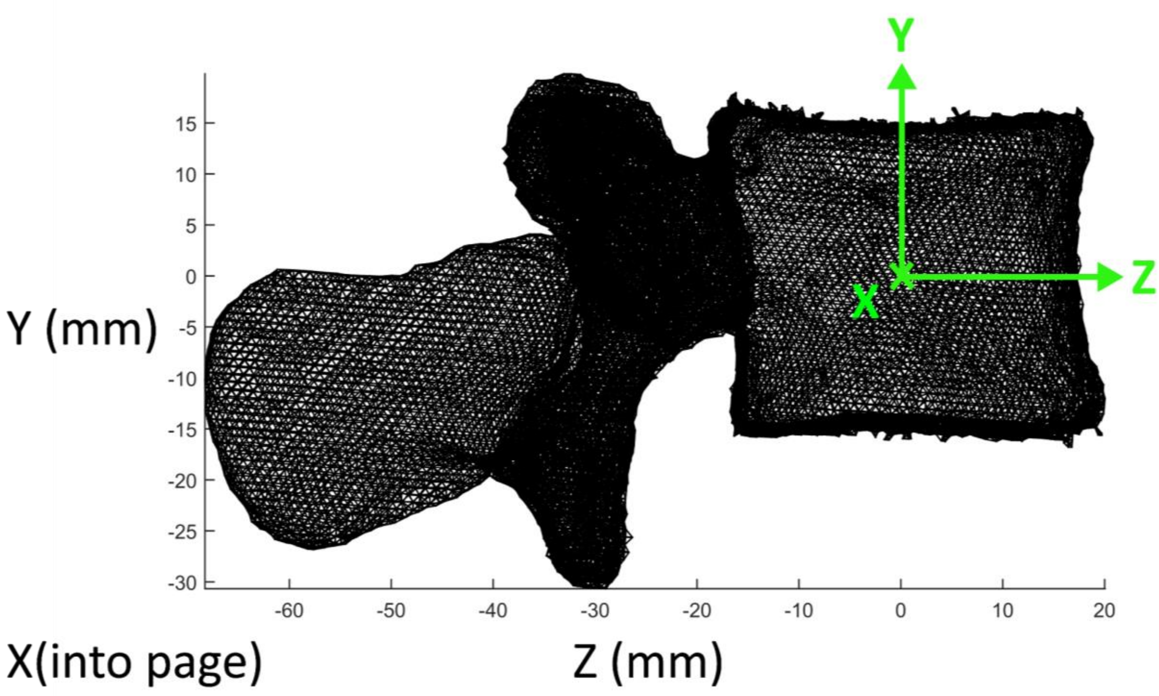

Figure 3: Vertices of all triangular elements forming the vertebra with coordinate system

A MATLAB algorithm was developed to generate a representation of each intervertebral disc as approximately 4000 line segments (exact number varies by bone size) between adjacent endplates of the vertebrae based on a previously published method[127]. A custom written algorithm was developed to isolate the vertebral endplates of each vertebral while it was placed in its local anatomical coordinate system (Figure 3). Triangular elements with a Y-coordinate greater than or less than zero were said to be located on the superior or inferior half of the vertebra, respectively. Any triangular element on the superior (or inferior) half of the vertebra with a centroid whose X-coordinate was further from the center than the superior (or inferior) left or right marker was excluded. Any triangular element with a centroid who Z-coordinate greater than 1.5 times that of the superior (or inferior) posterior or anterior points was also excluded; the extra 0.5 allowance was to prevent exclusion of the vertebral endplate's left and right posterolateral regions, which can curve slightly outwards from the center of the vertebra (Figure 4). For the L2 to L5, any triangular element whose centroid was between -7 and 7 mm in the Y-direction was excluded, as these were points located towards the center of the vertebral body. Since the anatomical coordinate system for the S1 was on its superior vertebral surface, any triangular element of the S1 whose centroid was less than -5 mm was excluded, as these points were located below the superior endplate (Figure 2). Altogether, these criteria effectively excluded the more central portions of the vertebral bodies which the disc would not contact. Next, any triangular element above the vertebral body center with a Y-component of the normal vector less than 0.3 was excluded, as it was considered to be located on the side of the vertebral, as opposed to the top or bottom endplate. Similarly, a triangular element below the vertebral body center with a Y-component of the normal vector greater than -0.3 was excluded. These two criteria excluded triangular elements on the curved edges present between vertebral surfaces and the vertebral body which faced more outwards (along AP or ML axes) than upwards or downwards (along SI axis). An example of the resulting surface after filtering these points is shown in Figure 4. After applying these criteria, each vertebra was represented only by an inferior and superior vertebral endplate.

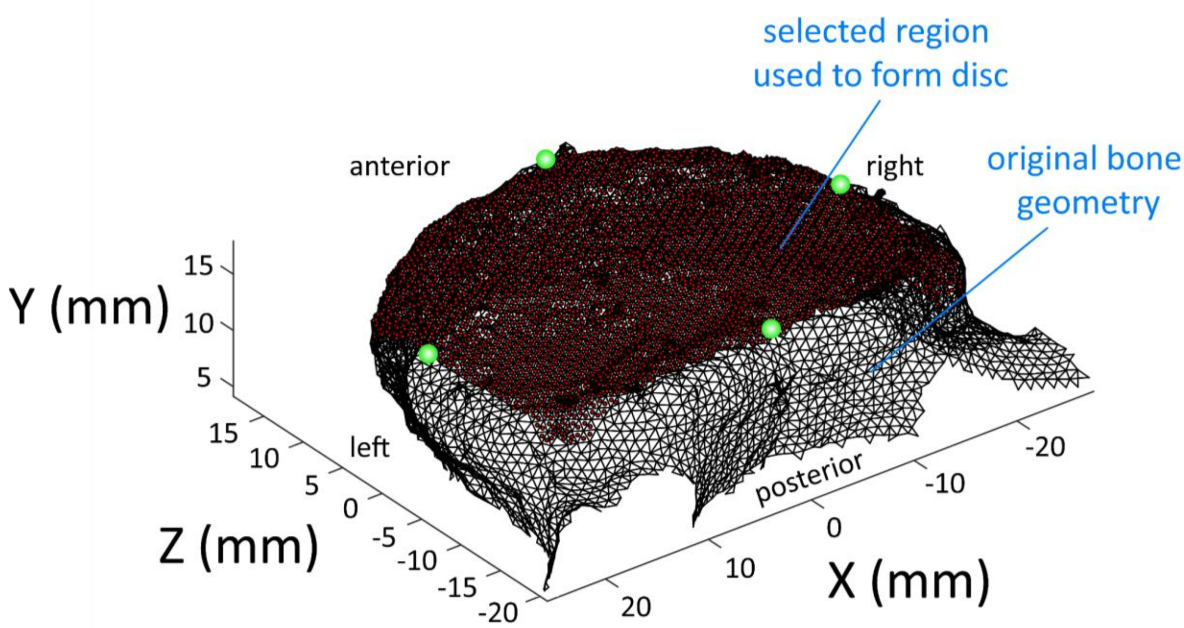

Figure 4: Superior endplate surface of a vertebra after filtering via MATLAB. Red points are the centroids of triangular elements considered to be part of the intervertebral disc area.

The point clouds for the L2 to S1 endplates were placed in their respective 3D orientation and position, in the S1 coordinate system, corresponding to the participant's recorded DSX positions and orientations while assuming the upright position. It was decided that the intervertebral disc would be formed by line segments starting from the inferior bone and intersecting the superior bone. The superior surfaces of the vertebrae (*inferior* surfaces of the discs) were represented by the triangular element *centroids*. While it is valid to model a line segment from any point on the surface – such as the centroid of an element – the locations of the triangular vertices and their connections with one another is what represents the actual CT-measured surfaces of the vertebrae, and are necessary to calculate the exact intersection point of the line segments with the superior vertebra. Thus, the inferior surfaces of the superior vertebrae (*superior* surfaces of the discs) were represented by the triangular element *vertices* and their connections with one another (Figure 5).

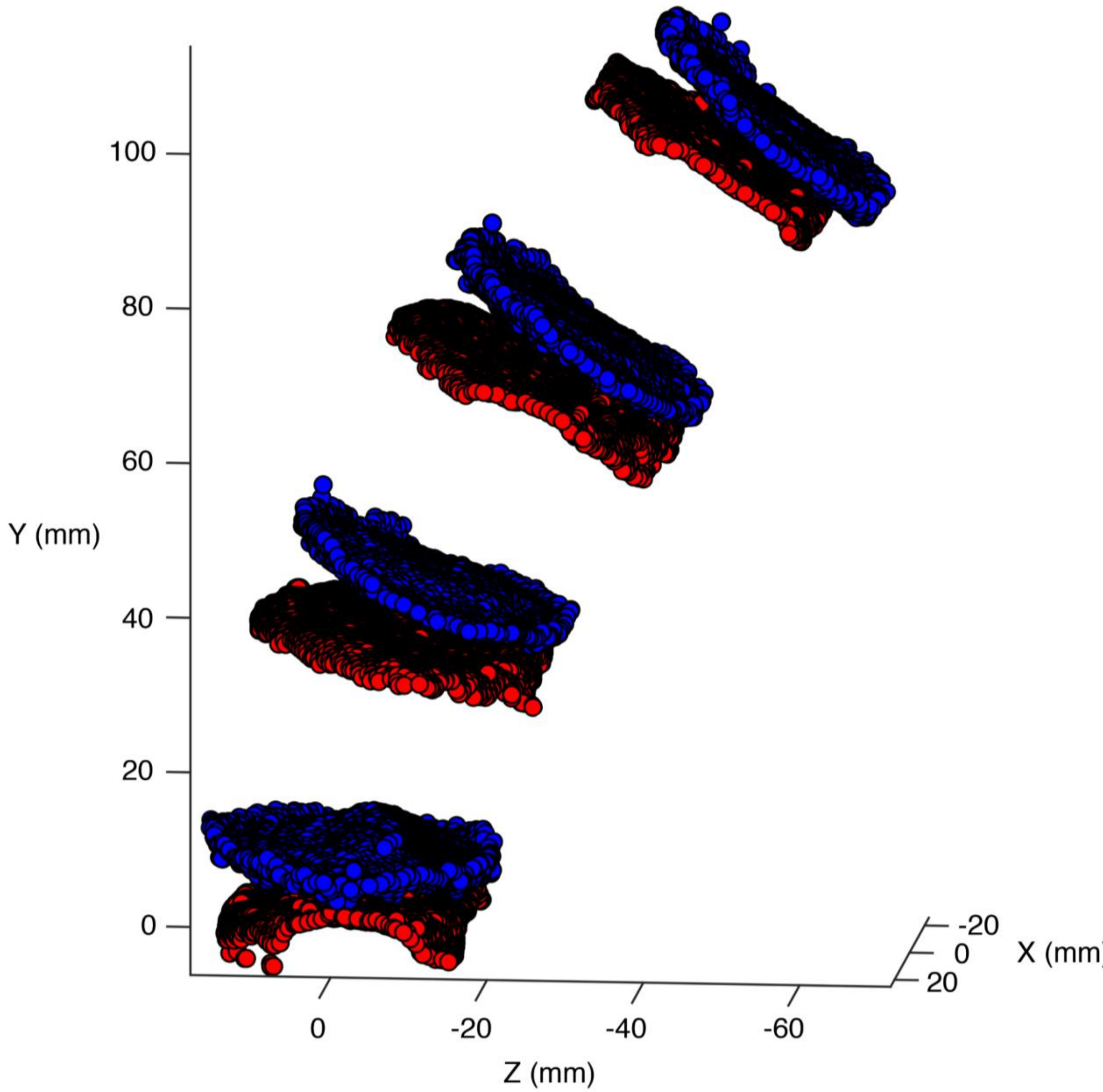

Figure 5: Inferior and superior surfaces of the intervertebral discs in the sacrum's coordinate system. Inferior surfaces of the discs (red) are represented by the centroids of the triangular elements, while the superior surfaces of the discs (blue) are represented by the vertices of the triangular elements

A plane was then fit to the full set of coordinates representing each inferior or superior vertebral endplate by finding the plane of least squared distance to the set of isolated centroids (Figure 6). The orientation of the plane was determined by finding its normal vector, which is the eigenvector ($\overrightarrow{v_1}$) associated with the lowest eigenvalue (λ) where:

$$[\boldsymbol{R}'\boldsymbol{R}]\vec{v} = \lambda\vec{v} \tag{2-1}$$

Here, $\boldsymbol{R}$ is an $N \times 3$ matrix (N = number of centroids) of centroid coordinates with respect to the average location of all centroids (**p**), and $[\boldsymbol{R}'\boldsymbol{R}]$ is the covariance matrix. The plane of each disc – which we will call the disc plane – from L2 to S1 was set to equal the average of the planes of the two adjacent surfaces (Figure 7).

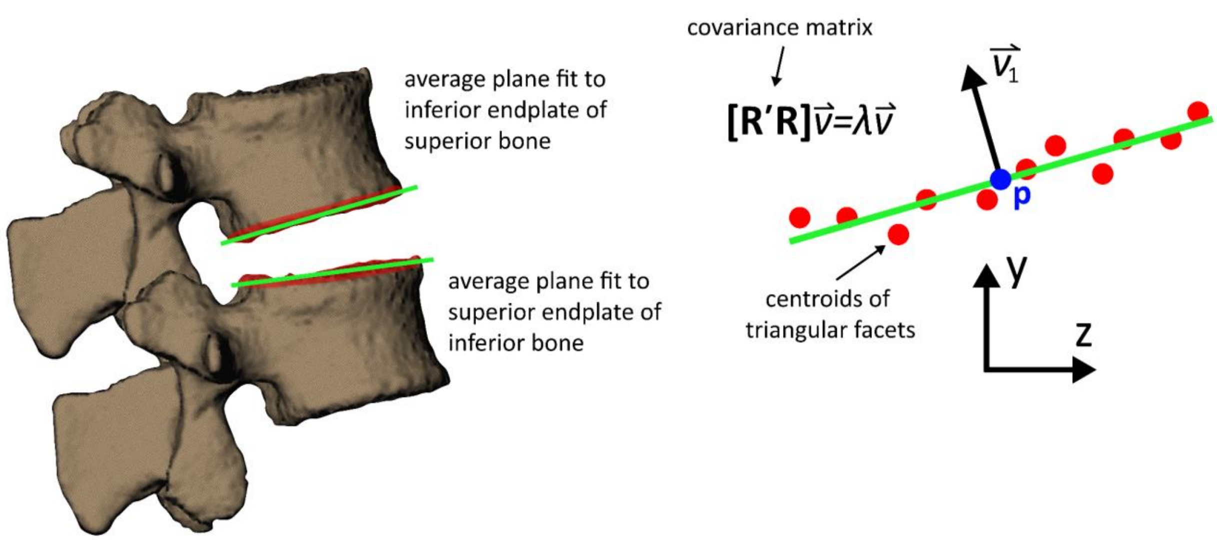

Figure 6: The average planes of the vertebral endplates were determined

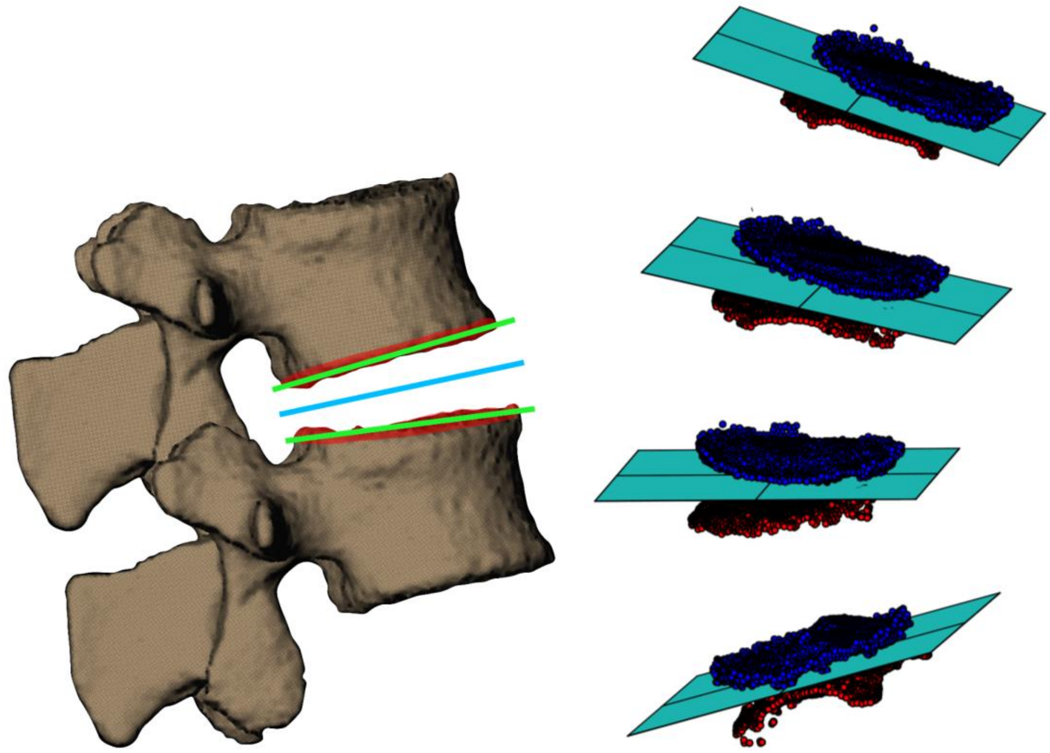

Figure 7: The disc plane at each joint was defined as the average of the two endplate planes

A line starting at the triangle's centroid on the superior surface of the inferior vertebra extended perpendicular to the disc plane and through the inferior surface of the superior vertebra (Figure 8). The triangular vertex on the intersected surface nearest to the line segment (T_2) was found. To maintain the line segment's perpendicularity with the normal plane, while also allowing it to intersect the surface, it was required to determine which triangular element consisting of vertex T_2 the line segment intersected. To do this, a ray-triangle intersection method was employed between the line segment and each of the triangular elements touching T_2. The ray-triangle intersection method involved two steps, the first of which determined the intersection point (p_1) between the line segment – extending from the centroid of the inferior vertebra (L_1) to an end point (L_2) defined to be beyond the superior vertebra – and the plane along which the triangular element lies:

$$L_{int}(p_1) = L_2 + p_1(L_1 - L_2) \qquad 2\text{-}2$$

where

$$p_1 = \frac{\mathbf{n}\cdot(T_0 - L_2)}{\mathbf{n}\cdot(L_1 - L_2)} \qquad 2\text{-}3$$

and **n** is the normal vector of the triangular element plane. However, this intersection point is where the line segment intersects the *infinite* plane on which the triangular element lies, not the plane bounded by the element's vertices. Thus, the second step calculated the parametric coordinates (*s*,*t*) with respect to the vertex T_0 of the element:

$$T(s,t) = T_0 + s\mathbf{u} + t\mathbf{v} \qquad 2\text{-}4$$

$$s = \frac{(\mathbf{u}\cdot\mathbf{v})(\mathbf{w}\cdot\mathbf{v}) - (\mathbf{v}\cdot\mathbf{v})(\mathbf{w}\cdot\mathbf{u})}{(\mathbf{u}\cdot\mathbf{v})^2 - (\mathbf{u}\cdot\mathbf{u})(\mathbf{v}\cdot\mathbf{v})} \qquad 2\text{-}5$$

$$t = \frac{(\mathbf{u}\cdot\mathbf{v})(\mathbf{w}\cdot\mathbf{u}) - (\mathbf{u}\cdot\mathbf{u})(\mathbf{w}\cdot\mathbf{v})}{(\mathbf{u}\cdot\mathbf{v})^2 - (\mathbf{u}\cdot\mathbf{u})(\mathbf{v}\cdot\mathbf{v})} \qquad 2\text{-}6$$

$$\mathbf{u} = T_1 - T_0,\ \mathbf{v} = T_2 - T_0,\ \mathbf{w} = L_{int} - T_0$$

When $s > 0$, $t > 0$, and $s + t < 1$, the line segment was confirmed to intersect within the triangle's boundary and the parametric coordinates were stored. This process was repeated for all centroids on the superior endplate of the inferior vertebra (Figure 9). If a point extending near the edge of the inferior vertebra's superior endplate didn't intersect the superior vertebra, the line segment was considered to be outside of the boundary of the intervertebral disc and was discarded. Endpoints of the line segments remained connected to the endplates at these defined locations as the vertebrae moved relative to each other during lumbar motion.

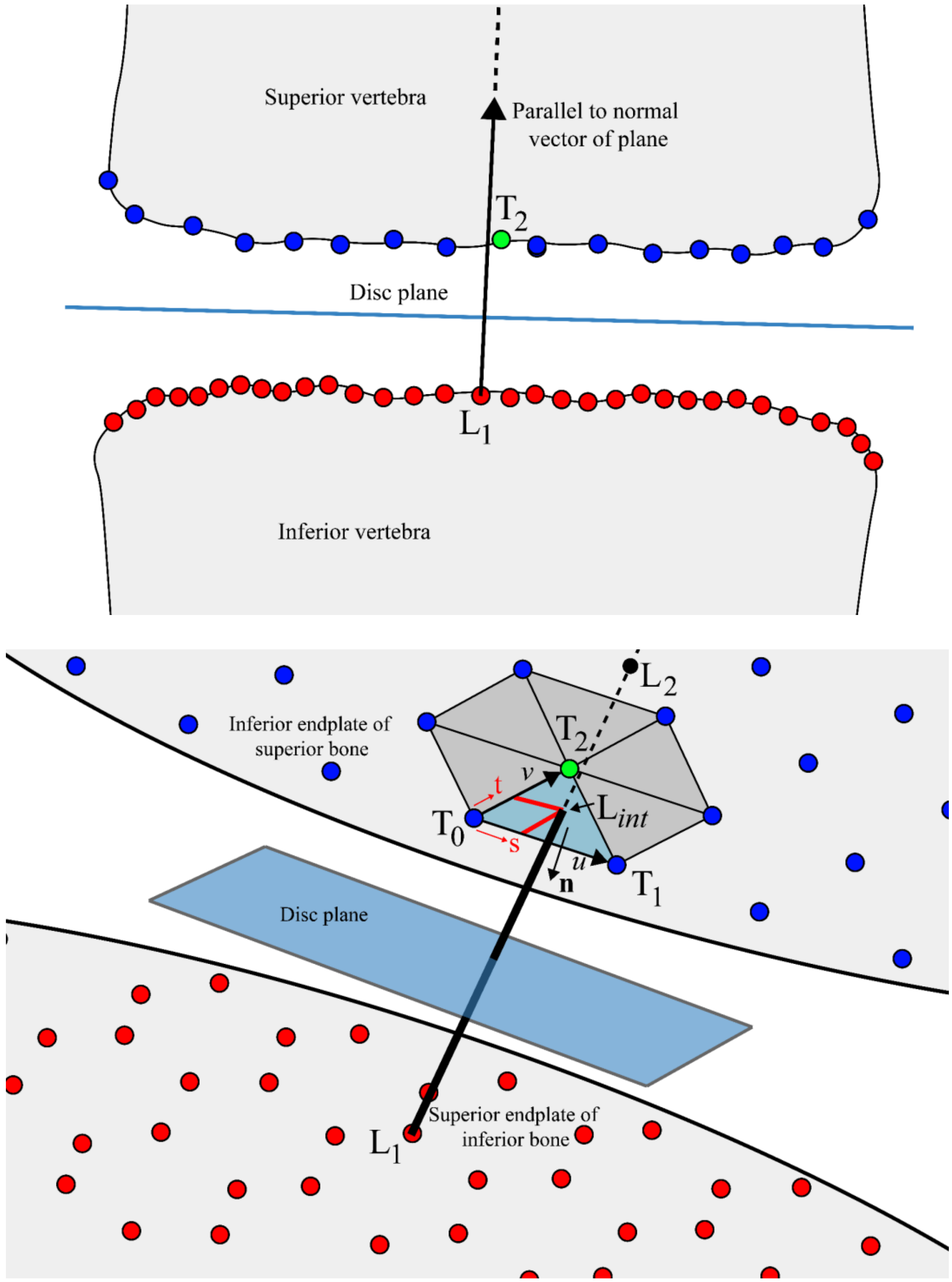

Figure 8: Line segments extended from inferior bone, perpendicular to the disc plane, until intersecting a triangular element on the superior bone.

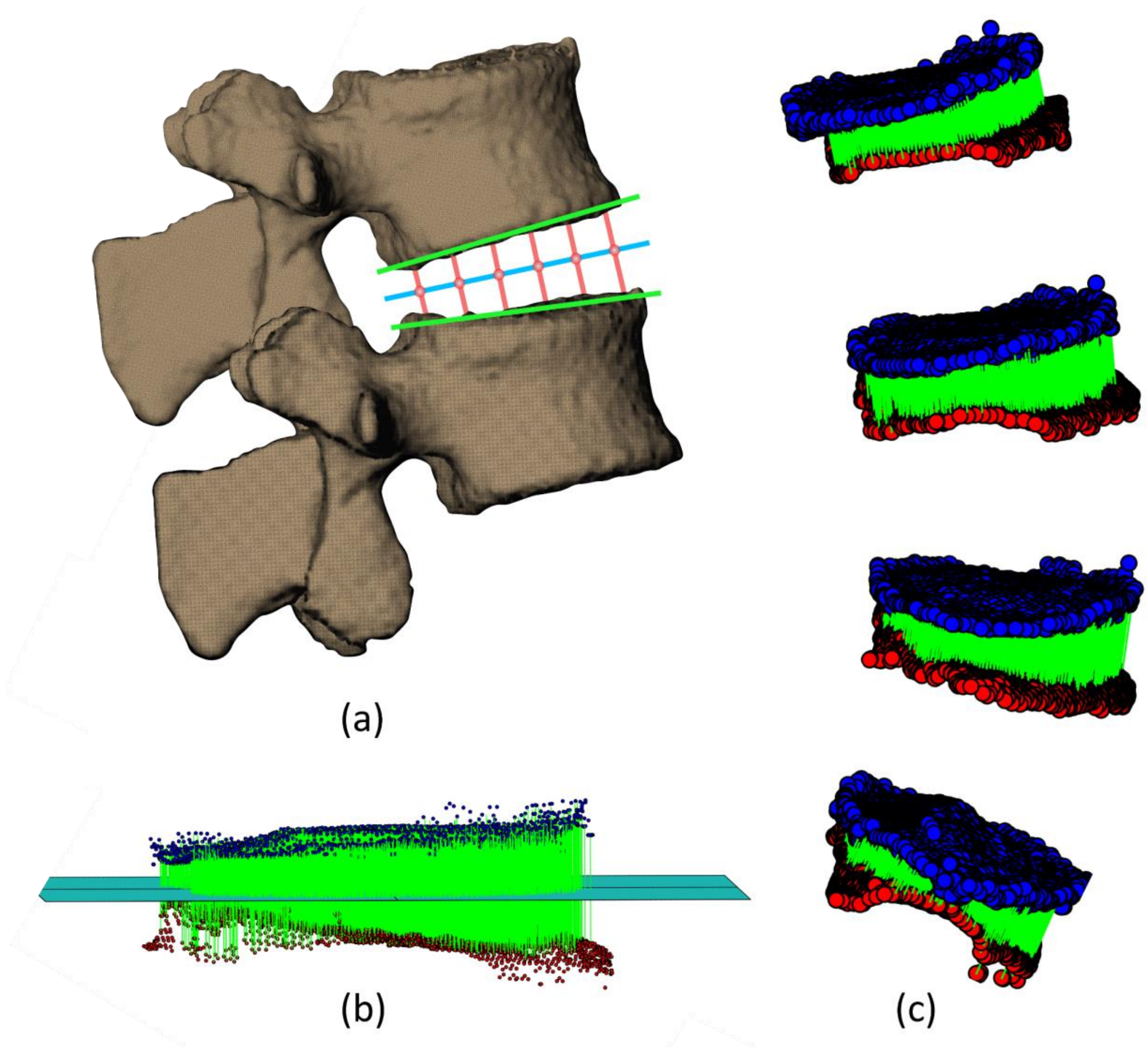

Figure 9: Line segments remained normal to disc plane and connected to adjacent vertebral endplates to form the discs.

2.2.2 Disc Height and Normalized Disc Height

A characteristic ellipse was fit to the superior endplate of the inferior disc, where the centroid was defined as the average location of four line segments at the maximum anterior, posterior, left and right locations of the disc (Figure 10). To capture the geometry of the intervertebral disc, as opposed to the vertebral end plates, the maximum left and right locations of the disc were defined to be the left-most and right-most line segments within 2mm in the AP direction of the vertebra's ML axis.

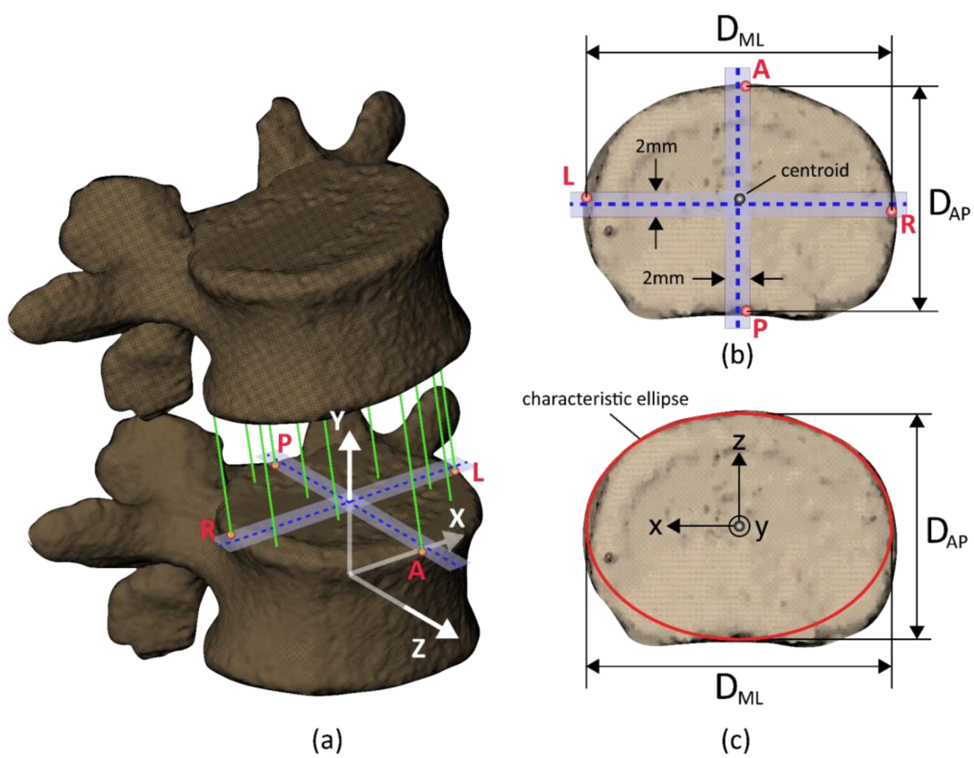

Figure 10: Definition of characteristic ellipse and geometric center of the disc.

Similarly, the maximum anterior and posterior locations were defined to be the anterior-most and posterior-most line segments within 2 mm in the ML direction of the vertebra's AP axis. Bounds of 2 mm were chosen so that the diameters of the ellipse were determined based on disc geometry in the approximate AP and ML directions, in case of irregular disc geometry. The directions of the AP and ML axes of the characteristic ellipse remained identical to those of the inferior vertebra, while the diameter of the ellipse in the ML and AP directions were defined as ($D_{ML} = x_L - x_R$) and ($D_{AP} = z_A - z_P$), respectively (Figure 10b-c).

The upright central disc height (h_c) was defined as the length of the line segment nearest to the geometric center of the characteristic ellipse. At the subject's upright standing position, the instantaneous length (disc height) of each line segment (h_i) within the disc was normalized to the disc's upright central disc height to obtain the upright normalized disc height (nDH) of all line segments forming the intervertebral disc.

$$nDH = \frac{h_i}{h_c} \qquad \text{2-7}$$

Transformation matrices describing the body-fixed rotations and translations of each bone during the dynamic lifting trials with respect to the lab's global coordinate system – determined by the DSX model-based tracking process – were used to place the superior points of the disc with respect to the inferior vertebra's coordinate system during the lifting tasks. To achieve this, the superior points of the disc (X_{sup}) – attached to the superior vertebra (*sup*) – were first transformed to the lab coordinate system (*lab*), then afterwards transformed from the lab coordinate system to the coordinate system of the inferior vertebra (*inf*).

$$X_{\sup\_to\_inf} = T_{lab\_to\_inf} T_{\sup\_to\_lab} X_{sup} \qquad \text{2-8}$$

After applying the transformation matrices (*T*) corresponding to the subject's position in the flexed posture (beginning of the lift), the nDH of all line segments – the distance between the two line segment endpoints – were calculated to determine the flexed disc height of each line segment.

2.2.3 Normal and Shear Strain

The intervertebral disc deformation is defined based on the relative motion between the two adjacent vertebral endplates, with the individual's upright standing position as the reference (Figure 11). Similar to the calculations for flexed disc height, the body-fixed rotation and translation matrices corresponding to the position and orientation of the vertebrae's origins with respect to the global coordinate system at every timeframe of the lifting motion were applied to the superior points (X_{sup}) of each disc to place them in the inferior (*inf*) vertebra's coordinate system (Equation 2-7). This provided the instantaneous locations of the superior points of each line segment with respect to the coordinate system of the inferior vertebra ($X_{\mathrm{sup}\ \_to\_inf}$) throughout the entire lifting motion.

Nominal strains of the line segments were calculated with respect to the disc height values at the upright position – defined as L_{ref} – and were decomposed into two orthogonal components: normal strain, defined as ($\Delta y/L_{ref}$), and shear strain, defined as ($\Delta x/L_{ref}$) (L_{ref},Δx,Δy = upright disc height, displacement along average disc plane and normal displacement, respectively). By this definition, positive and negative values of normal strain corresponded to distraction and compression, respectively, while shear strains are positive with their direction defined by the displacement of the superior point of the line segment with respect to the inferior point in the *xz* plane.

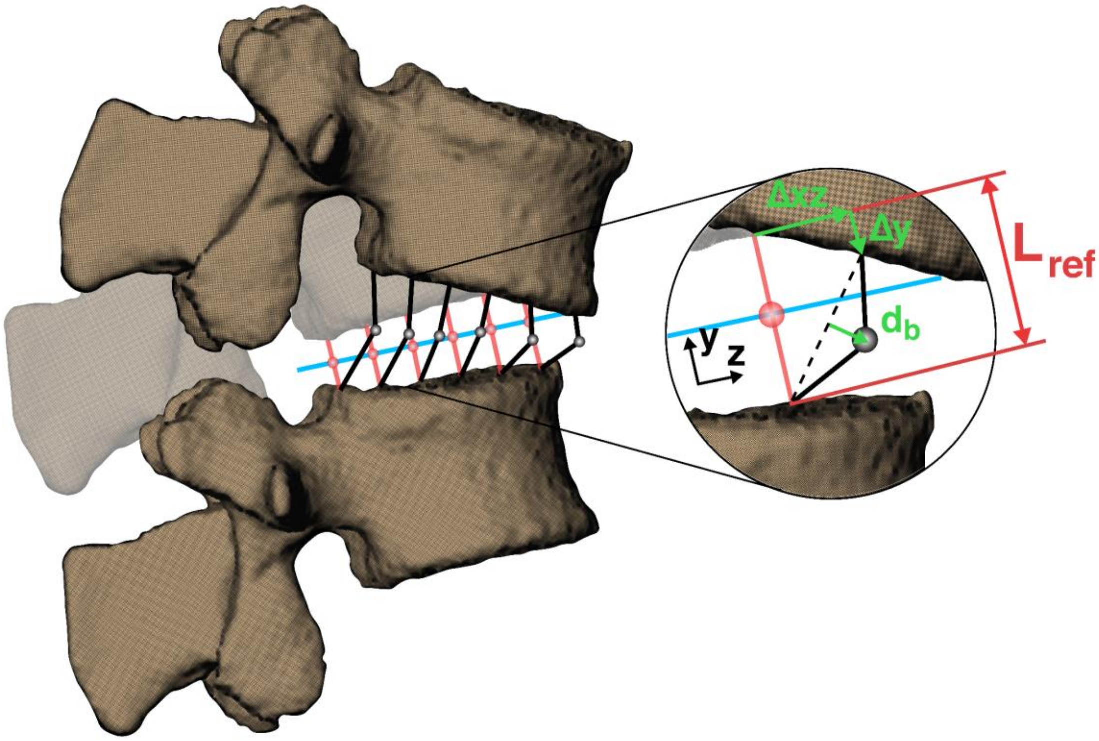

Figure 11: Schematic describing the calculation of disc height and deformation.

2.2.4 Disc Bulge

In FE simulations of the intervertebral disc, bulging of the disc is essentially a product of the intervertebral kinematics and the specified material and structural properties of the disc. While the radial displacements of the disc in the current study were not measurable, the radial displacement (d_b) at the mid-point of the line segment was approximated as the compressive displacement (Δy) of the line segment times a Poisson's ratio of 0.45, a value used in a number of lumbar spine FE models[98,128].

$$d_b = 0.45 \times \Delta y \tag{2-9}$$

The direction of radial displacement was defined as the vector connecting the mid-point of the central line segment to the mid-point of the particular line segment of interest. The bulging direction of the line segment directly in the center of the disc was said to equal the direction of shear displacement.

2.2.5 Point-wise Mapping

To compare the nDH, strain, and disc bulge values across all joint levels and participants, the geometry of each disc was mapped to consist of an identical number of line segments at the same locations relative to the disc's size. First, a 2D elliptical point grid was projected on the inferior disc, consisting of 60 equidistant ellipses concentric to the disc's characteristic ellipse and extending from the centroid up to 150% the size of the characteristic ellipse (Figure 12).

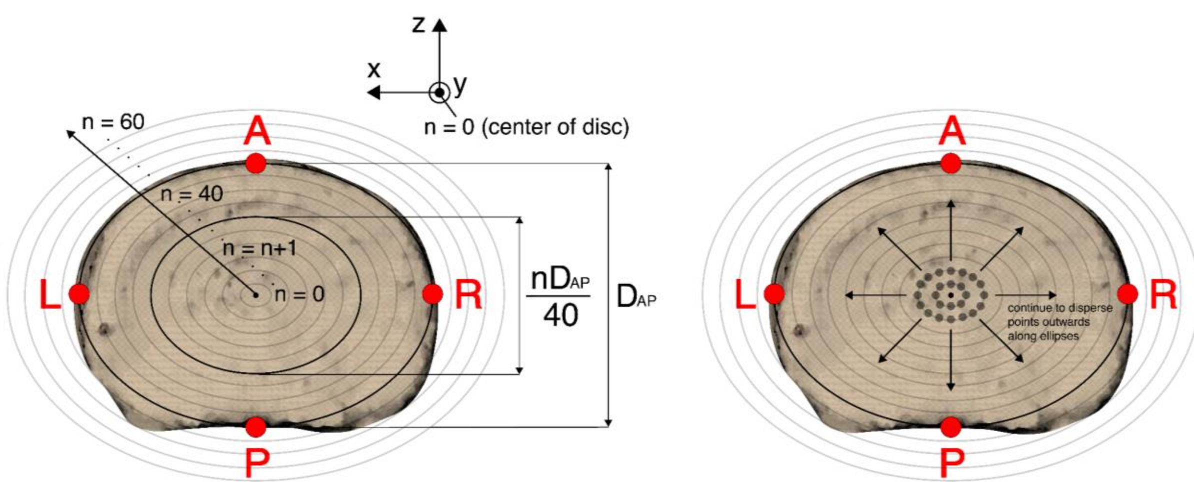

Figure 12: Projection of 2D elliptical point grid onto superior surface of inferior vertebra.

The point grid extended 50% beyond the characteristic ellipse to ensure inclusion of the entire disc area, as the intervertebral disc is not perfectly elliptical. Second, sample points were evenly distributed along each elliptical profile – each consisting of 8*n points, where n = number of ellipses away from the centroid (n = 0) – together forming a 2D point grid extending well beyond the outermost line segments of the disc's cross-sectional area. The exact number of points for each disc varied due to the irregularities and inconsistencies in shape, however on average the disc consisted of approximately 8,000 points. The upright standing nDH at each point on the elliptical grid was then defined to equal that of the nearest original line segment (prior to re-sampling), resulting in a consistently sampled 2D plot of upright disc height over the entire disc area. Any point on the elliptical grid greater than 1 mm away from all line segments was considered to be outside of the disc region, and was therefore excluded from the 2D plot. The reasoning behind this exclusion criteria was to be doubly sure that any random line segments connecting between spinous or transverse processes of adjacent vertebrae weren't part of the intervertebral disc. However, much work was done in previous steps to avoid these occurrences. By repeating this process at each intervertebral level across all participants, all discs were defined by approximately 8,000 distributed points scaled to their respective disc's characteristic ellipse. At the flexed position, the same methodology was used to map the nDH and strain values (Figure 13) of all line segments to a 2D color and vector map

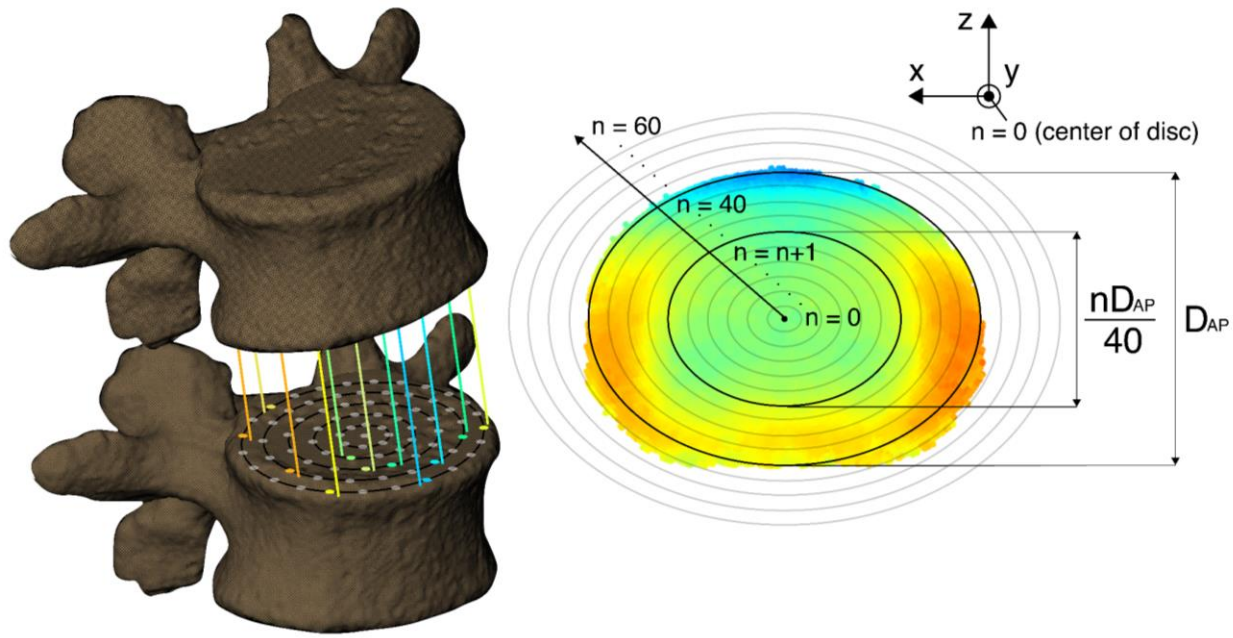

Figure 13: Mapping of line segment normalized disc height to elliptical point grid.

2.2.6 Regional Characteristics

The average nDH and deformation of the discs were quantified within five consistently identifiable regions: anterior, posterior, and central locations in the mid-sagittal plane; left and right locations in the mid-coronal plane. Each of the five regions was defined by a circular area on the superior endplate of the inferior vertebra, all with diameters equal to the AP distance between the 35^{th} and 40^{th} elliptical profiles (Figure 14). The average nDH and deformation among all line segments within each specified circular region were determined at the flexed and upright positions.

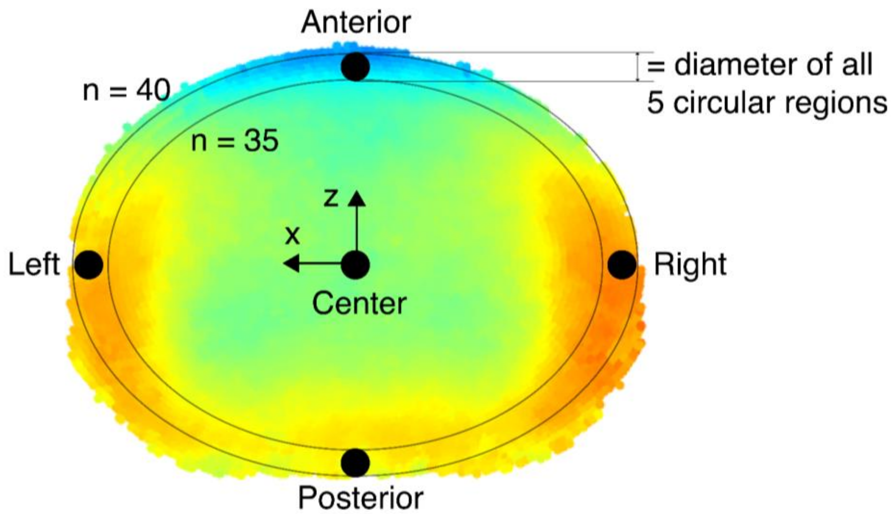

Figure 14: Five defined anatomical regions to quantify disc height and deformation.

2.2.7 Instantaneous Disc Deformation and Disc Bulge

In addition to quantifying deformation at the flexed position, the average deformation and bulging of line segments within each of the five circular regions was tracked throughout the lifting motion as well. Normal strains shear strains, and disc bulge were then plotted with respect to percent motion completion (%MC), a normalized representation of time based on the overall L2-S1 flexion angle, defined as (*i*, *c*, *f* = initial, current, and final L2-S1 lumbar flexion angle).

$$\%MC = \frac{\theta_c - \theta_i}{\theta_f - \theta_i} \times 100 \qquad 2\text{-}10$$

Additionally, magnitudes of disc bulge along the anterior-posterior axis of the intervertebral disc were compared with those found in the disc by the concurrent FE modeling study on the same dataset .

2.2.8 Statistical Analysis

2.2.8.1 Point-wise End-range Differences

Where data were successfully recorded from both trials per load for a participant, the two datasets were averaged into a single dataset to represent the participant's motion for subsequent analyses. Level-specific differences in upright and flexed disc height were determined by identifying regions of the disc exhibiting location-specific differences in nDH. At each segment level, the mean and 95% confidence interval (CI_{95}) of the mean nDH at the upright and flexed positions were calculated at every elliptical point corresponding to the same relative disc location. Each point exhibiting non-overlapping CI_{95} between segment levels or external load magnitudes indicated segment-wise or load-wise differences, respectively. Points close in proximity (within 3 mm) were grouped together to form anatomical areas of significantly different nDH characteristics. Any area containing less than three points was considered an outlier and was deemed insignificant. The same methodology used to quantify nDH differences was also utilized to determine areas of segment-wise or load-wise differences in normal and shear strain at the flexed position. As the reference frame for disc deformation was the upright standing position, deformation needed not be analyzed at this position as it was equal to zero.

2.2.8.2 Time Series Differences

Time series plots ("time", as indicated by %MC progression) of the instantaneous normal and shear strains at five distinct circular regions defined above — the anterior, posterior, left, right, and center — of disc at each segment level were generated. CI_{95} of the mean normal and shear strain at every decile of %MC from 0% to 80%MC were calculated. Instances of non-overlapping confidence intervals indicated time intervals for which deformation trends between the corresponding segment levels were significantly different. Data beyond 80%MC was not included in the time series data as multiple subjects failed to reach 90%MC during the lifting motion.

2.2.8.3 Repeated Measures and Post-hoc Tukey

Repeated measures analysis with data compiled as a mixed model was employed to identify segment-wise and load-wise differences in nDH and total disc strains at the five regions. The restricted maximum likelihood (REML) approach was used for the analysis. Segmental level (four levels: L2L3, L3L4, L4L5, L5S1) and load magnitude [three levels: 4.54 kg (10 lb), 9.1 kg (20 lb), 13.6 kg (30 lb)] were the two within-subject fixed-effect factors while "participant" was the random factor. The dataset comprised 10 groups (subjects) and a total of 116 observations. Starting with a null or empty model, the model was progressively updated by adding the fixed-effect factors, as below:

Empty Model Formula: ~1 + Random effect: Participant;

Update 1: Fixed effects: ~ Segment_Level;

Update 2: Fixed Effects: ~ Segment_Level + Load_Level;

Whenever a main or interaction effect was deemed significant, post-hoc Tukey Honest Significant Difference (HSD) comparison-of-means tests would follow to determine differences between the levels. The above-mentioned steps were implemented separately for each response variable. All analyses were performed using R® Statistical Software[129].

2.3 Facet Joint Kinematics

2.3.1 Facet Joint Coordinate System

Local coordinate systems (LCS) were defined on the inner and outer surfaces of the superior and inferior facet surfaces of the L2 to S1 based on four anatomical points chosen by the same researcher: the inferior, superior, posterior, and anterior (Figure 15). The average anatomical location of the four landmarks defined the LCS origin. The Z-axis represented the direction parallel to the facet faces *(sideways facet sliding)* and was defined to extend from the LBS origin parallel to the axis connecting the anterior and posterior points. A temporary axis was defined, extending from the inferior point to the superior point. The cross product of temporary axis and the Z axis defined the X-axis of the LCS, representing the direction normal to the facet faces *(facet gap)*. Lastly, the Y-axis was defined by the cross product of the Z- and X-axes, creating a right-handed orthogonal coordinate system on the facet surface. This procedure was done for all four facet surfaces of each vertebra; the inferior left and right, and the superior left and right. To represent facet joint kinematics in a sagittally symmetric manner at the left and right facet joints, the LCS X-axis of the left facets were flipped to point outwards, effectively creating a left-handed coordinate system.

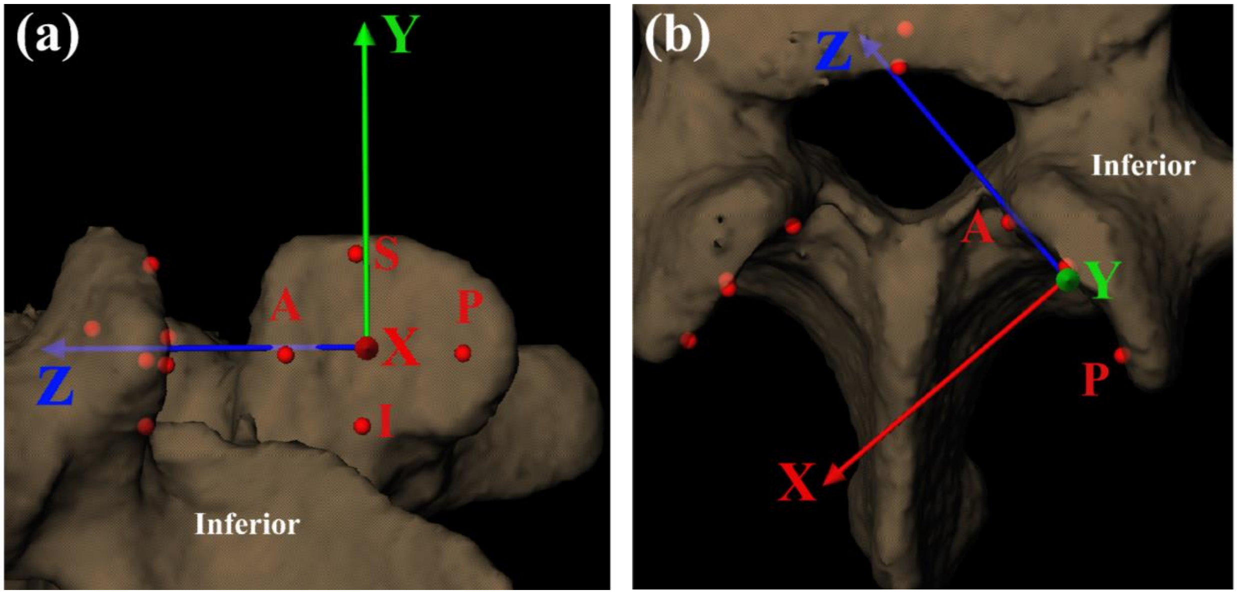

Figure 15: Local coordinate systems (LCS) on the inferior and superior facet surfaces.

2.3.2 Translational Kinematics

The DSX model-based tracking algorithm, initially run with the vertebral coordinate systems located at the vertebral body center, was re-run individually for each facet joint with the coordinate systems located at the facet surfaces. The algorithm calculated the 3D body-fixed transformation matrix of the inferior facet LCS of the superior vertebra with respect to the superior facet LCS of the inferior vertebra at every timeframe of the upright standing position and dynamic lifting motions (Figure 16). From the transformation matrices, the body-fixed translations along the X-, Y-, and Z- axes were extracted and reported with respect to the fully-flexed position at the beginning of the lifting motion and the more natural, upright reference position. Differences between the instantaneous translations between facet surfaces at the beginning of the lifting motion (flexed position) and at the static upright position were also reported.

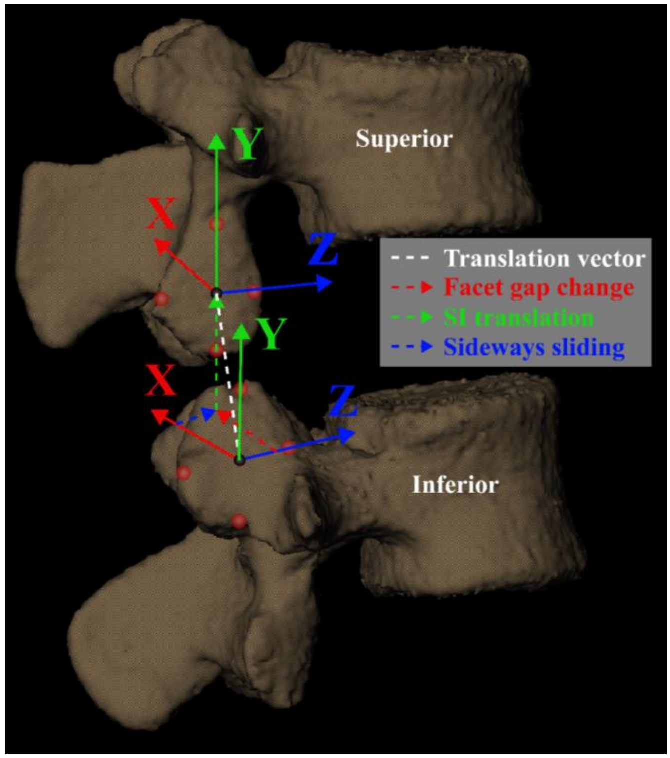

Figure 16: Facet joint translations between adjacent facet surfaces.

To normalize FJ kinematics across lifting trials and subjects, data were presented with respect to the progression of the lift, or percent task completion (%MC), as opposed to time.

2.3.3 Statistical Analysis

2.3.3.1 Effects of External Load and Segment Level

Data acquired from the two trials per task of identical external load magnitude were averaged into a single dataset. Further, results from the left and right FJ were not significantly different (except for X- component of L2L3 and L3L4 segments); hence these data were averaged. Mean (±CI_{95}) translations in the X-, Y- and Z directions for every decile of L2-S1 extension ROM were computed for each load-lifting task across participants to enable qualitative observations of differences across segments and across load levels. Time series plots (“time” as indicated by %MC) of the translations between 0%-80% of L2-S1 ROM were generated, with the start of the lift (fully flexed position) defined as our zero-translation reference position. Corresponding linear regression-based slopes were computed to identify migration trends, demonstrated by a slope significantly different from zero ($\alpha = 0.05$).

2.3.3.2 Repeated Measures and Tukey’s HSD

Repeated measures analysis was employed with data compiled as a mixed model, with segmental level (four levels: L2L3, L3L4, L4L5, L5S1) and load magnitude [three levels: 4.54 kg (10 lb), 9.1 kg (20 lb), 13.6 kg (30 lb)] as the two within-subject, fixed effect, categorical factors and “participant” as the random factor. The total translations in each of the three directions were the outcome variables. Differences across segments and load magnitudes were assessed based on post-hoc Tukey’s Honest Significant Difference (HSD) comparison-of-means tests. Similar analyses were also conducted for left and right facet X- translation components separately. The extent of overlap between the notches of the respective boxes in notched box plots of the left-right averaged datasets provided an additional, visual representation of the differences between the groups. The notches, which represent a 95% confidence interval (CI_{notch}) of the median, extend to $[\pm 1.58*IQR/((n)^{0.5})]$, where “IQR” = interquartile range between first to third quartile, and “n” = number of non-missing observations within the group. No overlap indicated significant differences. All analyses were performed in R® statistical computing software[129] (R_Core_Team (2015).

2.4 Subject-Specific Musculoskeletal Model

2.4.1 Objectives and Summary of Procedure

The objectives of the current subject-specific musculoskeletal modeling work and the steps taken to achieve such objectives are as follow:

1) What are the joint reaction forces (JRF) and muscle loads associated with a functional lifting task of 10 lb and 30 lb?
    a. A generic, full-body model was constructed in OpenSim by combining two existing models.
    b. The generic model was adjusted to include subject-specific parameters. These include surface marker measurements and ground reaction force data acquired during in vivo testing, DSX-measured lumbar kinematics during the lifting motion, lumbar vertebral positions and orientations at the upright and supine postures, and subject-specific nonlinear tissue stiffness properties derived from a displacement-controlled FE study.
    c. A sequence of OpenSim algorithms were run on the model:
        i. Inverse Kinematics (IK) to determine full-body kinematics,
        ii. Inverse Dynamics (ID) to determine generalized forces at each joint
        iii. Static Optimization (SO) to determine muscle forces
        iv. Joint Reactions Analysis (JRA) to determine the JRF.
2) How do JRF and muscle force estimates obtained with DSX-based subject specific 6-DOF kinematics differ from those obtained with pre-determined, generic rhythm-based rotational kinematics?

a. The OpenSim sequence of algorithms were run identically on models with two variations of prescribed L2 to S1 lumbar motion.

    i. DSX-measured 6-DOF L2-S1 kinematics of the subject

    ii. Rhythm-based 3-DOF rotational kinematics typically assumed in lumbar spine models, where the rotational motions of the entire lumbar spine are fractionally distributed across joint levels (e.g. L2L3 rotation = 30% of L2-S1 rotation).

3) How do joint tissue passive stiffness property assumptions influence JRF and muscle force estimates?

    a. The OpenSim sequence of algorithms were run identically on models with three variations of tissue passive stiffness properties;

        i. No bushing stiffness (NBS), where tissue passive stiffness was ignored,

        ii. Linear bushing stiffness (LBS), where generic force-displacement relationships from literature were prescribed at each joint.

        iii. Nonlinear bushing stiffness (NLBS), where force-displacement relationships derived from a subject-specific displacement-driven FE model were prescribed.

    b. In LBS and NLBS models, joint stiffnesses were modeled by a 6x6, uncoupled force-displacement matrix meant to represent the lumped stiffness of *all* tissues in the joint (intervertebral disc, ligaments, tendons, etc.)

4) What is the effect of the assumed initial, zero-stress state of the tissues – or “neutral” joint position (supine state vs. upright standing) – on muscle and JRF force estimates?

a. While tissues are preloaded *in vivo* and most always under stress, a zero-stress state must be assumed when prescribing force-displacement relationships at a joint; in rigid-body modeling, these are often assumed to be equal to the lumbar vertebral positions at the upright or supine posture.

b. The OpenSim sequence of algorithms were run identically on models with two variations of the neutral joint configurations.

    i. Joint positions and orientations at the upright standing posture, as measured by DSX.

    ii. Joint positions and orientations at the supine posture, as measured by CT.

2.4.2 Model Development

A generic full-body musculoskeletal model was constructed in OpenSim®[130-133] by combining an existing lower-body model developed by (Arnold et al., 2010) and an upper-body model developed by (Senteler et al., 2016)[22,134]. Overall, the generic model consisted of 114 body segments, 113 joints, 334 muscles, described by a total of 81 DOF.

2.4.2.1 Model Musculature and Marker Set

The OpenSim model consisted of a total of 334 muscle fascicles, all represented by the Thelen 2003 Muscle Model[135]. Based on the Hill muscle model, these muscles generate force as a function of activation value, as well as the normalized length and velocity of the muscle unit. The path of each muscle was determined by defining X, Y, and Z coordinates in the local coordinate system of at least two bodies in the model through which the muscle fascicle must connect. The parameters which characterize the muscle behavior are its maximum isometric force, tendon slack length, optimal fiber length, and pennation angle, and maximum contraction velocity. Initially, these parameters were set identical to those present in the Arnold and Senteler models used to compose the generic model. The back muscle parameters were adjusted to equal those derived from a recently published thoracolumbar spine model[54], where the maximum muscle stress of each muscle was set to 100 N/cm^2. A maximum muscle stress of 100 N/cm^2 is larger than typically used in many lumbar spine models, however (Bruno et al., 2015) determined that to support physiological flexion tasks, the back muscle properties had to be appropriately adjusted. The current work focuses on muscle activity in four major muscle groups (Figure 17); the multifidus (MF), iliocostalis lumborum (IL), longissimus thoracis (LT), and abdominal (ABD).

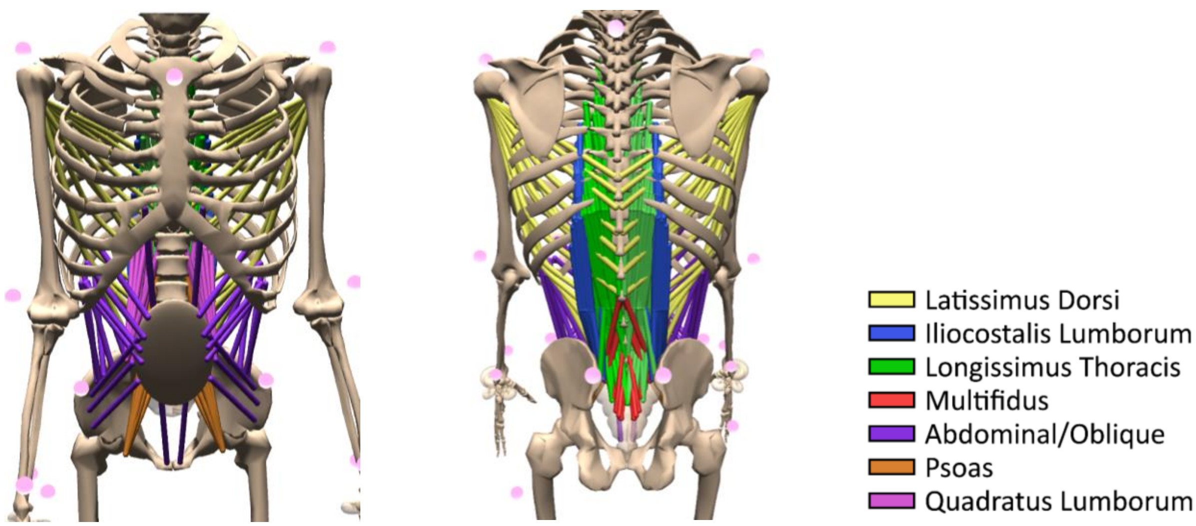

Figure 17: Musculature of the front (left) and back (right) of the upper body.

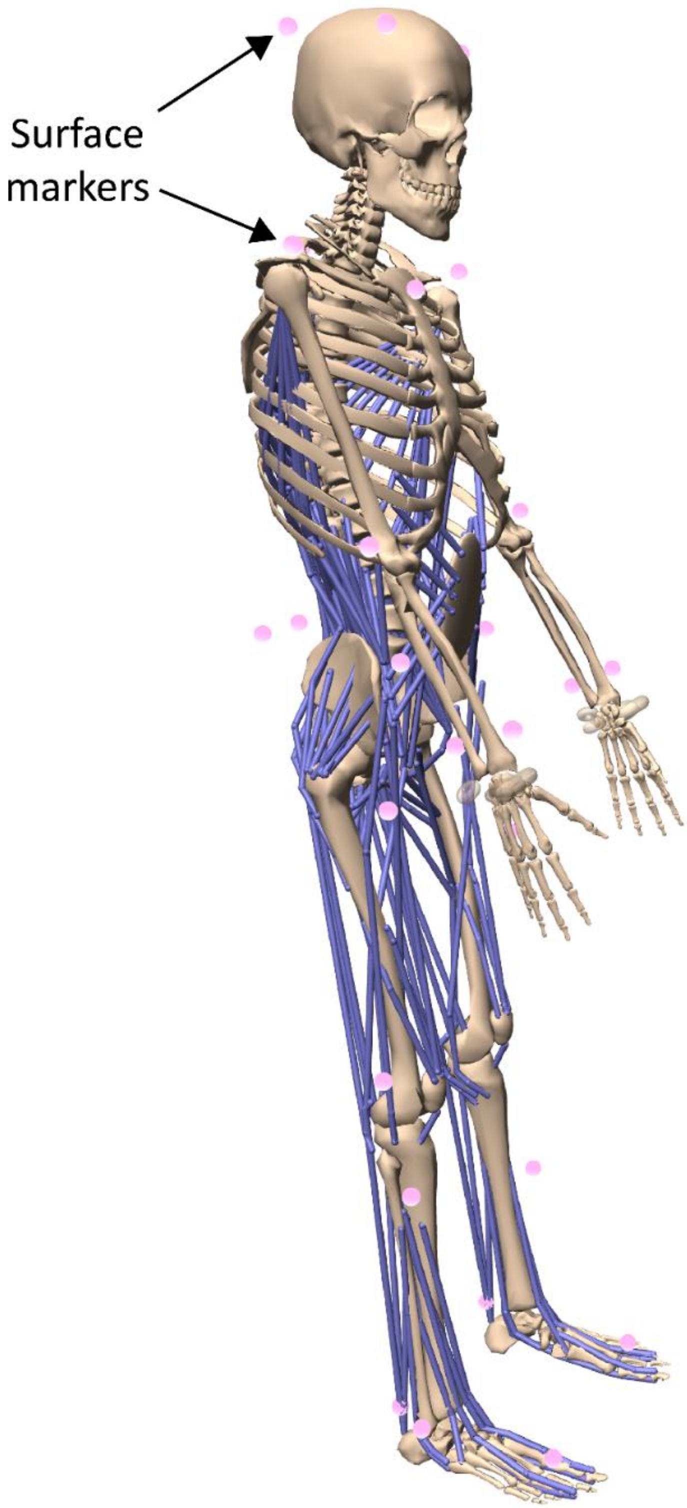

Figure 18: A set of virtual markers corresponding to the Plug-In Gait model was added to the generic model.

To incorporate the subject-specific full-body motion of the subject, virtual markers were added to the generic model to approximate those placed on the subjects during data acquisition (Figure 18). Markers were placed on the subject and model according to the Plug-In Gait Model[136,137].

2.4.2.2 Neutral State Configuration

At each level, the joint's position and orientation with which the soft tissues are at their zero-stress state – termed the "neutral state configuration" – was defined. This is the joint position and orientation where if passive elements were modeled by force-displacement relationships, no passive forces or moments would exist. Simulations were performed with two variations of the joint neutral state, corresponding to either the upright or supine positions. The upright neutral state was defined by adjusting the vertebral posture from the L2 to S1 based on the DSX-measured vertebral positions during upright posture with no external weight being held by the participant. The supine neutral state was defined by the CT-measured L2-S1 positions present as the participant lied in the supine position.

At the neutral state, the center of rotation (COR) of each joint was defined so that the lever arms from the COR to each vertebral body center were of equal length while also remaining parallel to the vertebrae's local Y axes. With this constraint and the prescribed FE rotation ($\emptyset_{up}$ or $\emptyset_{sup}$), an additional AP translation of the COR with respect to the inferior vertebral body coordinate system – x_{up} or x_{sup} – was prescribed to achieve the accurately measured kinematics. Generally, the position of the COR was approximately located at the center of the intervertebral disc to facilitate comparison of results to those derived from previous modeling studies using rhythmic-based kinematic input, which are usually implemented about a COR at the disc center[54,138] (Figure 19).

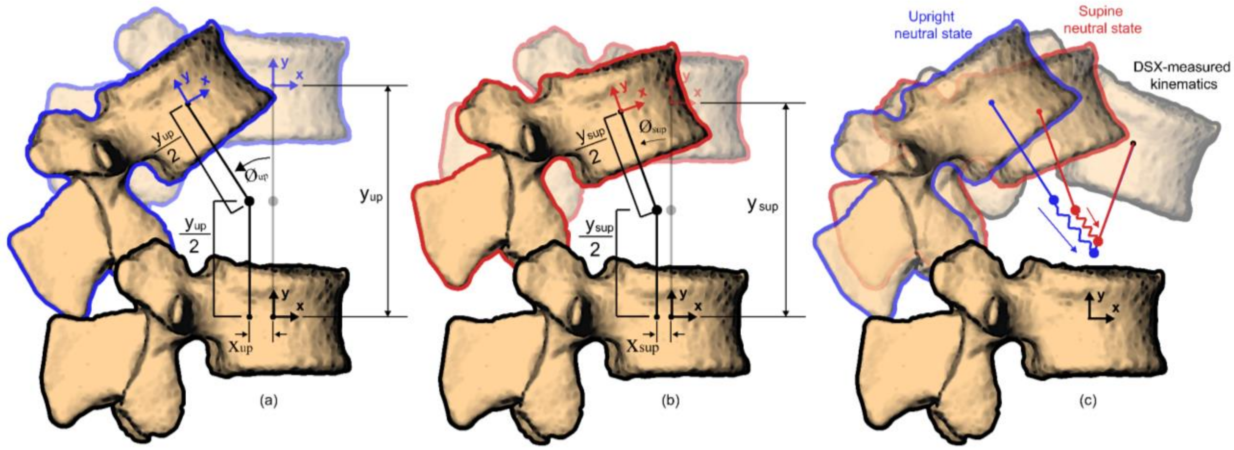

Figure 19: Two variations of joint neutral state; upright neutral state (a) and supine neutral state (b). Prescribed joint kinematics to achieve DSX-measured positions varied between the two neutral states (c).

2.4.2.3 Incorporation of DSX kinematics

The lumbar spine portion of the upper body model was adjusted to allow for the incorporation of measured DSX intervertebral kinematics. Each lumbar joint from L2L3 to L5S1 was modeled to describe 6-DOF motion – three rotations and three translations – of the superior vertebra with respect to the inferior vertebra about the joint's COR at the neutral state. 6-DOF motion was implemented first by prescribing three rotational DOF; flexion-extension (FE), lateral bending (LB), and axial rotation (AR). Through the OpenSim 3.3 Application Programming Interface (API) in MATLAB, these coordinates were prescribed (*prescribed_function* in OpenSim) within the model as spline functions (*SimmSpline*) based on the DSX-measured kinematics during the lifting motion versus the time. The location of the joint COR in the superior body was then allowed to translate along three axes in the inferior vertebra's coordinate system; anterior-posterior (AP), superior-inferior (SI), and medial-lateral (ML). Translational motion along each axis was defined by piecewise linear functions (*PiecewiseLinearFunction* in OpenSim) with respect to the FE rotation of the joint.

As the raw DSX data describing lumbar intervertebral motion were in the form of body-fixed kinematics of the superior vertebral body coordinate system (CS) with respect to the inferior vertebral body CS, the kinematic data were transformed to describe intervertebral motion with respect to the neutral state about the newly defined joint CORs. This transformation was performed for both the upright- and supine-relative neutral state configurations to ensure identical lumbar motion in space.

The raw DSX-measured data described intervertebral motion by ordered body-fixed rotations of the superior vertebral body coordinate system with respect to the inferior vertebral body coordinate system. Thus, the relation between the superior body's vertebral body center, $[x; y; z]$, with respect to the inferior vertebral body center, $[x'; y'; z']$, can be calculated by represented by a body-fixed rotational and translational transformation, $\overline{\boldsymbol{R}}$ and $\overline{\boldsymbol{T}}$, respectively:

$$\begin{bmatrix} x' \\ y' \\ z' \end{bmatrix} = R_z R_y R_x \begin{bmatrix} x \\ y \\ z \end{bmatrix} + \begin{bmatrix} T_x \\ T_y \\ T_z \end{bmatrix} \quad 2\text{-}11$$

However, the location of the vertebral body center in its own coordinate system is $[x = 0; y = 0; z = 0]$, so the position of the superior vertebra origin with respect to the inferior origin after transformation is simply:

$$\begin{bmatrix} x' \\ y' \\ z' \end{bmatrix} = \begin{bmatrix} T_x \\ T_y \\ T_z \end{bmatrix} \quad 2\text{-}12$$

In our OpenSim model we have modeled the lumbar joints such that the superior vertebral body rotates about the COR located between adjacent vertebrae, as opposed to rotating about its own local coordinate system with Euler body-fixed rotations. Furthermore, we have added an anterior-posterior (AP) translation and flexion-extension (FE) rotation between adjacent vertebrae. Due to the change in joint representation, prescribing the same exact values of rotations and translations to the joint would result in different spatial locations and orientations of the superior vertebra with respect to the inferior vertebra. Therefore, we must account for this when prescribing joint motion so that we can orient and position the vertebrae identically in space to that measured by DSX.

Accounting for the difference in angular orientation is rather straightforward. Regardless of whether a body is rotating about its own coordinate system axes or those of another coordinate system, if the coordinate systems are angularly oriented identically in space, the orientation of the body in space after a rotational transformation will remain the same; only the position of the body in space may differ based on the body's distance from the point in which it was rotated about. For our modeled joints, the only angular orientation adjusted when defining the neutral state of the joint is the FE rotation. Since FE rotation is the first ordered body-centered rotation in the DSX-derived data, applying the appropriate amount of FE rotation from the neutral state about the joint center – in this case, the DSX-derived FE rotation plus the *opposite* FE rotation present at the neutral state – will orient the superior vertebral coordinate axes exactly as the DSX-derived body-fixed FE rotation would. Thereafter, the values of AR and LB as measured by DSX can be directly prescribed about the joint center to match the angular orientation of the superior vertebra in space measured by DSX (Figure 20a). However, as previously stated, since the OpenSim joint is rotating about a joint center and not its own anatomical axes, the superior vertebra will not be *positioned* correctly (Figure 20b-c).

To place the superior vertebra of the L23 to L45 joints in the same respective position in space after rotation about the joint center and any translational offset present in the neutral state definition, an additional translational vector must be applied (T_{jc}):

$$\begin{bmatrix} x' \\ y' \\ z' \end{bmatrix} = \begin{bmatrix} T_x \\ T_y \\ T_z \end{bmatrix} = R_z R_y R_x \begin{bmatrix} 0 \\ SI/2 \\ 0 \end{bmatrix} + \begin{bmatrix} 0 \\ SI/2 \\ 0 \end{bmatrix} + \begin{bmatrix} 0 \\ 0 \\ AP\_offset \end{bmatrix} + \begin{bmatrix} T_{jc\_x} \\ T_{jc\_y} \\ T_{jc\_z} \end{bmatrix} \qquad \text{2-13}$$

Solving the expression for the joint center translational vector leads to:

$$\begin{bmatrix} T_{jc\_x} \\ T_{jc\_y} \\ T_{jc\_z} \end{bmatrix} = \begin{bmatrix} T_x \\ T_y \\ T_z \end{bmatrix} - R_z R_y R_x \begin{bmatrix} 0 \\ SI/2 \\ 0 \end{bmatrix} - \begin{bmatrix} 0 \\ SI/2 \\ 0 \end{bmatrix} - \begin{bmatrix} 0 \\ 0 \\ AP\_offset \end{bmatrix} \qquad \text{2-14}$$

For the L51 joint, the process is identical except that the distance between the joint center and the inferior and superior vertebral centers is SI/5 and 4*SI/5, respectively.

$$\begin{bmatrix} T_{jc} \\ T_{jc} \\ T_{jc} \end{bmatrix} = \begin{bmatrix} T_x \\ T_y \\ T_z \end{bmatrix} - R_z R_y R_x \begin{bmatrix} 0 \\ 4 * SI/5 \\ 0 \end{bmatrix} - \begin{bmatrix} 0 \\ SI/5 \\ 0 \end{bmatrix} - \begin{bmatrix} 0 \\ 0 \\ AP\_offset \end{bmatrix} \qquad \text{2-15}$$

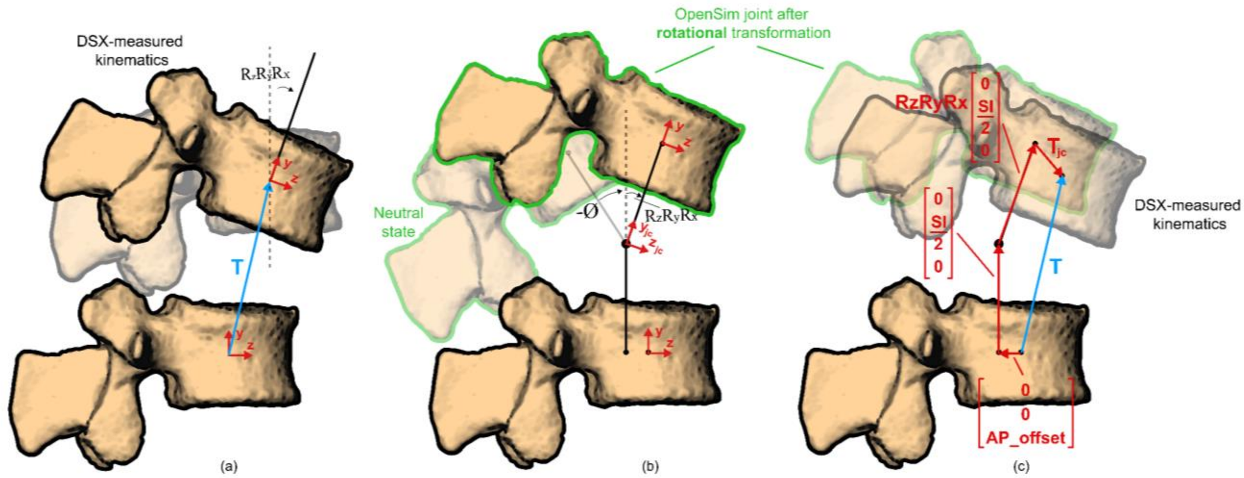

Figure 20: Transformation of DSX kinematics with respect to the neutral state of the joint defined in OpenSim. DSX-measured rotations were body-fixed (a), while rotations in OpenSim were applied about a joint center (b), requiring an additional translation of the superior body to match it's DSX-measured position and orientation (c).

It's important to note that the instantaneous location of the joint center is not necessarily equal to the instantaneous center of rotation (ICR) of the joint, as calculated in a previous study on the same dataset. ICR is calculated based on the instantaneous translational and rotational motion of the joint, whereas the location of the joint center in our study is simply the translation necessary so that the vertebrae can be positioned and oriented in space identically to the location and orientation measured by DSX *after* the rotations have already been applied.

2.4.2.4 Intervertebral Passive Stiffness

Uncoupled stiffness matrices describing the force- or moment-displacement relationship between consecutive bodies were defined at each joint from L2L3 to L5S1 for the linear (LBS) or nonlinear (NLBS) models. For LBS models, the rotational and translational stiffness constants at each joint were identical to those used in a previous musculoskeletal model[22], and were implemented in OpenSim via the *BushingForce* (Table 1). The passive forces and moments corresponding to the translation and rotational motion of the superior body with respect to the inferior body – u and θ, respectively – were defined by a 6x6 matrix.

$$\begin{bmatrix} F_{AP} \\ F_{SI} \\ F_{ML} \\ M_{LB} \\ M_{AR} \\ M_{FE} \end{bmatrix} = \begin{bmatrix} k_{AP} & 0 & 0 & 0 & 0 & 0 \\ 0 & k_{SI} & 0 & 0 & 0 & 0 \\ 0 & 0 & k_{ML} & 0 & 0 & 0 \\ 0 & 0 & 0 & k_{LB} & 0 & 0 \\ 0 & 0 & 0 & 0 & k_{AR} & 0 \\ 0 & 0 & 0 & 0 & 0 & k_{FE} \end{bmatrix} \begin{bmatrix} u_{AP} \\ u_{SI} \\ u_{ML} \\ \theta_{LB} \\ \theta_{AR} \\ \theta_{FE} \end{bmatrix} \tag{2-16}$$

NLBS model stiffness relationships in non-sagittal directions remained the same as LBS models. The sagittal plane stiffnesses were defined as piecewise linear functions based on force-displacement relationships derived from a displacement-controlled finite element study on a single subject's L4L5 segment (Figure 21)[139]. In this study, a 3D hexahedral mesh was created for the L4 and L5 based on the CT-derived vertebral surface data. An intervertebral disc mesh was fit to the space between the subject's L4 and L5 meshed vertebral surfaces and consisted of a nucleus pulposus surrounded by an 8-layer annulus. The DSX-measured kinematics of the L4L5 segment during the lifting motion were prescribed to the FE model, and the resulting compressive forces, shear forces, and reaction moments of the model were outputted at various time steps during the lifting motion. Using the force and moment outputs from this study, along with the prescribed DSX kinematics, force- or moment-displacement relationships for the AP, SI, and FE motions were prescribed to the L2L3 to L5S1 joints in the OpenSim model. These were defined as piecewise linear functions via the *FunctionBasedBushingForce* function. Based on the differences in rotations and translations between adjacent vertebra, with respect to the defined neutral state, equal and opposite passive forces and moments were applied to each body at the location of the joint center.

Table 1: LBS and NLBS uncoupled stiffness properties prescribed to each joint.

Joint – Bushing type	k_{AP} (N/m)	k_{SI} (N/m)	k_{ML} (N/m)	k_{LB} (Nm/rad)	k_{AR} (Nm/rad)	k_{FE} (Nm/rad)
L23 – LBS	246348	1783989	135000	64	268	37
L23 – NLBS	*Figure 21a*	*Figure 21b*	135000	64	268	*Figure 21c*
L34 – LBS	148855	1890170	135000	69	291	51
L34 – NLBS	*Figure 21a*	*Figure 21b*	135000	69	291	*Figure 21c*
L45 – LBS	85714	1962000	135000	94	293	65
L45 – NLBS	*Figure 21a*	*Figure 21b*	135000	94	293	*Figure 21c*
L51 – LBS	386511	1669000	135000	131	281	79
L51 – NLBS	*Figure 21a*	*Figure 21b*	135000	131	281	*Figure 21c*

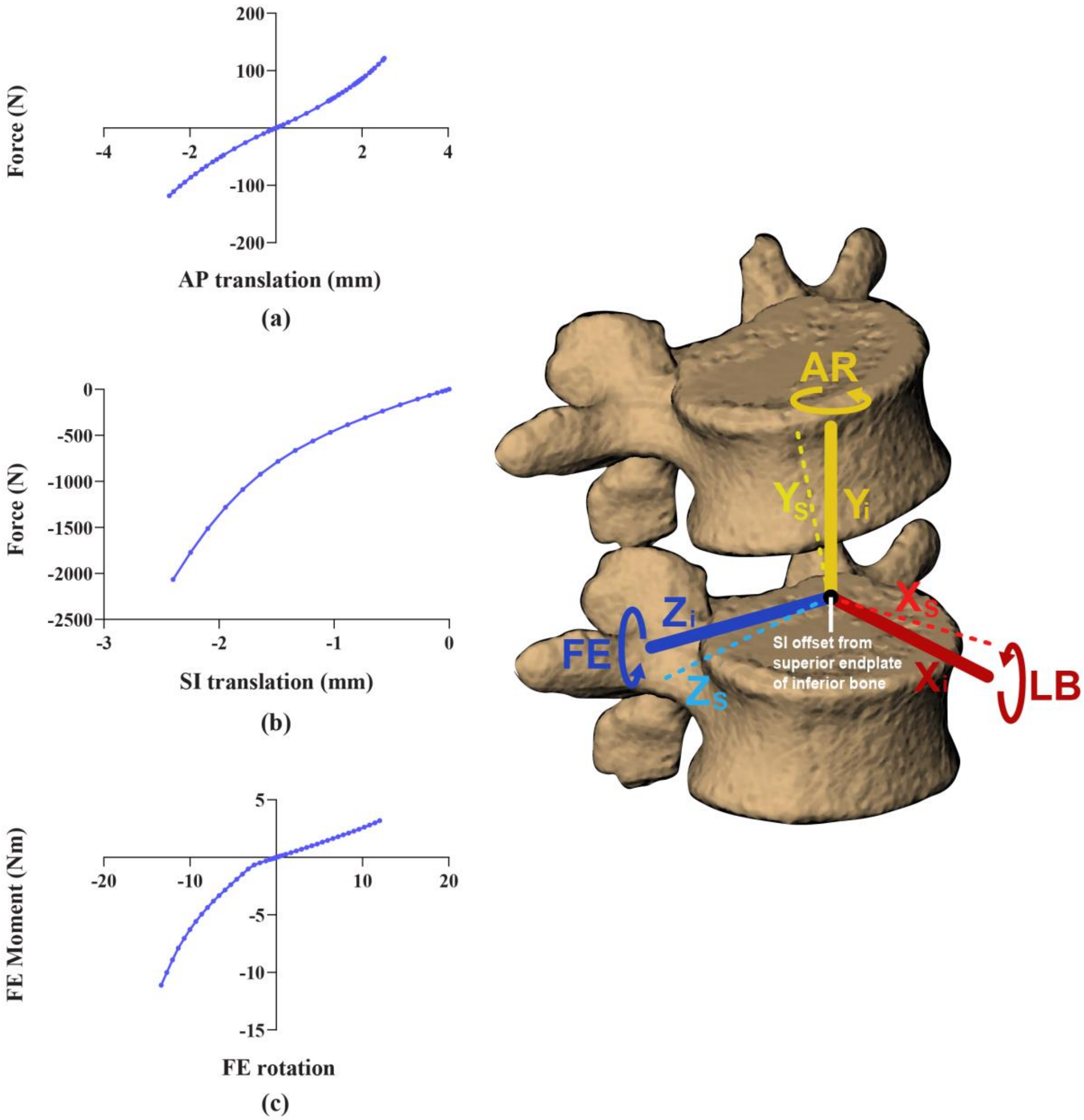

Figure 21: Nonlinear stiffness curves derived from displacement-controlled FE study.

2.4.3 Simulation Pipeline

A sequence of OpenSim algorithms was run on the model to quantify subject-specific joint reaction force and muscle forces estimates in the lumbar spine during the functional lifting tasks. The main steps include scaling of the generic model, Inverse Kinematics (IK), Inverse Dynamics (ID), Static Optimization (SO), and Joint Reactions Analysis (JRA).

2.4.3.1 Scaling the Model

The generic model was scaled using the surface marker locations recorded by the 8-camera Vicon system while the subject assumed the upright standing posture. The scaling process employed was a two-step process. First, OpenSim adjusted the length and mass of the body segments in the model by a scaling factor equal to the ratio of the measured distance between 2 or more real markers attached to the segment to the distance between the model’s virtual markers (Figure 22). Body segments for which no markers were placed, such as the fingers and skull, were not scaled during this step. During the second step, each body was scaled once more by the ratio of the total body mass measured during data acquisition to the total mass of the scaled model. With exception of the lumbar spine, the muscle attachment points, joint frame locations, and mass center locations of the remaining body segments were modified by the calculated scaling factors. The lumbar spine was not scaled, as the subject-specific joint locations were defined based on accurately measured bone kinematics.

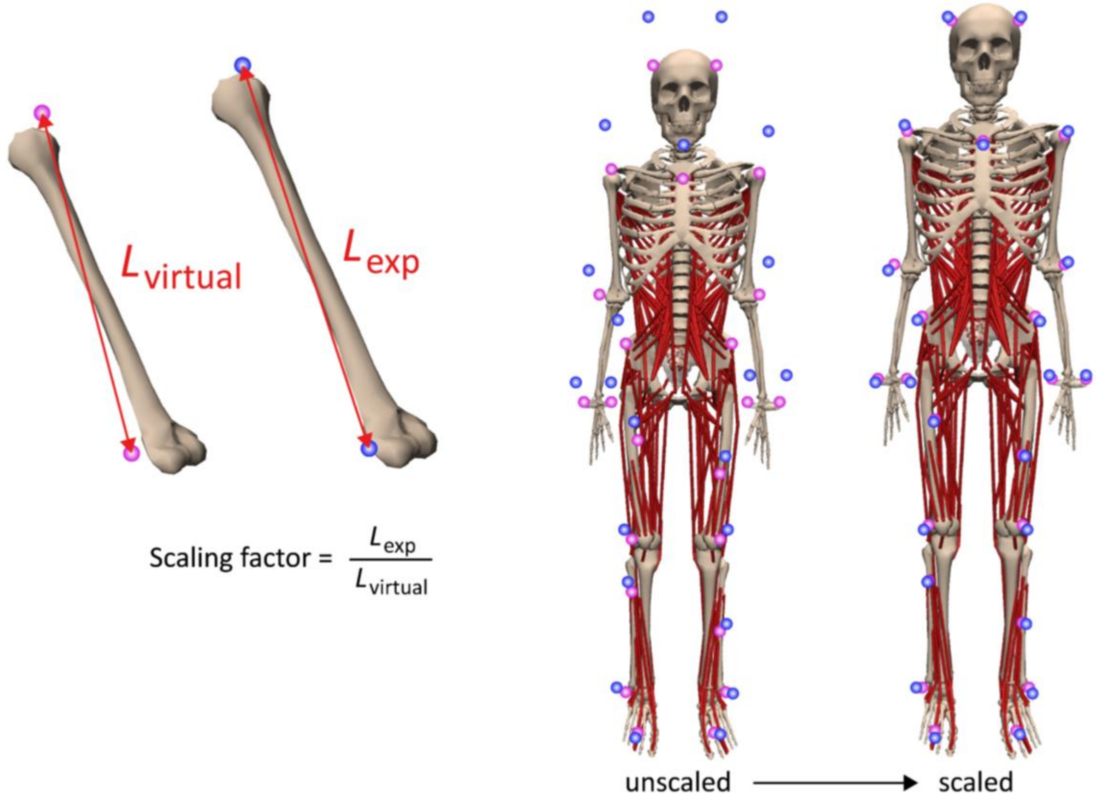

Figure 22: Scaling of the generic model based on virtual and experimental surface markers.

2.4.3.2 Inverse Kinematics

Through the OpenSim GUI, *Inverse Kinematics (IK)*[130] was performed on the model at each time step during the lifting motion. IK solved the weighted least squares equation to determine the joint angles necessary to achieve maximum correlation between the model's virtual marker set and the measured experimental surface marker positions recorded by Vicon throughout the lift (Figure 23):

$$min_q \left[\sum_{i\in\text{markers}} w_i \left\| x_i^{\text{exp}} - x_i(\text{q}) \right\|^2 + \sum_{j\in\text{unprescribed coords}} \omega_j \left(q_j^{exp} - q_j\right)^2\right] \qquad 2\text{-}17$$

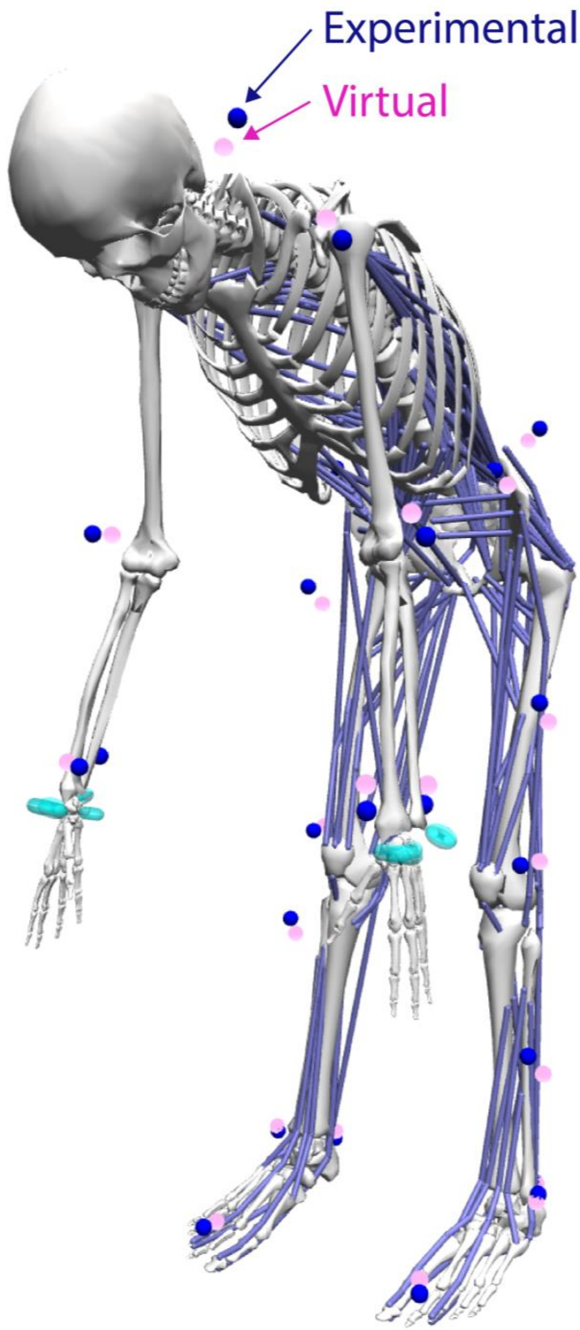

Figure 23: Inverse kinematics maximized correlation between virtual and experimental markers.

Here, **q** is the vector of generalized coordinates being solved for, x_i^{exp} is the experimental position of marker *i*, $\mathbf{x_i(q)}$ is the position of the corresponding marker on the model, and q_j^{exp} is the experimental value for coordinate *j*. w_i and ω_i are the marker weights and coordinate weights prescribed, respectively. For the current work, marker weights were set equal to one for all surface markers, with exception of the four head markers which were set to 0.2. Furthermore, the surface marker trajectories recorded by Vicon were put through a Butterworth filter with a frequency of 6 Hz, the recommended frequency by OpenSim. L2S1 kinematics were explicitly prescribed according to those measured by the DSX system during the lifting motion and were completely independent of surface marker locations. Thus, $\boldsymbol{q_j^{exp}} = \boldsymbol{q_j}$ for lumbar joints form L2L3 to L5S1. During the IK process, the sacrum was assumed to be rigidly attached to the pelvis (pelvic motion was based on surface marker data), while motion from the L12 and upwards was not considered. IK was run on the model for each lifting trial performed during data acquisition, resulting in a motion file describing the complete set of joint kinematics of the model throughout the lifting task.

2.4.3.3 Inverse Dynamics

Inverse Dynamics (ID) solved the classical equations of motion to determine the generalized forces (τ) at each joint necessary to generate the generalized positions (q), velocities ($\dot{q}$), and accelerations ($\ddot{q}$) in the full-body motion derived by IK.

$$M(q)\ddot{q} + C(q,\dot{q}) + G(q) = \tau \qquad \text{2-18}$$

In addition to forces present from the acceleration of the mass matrix (*M*), the Coriolis forces (C) and gravitational forces (G) were also considered. The net joint forces and moments calculated from ID represent the loads at each joint which must be stabilized to satisfy the classical equations of motion.

2.4.3.4 Static Optimization

Subsequently, *Static Optimization (SO)* was performed in MATLAB via the OpenSim API to compute the individual muscle activations (a_m) and forces necessary to produce the calculated net joint moments from ID at each time step of the lifting motion (Figure 24). Inputs to the SO algorithm included a *.mot* file describing the joint kinematics from IK, an *.xml* file describing the ground reaction forces applied at the feet collected during data acquisition, and an *.xml* file consisting of residual actuators and coordinate actuators necessary to help drive them model.

The activation patterns of the muscles were constrained so that the sum of the muscle activation squared was minimized: $min(\sum_{m=1}^{n}(a_m)^2)$, which is approximately equivalent to minimizing the total muscle stress. Furthermore, the muscle activations were constrained by force-length-velocity properties described by the maximum isometric force (F_m^0), muscle length (l_m), muscle shortening velocity (v_m), and moment arm about the joint axis ($r_{m,j}$):

$$\sum_{m=1}^{n}[a_m f(F_m^0, l_m, v_m)]r_{m,j} = \tau_j \qquad \text{2-19}$$

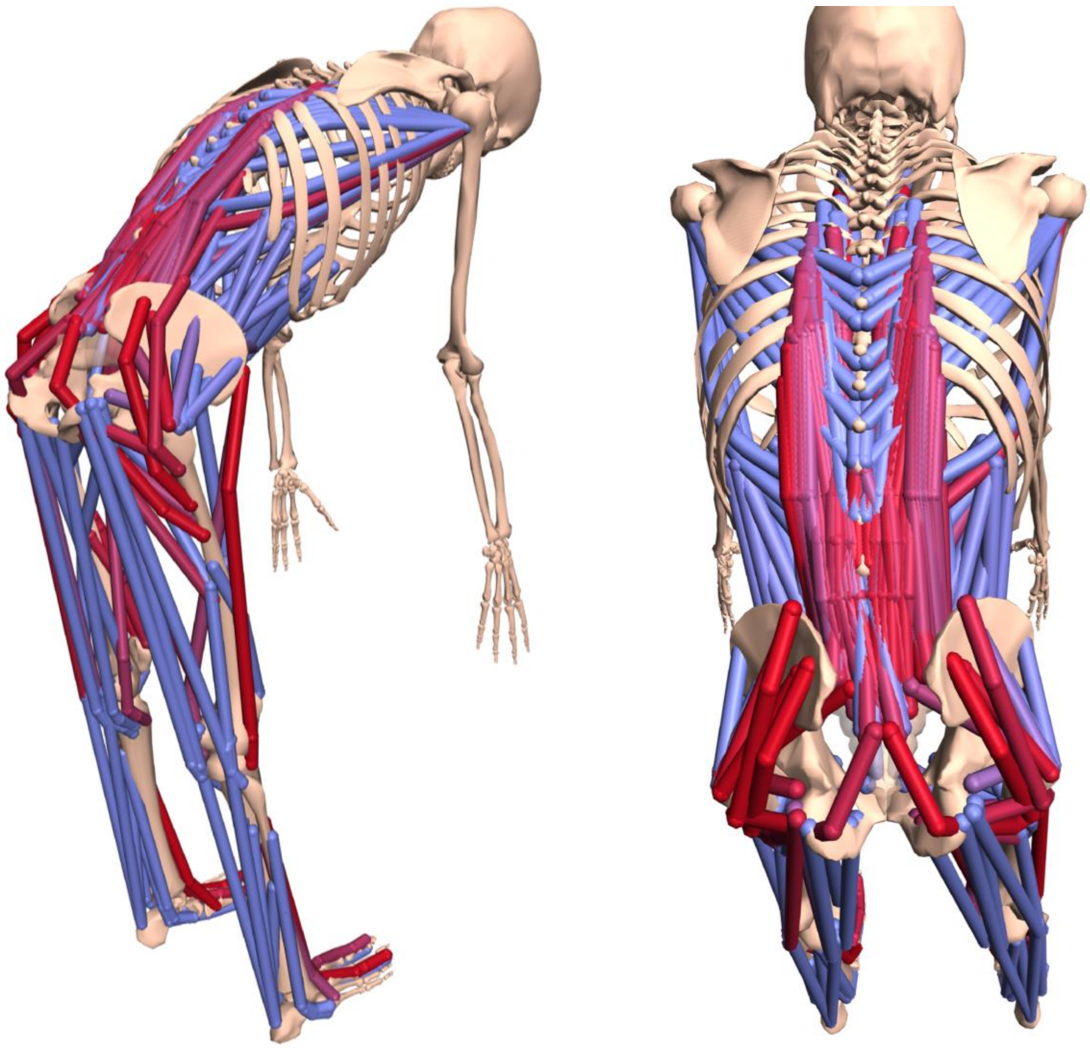

Figure 24: Muscle activations derived from static optimization during the lifting task. Red indicates activation = 1 (max)

The ground reaction forces and moments measured by two force plates during data acquisition were applied to the right and left calcaneus muscles of the OpenSim model. Given the difference in coordinate system orientation between Vicon and OpenSim, the force and moment values were appropriately transformed before being applied during SO.

A good practice during SO is to apply residual actuators to the model to help resolve any dynamics inconsistencies that may be present between the ground reaction force data and the model's estimated accelerations. However, it is preferred that these residuals are low, as high residual forces or moments indicate potential issues with either the surface marker data or inertial properties of the model. Thus, residual actuators were added to the four degrees of freedom describing motion of the pelvis; FE rotation and AP, SI, and ML translation. To ensure that activation of the residual actuators was highly penalized during SO compared to the muscles, the optimum generalized force of the actuators was set equal to 5 N or 5 Nm. Furthermore, Coordinate Actuators were added to each degree of freedom of the model to aid the muscles in achieving dynamics stability if the muscles were incapable of producing the necessary generalized forces of the joint. Similar to the reserve actuators, the optimum generalized force was set to equal 5 N or 5 Nm to discourage use of the coordinate actuators unless a high penalty was applied.

SO is performed separately at each time step, and does not depend on the time steps prior to or after. Thus, the default algorithm in the OpenSim for SO sets the time variable equal to zero ($t = 0$) regardless of the instance of the lift being examined. Because of this, it was necessary to disable the lumbar spine *SimmSpline* functions within the model architecture; if not done so, the lumbar kinematics at every time instance of the lift would have equaled the values of intervertebral kinematics at the beginning of the lift (t = 0). The appropriate L2-S1 joint kinematics were accessed via the joint coordinates file from IK, used as an input to SO. Once run, SO output an *.sto* file describing the time history of muscle activations during the lifting motion, an *.xml* file describing the muscle controls, which also stores the time history of muscle activations, and an *.sto* file describing the time history of muscle forces. The total muscle forces in the four muscle MF, LT, IL, and ABD – were calculated at each time step during SO by summing up the individual muscles forces within each group.

2.4.3.5 Joint Reactions Analysis

Lastly, *Joint Reactions Analysis (JRA)* was run on the model to compute joint reaction forces from the L2L3 to the L5S1 during the lifting motion. In addition to the IK *.mot* file, actuator force *.xml* file, and the ground reaction force *.xml* file, input files to run JRF via the OpenSim API included the muscle control *.xml* file and the muscle force *.sto* file. JRA was run at each time step of the lifting motion for each recorded trial, outputting an *.sto* file describing the net joint reaction forces and moments present at each joint throughout the lift

It is useful to preface these results with a brief clarification on the calculation of bushing (IVD) forces and its incorporation into the net joint reaction force calculations in the *Joint Reaction Analysis* (JRA) step in OpenSim®. *JRA* in OpenSim is a *post hoc* calculation which determines the resultant forces and moments carried by all *un-modeled joint structures* required to produce the specified joint kinematics. Thus, the decision to either include or exclude certain structural components of the joint within the model will directly affect the resultant loads calculated by JRA. In a purely rigid body dynamics analysis of the lumbar joint – where no passive soft tissue structures are modeled (NBS model) – these forces, referred to as *net joint reaction forces (Rx, Ry, Rz),* collectively represent the *total* load to be resisted by all passive structures within that joint. In this study, we have also explicitly modeled passive tissue stiffness by prescribing either linear (LBS) or nonlinear (NLBS) bushing-based force-kinematic relationships at the joint. Under this scenario, the *net* joint reaction force will not represent the *total* load acting at that particular joint, as the resisting forces of the passive tissue are explicitly modeled (they are no longer *un-modeled joint structures*). In order to obtain the *total* joint reaction forces – including those carried by the passive tissues – in LBS and NLBS models and allow comparison with the corresponding the NBS model output, we must add the *modeled* passive (bushing) forces back to the *net* force output from JRA (Figure 25).

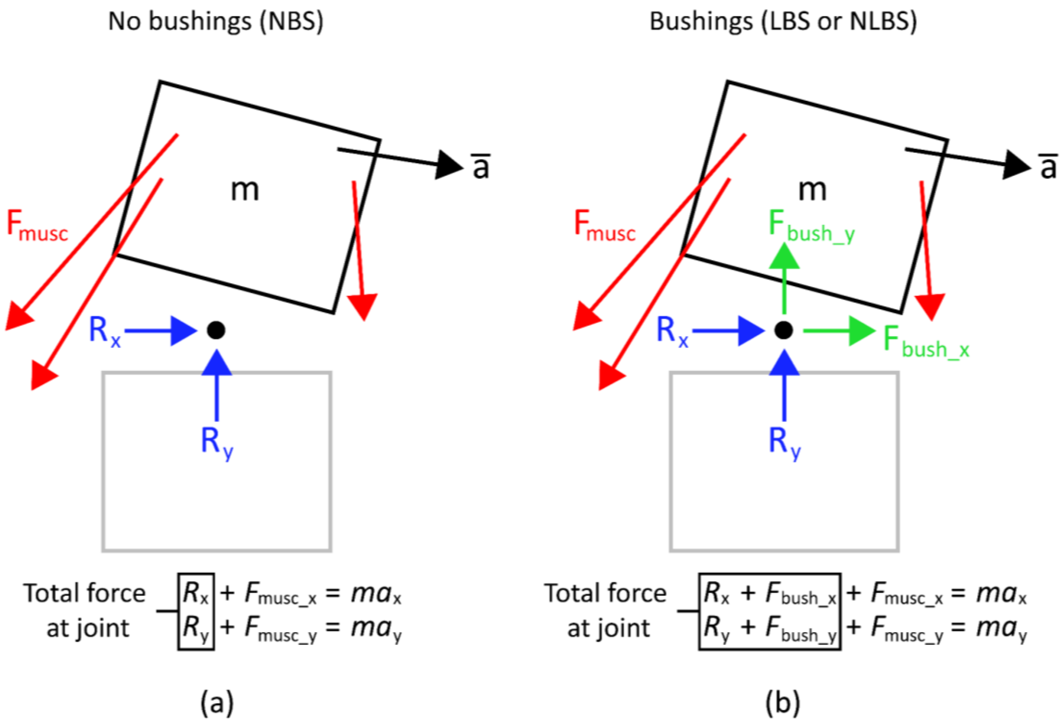

Figure 25: Representation of "total joint reaction force" for NBS, LBS, and NLBS models.

2.4.4 Influence of Input Parameters

The same sequenceof analyses was implemented on 24 model variations; all with different combinations of the two variations of input kinematics, two variations of the neutral state configurations types, three variations of passive stiffness properties, and two variations of external load magnitude lifted. To study the effects of the adjusted parameters on results from simulation, the total joint reaction forces at the L2L3, L3L4, L4L5, and L5S1, along with the total muscle forces in the four muscle groups were estimated for each variation of the OpenSim model. Brief descriptions of the varied parameters are described below.

2.4.4.1 Joint Neutral State Configuration

The influence of neutral state configuration – whether modeled based on the upright and supine kinematics – on estimated joint reaction loads and muscle forces was investigated. The location and orientation of the neutral state, or "reference frame" of the joint, has potential effects on estimated loads in two ways. First, the definition of the neutral state determines where the joint center is located with respect to its adjacent vertebrae. Thus, the location within the joint from which the joint reaction forces reported by *Joint Reactions Analysis* will be slightly different based on neutral state definition. Second, the neutral state defines the intervertebral position and orientation where no passive forces or moments are present at the joint, and thus alters the passive forces and moments present at the joint at every time instance during the lifting motion.

2.4.4.2 Vertebral Kinematic Input

Load estimates from subject-specific 6-DOF DSX-measured kinematics (DSX) were compared to those resulting from running the same OpenSim sequence on models consisting of generic, rhythmic (Rhy) vertebral kinematics. Rhythmic kinematics, which are often used throughout the literature in modeling studies, neglect translational motion of the joint and prescribe a constant ratio of flexion-extension (FE) motion at each joint based on the total lumbar flexion-extension motion. The ratios were defined based on the distribution of the total L2S1 flexion-extension motion across individual segments present in literature based on measured motion from in vitro and in vivo studies[14,22,104]:

$$FE_{L2L3} = 0.349*FE_{L2S1} \quad \text{2-20}$$

$$FE_{L3L4} = 0.29*FE_{L2S1} \quad \text{2-21}$$

$$FE_{L4L5} = 0.204*FE_{L2S1} \quad \text{2-22}$$

$$FE_{L5S1} = 0.256*FE_{L2S1} \quad \text{2-23}$$

In the case of the current modeling study, FE_{L2S1} represents the instantaneous FE rotation of the lumbar spine from L2 to S1 with respect to the neutral state configuration. While distribution of lumbar FE motion was assumed in rhythmic models, the lateral bending and axial rotation of the lumbar spine was not, and instead remaining equal to the DSX-measured values.

2.4.4.3 Intervertebral Stiffness

The influence of passive (bushing) joint stiffness – meant to approximately represent the passive loads carried by the intervertebral disc and in some cases, the ligaments – on JRF and muscle forces were also investigated. Simulations were run on models with either no bushing stiffness (NBS), linear bushing stiffness (LBS), or nonlinear bushing stiffness (NLBS) properties. As previously described, the net JRF resulting from JRA have different representations based on whether passive stiffness properties were included within the model. To ensure a valid comparison, the *total* JRF was compared between models of varying stiffness properties.

2.4.4.4 External Load Magnitude

Individuals participating in the study performed the dynamic lifting task with 10 lb (4.5 kg) and 30 lb (13.6 kg). The magnitude of load lifted was added to the hands of the musculoskeletal model, distributed evenly between the left and right hand. How the magnitude of external load lifted during the dynamic lifting tasks affected estimates of joint reaction loads and muscle forces was quantified. While the external load magnitude was the only experimental variable explicitly changed in between trials during data acquisition, it should be noted that this change also corresponds with a new dataset of DSX-measured kinematics, surface marker measurements, and ground reaction forces. Thus, the effect of external load magnitude on simulation results with DSX kinematics incorporated is not simply the effect of adding a larger load to the hands of the subject-specific model, but also the indirect effects of the corresponding input kinematics.

2.4.4.5 Statistical Comparisons

The *main effect* and *interactions* of input kinematics, neutral joint configuration, and passive stiffness on estimated JRF and muscle forces were determined separately for 10 lb and 30 lb trials at 0%, 25%, 50%, 75%, and 100% percent motion completion (%MC) of the lifting task. The *main effect* was quantified by averaging results across all model variations containing the independent of variable of interest, while ignoring the effects of the other variables. For example, to observe the *main effect* of bushing stiffness, the values from all 10 lb models consisting of LBS stiffness properties were averaged (Figure 26), and similarly done for NLBS and NBS models. The same was then done for the 30 lb models. In addition to the average values of each group, the standard error of the mean was calculated as $SEM = \frac{SD}{\sqrt{n}}$, where SD is the sample standard deviation. Following, the differences in average JRF or muscle forces between groups of different independent variables – but of the same parameter type (e.g. NBS vs LBS, DSX vs RHY) – were determined. The *interactions* of between multiple independent variables within another level of other independent variables were examined as well. For example, within LBS models, the effect of neutral joint configuration in DSX kinematic models was observed; with differences defined as (*LBS_DSX_SUP* - *LBS_DSX_UP*). Interactions of each independent variable on the dependent variables were determined across the 10 lb and 30 lb trials.

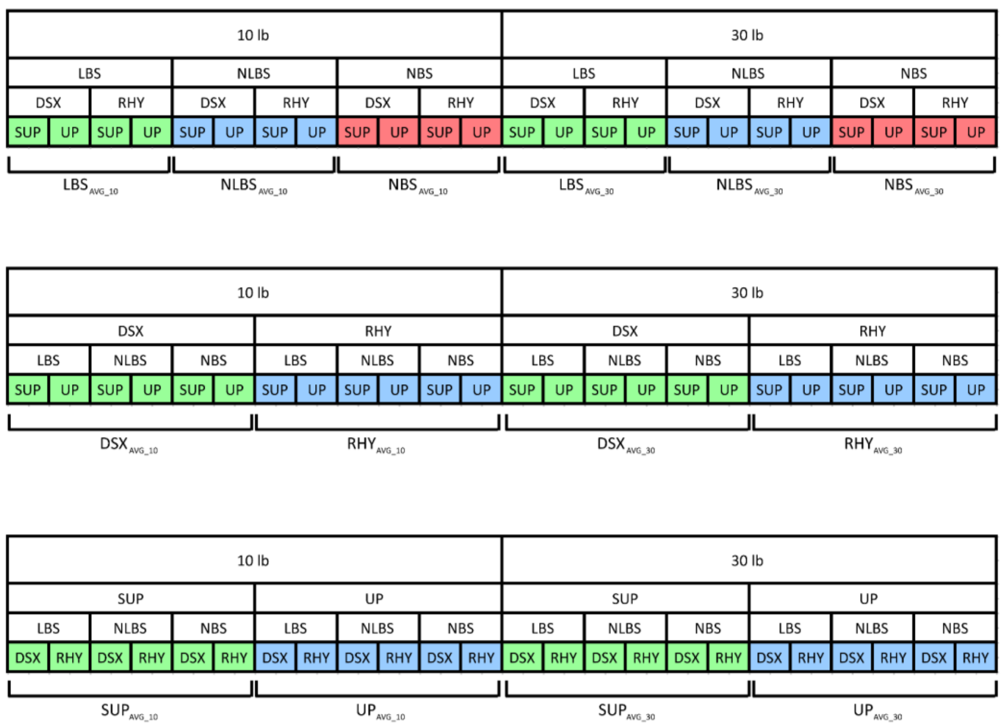

Figure 26: Schematic showing how the average forces across all model variations were averaged to calculate the main effect differences.

Differences describing the main effect and interactions of the three varied parameters were calculated as follows.

1) **Joint neutral state**: Difference = $F_{SUP_{AVG\_10}} - F_{UP_{AVG\_10}}$; $F_{SUP_{AVG\_30}} - F_{UP_{AVG\_30}}$

2) **Kinematic input**: Difference = $F_{DSX_{AVG\_10}} - F_{RHY_{AVG\_10}}$; $F_{DSX_{AVG\_30}} - F_{RHY_{AVG\_30}}$

3) **Bushing stiffness**: Difference = $F_{LBS_{AVG\_10}} - F_{NBS_{AVG\_10}}$; $F_{LBS_{AVG\_30}} - F_{NBS_{AVG\_30}}$

Or Difference = $F_{LBS_{AVG\_10}} - F_{NLBS_{AVG\_10}}$; $F_{LBS_{AVG\_30}} - F_{NLBS_{AVG\_30}}$

2.4.5 Simplified Model Validation

While the complexity of the developed model allows for detailed analysis of lumbar mechanics during the functional lifting task, it is not conducive for easily identifying the direct causes of variation between all models. A simplified model of the lumbar joint was therefore developed to ensure that the lumbar joints are behaving as intended. The model comprised of only two bones, two posterior muscles, and two anterior muscles. While the included muscles were not physiologically representative of all muscular components which act on the joint in vivo, their placement allowed for stability of the joint under different circumstances to analyze the relationship between muscle forces and joint reaction forces reported by OpenSim. Rhythmic kinematics of the L4L5 during the 10 lb lift of a single subject were prescribed to the joint. Thereafter, SO and JRA were run on the model to calculate the muscle forces and joint reaction forces which stabilized the joint and satisfied the dynamic equations of motion. The relationships between joint motion, muscle forces, and joint reaction forces were observed.

3.0 Results

3.1 Disc Height and Disc Deformation

Results on disc morphometry, measured as normalized disc height (nDH) between adjacent endplates, and disc strains are presented in different ways to visualize their variations along one or more of the following dimensions: (1) across lumbar segmental levels; (2) over the entire surface or transverse planar area; (3) between two discrete positions, the flexed position at the beginning and the upright standing position at the end of a motion; (4) over time or the range of motion; and (5) across five selected, consistently identifiable disc regions: anterior, posterior, left, right, and center.

3.1.1 Intervertebral Disc Height

The nDH measurements for trials of different external load magnitudes for each subject are pooled, as no load effect is observed across each disc's entire transverse planar area. In general, the relative distribution of disc height along the anterior-posterior axis compared to the central disc height is consistent with disc height data from previous computed tomography (CT) studies (Bach 2018, Albietz 2012). The L5S1 nDH data from the current study show distinct patterns, as compared to the L2L3, L3L4 and L4L5 discs, which all displayed similar nDH values across the disc area at the upright and flexed positions. Discs from L2L3 to L4L5 have the smallest nDH at the posterior (≈ 0.5) and anterior (≈ 0.7) regions in the upright and flexed positions, respectively.

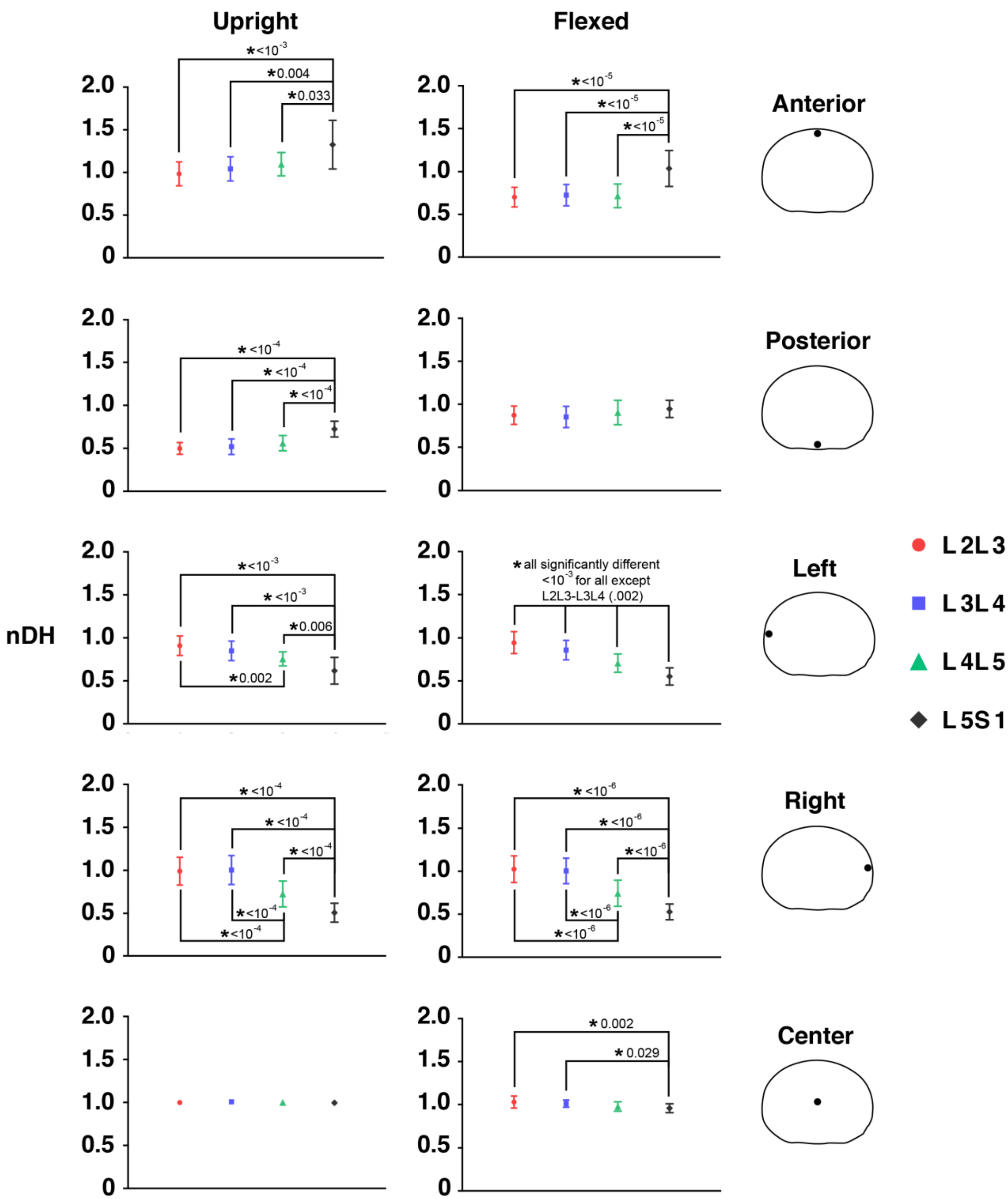

Figure 27: Average normalized disc height (nDH) of five regions of each disc.

L5S1 nDH at corresponding locations are much greater, with values of approximately 0.7 ($p<1e-04$) and 1 ($p<1e-05$), respectively (Figure 27). The L5S1 nDH is smallest (≈ 0.5 – 0.6) at the left and right regions of the discs in both upright and flexed positions (Figure 28); these were significantly lower than the left ($p<0.01$) and right ($p<1e-04$) regions of the other discs (nDH ≈ 0.7 – 1.0). In general, nDH at the left and right regions of the disc becomes progressively smaller moving from the cranial to caudal intervertebral levels (Figure 28). This pattern appears consistent with disc height patterns measured in the supine and axially twisted positions[73] and may be attributed to the increased inferior endplate concavity of lower lumbar vertebrae observed in previous lumbar morphometry studies[140,141].

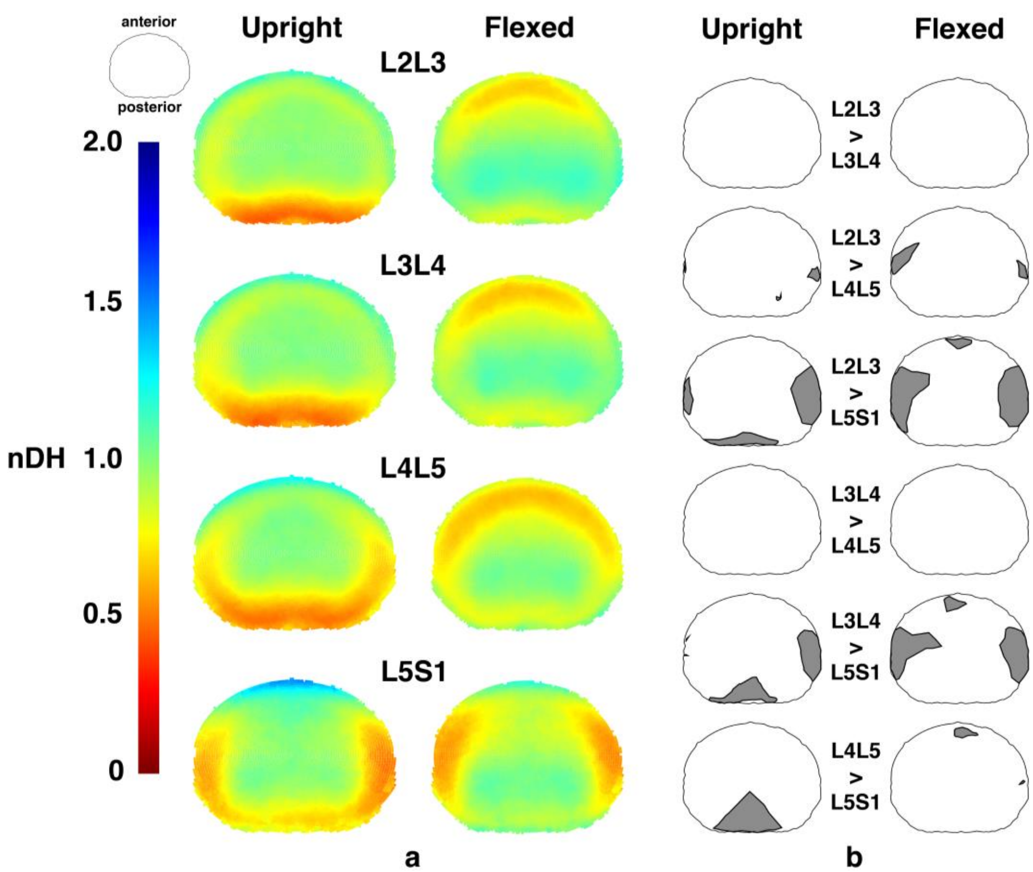

Figure 28: Mapping of nDH across the axial planar surfaces of the lumbar discs.

The regions within the discs exhibiting nDH approximately equal to one (0.95 – 1.05) span approximately 50% to 66% of the disc width (medial-lateral axis) and 33% to 50% of the disc depth (anterior-posterior axis) in the upright position. These areas roughly correspond to the location of the hydrostatically pressurized and incompressible nucleus pulposus (NP) component of the discs[142,143]. At the flexed position, these regions are shifted posteriorly relative to their location in the upright position (Figures 28-29).

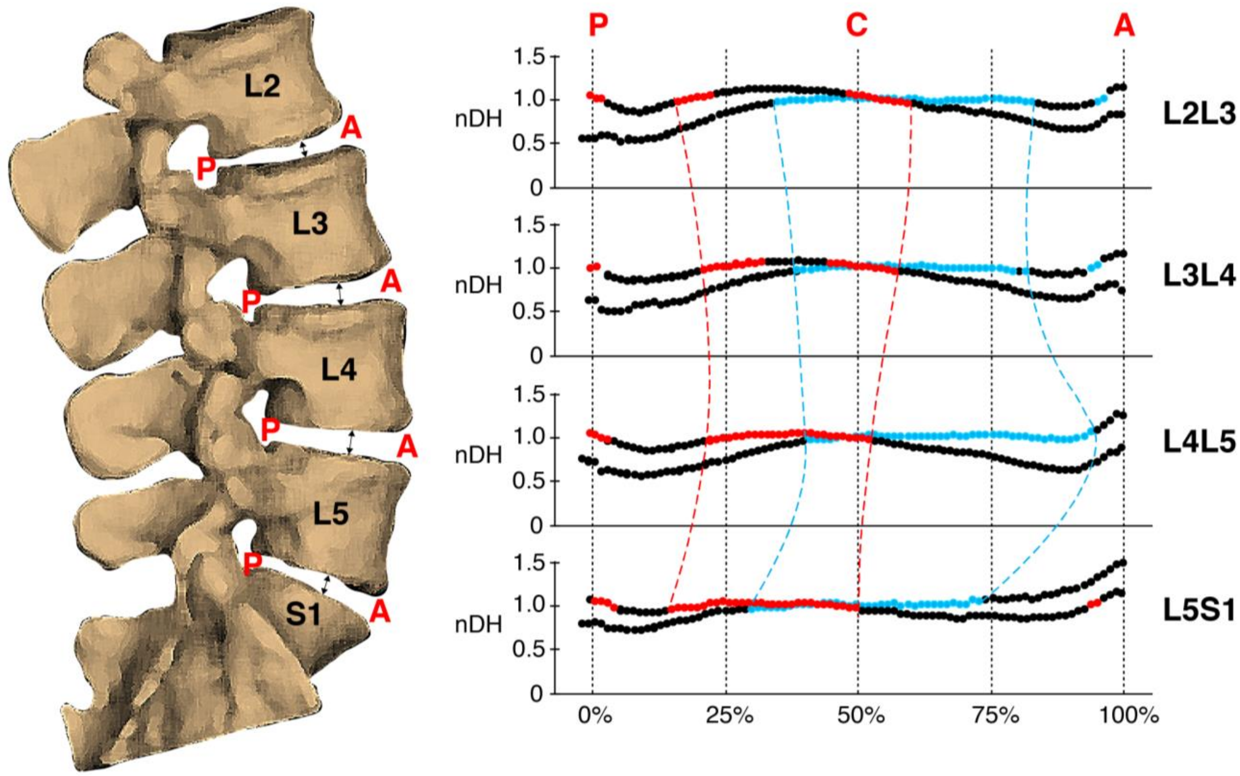

Figure 29: Average normalized disc height (nDH) along the AP axis of each disc.

Past *ex vivo* magnetic resonance imaging (MRI)-based studies have also reported NP posterior and anterior migration in the presence of joint flexion and extension, respectively[58,144]. While the current results reinforce this notion, subtle segment-specific differences are identified:

distributions of nDH along the anterior-posterior axis of the L2L3 and L3L4 show similar trends at both positions; however, compared to the cranial discs, the NP regions are more anterior in L4L5, and more posterior in L5S1 at the upright position (Figure 29).

3.1.2 Intervertebral Disc Strains

External load magnitude had no effect on the normal or shear strain at any of the five regions. Furthermore, Post-hoc Tukey results indicate no effect of external load magnitude on any regional normal or shear strain at the flexed position. Therefore, normal and shear strain data for trials of differing external load magnitudes are pooled before displaying the instantaneous strains over the entire ROM (Figure 30).

Normal strains at the anterior and posterior regions demonstrate strong linear correlations with the amount of lumbar flexion, as indicated by high R^2 values resulting from linear regressions with percent motion completion (%MC) as the single explanatory variable; correlations for normal strains at the left, right, and center are moderate or weak (Table 2, Figure 30). Shear strains at all regions of the L2L3, L3L4, and L4L5 discs demonstrate strong linear correlations with lumbar flexion as well, while correlations at the L5S1 are notably weaker (Table 2, Figure 30).

The L5S1 disc displays unique shear strain patterns compared to the other discs. First, L5S1 shear strain magnitudes (~0.2 on average) are significantly less than others discs across most of the disc cross-sectional area at the fully flexed position, as suggested by non-overlapping ±95% confidence intervals (Figure 31b). Post-hoc Tukey tests ($p<0.001$, Figure 32) confirm this observation at the anterior and posterior regions. Second, L5S1 shear strains remain more or less constant over the entire ROM while the L2-L5 discs exhibited a linearly decreasing trend (Figure 30f-j). This contrast is particularly noticeable in the posterior region of the discs, where shear strains in L2-L5 discs at the flexed position are significantly higher. Normal strain trends show similar differences: L5S1 exhibits significantly less distraction ($p<0.001$) and compression ($p<0.001$) compared to the other discs at the posterior and anterior regions, respectively (Figure 32). (Nagel et al., 2014) also identified L5S1 posterior normal strain (~29%) to be less than L3L4 (~50%) and L4L5 (~65%); however, no differences were realized at the anterior region of the disc[145].

The overall magnitudes of strains at the posterior and anterior regions are comparable to those measured by previous studies during flexion or lifting tasks[58,70,145,146]. (Costi et al., 2007) measured physiological maximum shear strains (MMS) to be 38% during simple flexion of the lumbar spine[58]. When simulating a repetitive lifting task, MMS values of approximately 50% and 75% were measured at the posterior and anterior ends of the disc’s AP axis by (Amin et al., 2019)[146]. Similar to the current results, they also showed the anatomical center of the disc to be in compression with respect to the reference state of the functional spinal unit.

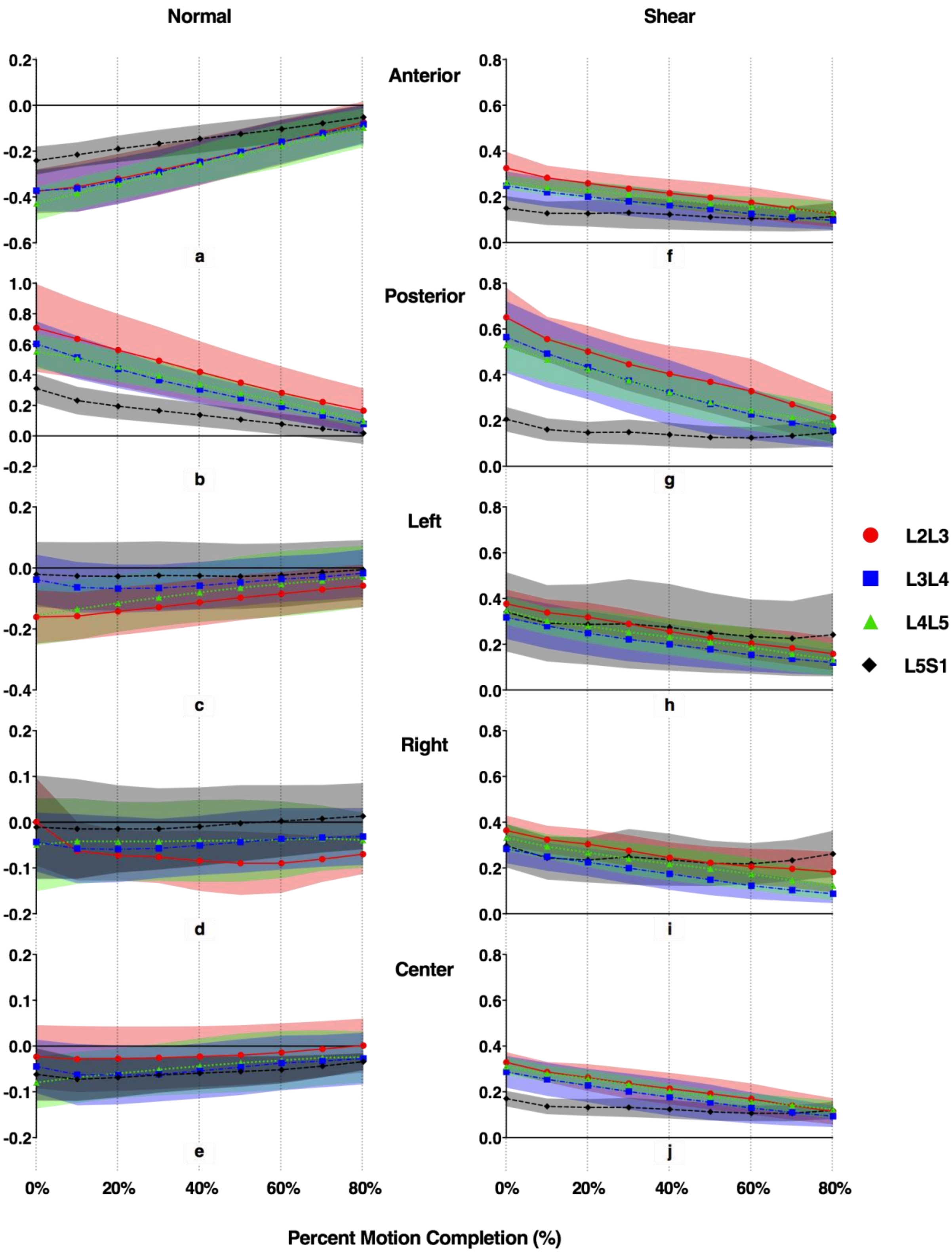

Figure 30: Level-specific disc strains at the five disc regions during the lifting motion.

Further, L5S1 shear direction transitions gradually from about 120° to the medial-lateral (ML) axis in the posterior regions to about 80° in the anterior regions, indicating a changing anterior-posterior (AP) and ML coupled shear pattern from the posterior to the anterior region. On the other hand, the direction of shear remains more consistent throughout the other discs – approximately 75° to 85° off the ML direction (Figure 31a).

Differences in L5S1 strain patterns compared to the other lumbar discs extend to the entire ROM. The clearest differences are seen in the posterior region, where L5S1 exhibits significantly smaller normal and shear strains through about half the range of motion (~50%MC). The anterior region shows a similar trend, although these are less pronounced than in the posterior region. For example, L5S1 anterior normal strain appears to be only significantly less than L4L5 (Figure 30a), while L5S1 anterior shear strain is significantly less than the L2L3 and L4L5 from the flexed position through 20%MC, based on the CI_{95} values (Figure 30f).

The center region of the L5S1 exhibits significantly less shear strain than all other discs (Figure 32) at the flexed position ($p<1e-04$) and at multiple time points during the lifting motion (Figure 30j). No differences among segment levels were observed with regards to normal strain at the center of the disc. Ex vivo studies show reduced shear strains at the nucleus region of the disc compared to the annulus regions, which was not identified in the current work[58,146].

Interestingly, the left regions of the cranial levels (L2L3 and L3L4) exhibit significantly less normal strain than the caudal levels (L4L5 and L5S1) at the flexed position (L2L3: $p<0.001$, L3L4: $p<0.02$), while no differences in normal strain between segment levels were observed at the right region.

Table 2: Linear R-squared coefficients of strain vs. percent motion completion

Disc	Normal strain					Shear strain				
	A	**P**	**L**	**R**	**C**	**A**	**P**	**L**	**R**	**C**
L2L3	.92	.97	.43	.54	.44	.84	.86	.83	.86	.86
L3L4	.94	.97	.49	.52	.51	.83	.87	.80	.88	.87
L4L5	.97	.99	.78	.38	.69	.81	.84	.88	.79	.85
L5S1	.88	.92	.65	.46	.62	.44	.50	.43	.36	.47

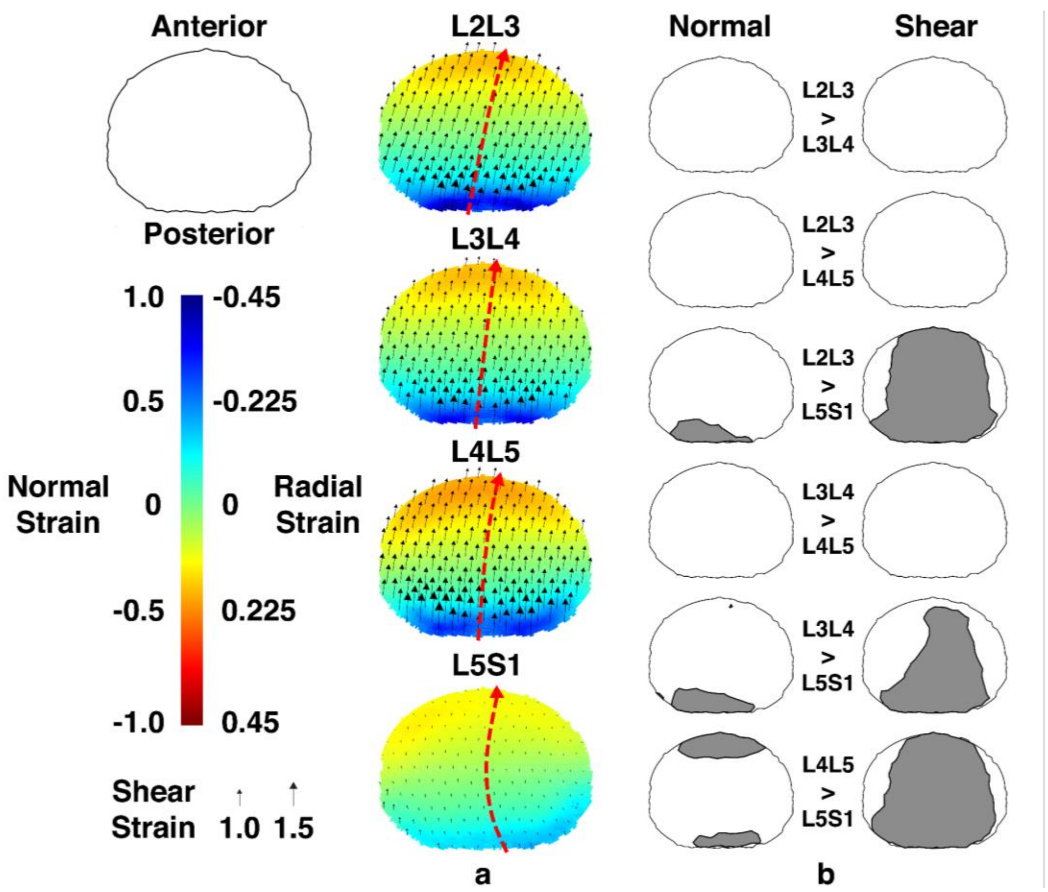

Figure 31: Mapping of disc strain across the axial planar surfaces of the lumbar discs.

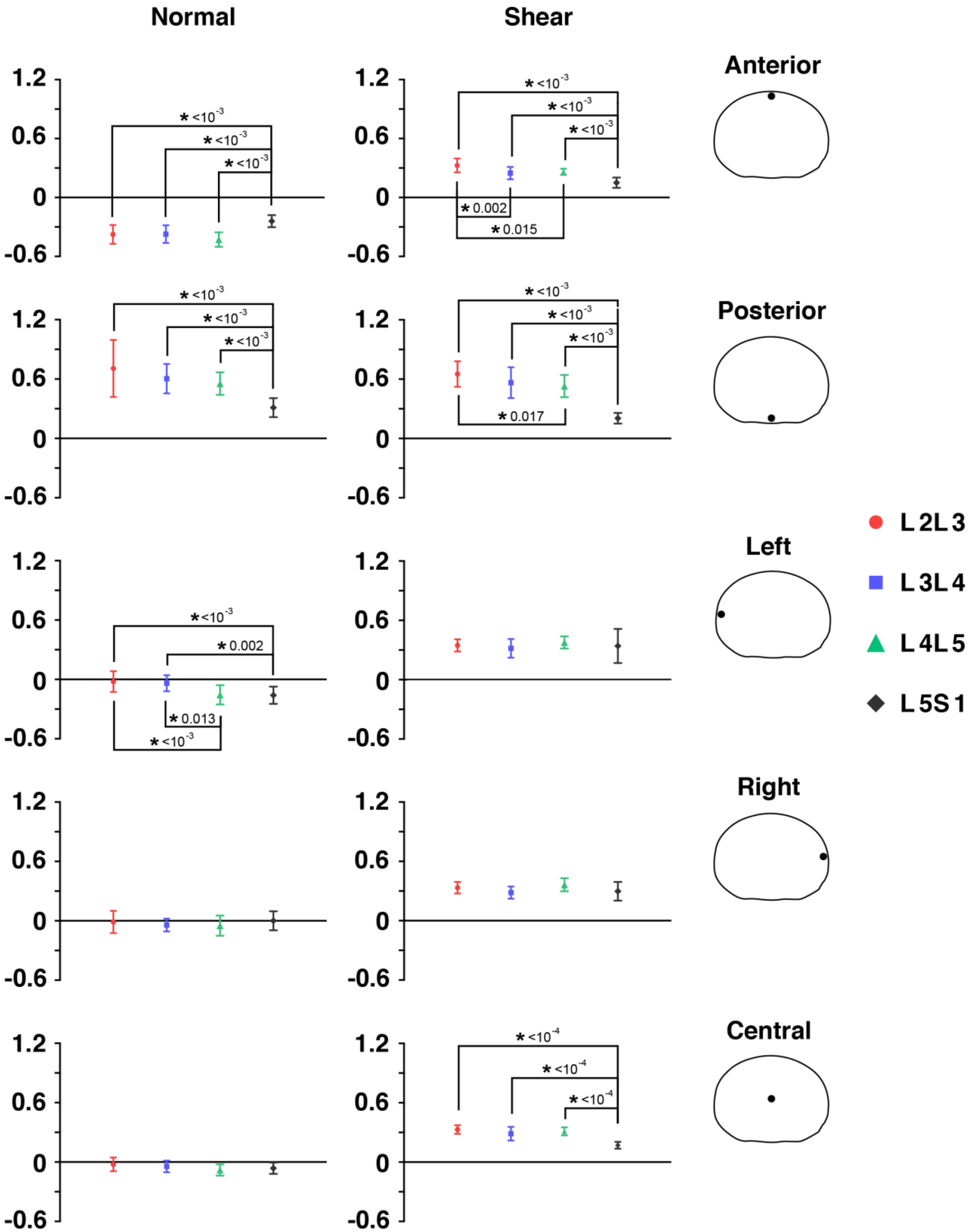

Figure 32: Average disc deformation of five regions of the disc at each segment level.

3.1.3 Intervertebral Disc Radial Strains and Bulging

Average radial strains across all subjects ranged from approximately -0.3 at the posterior region to 0.2 at the anterior region, with respect to the upright standing position (Figure 33). These values corresponded to bulging of the disc of approximately -1 mm and 1 mm at the posterior and anterior regions, respectively (Figure 34). Radial strains were small and generally close to zero at the left, right, and center regions throughout the lifting motion. L5S1 posterior radial strains were significantly smaller in magnitude than other segments during the first half of the lifting motion, while L5S1 anterior radial strains were significantly smaller than the L4L5 segment. Regions of significant differences in radial strain between segment levels were identical to those identified for normal strains, given the direction relationship defined between the two measures (Figure 31). Magnitudes of radial strains were larger than those observed by (Tsantrizos et al., 2005), however this can be explained by the increased loading conditions imposed on the lumbar spine in the current study[144]. (Amin et al., 2019) reported radial displacements of approximately 1.5-2.0 mm at the posterior and anterior ends of the AP axis when simulating a lifting task on cadaver functional spinal units[146]. While magnitudes differed slightly between studies, the inward and outward bulging of the disc at the posterior and anterior regions of the disc, as observed in the current work, is consistent.

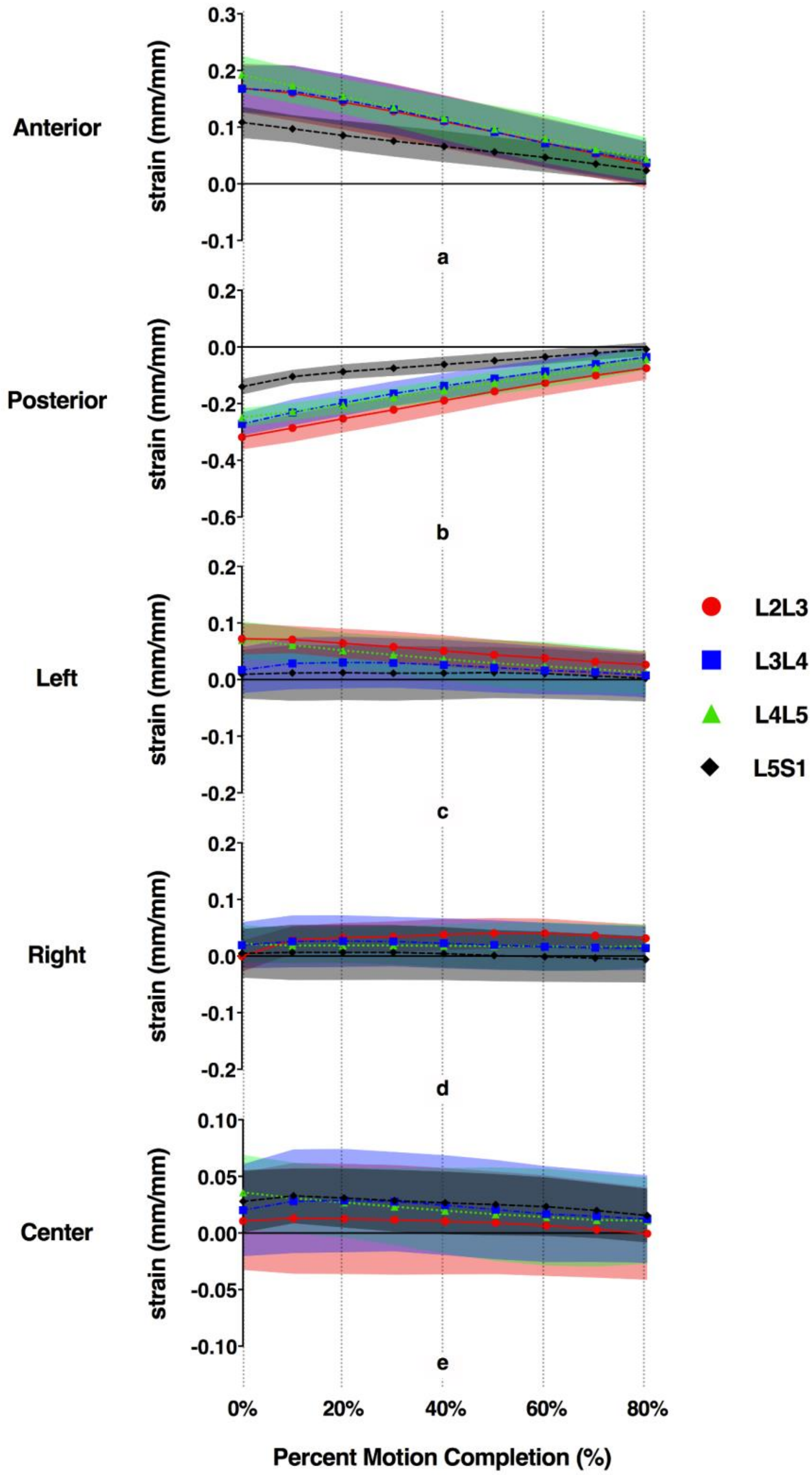

Figure 33: Level-specific disc radial strains at the five disc regions during the lifting motion. Positive strains indicate radial strain outwards from the disc center.

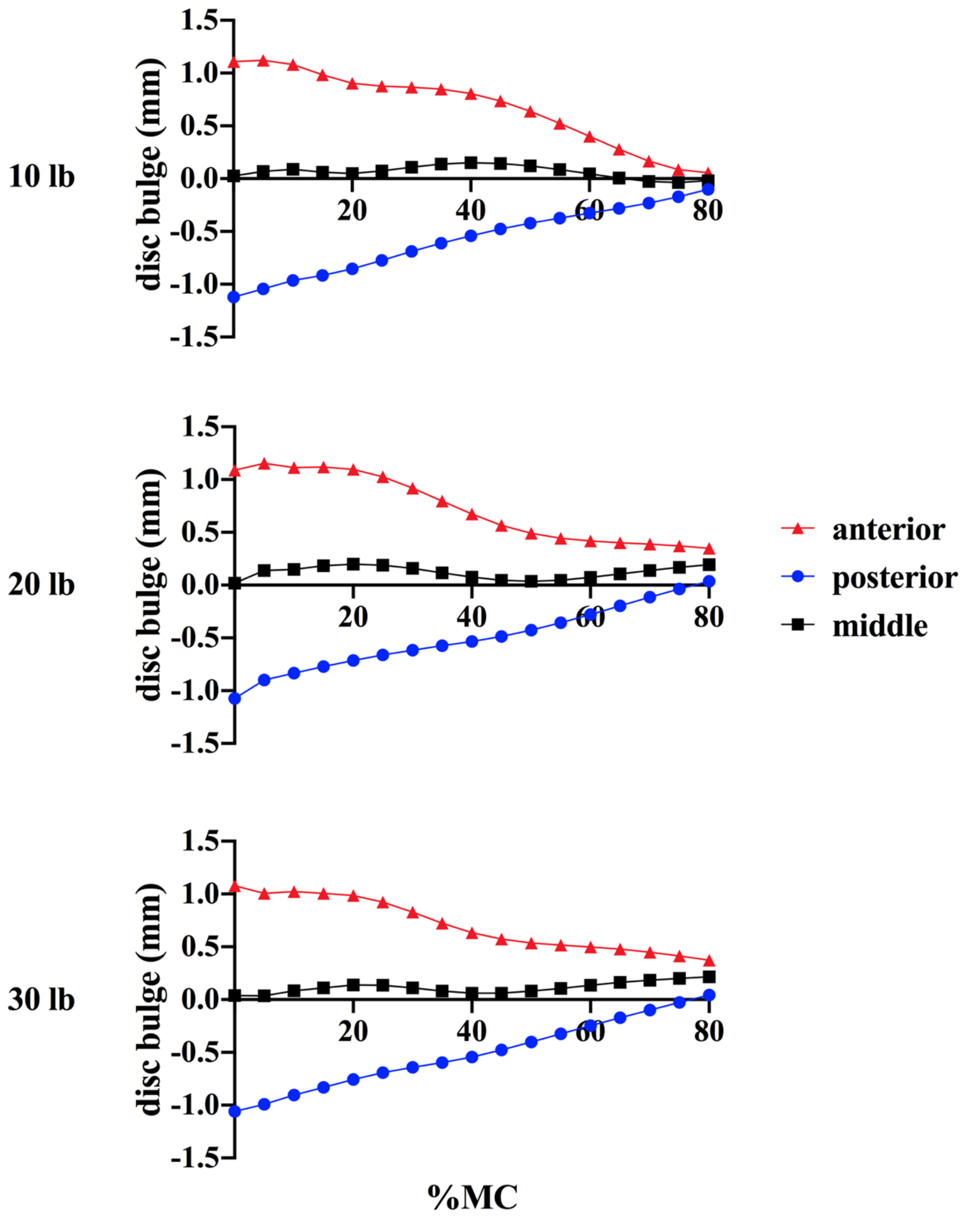

Figure 34: Radial bulge at the anterior, middle, and posterior regions of the disc across all subjects.

Disc bulging at the L2L3 to L5S1 of a single subject was compared with results from a concurrent displacement-controlled FE study utilizing the subject's identical subject-specific data (Figure 35). Approximating disc bulging from the normal strains during the 10 lb lift led to greater anterior and posterior bulge compared to the FE study with respect to the upright standing position. Results were less comparable during the 20 lb lift and were generally bulged more inwards compared to the upright position than as observed in the FE model. However, at the point of furthest flexion the bulge data seemed fairly comparable between the two methods.

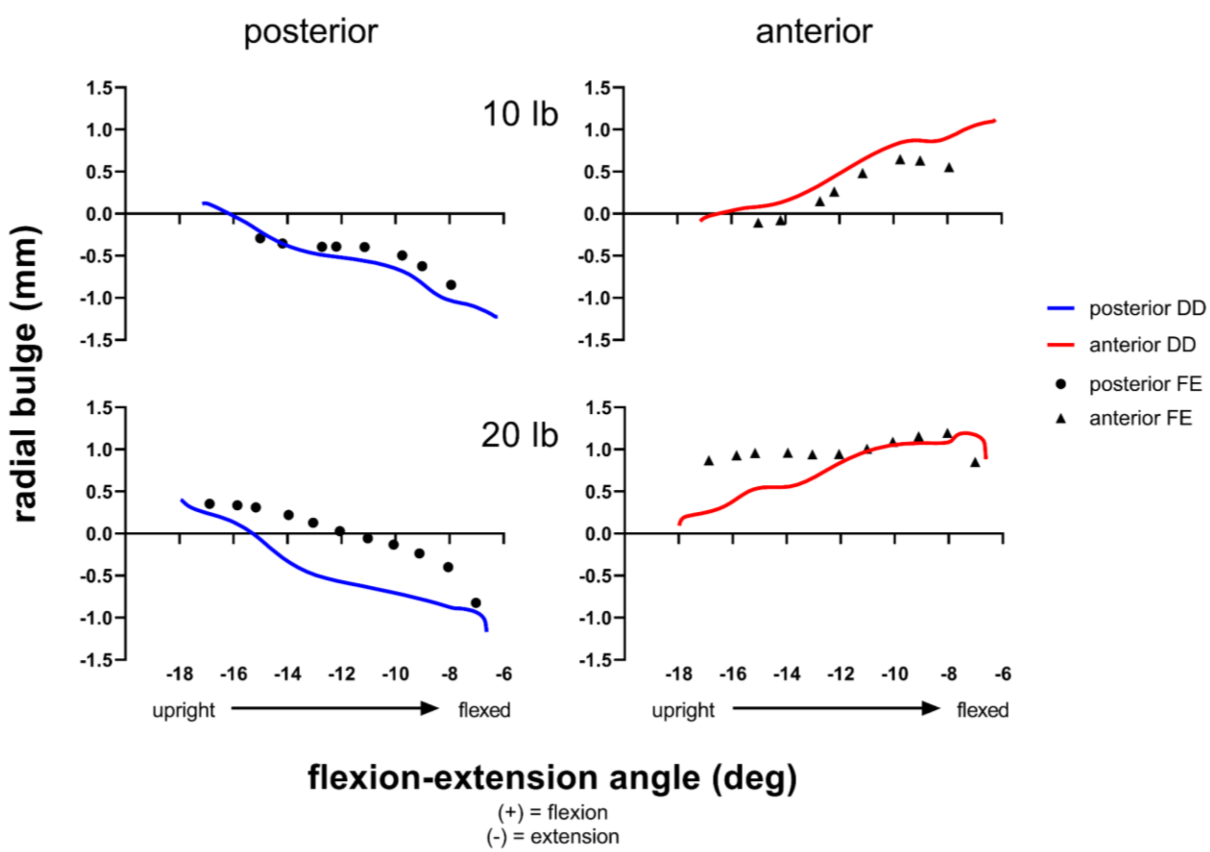

Figure 35: Disc bulging (mm) estimates from disc deformation analysis (DD) and FE simulation.

3.1.4 Disc Height and Rotational Kinematics

Correlations between disc height and range of intervertebral rotation were weak at all segment levels, regardless of whether the FE joint rotations were normalized with respect to the overall L2-S1 FE rotation (Figure 36). Positive slopes were present at nearly every segment during all lifting trials, while linear R-squared coefficients between intervertebral rotation and central disc height were all under 0.45 (L2L3, 30 lb lift), the majority of which were between 0 and 0.2. While normalization of intervertebral range of FE rotation to the overall L2S1 range of FE rotation led to a slight increase in linear R-squared coefficients, they remained weak – the majority were around 0.1 to 0.4, with the maximum being 0.69 (L2L3, 30 lb lift).

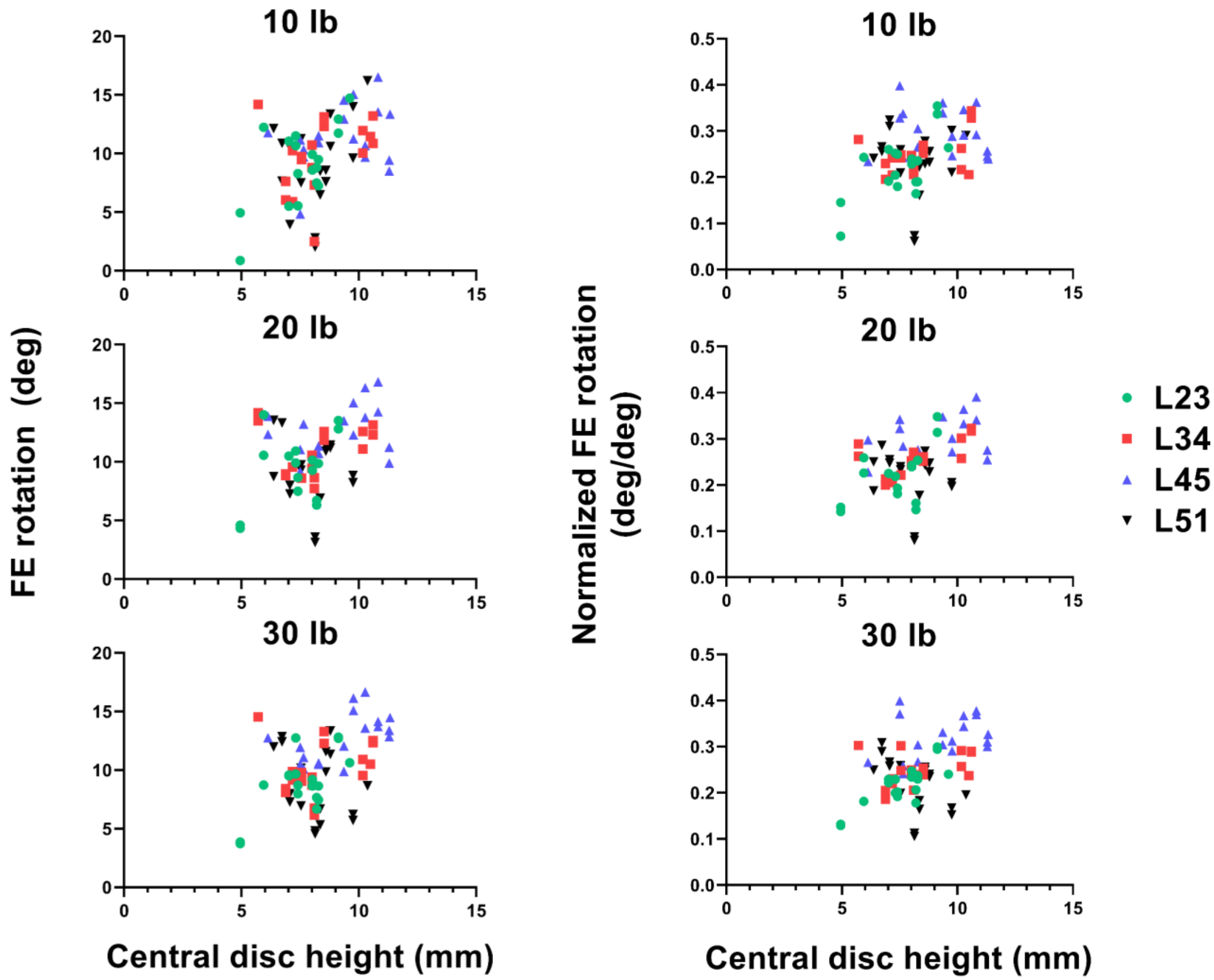

(a) (b)

Figure 36: (a) Range of FE rotation (degrees) vs. central disc height (mm) across all subjects. (b) FE rotation was also normalized to total L2-S1 FE rotation to observe potential changes in relationships.

3.2 Facet Joint Kinematics

Data from three participants were excluded owing to poor image capture quality and tracking issues. One additional participant was excluded due to poor image quality for the static trials making 10 participants' data available for processing yielding 116 observations.

3.2.1 Upright translational kinematics

Static, upright (reference) SI spacing was substantially larger at L5S1 compared to other segments (Table 3), measuring approximately 2 mm compared to -0.4 mm to -0.9 mm for the other segments. In general, sideways sliding and facet gap spacing were small in magnitude; the mean +-SD for nearly all segments spanned zero mm. No differences in upright kinematics were detected between left and right facet joints at any segment level. For most translational measurements across all segment levels and kinematic directions, the standard deviation across all subjects were larger than the average.

Table 3: Segment-specific FJ translations at the upright standing position. Mean ± CI_{95}

	(a) X (facet gap) (mm)			(b) Y (SI sliding) (mm)			(c) Z (sideways sliding) (mm)		
Segment	Left	Right	Average	Left	Right	Average	Left	Right	Average
L2-L3	0.39 ± 0.31	0.33 ± 0.42	0.36 ± 0.27	-0.39 ± 0.89	-0.60 ± 0.79	-0.50 ± 0.72	0.03 ± 0.80	-0.51 ± 0.46	-0.24 ± 0.44
L3-L4	0.29 ± 0.47	0.26 ± 0.58	0.28 ± 0.49	-0.66 ± 1.22	-0.84 ± 1.23	-0.75 ± 1.17	0.29 ± 0.88	-0.22 ± 0.67	0.03 ± 0.74
L4-L5	0.51 ± 0.47	0.90 ± 0.47	0.70 ± 0.43	-0.86 ± 1.25	-0.88 ± 1.22	-0.87 ± 1.06	-0.13 ± 0.75	0.29 ± 1.03	0.08 ± 0.71
L5-S1	-0.22 ± 0.56	0.13 ± 0.58	-0.04 ± 0.49	1.63 ± 1.13	2.51 ± 1.30	2.07 ± 1.12	0.67 ± 0.75	0.74 ± 0.98	0.70 ± 0.77

3.2.2 Dynamic Translation Kinematics

Although coupled translation was observed, translation in the superior-inferior (SI, local Y-axis) direction was the dominant contributor. SI translation was significantly lower in L5S1 *[p<0.001]* compared to L2L3, L3L4 and L4L5 segments. No significant differences were detected between the other segments (p>0.5, Figure 37, Table 4). Time series plots including the mean (±CI_{95}) for the segment-specific translations for each of the three load cases are shown in Figure 38. Corresponding linear regression-based slopes (Figure 39) revealed strong linearity (r^2 >0.94) for SI translation component and reasonably good linear fit for the sideways sliding (Z-) component (r^2 > 0.8), with a much lower correlation coefficient for X-component (facet gap, r^2 ~0.5). L4L5 and L5S1 exhibited larger translations along the averaged, local X- *(Md=0.4mm and 0.4mm, respectively)* and Z-axes *(Md=1.5mm and 1.6mm, respectively)* compared to L2L3 and L3L4 *((x-axis Md = 0.2 mm and 0.03 mm, respectively; z-axis Md = 0.7mm and 0.7 mm, respectively)*. Following differences were significant along Z- (L5S1>L3L4, p=0.01; L4L5>L3L4, p=0.04, L5S1>L2L3, p <0.001; L4L5 >L2L3, p=0.0016). For the right side, L5S1 and L4L5 X-components were significantly greater than L3L4 (p = 0.01 and 0.04 respectively). Averaged X-component translations as well as those for the left facets were not significantly different across segments. No significant effect of the magnitude of weight lifted was detected (p>0.7, Figure 40, Table 5). Overall magnitudes of translation in the cranial (L2-L5) segments were quite similar *(Md = 5.9mm, 6.3mm and 6.6mm respectively)*, but L5S1 facet translations were markedly different *(Median (Md) = 3.5mm, p<0.0001)*.

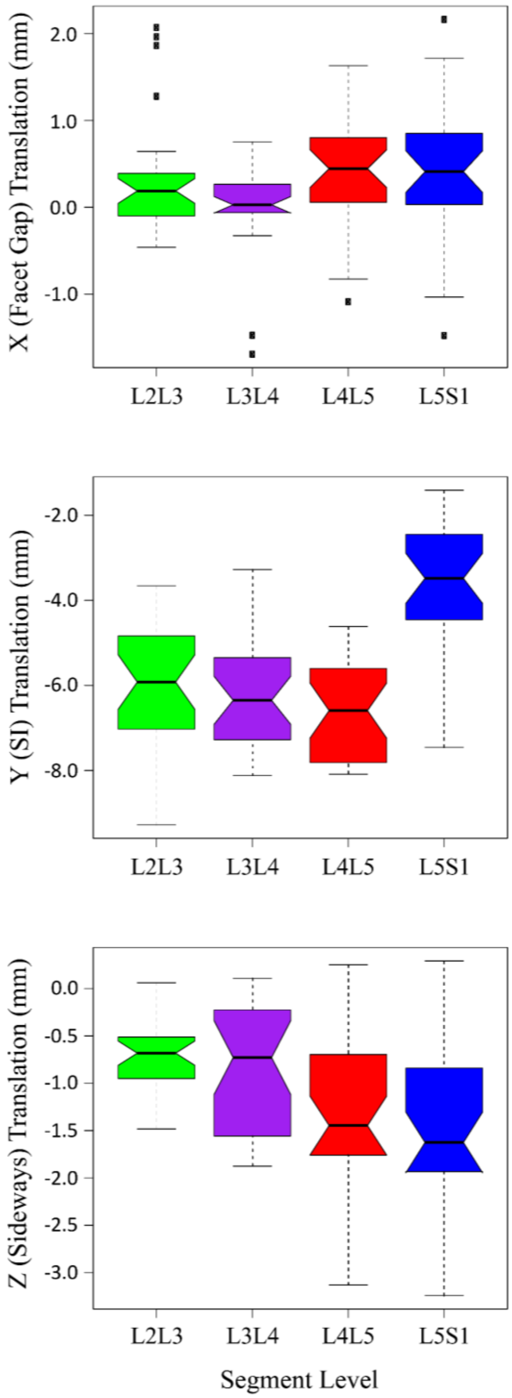

Figure 37: Effect of segment level on FJ translation in the X-, Y-, and Z- directions. Notches indicate confidence intervals of the median. Lack of overlap indicates significant difference, while plot whiskers encompass the total range of data in each group.

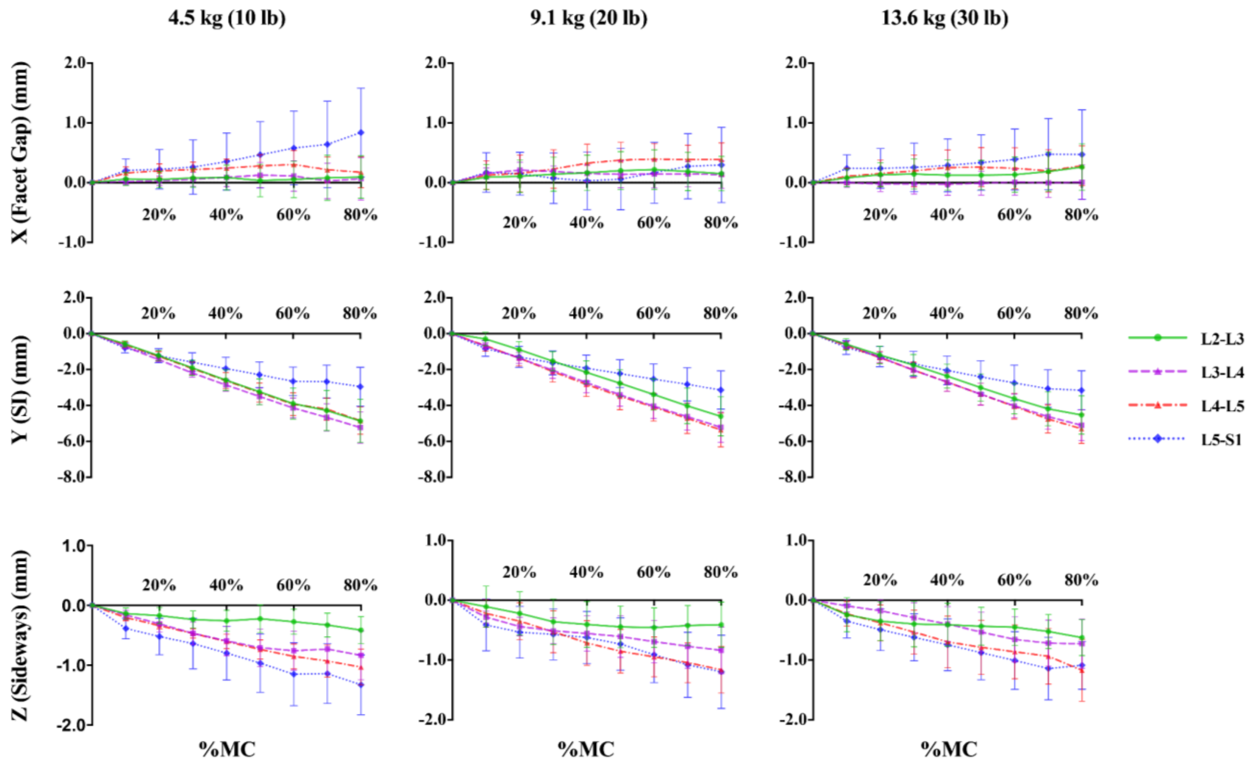

Figure 38: Lumbar facet translations in the X-, Y-, and Z- directions from the starting flexed position to 80% percent task completion – flexed position being the zero point. Errors bars represent ±95% confidence intervals.

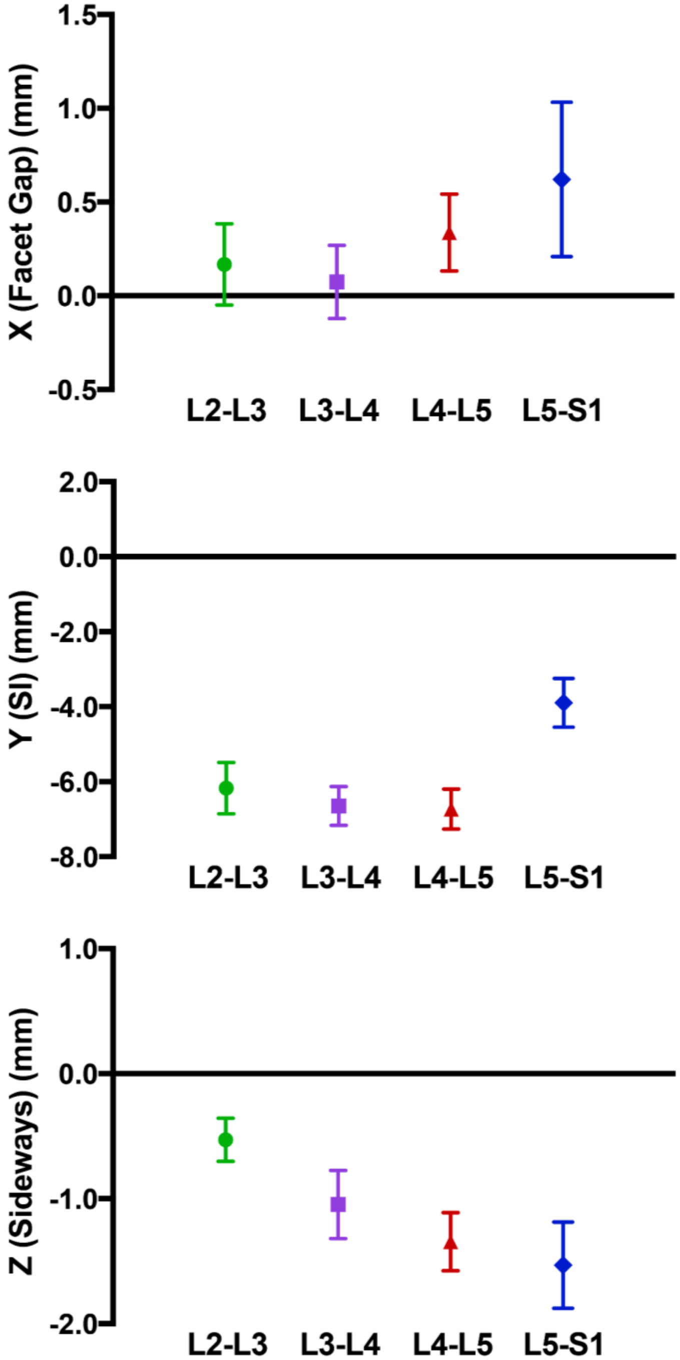

Figure 39: Linear regression-based slopes of the facet joint translation components for each segment. Lack of overlap between error bars between groups indicates significant difference.

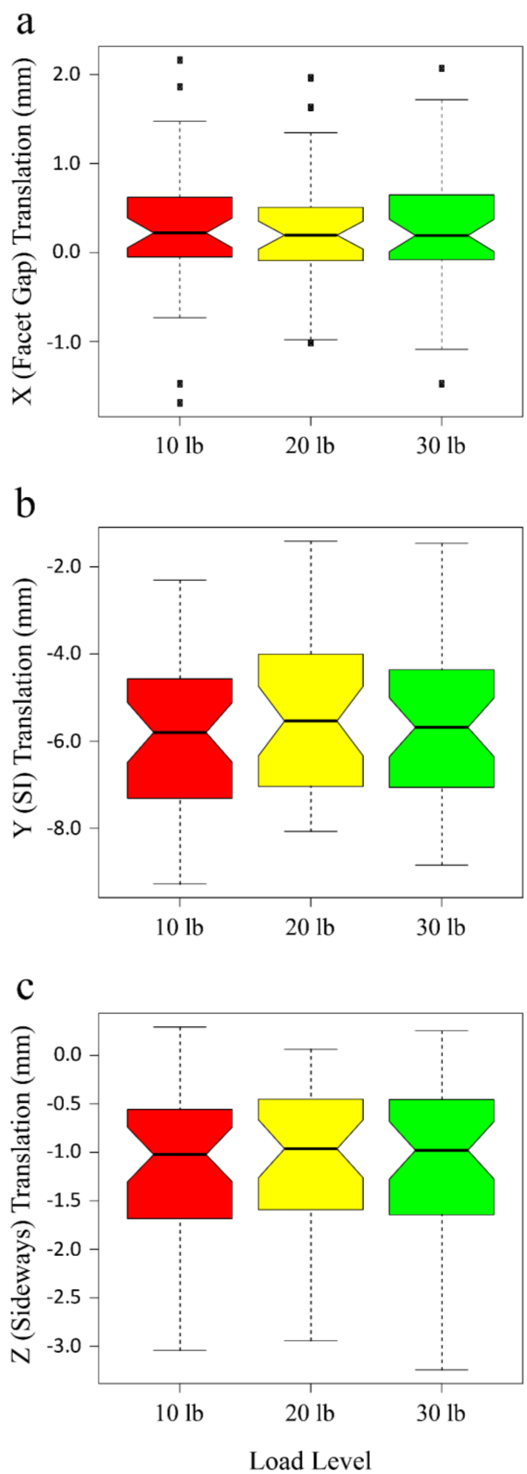

Figure 40: Effect of load magnitude on facet translations. Lack of overlap between notches indicates significant difference, while plot whiskers encompass the total range of data in each group.

Table 4: Segment-specific facet joint translations at the upright standing position with respect to the fully flexed position. Median (confidence interval range based on ± CInotch).

	(a) X (facet gap) (mm)			(b) Y (SI sliding) (mm)			(c) Z (sideways sliding) (mm)		
Segment	**Left**	**Right**	**Average**	**Left**	**Right**	**Average**	**Left**	**Right**	**Average**
L2L3	0.59 [a] (0.30 – 0.87)	-0.10 [bc] (-0.28 – 0.08)	0.19 [ac] (0.04 – 0.33)	-5.66 [a] (-6.39 – -4.92)	-6.07 [a] (-6.71 – -5.42)	-5.92 [a] (-6.56 – -5.28)	-0.56 [a] (-0.76 – -0.37)	-0.72 [a] (-0.91 – -0.53)	-0.68 [a] (-0.81 – -0.55)
L3L4	0.32 [a] (0.17 – 0.46)	-0.29 [b] (-0.40 – -0.17)	0.03 [c] (-0.07 – 0.12)	-5.97 [a] (-6.58 – -5.36)	-6.06 [a] (-6.59 – -5.52)	-6.34 [a] (-6.91 – -5.78)	-0.60 [a] (-0.84 – -0.36)	-0.65 [a] (-1.15 – -0.14)	-0.73 [a] (-1.12 – -0.34)
L4L5	0.30 [a] (-0.01 – 0.61)	0.39 [ac] (0.05 – 0.72)	0.44 [a] (0.23 – 0.66)	-6.51 [a] (-7.03 – -6.00)	-6.11 [a] (-6.80 – -5.43)	-6.59 [a] (-7.24 – -5.94)	-1.17 [b] (-1.43 – -0.92)	-1.56 [b] (-1.95 – -1.17)	-1.45 [b] (-1.76 – -1.14)
L5S1	0.45 [a] (0.17 – 0.74)	0.46 [ac] (0.07 – 0.86)	0.41 [a] (0.17 – 0.65)	-3.98 [b] (-4.70 – -3.25)	-3.01 [b] (-3.58 – -2.43)	-3.48 [b] (-4.07 – -2.89)	-1.61 [b] (-2.27 – -0.96)	-1.03 [ab] (-1.50 – -0.57)	-1.63 [b] (-1.95 – -1.30)

Note: Within each translational component, values with one or more like superscripts (a,b,c,d) across side (left, right, average) *or* across segment level (L2L3, L3L4, L4L5, L5S1) indicates no significant differences. Dissimilar superscripts indicate significant differences

Table 5: Load-specific facet joint translations at the upright standing position with respect to flexed position. Median (confidence interval range based on ± CInotch).

	(a) X (facet gap) (mm)			(b) Y (SI sliding) (mm)			(c) Z (sideways sliding) (mm)		
Segment	**Left**	**Right**	**Average**	**Left**	**Right**	**Average**	**Left**	**Right**	**Average**
4.5 kg (10 lb)	0.32 [a] (0.08 – 0.55)	-0.01 [a] (-0.21 – 0.21)	0.22 [a] (0.05 – 0.39)	-6.04 [a] (-6.80 – -5.27)	-5.49 [a] (-6.21 – -4.76)	-5.80 [a] (-6.48 – -5.12)	-0.94 [a] (-1.21 – -0.67)	-1.11 [a] (-1.44 – -0.78)	-1.02 [a] (-1.30 – -0.74)
9.1 kg (20 lb)	0.39 [a] (0.16 – 0.61)	-0.07 [a] (-0.31 – 0.18)	0.19 [a] (0.04 – 0.35)	-5.72 [a] (-6.56 – -4.88)	-5.59 [a] (-6.44 – -4.75)	-5.54 [a] (-6.34 – -4.74)	-0.69 [a] (-0.94 – -0.43)	-1.07 [a] (-1.51 – -0.63)	-0.96 [a] (-1.26 – -0.66)
13.6 kg (30 lb)	0.34 [a] (0.08 – 0.60)	-0.06 [a] (-0.32 – 0.19)	0.19 [a] (0.01 – 0.37)	-5.87 [a] (-6.62 – -5.12)	-5.64 [a] (-6.33 – -4.96)	-5.68 [a] (-6.36 – -5.01)	-0.81 [a] (-1.04 – -0.58)	-0.99 [a] (-1.30 – -0.68)	-0.98 [a] (-1.28 – -0.68)

Note: Within each translational component, values with one or more like superscripts (a,b,c,d) across side (left, right, average) *or* across load level (4.5 kg, 9.1 kg, 13.6 kg) indicates no significant differences. Dissimilar superscripts indicate significant differences

3.3 Musculoskeletal Modeling

JRF and muscle forces from the 24 model variations are compiled to illustrate the sensitivity to choices made within the three primary input parameters: vertebral kinematics, passive stiffness and neutral state. JRF and muscle force estimates for each model variation are also reported (Tables 6-14, Appendix). Additionally, differences due to interactions of choices made within the primary parameters were calculated (Tables 15-41, Appendix).

It is useful to preface these results with a brief clarification on the calculation of bushing (IVD) forces and its incorporation into the net joint reaction force calculations in the *Joint Reaction*

Analysis (JRA) step in OpenSim®. Joi*nt Reactions Analysis* in OpenSim, is a *post hoc* calculation, which determines the resultant forces and moments carried by all *un-modeled* joint structures required to produce the specified joint kinematics. Thus, the decision to either include or exclude certain structural components of the joint within the model will directly affect the resultant loads calculated by JRA. In a purely rigid body dynamics analysis of the lumbar joint – where no passive soft tissue structures are modeled (NBS model) – these forces, referred to as *net joint reaction forces,* collectively represent the *total* load to be resisted by all passive structures within that joint. In this study, we have also explicitly modeled passive disc (and ligament) stiffness by prescribing either linear (LBS) or nonlinear (NLBS) bushing-based force-kinematic relationships at the joint. Under this scenario, the *net* joint reaction force output from JRA already includes the resisting forces generated within the bushing. Hence this value will not represent the *total* load acting at that particular joint. In order to obtain the *total* joint reaction forces in LBS and NLBS models and allow comparison with the corresponding the NBS model output, we must add the *modeled* passive (bushing) forces back to the *net* force output from JRA.

3.3.1 Joint Reaction Forces

Joint reaction forces (JRFs) were reported on the inferior vertebra, in the inferior vertebra's coordinate system (Tables 6-11, Appendix). Positive JRF in the SI and AP directions correspond forces in the superior and anterior directions, respectively (Figure 41). Thus, SI JRF were always negative, indicating a compression, while AP JRF were typically positive, indicating anterior shear force. In general, compressive JRF were similar across all four segment levels in each of the three subjects (Figure 42). Compressive JRF ranged from approximately -32 N/kg to -55 N/kg (-2000 N to -4000 N) at the beginning of the lifts to approximately -14 N/kg to -35 N/kg (-1000 N to -

2500 N) near the upright position depending on the particular subject and magnitude of external load carried.

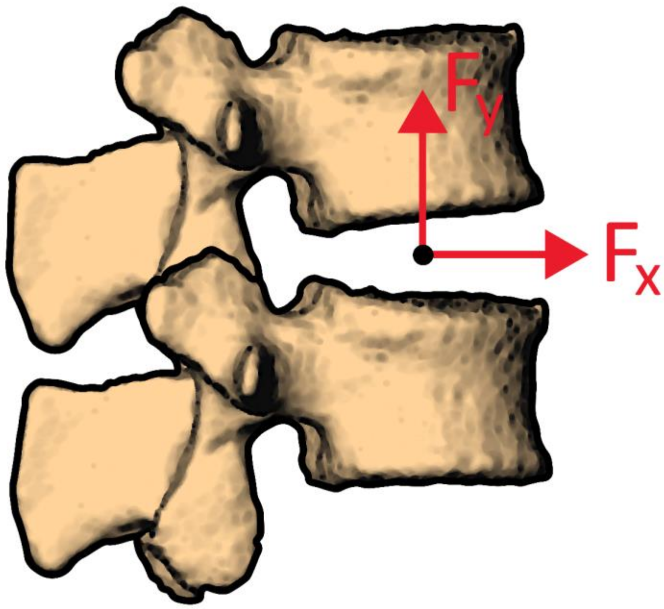

Figure 41: SI (Y-axis) and AP (X-axis) joint reaction forces were reported on the inferior vertebra, and were positive in the superior and anterior directions, respectively.

Maximum shear JRF experienced at the joint throughout the lifting motion varied significantly between subjects and segment levels, ranging from approximately 2-26 N/kg (100-1600 N) at the L5S1 (Figure 43). Magnitudes of shear JRF were smallest and of similar magnitude at the L23 and L34 near the beginning of the lift, and were largest at the L51. While L23 shear forces dissipated towards zero while approaching the upright standing position, shear JRF from L34 to L51 did not, and in some cases even increased. The effect of added external load was noticeable at the L45 and L51, but was not as significant as for compressive JRF.

Results are comparable to those reported by previous studies examining flexion and lifting tasks, which have focused mostly on estimating lumbar loads at the L4L5 and L5S1 levels.

(Eskandari et al., 2017) reported compressive JRF of approximately -25 N/kg at the L4L5 and L5S1 during 70 degrees of flexion – approximately equal to the 75 degrees of flexion achieved by subjects in the current lifting study – while holding no load in the hands[109]. Magnitudes of shear JRF were low at both joint levels, ranging anywhere from approximately 0-3 N/kg. (Ghezelbash et al., 2018) reported L5S1 compressive and shear JRF ranging from -19 to -35 N/kg and 6 to 12 N/kg, respectively, with flexion of the lumbar spine[147]. When performing tasks with loads in the hands, studies have reported L4L5 and L5S1 compressive JRF to be approximately -40 N/kg and -55 N/kg during 70 degrees of trunk flexion while holding 5 kg and 15 kg, respectively. Results from these two studies report L4L5 shear JRF to have reached approximately 2 N/kg and 6 N/kg while holding 5 kg and 15 kg, respectively, while maximum L5S1 shear JRF were 7 N/kg and 17 N/kg for the 5 kg and 15kg load. While the exact trunk rotations in another study were not reported, another study reported L4L5 compression loads to be approximately -40 N/kg to -60 N/kg while lifting 6 kg and 14 kg load, respectively, using a two-handed stoop lifting technique – similar to the straight-legged lifting motion the subjects in the current study were asked to perform. The same study reported L5S1 compressive loads to be approximately -50 N/kg while lifting 15 kg. Shear loads at the L4L5 and L5S1 ranged from 10-15 N/kg and 20 N/kg at the L4L5 and L5S1, respectively.

The increase in shear JRF at the L5S1 compared to the L4L5 align well with results from literature. Furthermore, the noticeably higher JRF due to additional external load lifted agree with results reported by the literature. Maximum shear JRF during the lifting study were at the higher end of ranges reported in literature and aligned best with those measured by (Gauvreau et al., 2019)[148]. One distinct difference of the current results is that L5S1 shear JRF at the upright standing position were larger than those reported in literature. A potential explanation for this is that the lumbosacral angle of the subjects at their upright position in this study were larger than those present in previous literature. This may have particularly been the case due to the pelvic rest which sustained light contact with the lower back during the lifting task. Increasing the external load from 10 lb to 30 lb resulted in an approximate -10 N/kg to -15 N/kg (-500 N to -1000 N) increase in estimated compressive JRF throughout the lifting motion for all three subjects. Trends in compressive JRF throughout the lifting motion remained fairly consistent across all segment levels.

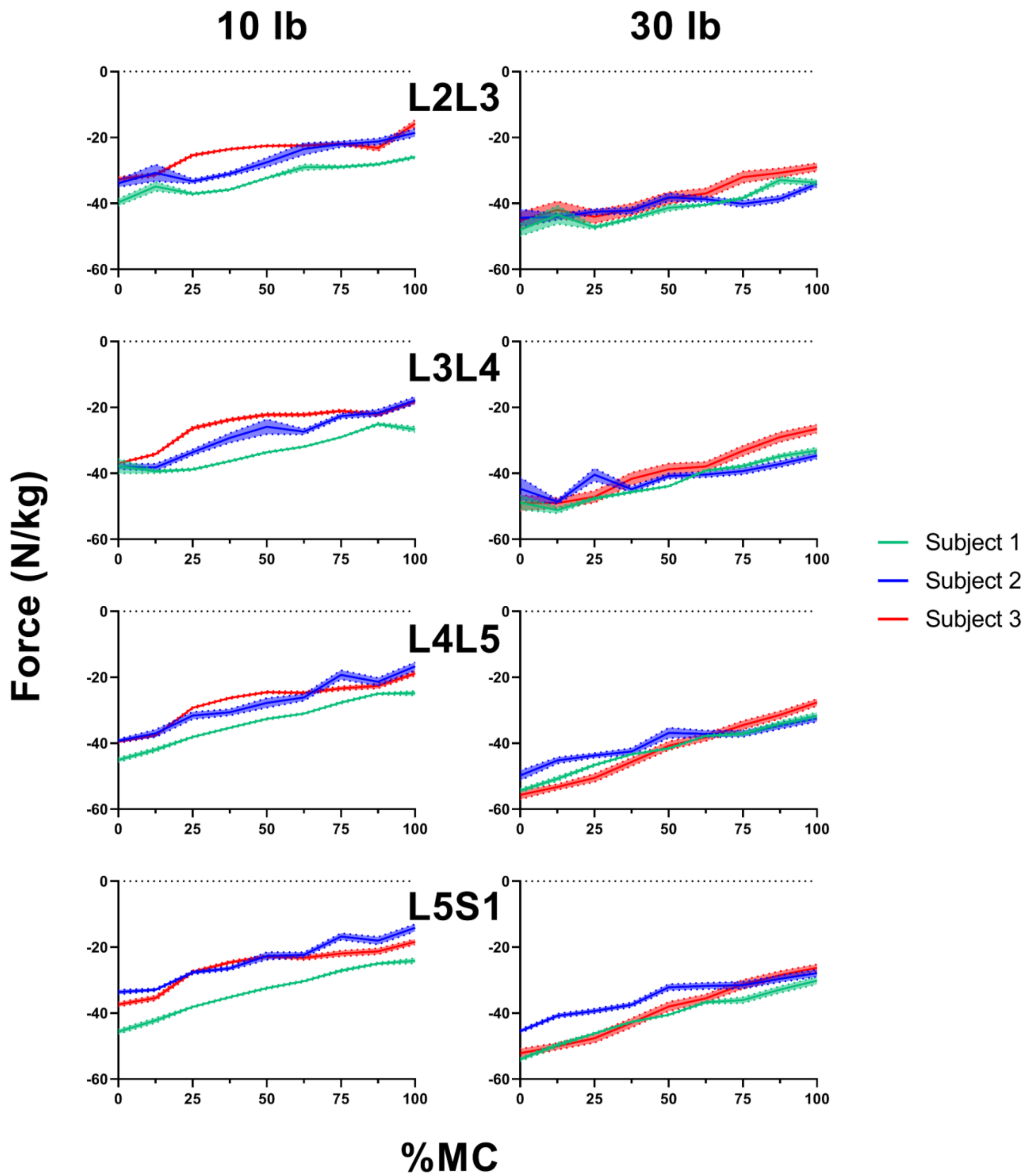

Figure 42: Compressive joint reaction forces from the beginning to end of the lifting motion (mean + SEM).

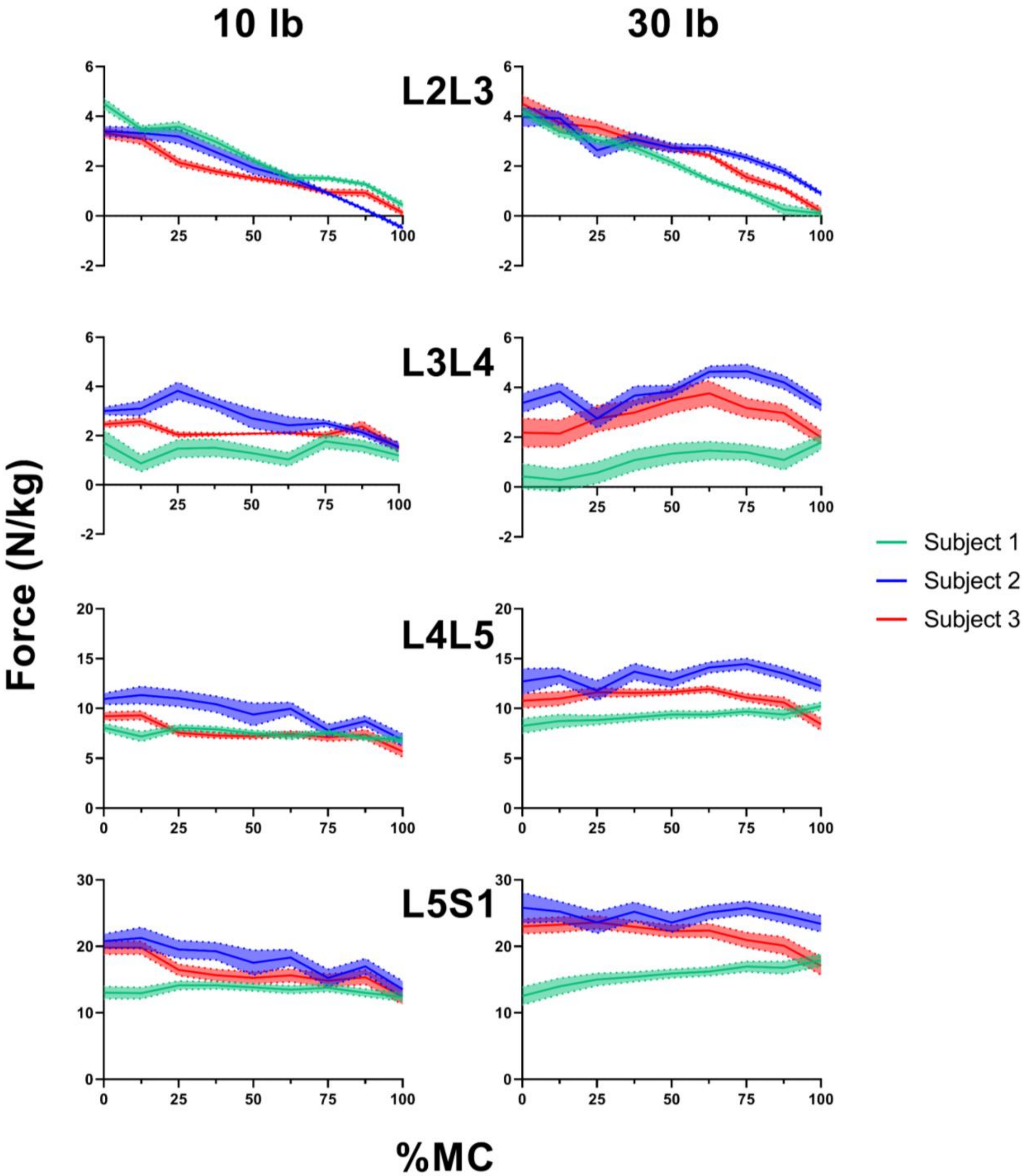

Figure 43: Shear joint reaction forces from the beginning to the end of the lifting motion (mean + SEM).

3.3.1.1 DSX vs Rhythmic Kinematics

The effect of input kinematics varied considerably by the subject being investigated, however input kinematics had an obvious effect on JRF estimates for each subject (Figures 44-45). JRF estimates were substantially lower in magnitude in DSX-based models compared to rhythm-based kinematics at several instances from the beginning of the lift to approximately mid-range. In general, these differences reduced greatly nearer to the upright position. Peak differences over the whole range of motion (ROM) due to inclusion of DSX kinematics reached 1351 N in SI JRF, indicating a *reduction* in compressive force, and -841 N in AP JRF, also indicating a *reduction* in shear force, when calculated based on assessing the *main effect* of kinematic input (Figure 46). Secondly, assumptions with respect to passive stiffness properties and the neutral state modulated these differences, however the manner in which they differed depended on the subject being investigated (Tables 15-20, Appendix). For example, differences in the second subject's compressive JRF due to input kinematics were greater in models consisting of the upright- neutral state configuration. Furthermore, the differences in compressive JRF at the L4L5 and L5S1 increased in magnitude with the presence of stiffness properties (LBS or NLBS) in the upright neutral state configuration models. In subject 3, the introduction of DSX kinematics, as opposed to rhythmic, led to greater magnitudes of difference in models with a supine neutral state configuration. A generally consistent trend was that models with DSX kinematics tended to reduce the amount of shear JRF at the joint, particularly at lower levels of the lumbar spine (L4L5 and L5S1) (Figure 46). Furthermore, values of compressive JRF reduction due to inclusion of DSX kinematics were of much greater magnitudes than instances of compressive JRF increase. Overall, differences in compressive JRF due to kinematic input across all bushing stiffness types and neutral state configurations ranged from -612 N to 2017 N across all subjects during the lifting motions, while differences in shear force ranged from -1150 N to 405 N.

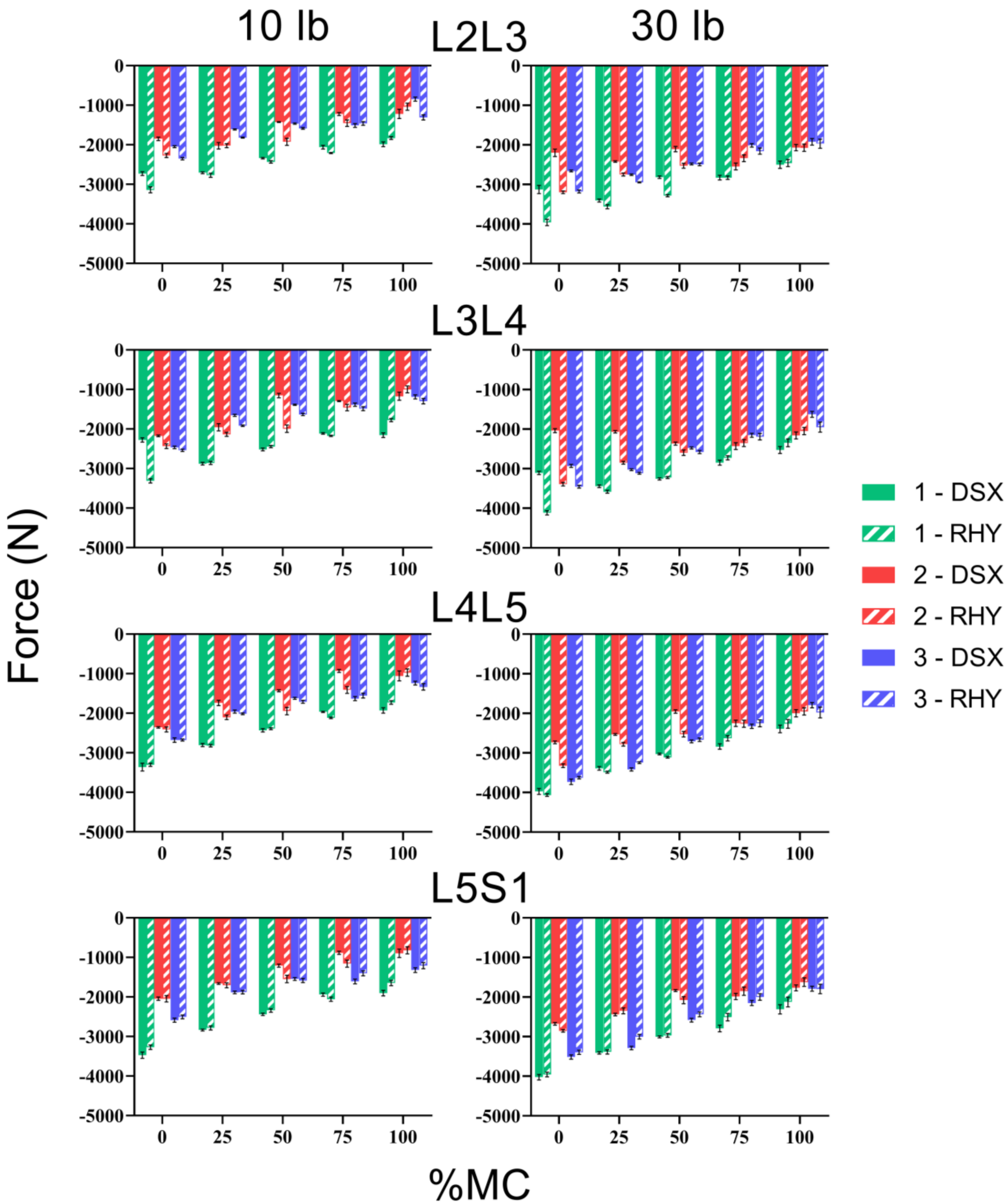

Figure 44: Main Effect of kinematic input on compressive joint reaction forces.

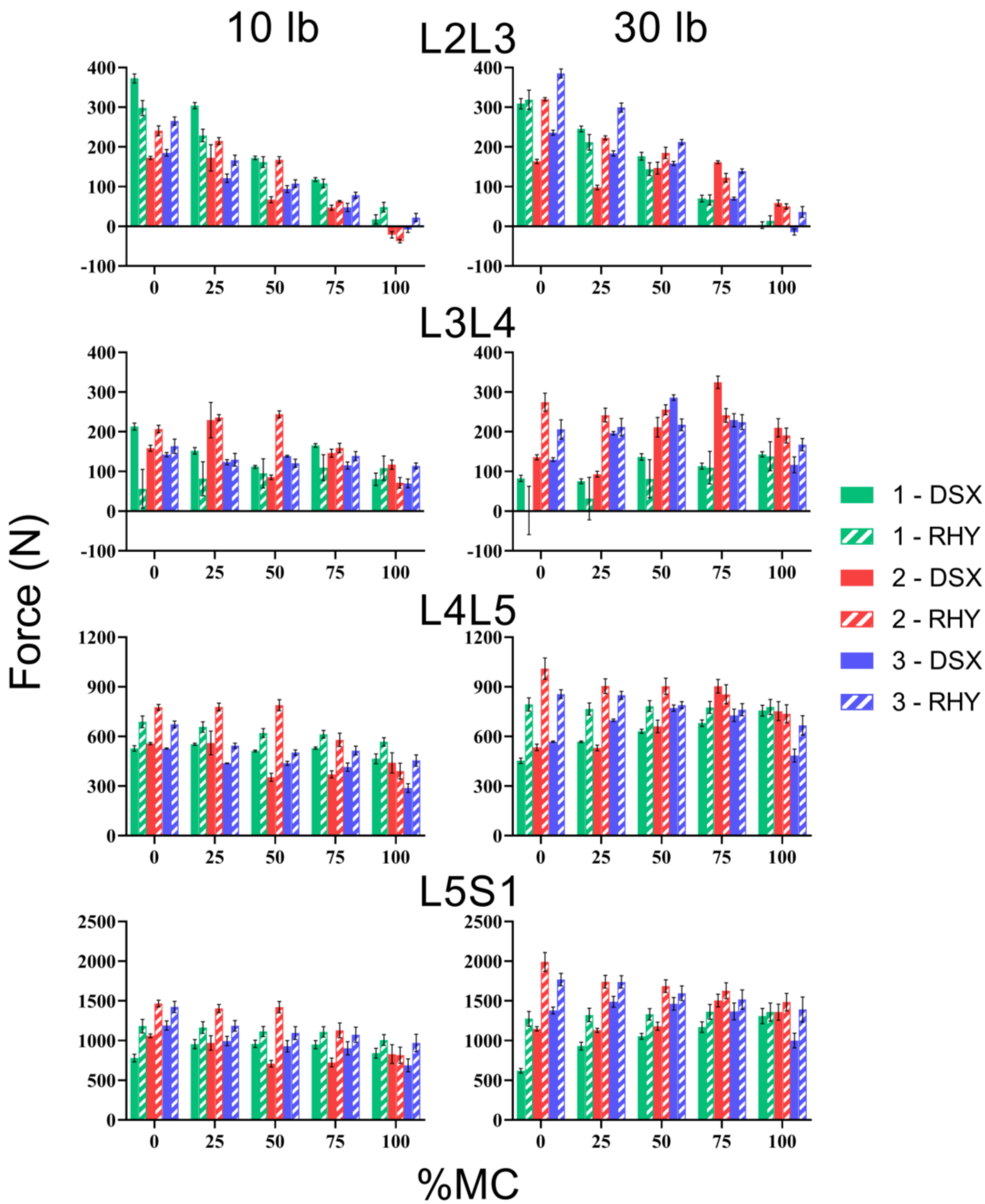

Figure 45: Main Effect of kinematic input on shear joint reaction forces.

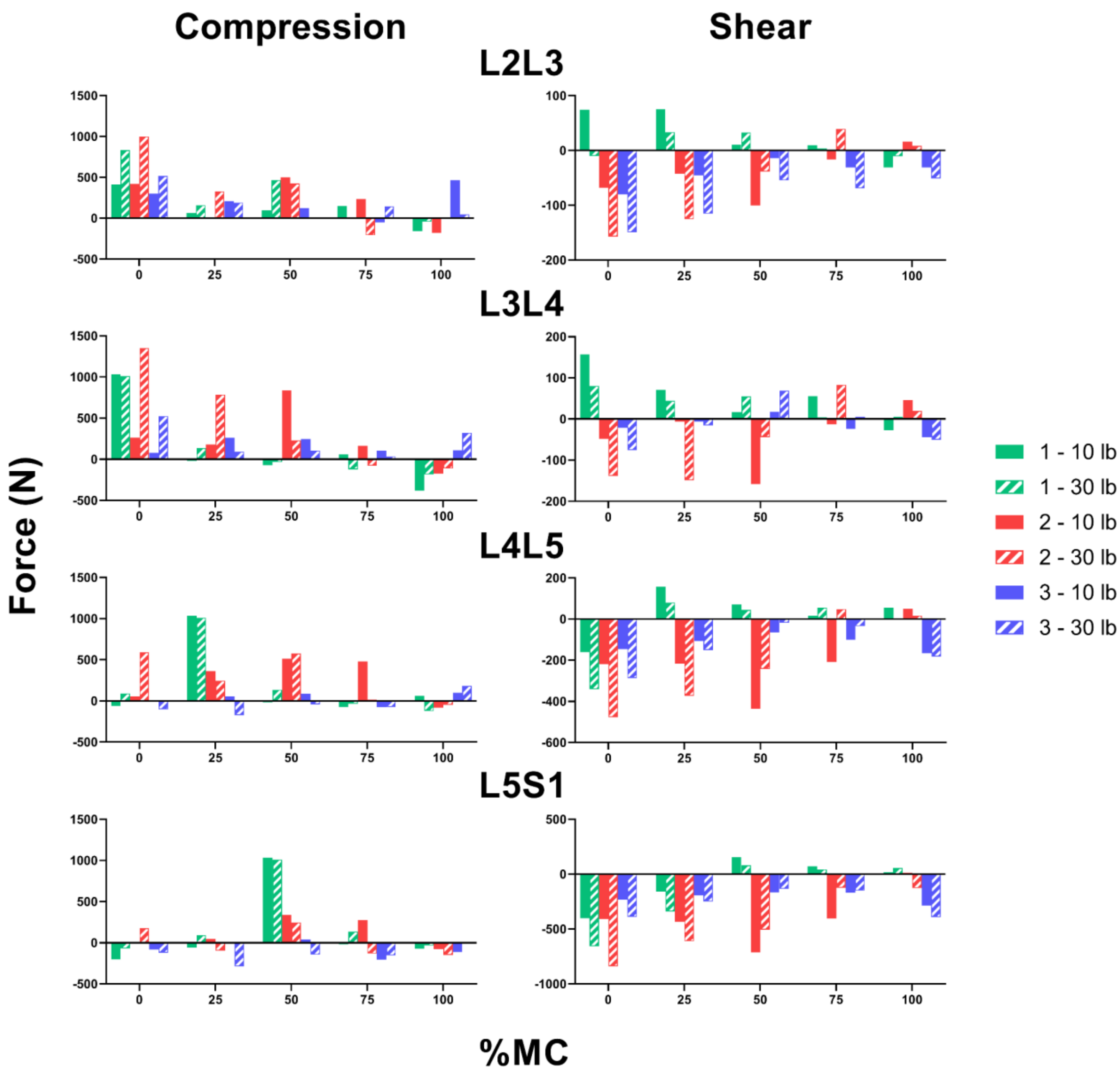

Figure 46: Joint reaction force differences due to input kinematics (F_DSX-F_RHY). Values are reported on the inferior vertebra. Positive values in compression and shear represent decreased compressive force and increased anterior shear force, respectively.

3.3.1.2 Passive Stiffness Properties

While differences varied by segment level and subject, LBS and NLBS- model-based compressive and shear JRF varied only marginally in all three subjects (Figures 47-48). The largest magnitudes of difference seen in compressive and shear JRF when assessing the main effect were approximately 200 N or lower. LBS- and NLBS model-based shear JRF estimates showed only subtle difference at the L2L3 and L3L4 based on the main effect of bushing stiffness, while at the L4L5 and L5S1 led to an increase in shear JRF, which appeared to grow with lumbar extension. While differences in SI JRF were generally positive, they began to decrease and eventually become substantially negative (more compressed) with extension of the lumbar spine to the upright position. Across the three subjects, peak differences in SI JRF based on the main effect of bushing stiffness ranged from -550 N to 490 N towards the end of the lifting task, respectively (Figure 49). Furthermore, these differences were rather consistent across all joint levels, while major differences in shear JRF occurred only at the L4L5 and L5S1, reaching approximately 540 N. In general, interaction effects of the neutral state configuration and kinematic input type on JRF differences due to stiffness properties were small (Tables 21-26, Appendix). However, there were some instances of notable interaction effects with. For example, the effect of stiffness properties on 25-75%MC differed noticeably between DSX and RHY models in the second subject, particularly at the upper joint levels. Additionally, the presence of rhythmic kinematics in combination with the supine neutral state led to increased compressive JRF (more negative) near the upright position (75-100%MC) during the third subject’s 30 lb lift.

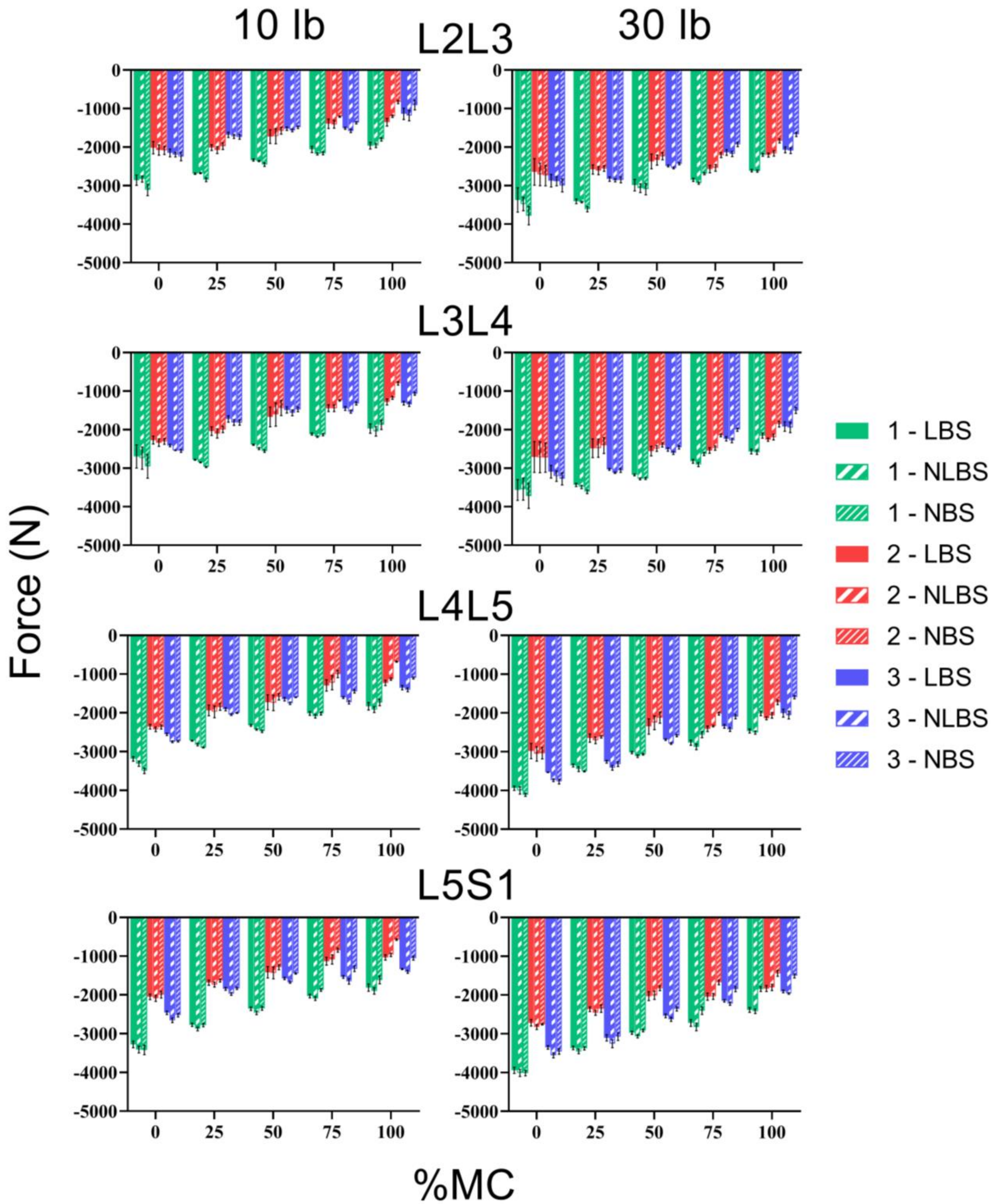

Figure 47: Main Effect of bushing stiffness on compressive joint reaction forces.

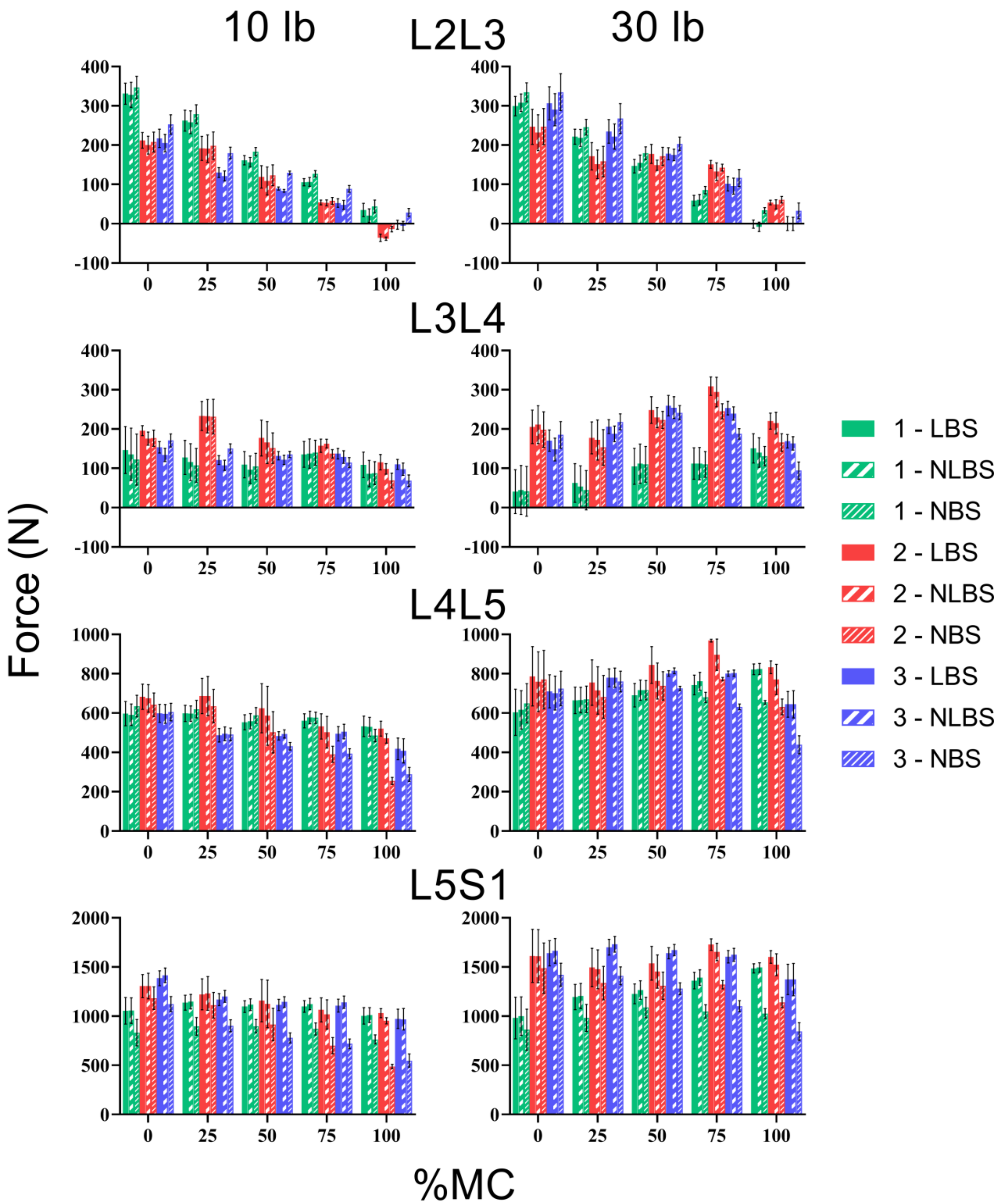

Figure 48: Main Effect of bushing stiffness on shear joint reaction forces.

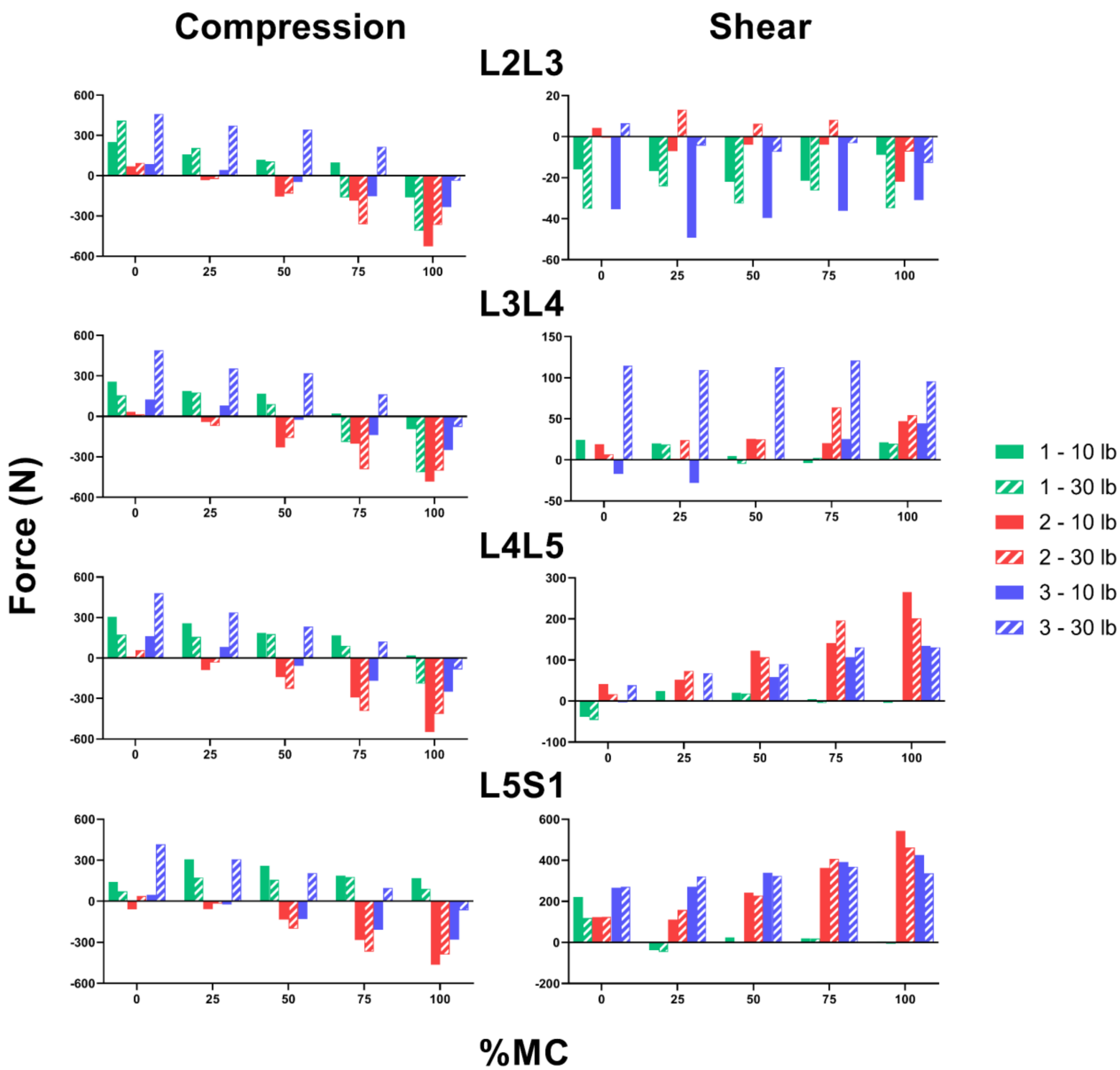

Figure 49: Joint reaction force differences due to bushing stiffness properties (F_LBS-F_NBS). Values are reported on the inferior vertebra. Positive values in compression and shear represent decreased compressive force and increased anterior shear force, respectively.

3.3.1.3 Supine vs Upright Neutral State

Although still substantial, the main effect of neutral state was the smallest of the three primary input factors (Figures 50-51): differences in compressive JRF ranges from -292 N to 238 N, while differences in shear JRF ranged from -167 N to 277 N. No consistent trends in the main effect across subjects were identified. However, the effect of neutral state configuration on L5S1 compressive JRF was unique compared to other joint levels, in that the supine neutral state models consistently reduced compressive JRF compared to the upright neutral state models (Figure 52). Interaction effects with the choice of kinematic input and bushing type on SI JRF were evident in all subjects (Tables 27-32, Appendix). For the second subject, inclusion of the supine neutral state led to an increase in compression in DSX models, but a decrease in compression in RHY models. At the L23, the magnitude of increased compression at 0%MC in DSX models was greater with the presence of LBS stiffness properties (-630 N) compared to NBS or NLBS models (-195 N and -57 N, respectively).

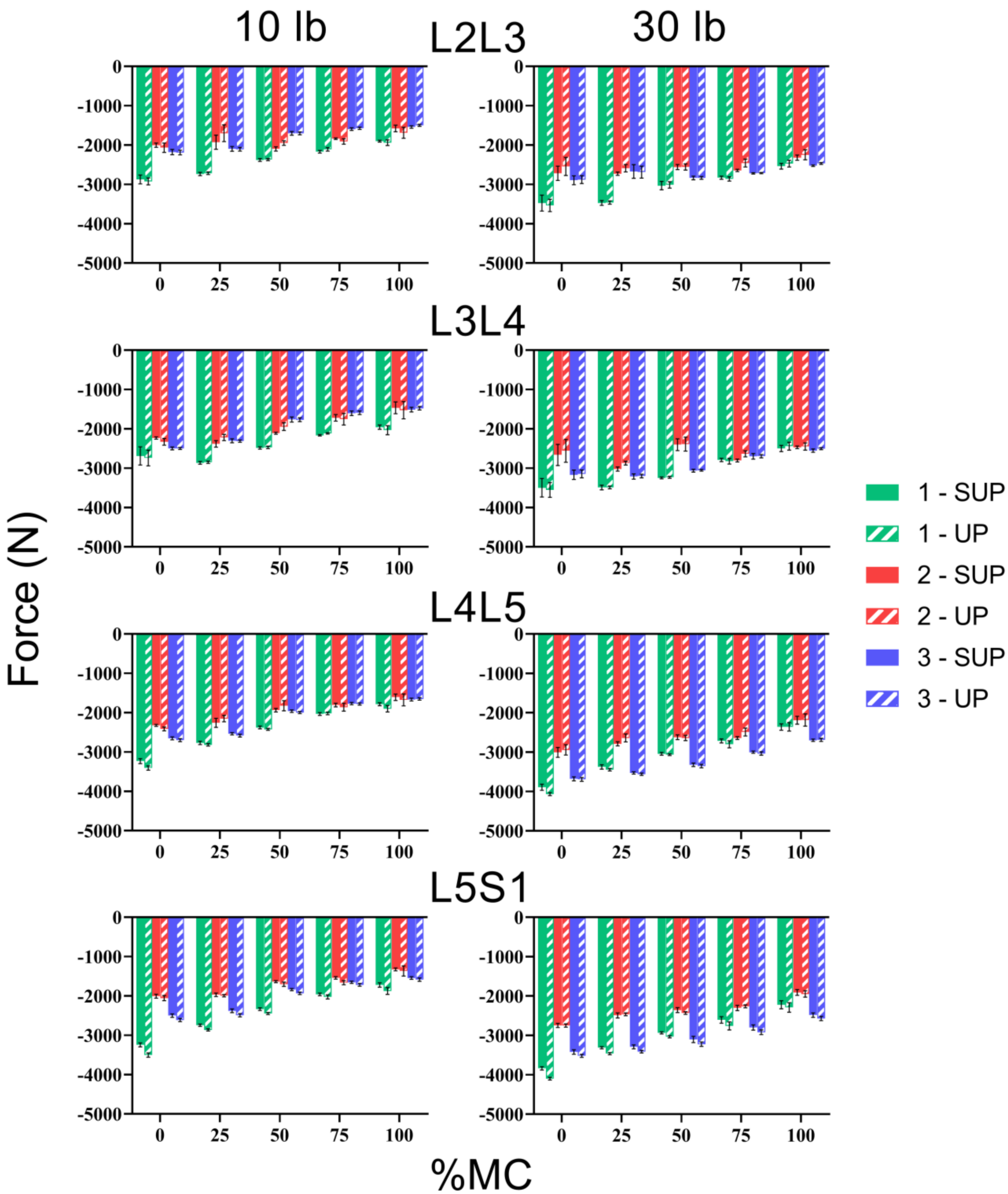

Figure 50: Main Effect of neutral state configuration on compressive JRF.

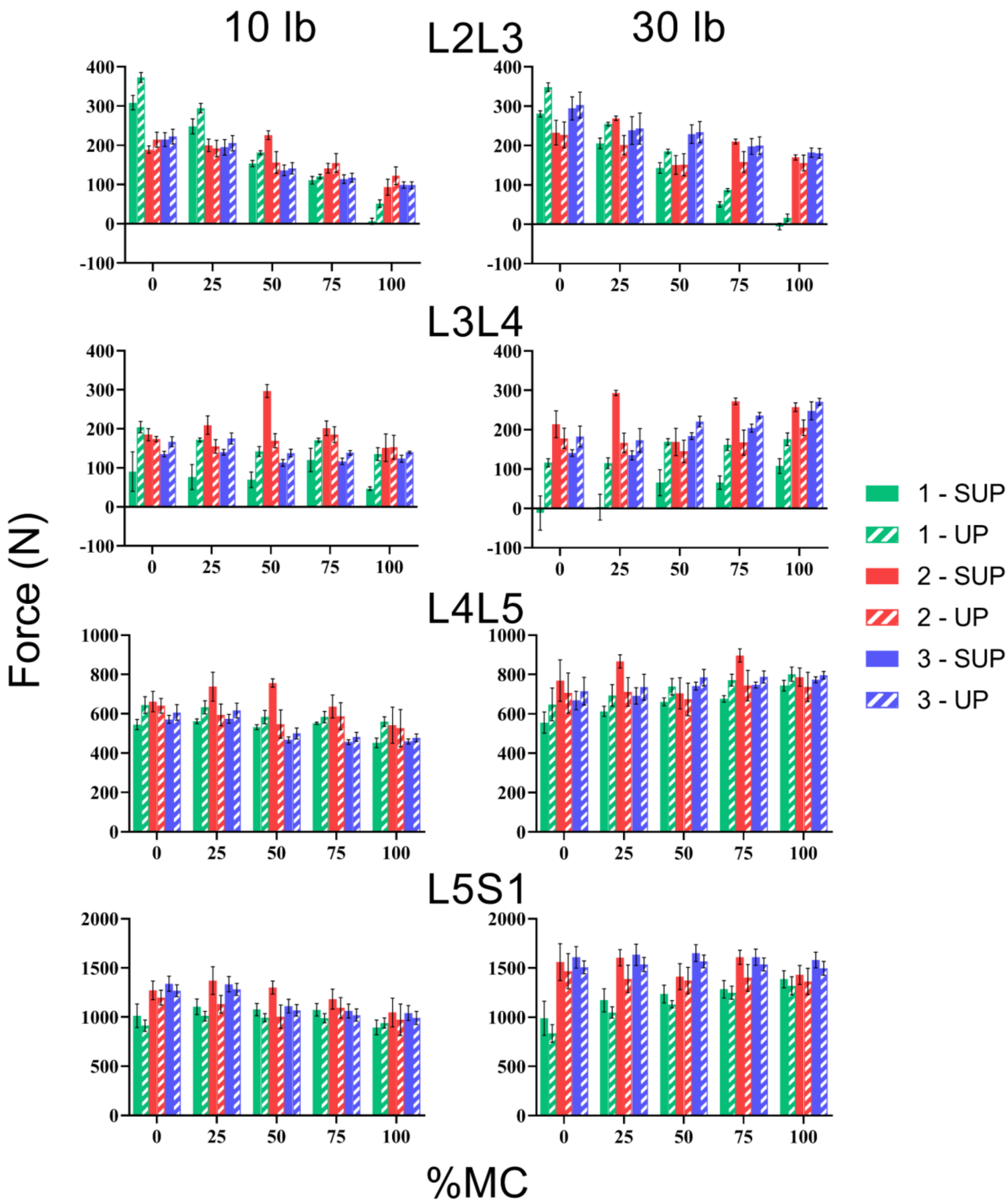

Figure 51: Main Effect of neutral state configuration on shear joint reaction forces.

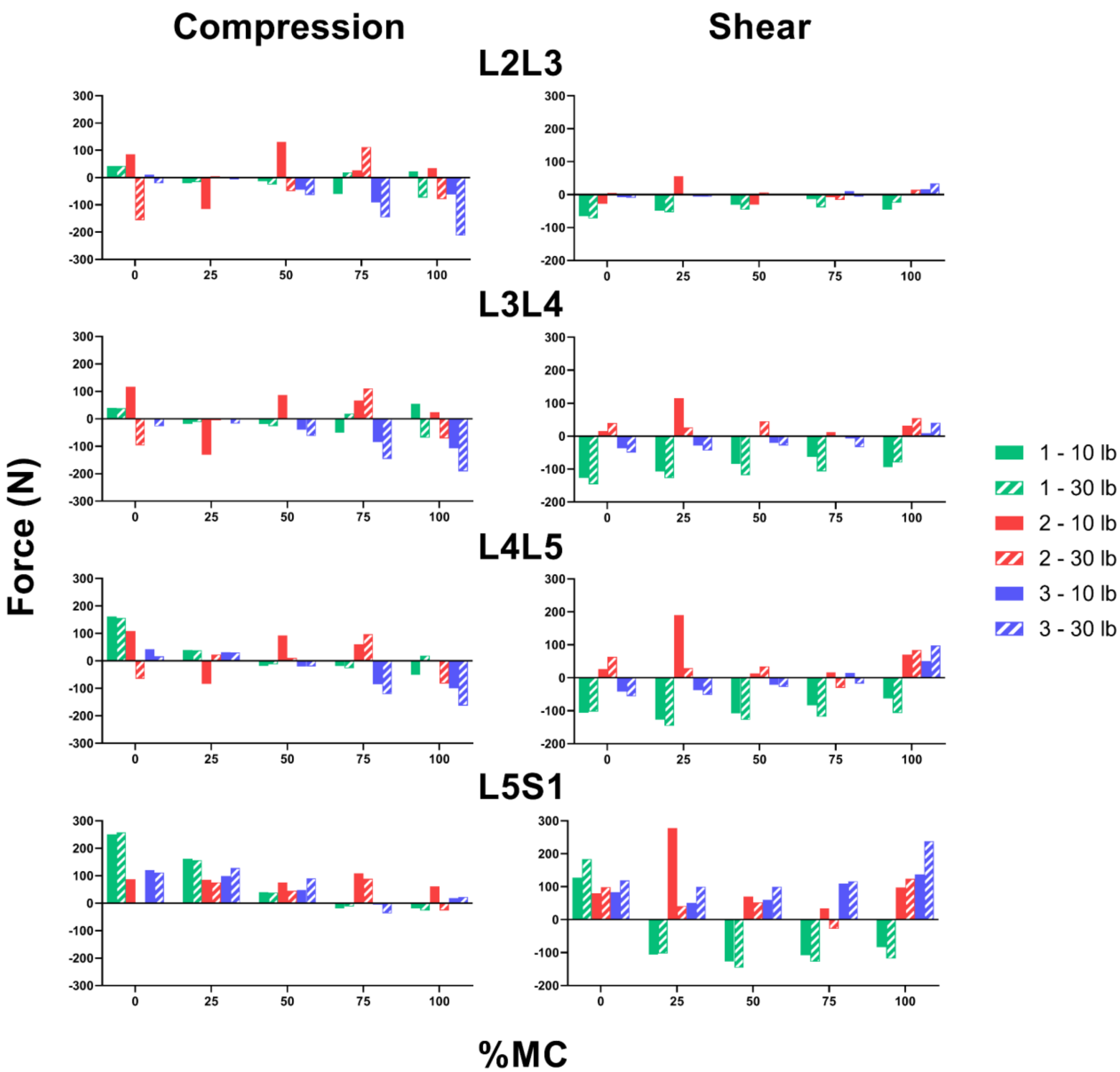

Figure 52: JRF differences due to neutral state configuration (F_SUP-F_UP). Values are reported on the inferior vertebra. Positive values in compression and shear represent decreased compressive force and increased anterior shear force, respectively.

3.3.2 Muscle Forces

Muscle forces of the multifidus (MF), iliocostalis lumborum (IL), longissimus thoracis (LT), and abdominal (ABD) muscle groups were reported throughout the lifting motion (Tables 12-14, Appendix). In general, muscle forces were largest at the LT muscle group, reaching approximately 1000 N and 1500 N at the beginning of the 10 lb and 30 lb lifts, respectively (Figure 53). IL forces were nearly just as high, ranging approximately 600-1000 N and 900-1500 N for the 10 lb and 30 lb lifts, respectively, across the three subjects at the beginning of the lift. MF forces were also substantial, reaching approximately 600-800 N during the lifting tasks., while ABD forces were considerably lower. As expected, muscle forces in these four groups reached peak levels at the beginning of the lifting motion and continued to decrease with extension of the lumbar spine to the upright position; however with exception of ABD muscles of a single subject during the middle portion of the lifting motion. LT and IL forces increased by approximately 300-400 N with an increase in external load from 10 lb to 30 lb, while similar trends were seen at the MF and ABD to the degree of approximately 200 N and 50 N, respectively. Such increases were present throughout the lifting motion, including the end of the lifting task where the subjects reached approximately the upright standing position.

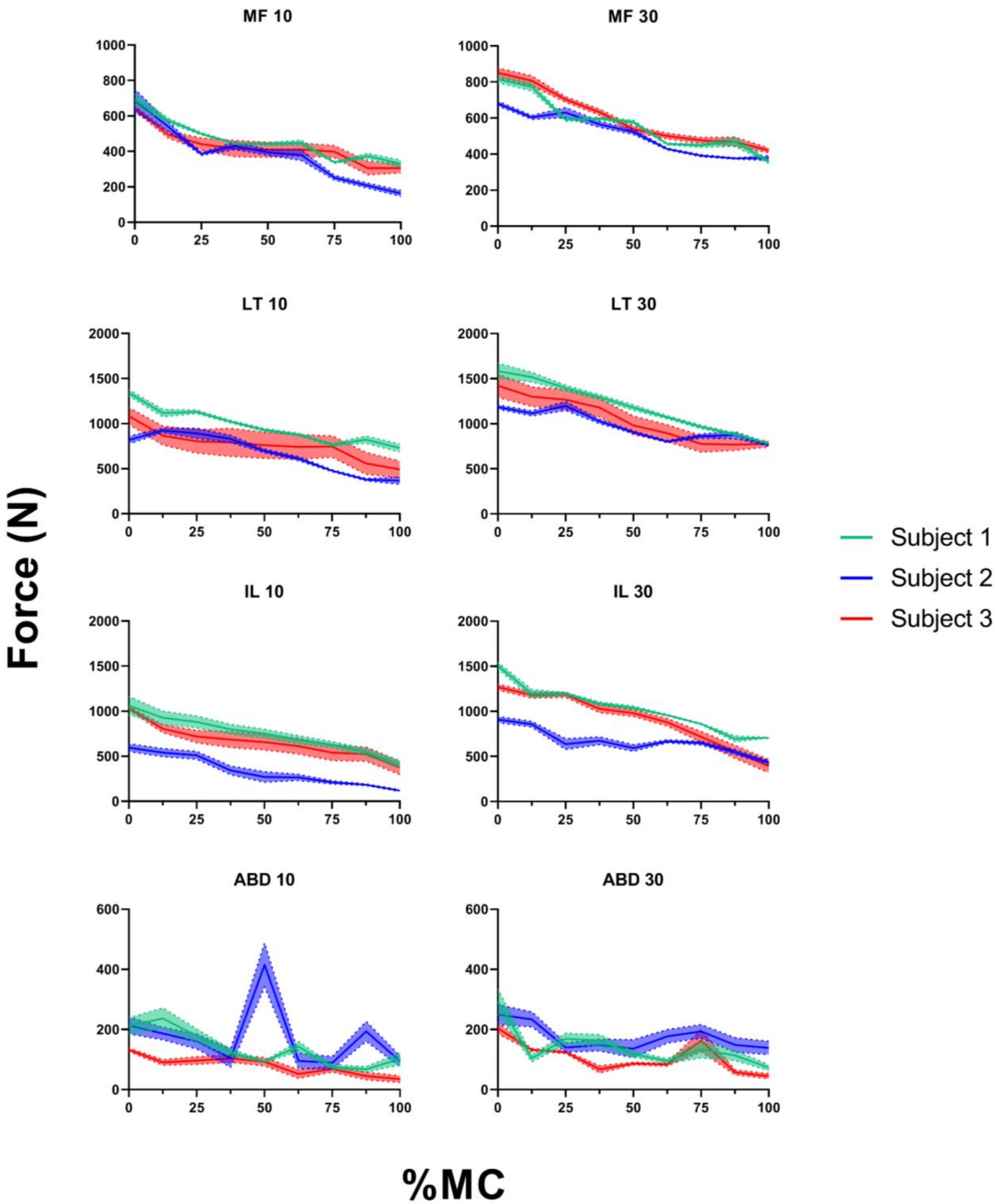

Figure 53: Muscle forces at the multifidus (MF), latissimus dorsi (LT), iliocostalis lumborum (IL), and abdominal (ABD) muscle groups during the lifting motion.

While the tasks simulated vary by study, total muscle force in the current study agree well with those estimated by previous lumbar spine modeling studies simulating flexion or lifting tasks. Across the three subjects, the combined muscle forces form the four studies muscle groups ranged approximately 2200-3000 N and 3000-4000 N at the beginning of the 10 lb and 30 lb lifts, respectively. A study by (Kim et al., 2017) reported total muscle forces of over 5000 N simulating the lifting of a 12 kg crate from the floor to a table; over 4500 N of the total muscle force was produced by the IL muscle group, while the LT, MF, and ABD muscles groups accounted for approximately 300 N, 100 N, and 100 N, respectively. In a study by (Ghezelbash et al., 2015), the local and global muscle forces were reported at various flexion angles of the trunk while holding zero or 180 N in the hands. Total muscle forces exceeded 2500 N at the 40 degrees trunk flexion and continued to grow past 3500 N with 80-90 degrees of flexion. (Eskandari et al., 2017) and (Arshad et al., 2017) reported total muscle loads of approximately 2500 N when simulating inclination of the upper body with loads in the hand of the subjects.

While some studies did not report specific force estimates of individual muscle groups, MF forces in the current study – which reached 700-800 N at the beginning of the lifting motion – are higher than those estimated by previous studies, which have estimated MF forces to be around 500 N, at most, during flexion or lifting tasks[108-110]. The current study also displayed a fairly even distribution of erector spinae muscle forces between the IL and LT muscle groups. While magnitudes of muscle forces were smaller in (Arshad et al., 2017), the relative distribution was also quite even between the two groups in this study[108]. (Eskandari et al., 2017), on the other hand, reported LT forces greater than 1100 N at 40 degrees of trunk inclination, over twice as large as IL forces[109]. (Kim et al., 2017) reported the majority of muscle force located at the IL group (>4500 N)[110]. Differences in muscle distribution between studies is most likely due to differences in muscle parameters between models, which has a direct effect on how optimization algorithms distribute loads across the muscles to produce the necessary moments. The reported abdominal muscle forces in this study (including the internal and external obliques, and the rectus abdominus) align well with those estimated by other models. In general, activation of these muscles were relatively lower than in other groups, and varied from approximately 0 to 400 N depending task being simulated.

3.3.2.1 DSX vs Rhythmic Kinematics

Compared to models with rhythmic vertebral kinematic input, predicted muscle forces in models with DSX input kinematics showed uniquely different trends (Figures 54-55). While the muscle groups experiencing the largest differences varied by subject, all muscle groups showed considerable main effect differences during the lifting motion. For example, while LT forces were greatly reduced at the beginning of the 30 lb lift in the first subject with the inclusion of DSX kinematics, differences were not nearly as significant for the other subjects. Furthermore, the relative direction of these differences with respect to the rhythmic models largely varied even throughout the same lifting task. For example, while the second subject's LT forces in DSX models were 133 N *less* at the beginning of the lift, just 25%MC later they were *greater* by 259 N. Despite their relatively low magnitudes of force compared to other muscle groups, differences in ABD forces due to kinematic input remained large, with peak differences across all subjects reaching nearly 430 N, when calculated based on the main effect. Furthermore, MF increased with inclusion of DSX kinematics, while IL forces decreased: maximum peak main effect differences for each group were 417 N and -242 N, respectively. In many cases there were also significant interaction effects with kinematic input and other input parameters (Tables 33-35, Appendix). For example, the inclusion of DSX kinematics in the second subject had a much larger effect on IL muscle forces in models with the upright neutral state configuration than those with supine neutral state configuration.

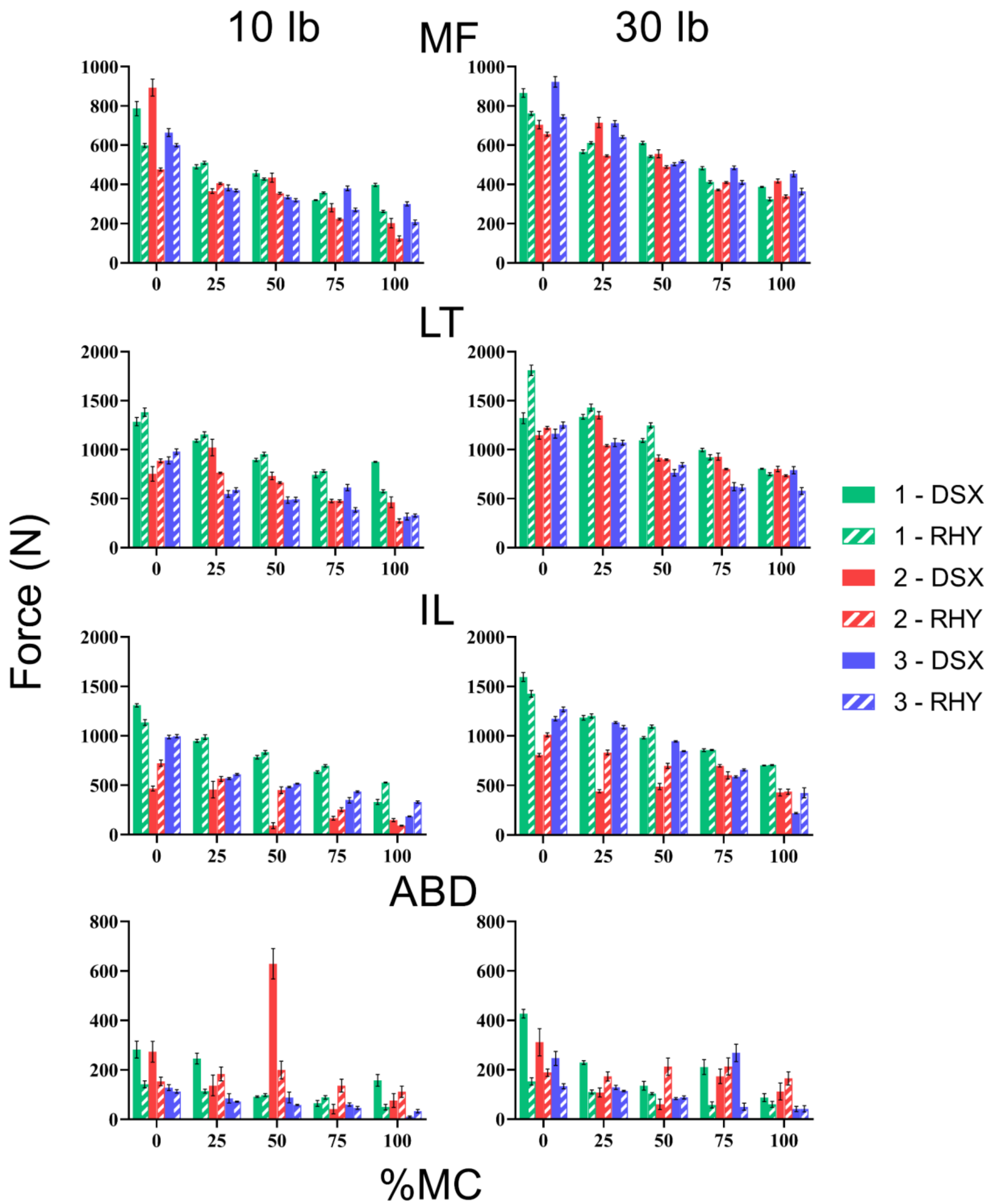

Figure 54: Main effect of kinematic input on muscle forces.

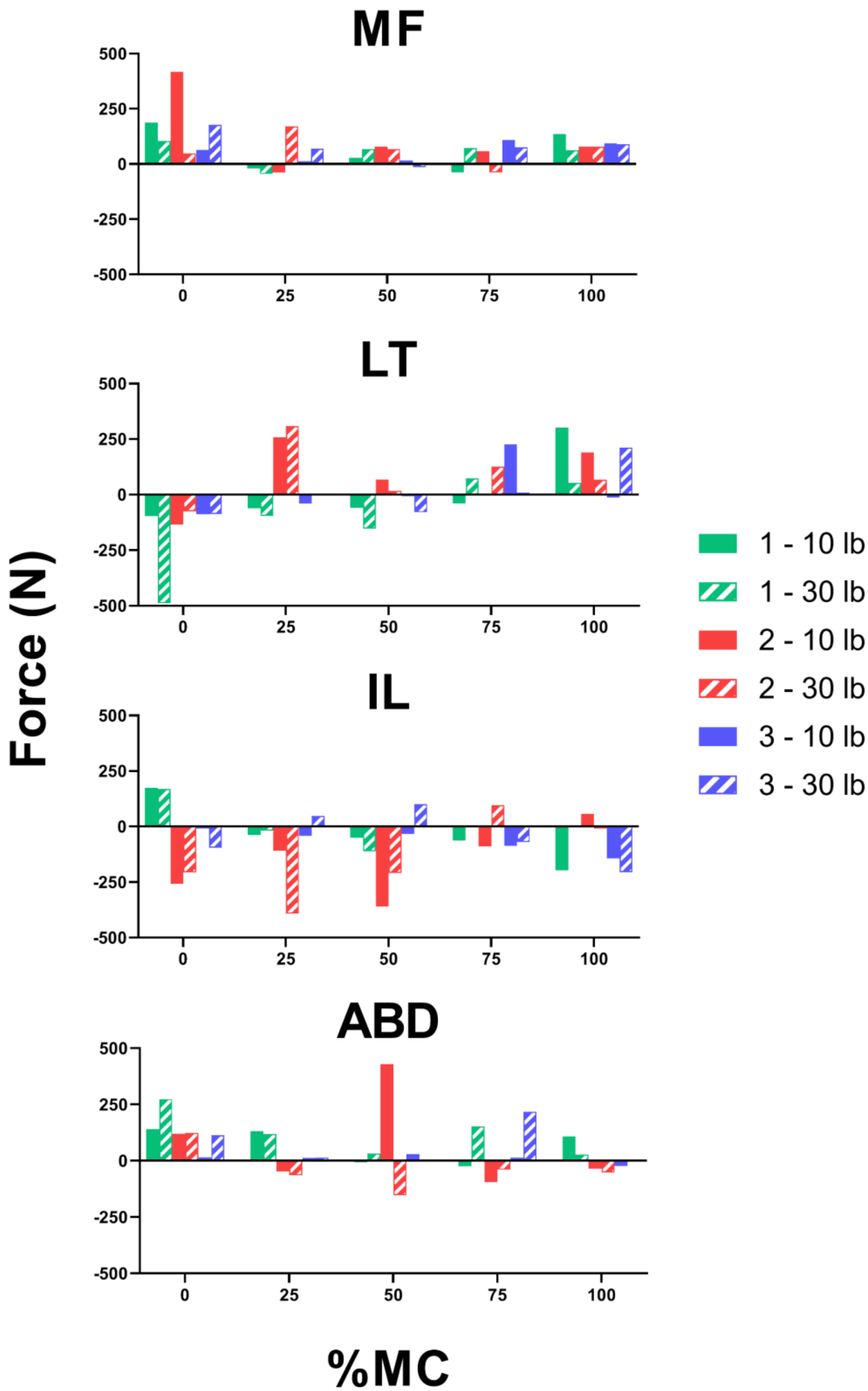

Figure 55: Muscle force differences due to kinematic input (F_DSX-F_RHY).

3.3.2.2 Passive Stiffness Properties

Effects of passive stiffness properties varied across muscle groups, although the largest differences generally appeared at the beginning of the lifting motion (Figure 56). The introduction of LBS stiffness as opposed to NBS stiffness led to decreased LT force across all, with peak main effect differences reaching nearly -240 N and mitigating with extension of the lumbar spine to the upright position (Figure 57). Differences observed in other muscle groups varied by subject: while IL forces were greatly reduced in subject one, particularly near the beginning of the lift, differences were of lesser magnitude in the other two subjects. And while subject two experienced generally larger ABD forces in LBS models, differences were mitigated in the other two models. Differences in muscle force between LBS and NLBS models were generally smaller than those between LBS and NBS, with exception of a few instances where ABD, LT, and IL forces were reduced by 80-120 N. In general, it was difficult to pinpoint consistent trends due to variation of bushing stiffness properties in DSX models. Closer to the upright position, models with bushing forces included tended to predict higher MF and ABD muscle forces compared to NBS models. As was the case for input kinematics, other input parameters had interaction effects on differences in muscle force estimates due to variation of stiffness properties (Tables 36-38, Appendix). However, the degree to which interaction effects were present differed largely by the subject. For example, the magnitude of differences in muscle force estimates due to passive stiffness properties varied much more substantially based on kinematic input (DSX or RHY) in the second subject than the other two subjects.

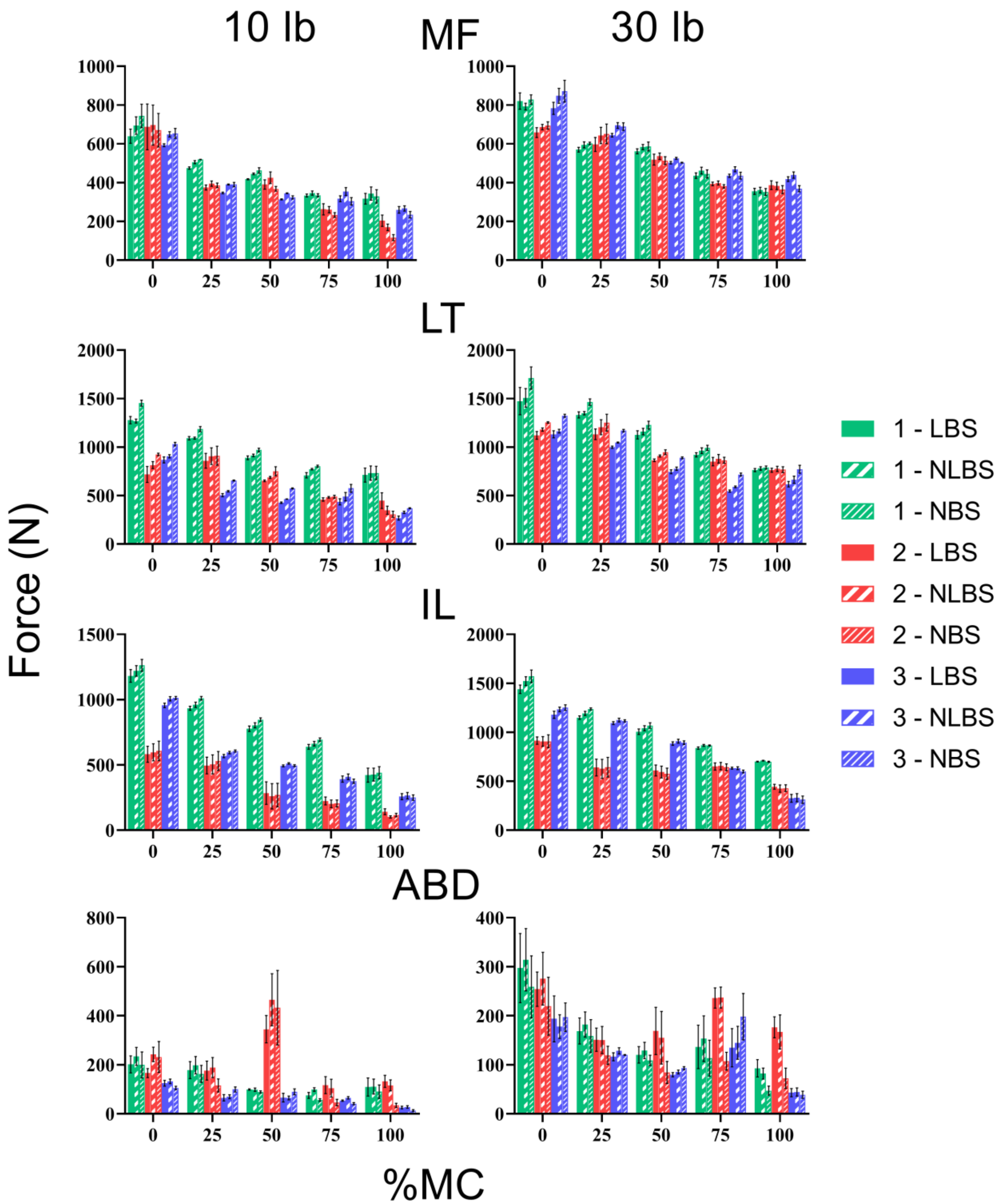

Figure 56: Main effect of bushing stiffness properties on muscle forces.

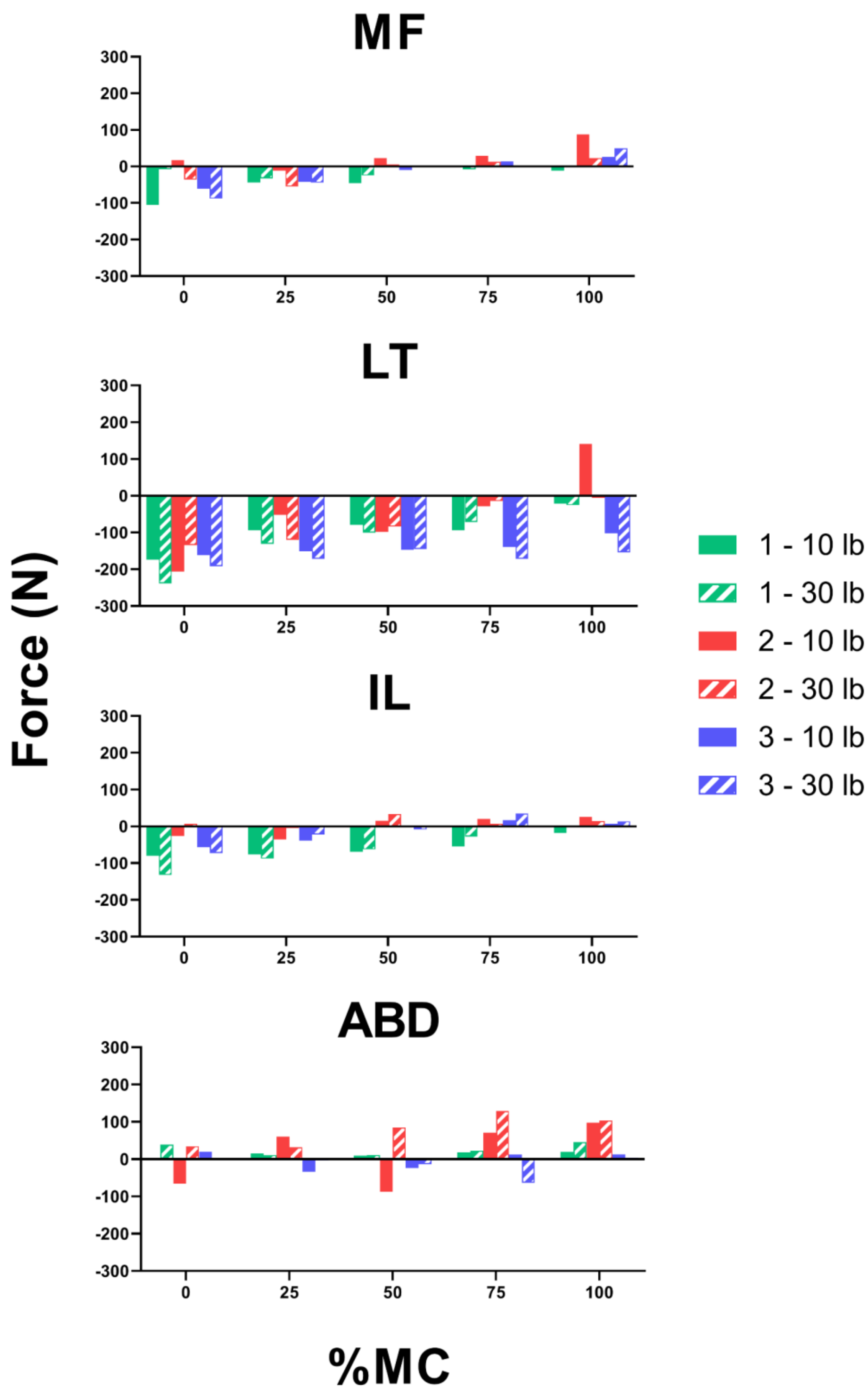

Figure 57: Muscle force differences due to bushing stiffness properties (F_LBS-F_NBS).

3.3.2.3 Supine vs Upright Neutral State

While IL forces were substantially reduced at the beginning of the lift for a single subject, the main effect of neutral state configuration on muscle forces was smallest of the three main parameters (Figure 58). Only at a few instances of the lifting motion did differences in any muscle force group exceed magnitudes of 100 N (Figure 59). Overall, the MF muscle group seemed least affected by the inclusion of the supine neutral state. Neutral state had a minimal effect on MF and LT muscle forces. However, the effects of neutral state on ABD and IL forces were considerable, particularly with greater external load and during the latter half of the lifting motion. As previously noted, differences due to neutral state configuration had strong interaction effects with the type of kinematic input depending on the particular subject. While LBS or NBS passive stiffness properties had a moderate effect on MF muscle force differences due to neutral state configuration during the 10 lb lift, interaction effects between the two parameters were lower for other muscle groups, and also during the 30 lb lift (Tables 39-41, Appendix).

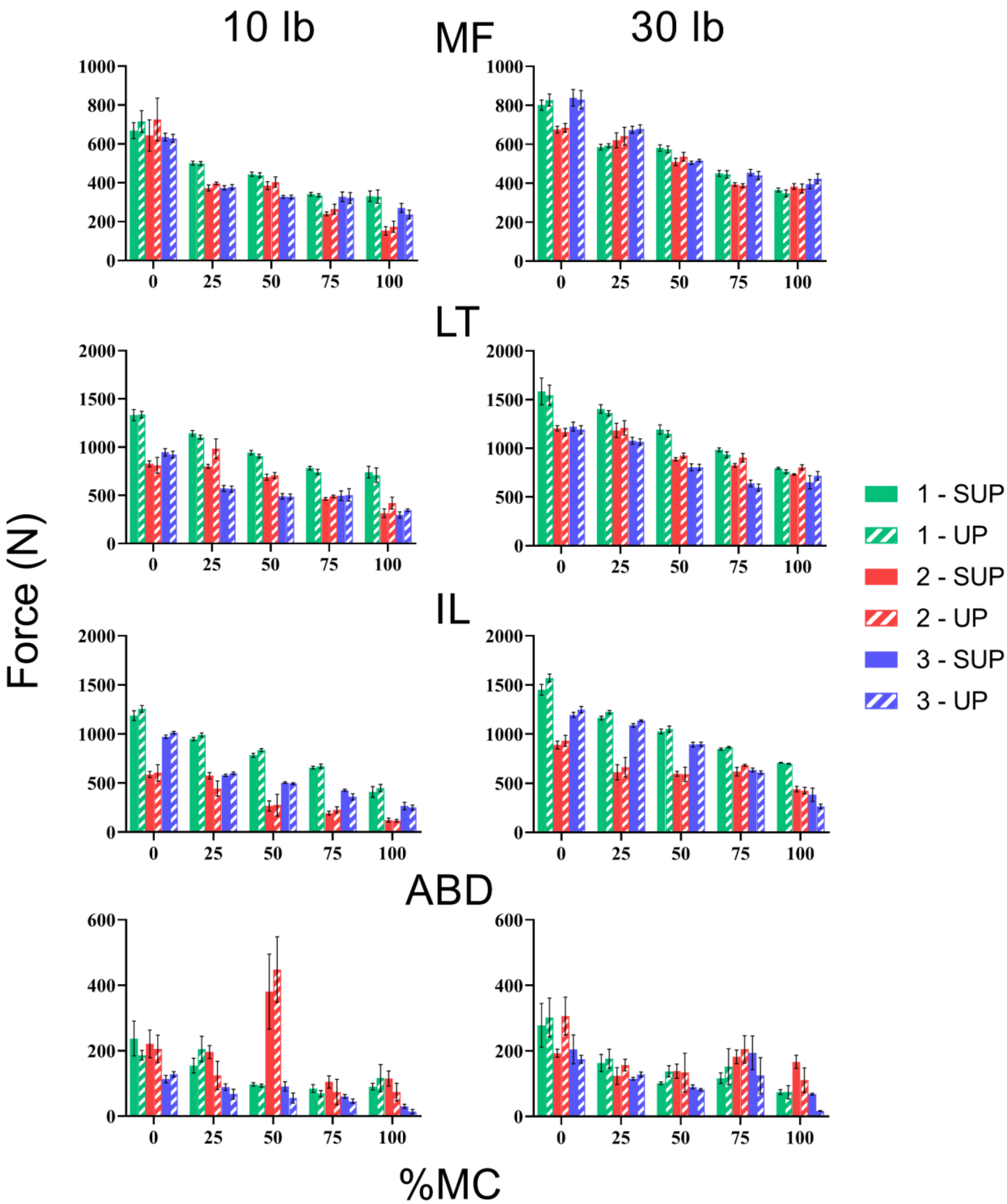

Figure 58: Main effect of neutral state configuration on muscle forces.

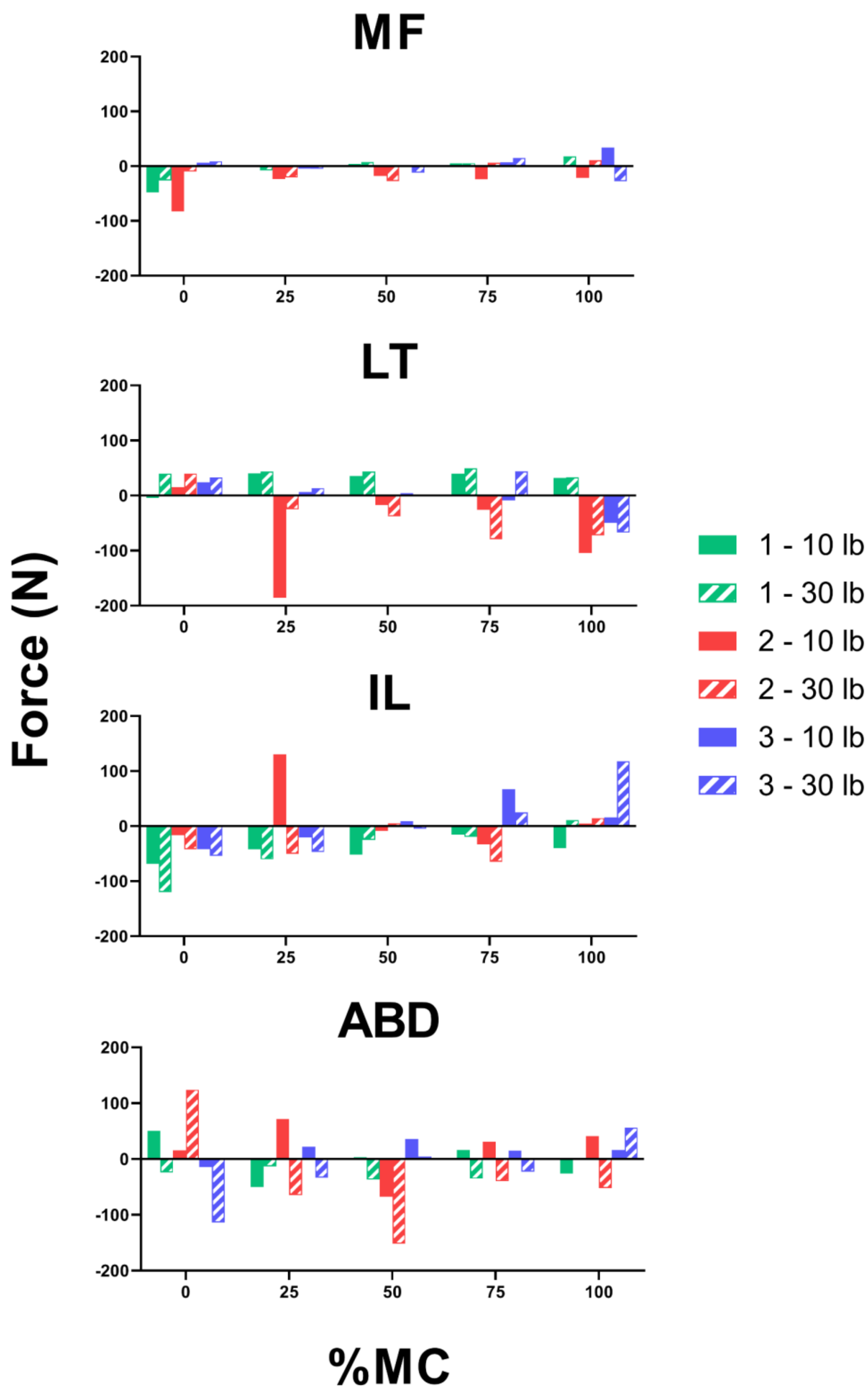

Figure 59: Muscle force differences due to neutral state configuration (F_SUP-F_UP)

3.3.2.4 Intervertebral Input Kinematics

Differences in intervertebral kinematics at the upright and supine positions – as captured by DSX and CT, respectively – led to slight differences in upright- and supine-relative input kinematics. For example, flexion-extension (FE) kinematics of a single subject's (subject 1) L45 were shifted approximately two degrees (more negative) when described with respect to the upright position compared to the supine position (Figure 60), while AP and SI translation were shifted by approximately -1 mm each. LB and AR motion, along with ML translation, were the same regardless of neutral state definition, as only the sagittal plane kinematics were taken into account when defining the neutral state.

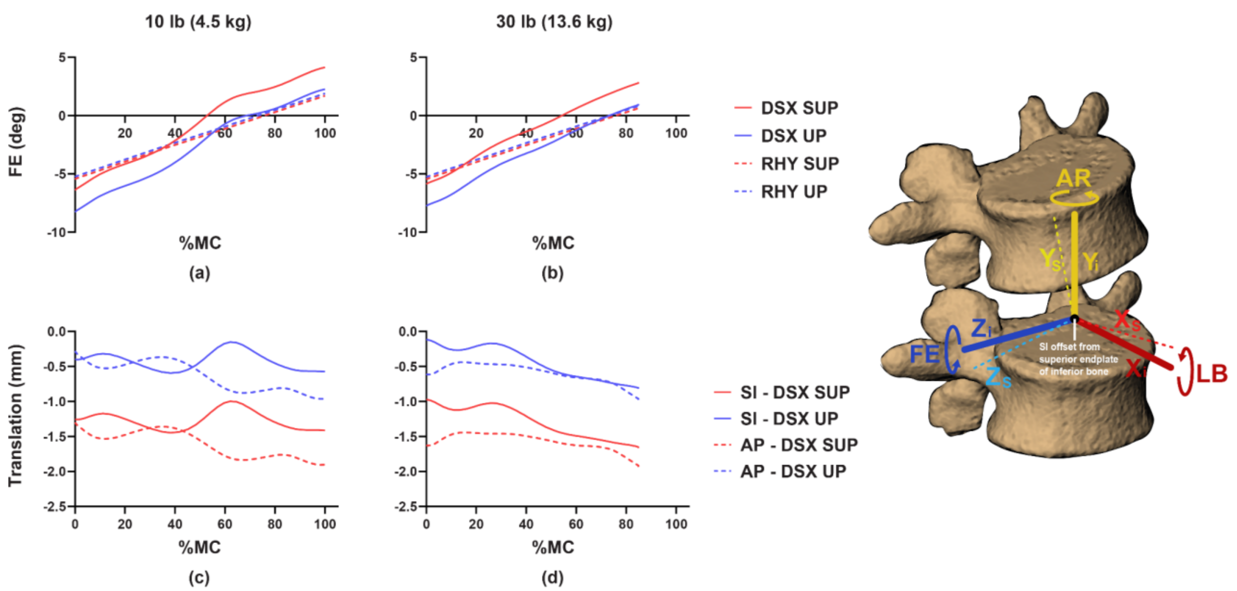

Figure 60: Variation of a single subject's (subject 2) L4L5 sagittal plane kinematics based on neutral state configuration and type of input kinematics.

3.3.2.5 Simplified Model Results

When the joint was placed in flexion with respect to the reference orientation of the joint, models with LBS stiffness required *less* muscle force to stabilize the external moments compared to NBS models (Figure 61). This led to *lower* magnitudes of JRF in models with bushing stiffness compared to NBS models. When the joint was in extension, with respect to the reference orientation, models with rotational stiffness required *greater* muscle force to stabilize the external moments, which correspondingly resulted in *larger* magnitudes of JRF compared to NBS models. These results are to be expected. In flexion, the reaction moment corresponding to the rotational stiffness acts in extension, thus aiding the muscles to help stabilize the external moments and decreasing joint reaction forces. In extension, the reaction moment of the passive stiffness element acts in flexion, producing an additional external moment for which the muscles must stabilize, therefore increasing muscle forces and joint reaction forces. Overall, the results ensured that the relationships between the kinematics, muscles and joint reaction forces in the musculoskeletal model were behaving as intended.

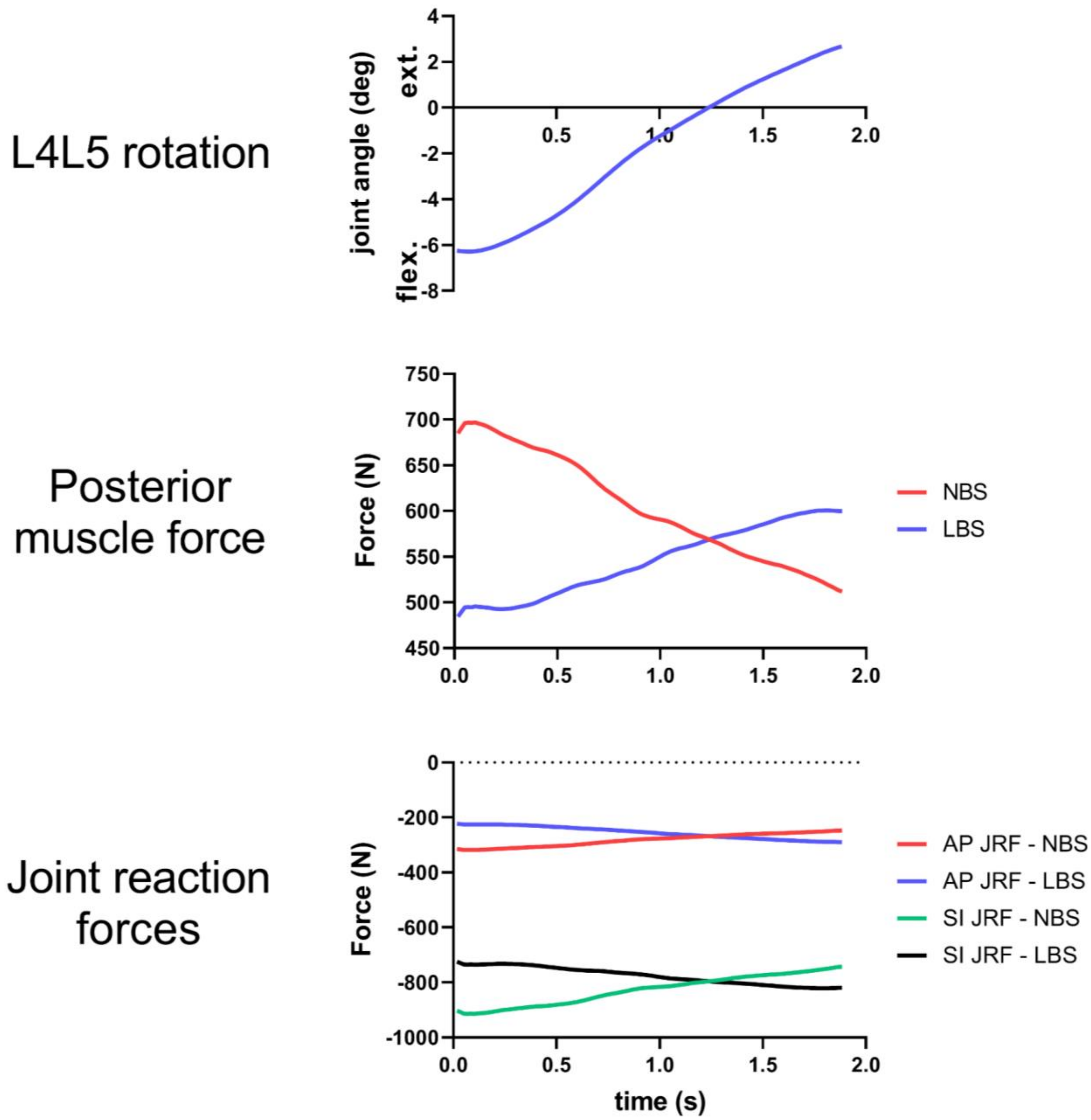

Figure 61: Joint kinematics, muscle forces, and joint reaction forces for simulation of simple model

3.3.2.6 Joint Reaction Forces and Anterior Disc Deformation

Relationships between JRF and disc deformation varied between the three subjects investigated. At a particular instance of anterior compression, compressive JRF could vary up to 2000 N or even higher depending on the subject or lifting trial being investigated (Figures 62-63). Despite having similar ranges of anterior compression in 10 lb and 30 lb trials, the compressive JRF at the L23 to L45 estimated by the musculoskeletal model were significantly increased during 30 lb trials. This was especially apparent for subjects 5 and 10, where estimated compressive JRF could be about 500-100N greater during the 30 lb lift despite having the same magnitude of anterior compression as the 10 lb lift. However, relationships between compressive JRF and anterior compression at the L5S1 appeared more maintained between trials of different external load magnitude. While the magnitude of L23 shear JRF tended to increase with the amount of L23 anterior shear strain, such a relationship was not seen at other segments. L34 shear forces remained at a similar magnitude despite changes in anterior shear strain. At any particular instance of anterior shear strain, the estimated shear JRF at the L45 and L51 varied widely depending on the subject and lifting trial. Where anterior shear strain magnitudes were similar between the 10 lb and 30 lb trials, L45 and L51 shear JRF were generally larger during the 30 lb lift.

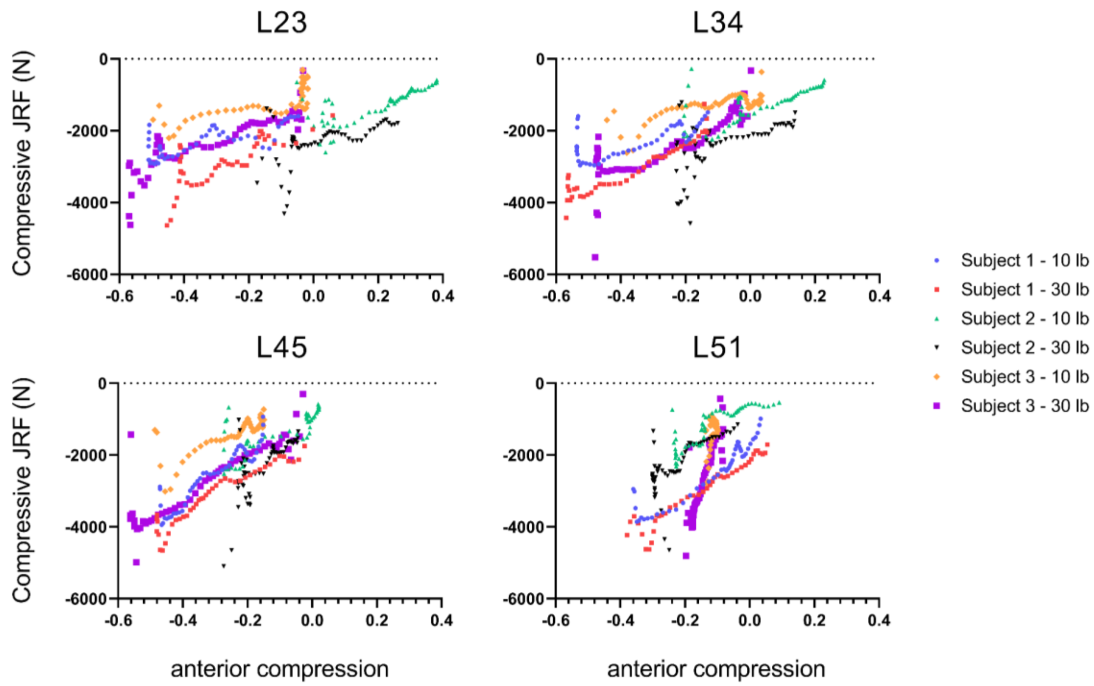

Figure 62: Compressive joint reaction force vs. anterior normal strain of the disc.

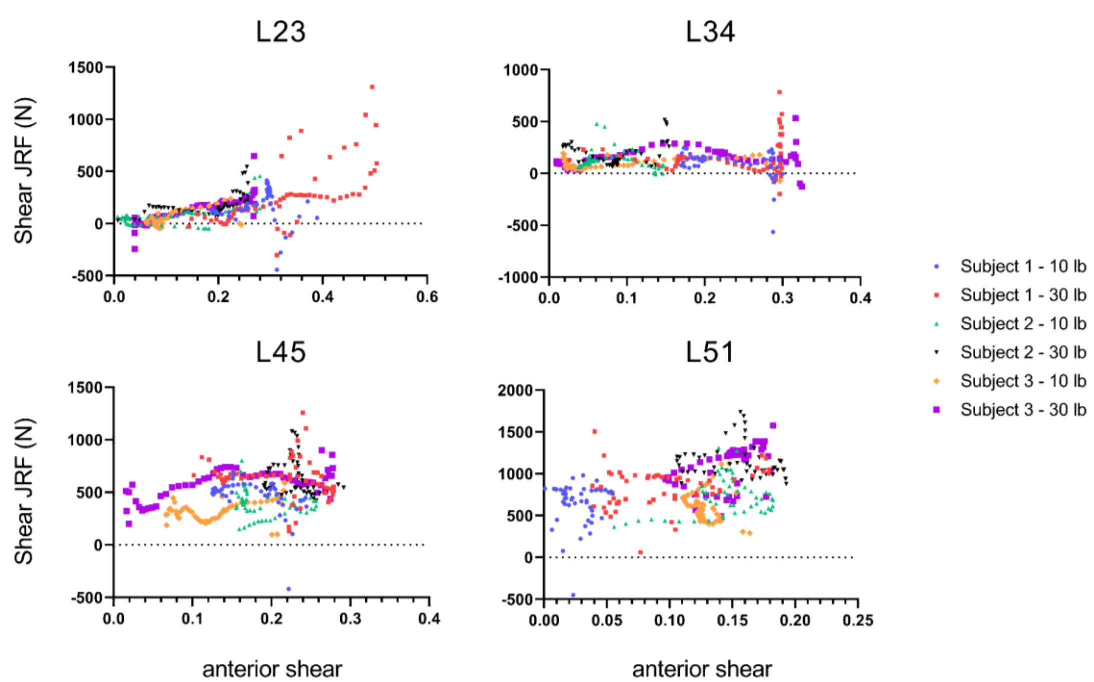

Figure 63: Shear joint reaction force vs. anterior shear strain of the disc.

4.0 Discussion

4.1 Disc Height and Deformation

The data presented here demonstrate how dynamic X-ray imaging of the vertebral bone motion enables a detailed accurate characterization and analysis of the morphometry and deformation of lumbar intervertebral discs *in vivo*. The results clearly show that the morphometry and deformation characteristics of the L5S1 disc are uniquely different from the rest of lumbar intervertebral discs. The substantial reduction of normal and shear strains at the L5S1 disc has three possible mechanistic explanations. First, the L5S1 material properties and morphological structure form an intervertebral disc of greater elastic modulus compared to the cranial discs. While *in vivo* material property data for the discs remain unattainable, the effect of intervertebral disc height on segment stiffness determined by previous studies[149-151] may suggest that the different disc height patterns observed at the L5S1 may play a role in facilitating increased segment stiffness, effectively reducing the magnitudes of normal and shear strain. Generally, these studies have found that a disc exhibiting lower disc height, typically measured at the center of the disc, would result in a stiffer motion segment of the spine. And while the loading conditions likely varied between segment levels and across subjects, the lack of positive correlation across subjects between central intervertebral disc height and intervertebral range of motion during the functional lifting task challenges this explanation. A recent study also found that while disc height was directly correlated to axial stiffness of a segment, it was not correlated to any of the rotational stiffnesses of the segment[152]. However, the effect of regional changes in disc height, or a significantly altered distribution in disc height, is not well understood. It is plausible that disc height distribution throughout the disc cross-sectional area may play a significant role on the stiffness of a segment. An alternative explanation is that active forces of the muscles stabilizing the L5S1 segment produce a larger portion of the load compared to the cranial segments, therefore reducing the load experienced by the L5S1 disc. However, modeling studies have estimated L5S1 normal and shear loads to be comparable to discs at other levels[52,53], implying a substantial disc load reduction being implausible. A third explanation is that the L5S1 disc, contrary to the other lumbar discs, is substantially more pre-loaded at the upright position compared to the flexed position. This would explain the smaller L5S1 strains observed throughout the lifting motion, as deformation of the disc at the upright position compared to its non-deformed state would remain undetected given that the upright position was used as the reference frame for computing disc deformation. Past studies have also observed significantly different behavior of the L5S1 when compared to other lumbar segments, and have determined the L5S1 segment to have greater contribution during extension of the spine than in flexion[70,153]. Furthermore, disc degeneration and facet joint osteoarthritis have been found to occur independently at the L5S1, while associations between the two degenerative diseases were found at the L3L4 and L4L5[153]. These findings, along with the new insight from the current study, suggest that the mechanical environment of L5S1 and its related biochemical environment may be distinctly different from the other intervertebral discs.

Establishing deformation characteristics baselines in healthy lumbar intervertebral discs has important implications on the understanding and modeling of disc degeneration. Degenerative conditions in the intervertebral discs are often associated with changes in disc height and segment mobility, although the degree to which the *in vivo* mechanical environment causes these changes remains unclear. High mechanical strain of the disc tissues has been related to the secretion of inflammatory cytokines associated with disc degeneration and low back pain[43]. Therefore, knowledge of dynamic strain responses in the lumbar spine during a functional activity provides a crucial link between *in vivo* mechanical and biochemical milieus of the intervertebral discs in understanding different cellular responses *in vivo*.

It is envisioned that the data from the current study will add a critical piece of scientific evidence for designing treatments aimed at mitigating low back pain attributed to mechanically damaged or degenerated discs and restoring spine function. There has been much discussion surrounding the comparison of lumbar fusion – the current gold standard procedure – and various artificial disc replacement strategies as potential alternative surgical approaches for treating low back pain. Despite a theoretical mobility advantage offered by the total disc replacement, several clinical trials and meta-analyses failed to find sufficient evidence to support the claim[154]. The majority of current total disc replacement techniques focus on emulating the biomechanics of a spine motion segment as a whole but pay little attention to the mechano-physiological characteristics of the disc[155]. However, mimicking a healthy disc's mechanical responses, i.e., motion and deformation, is the ultimate goal of implants designed to achieve full functional restoration[35]. To date, attempts to replicate the physiological elastic-type characteristics or the more 'organic' aspects of intervertebral discs have been unsuccessful[155]. Critically missing in the prior efforts are data and knowledge regarding *in vivo* loading and deformation behavior of the intervertebral discs[40].

The current work provides insight into hitherto unavailable time-dependent disc deformation trends and their differences between segments, and demonstrates the importance of acquiring dynamic, functional benchmarks as opposed to those determined by static or nonfunctional modes. For example, the significantly lower L5S1 posterior distraction compared to the L2L3-L3L4 from 0% to 40%MC may not have been identified in a study examining a midflexion static pose or a flexion pose without any external load. This implies that conclusions based on static or nonfunctional in vivo behavior may not be sufficient to accurately describe level-specific deformation patterns.

Despite the ability to accurately measure the overall lumbar disc deformation, a major limitation of such an analysis is the inability to accurately measure bulging of the disc or localized, cell-level strains or bulging of the disc. Comparing estimates of disc bulging based on tissue level compressive strains to those derived from FE simulations provided mixed results based on the lifting trial being investigated. Despite the kinematic boundary conditions being identical, disc bulge values estimated based on nominal compressive and tensile strain values did not align well with results from an FE simulation during the 20 lb lift; however, did they were much closer at the very beginning and end positions of the lift. Without *in vivo* measurements, it cannot be determined which of the two may be more accurate in estimation of disc bulge. While accurate tissue-level deformations were measured via DSX imaging, the preloading and internal mechanics of the disc cannot be accounted for in the current methodology. Furthermore, there was a limitation in assumed disc properties by the lack of distinction between the nucleus and annulus regions when prescribing a Poisson's ratio to estimate radial strain of the disc. A value of 0.45 was prescribed to the midpoints of all line segments of the disc, while typically values of 0.49, 0.495 or 0.499 are more indicative of nucleus pulposus properties. This should be taken into account when evaluating radial strains and displacements nearer to the center of the disc. When comparing intervertebral disc strains with data from literature, the current methodology was also incapable of accurately measuring the decrease in shear strains towards to the incompressible nucleus of the intervertebral disc as commonly seen in literature[58,146]. Estimates of shear strains were much more comparable in magnitude at the anterior and posterior annulus regions of the disc.

An additional limitation of this study was defining the reference frame for disc deformation as the upright standing position. By this definition, no strains or disc bulging occurred at the intervertebral discs during the standing position. However, it is known that strains are present within the intervertebral disc even during tasks of low exertion such as sitting or standing. Studies have reported average peak radial strains of approximately 8%, and normal and shear strains of approximately 10-20%, at annulus regions under loading conditions representative of sitting or standing[71,142,156]. It therefore must be noted that the deformation values provided by the current disc deformation analysis do not account for such strains at the upright position, and likely do not represent the true magnitude of strains present in vivo.

4.2 Facet Joint Kinematics

The current study used a previously acquired lumbar kinematics dataset from a dynamic, sagittally symmetric lifting task to quantify facet joint translations in healthy, asymptomatic individuals. Variations across the individual lumbar segments and the sensitivity of the motion to magnitude of external load lifted were assessed.

4.2.1 Segment-specific Differences

The clearest differences were observed in SI translation, which was about 45% less at L5S1 compared to the rest, on average. Continuous time-series curves (Figure 38) generally indicated a linear translation pattern with respect to L2-S1 extension. The highly linear ($r^2 \geq 0.94$) "time-series" curves imply that, at least for healthy and asymptomatic individuals, accurate end-ROM based measurements at flexed and upright poses *might* be adequate to estimate SI translations within the lumbar facet joints. However, comparing SI translation results with the limited number of previous studies based on end-ROM static imaging techniques yields somewhat mixed results. For example, (Svedmark et al., 2012) reported overall translation magnitudes of 6.5 mm and 4.6 mm at the L4L5 and L5S1 facets respectively, although these were based on CT measurements of supine flexed- and extended spines[91]. On the other hand, (Kozanek et al., 2009) reported L4L5 translations to be much lower than L2L3 and L3L4 segments. Moreover, the overall magnitudes reported were also much lower ($\bar{x} < 4\ mm$) than those measured in the current study[93].

Interestingly, although SI *translations* at the L5S1 facets were of a smaller magnitude, SI FJ *spacin*g at the static upright position was considerably larger compared to the other segments. A possible explanation could be that in the standing position, there is an inherent superior shift in FJ spacing at L5S1 compared to other segments on account of a difference in vertebral orientation and lordosis. Although the SI spacing is approximately 2 mm larger for L5S1 in upright stance compared to the upper segments, it should necessarily reduce further in hyperextension, when the facet joints bear a larger proportion of the lumbar loads, with the magnitude of translation being proportionally larger in L5S1. Given the special orientation of the L5S1 segment (lordosis) compared to the remaining segments, the uniquely different patterns within the L5S1 facet joints compared to the rest appear to reflect an adaptation to allow for more load-bearing to occur in a hyperextended pose. Orientation and translation patterns also suggest greater contact forces and hence higher risk of wear at the lower extremities of the superior (L5) facets; however, few studies are available to directly confirm this hypothesis. FE models of functional spinal units simulating sagittal rotation have predicted greater contact at relatively superior locations on the inferior facet of the superior bone (L2) for the L2-L3 joint[157] but relatively more inferior locations on L4 inferior facets for the L4-L5 joint[21], implying a progressive downward shift of the contact location from cranial to caudal segments. Secondly, the combination of a larger SI spacing along with a smaller *facet gap* for L5S1 facets, which narrows further into a flexion pose, also suggests upper extremities of the S1 facet could be at higher risk for wear and degeneration, particularly with any disc height loss following an onset of disc degenerative conditions. Results from a recent FE study[158] appear consistent with this hypothesis: contact forces during flexion movement appeared exclusively in the L5S1 segment on the upper extremities of the superior facets of S1. Facet contact did not appear to occur within the upper (L1-L5) segments during flexion.

Translations in the *X*- (*facet gap* normal to facet face) and *Z*- (facet sliding parallel to facet face) directions were relatively small and similar to those reported by (Kozanek at al., 2009)[93]. The results indicated that coupled translation patterns in the caudal segments, while small, are significant, particularly for L5S1. Some of the segment-wise differences in X- and Z-directions could be due to differences in articular facet orientation. (Masharawi et al., 2004) reported progressively more coronally oriented facet surfaces as one moved caudally along the thoracolumbar spine, postulating this to be an adaptation to allow a progressively increased range of movement in the lumbar segments[159]. (Masharawi et al., 2014) also showed that the mismatch in both transverse orientation (angle made with the sagittal plane) and longitudinal orientation (angle made with the frontal plane) between the adjacent facets increased from the cranial to the caudal segments. This "opening up" of facet surfaces in the two directions could explain the larger changes in facet gap and facet sliding observed at the caudal segments in the current study, further supporting Masharawi et al.'s speculation that a mismatch in orientation of adjacent facets encourages more coupled translations.

One peculiarity in the results was the difference in X- (facet gap) translation magnitudes between left- and right sides for the cranial segments L2L3 and L3L4. Our previous analyses on vertebral 3D rotations did show coupled, non-sagittal translations and rotations to be small, but significantly greater than zero[116] (Aiyangar et al., 2014). Although differences were not statistically significant, cranial segments exhibited slightly larger lateral bending, which might partially explain these differences by simultaneously increasing *facet gap* on one side while reducing it proportionally on the other.

4.2.2 Load-specific Differences

No significant differences in facet translations were observed due to magnitude of the lifted load. Previous investigations into effect of the external load on intervertebral rotations patterns and migration patterns of the instantaneous centers of rotation based on this dataset also failed to discern statistically significant differences[115,160]. However, this does not necessarily imply that external weight does not have any effect on FJ motion. It is plausible that the incremental increase in load for this study was not enough to produce significant effects on lumbar facet kinematics.

4.2.3 Implications For Facet-based Pain

The study presents a hitherto unavailable baseline dataset of facet translations measured accurately and with high precision during dynamic, functional activities. The primary motivation for documenting a benchmark for FJ translations in a health cohort, however, was to enable future investigations of the biomechanical antecedents of pathological conditions. It is then worthwhile to ponder the implications of deviations from the relatively small translations observed in this study.

Although motion between facet surfaces is relatively small, nominal strains developed within the facet capsules during the course of a normal range of motion can be quite large. For example, (Ianuzzi et al., 2004) demonstrated that principle strains in the facet capsules reached upwards of 14% at the maximum prescribed lumbar flexion angle (40°)[161]. It is also understood that strains developed within the lumbar facet capsules can activate pain receptors. *In vitro* studies have suggested the strain threshold for sustained painful capsular stretching to be anywhere from 20% to 47%[81,162-166]. Relatively minor increases in translation = of the order of a millimeter – could significantly increase capsular strains and consequently the likelihood of pain, particularly if these translations were sustained or occurred repeatedly during daily activity. Secondly, small deviations from the normal ranges of translation could increase the risk of adjoining facet face impingement and surface cartilage. For example, observations of facet kinematics in patients with DDD revealed a marked increase in coupling of the translation components compared to asymptomatic controls[5]. These increases were observed at the index- as well as the adjacent level. The situation could be particularly exacerbated in conditions associated with lumbar instability, where sudden but transient deviations in translation patterns could momentarily cause impingement within the facet joints, or cause facet capsular strain levels to exceed the pain threshold. Further studies are needed to quantify the threshold for kinematics deviations leading to the onset of painful FJ pathological conditions.

Several limitations are present within this study. First, a few participants' data were not useable, reducing the sample size of our study to 10. Additionally, we were unable to include the L1 in our study due to capture volume limitations of the DSX system. The age range of participants included in this study was very limited as well and is not representative of the general demographics. However, since our goal was to provide a dataset of healthy lumbar kinematics, the relatively young age group included in this study may be adequate. Although all participants were instructed and trained to finish the lifting motion within a 2-second time period, not all participants were able to reach their upright position during DSX imaging, limiting our ability to quantify lumbar facet motion at these time instances exceeding 80%.

4.3 Musculoskeletal Modeling

4.3.1 Load Estimates

The current study describes, in detail, the steps implemented for incorporating detailed 6-DOF subject-specific kinematics and passive stiffness properties into a full-body OpenSim® musculoskeletal model. While no specific validation studies were conducted, the magnitudes of estimated L23-L51 JRF across the three investigated subjects were within bounds reported by previous studies examining lumbar flexion or lifting motions[108,109,148,167]. Maximum compressive and shear loads ranged from approximately 2000N – 4000N and 100N – 1600N, respectively, across all segments and model variations. Results showed that while lumbar compressive loads of were distributed rather evenly across segments, the lower segments – particularly the L5S1 – accounted for the bulk of shear loads during the lifting tasks. While peak muscle forces varied widely by muscle group, the largest forces were observed at MF, LT, and IL, reaching approximately 900N, 1500N, and 1600N, respectively, during the lifting tasks. While variation in the grouping of muscle fascicles complicates comparison across studies, muscle forces appeared to be within range of those calculated by previous studies[108,109].

4.3.2 Effect of Input Kinematics

In general, implementing 6-DOF DSX-based kinematics predicted lower magnitudes of JRF compared to a rhythm-based distribution of lumbar segmental motion without translational DOF through the first half of the lifting motion. This result is consistent with a previous musculoskeletal modeling study, which showed that the optimal COR location for minimizing JRF may vary for each instantaneous flexed position of the lumbar spine[123]. A preceding analysis of instantaneous CORs using the finite helical axis method also showed that these CORs migrated over the range of the lifting motion[160]. Since rhythm-based models had no translational motion, the fixed joint CORs could additionally constrain the model, resulting in larger JRF estimates. Maximum differences in compressive and shear JRF at the beginning of the lift reached over 1300 N and 800 N, respectively, but varied substantially by the subject and segment level.

The DSX-based kinematics also revealed differences in forces generated within the muscles. For example, multifidus forces tended to increase with inclusion of DSX kinematics, as opposed to RHY kinematics, however the magnitude of this differences depended highly on the subject being investigated. Multifidi are considered to be stabilizing muscles, which act to constrain excessive vertebral translations[168]. Thus, including intervertebral translations could provide insights into stabilizing aspects of the muscles against excessive translations, which may not be revealed when using rhythm-based, rotation-only inputs. Furthermore, inclusion of DSX-based kinematics consistently led to lower iliocostalis lumborum forces in all three subjects compared to models with rhythmic kinematics.

4.3.3 Effect of Intervertebral Bushing Stiffness

The effects of bushing stiffness on lumbar loads were highly dependent on the model's kinematic input. The inclusion of bushing stiffness (LBS or NLBS) had a relatively small effect on JRF near the beginning of the lifting motion compared to those calculated from NBS models. Theoretically, the inclusion of rotational stiffness should produce an extension moment when the joint is placed in flexion, which should aid the muscles in stabilizing the joint, leading to reduced muscle forces and corresponding JRF compared to those in NBS models. However, it should be noted that non-sagittal kinematics and stiffness parameters were also present in this simulation. Thus, the non-sagittal motions experienced during the lifting task impose additional passive moments which must be stabilized by the muscles. While the muscle forces require less force to stabilize the FE moment in LBS and NLBS models compared to NBS models, they also require more force to stabilize the non-sagittal motions at the joint. It is for this reason we do not observe differences between models with or without rotational stiffness near the first half of the lift. However, estimated JRF from LBS and NLBS grew larger compared to NBS models with lumbar extension towards the upright position, suggesting that the sensitivity of the model to non-sagittal stiffness is increased nearer to the upright position. These differences were further compounded in the second subject from approximately 75-100%MC degrees L2S1 extension until the end of the lift. Interestingly, it is around this same interval of time during the lift where the L4L5 segment transitions from a flexed pose to extension in relation to its neutral state (Figure 60). This is significant for models which consist of rotational stiffness at the joint – particularly those modeled to have greater stiffness such as the L45 and L51 – as the reaction moment of an extended joint will act in the flexion direction, placing an additional moment which the muscles must account for when achieving the desired kinematics. This may explain the relatively larger compressive and shear JRF in LBS and NLBS models as the subject progressed through the lift.

4.3.4 Effect of Neutral State

Overall, although model outputs were least sensitive to changing the neutral state position, the effects were magnified with the presence of either LBS translational stiffness or generic, rhythm-based kinematics. These results demonstrate the need for further characterization of the pre-stressed state of the intervertebral joint, particularly when used in musculoskeletal models using simplified assumptions for kinematics and passive stiffness inputs.

4.3.5 Comparisons to Previous Studies

Although comparatively more modest, previous modeling studies investigating effects of ignoring translations have reported similar trends as in the current study. For example, (Ghezelbash et al., 2015) reported a low-to-moderate effect of ignoring translational DOF on JRF predictions (~15% for compression and ~36% for shear) in a custom-developed nonlinear finite element-based model of the lumbar spine[96,112,169]. Deploying a force-dependent-kinematics (FDK) approach with an OpenSim®-based upper trunk model[54,122] showed a modest reduction in compressive force estimates with coupled stiffness models for the intervertebral bushings, although the estimates were much more sensitive to rotational stiffness values than the translational stiffnesses. (Arshad et al., 2017) demonstrated modest (7%) reductions in compressive force estimates at L4L5 when translational stiffnesses (and, implicitly, translational DOF) were incorporated into an AnyBody®-based model (de Zee 2007) with an FDK approach[15,108]. (Bruno et al., 2017) demonstrated the sensitivity of predicted forces to assumed spinal curvature[138]. Incorporating CT-derived subject-specific spinal curvatures resulted in a median difference of approximately 15% in computed compressive forces at the L3 level compared to a generic, scaled model based on subject's height and weight, when simulating a 40° flexed posture with a 10kg weight. This parameter could be considered to be somewhat similar to the neutral state parameter in the current study, although the bushing stiffnesses were not adjusted to the defined initial states. Further, these were *inverse static* model-based studies, with most limited to investigating specific poses.

Building on these past studies, the current study demonstrates how input kinematics, intervertebral disc stiffness, and joint neutral state definition affect model estimates of net joint reaction loads and muscle forces in the lumbar spine during a functional, dynamic task. The study not only highlights model sensitivity to choices made regarding these parameters separately, but also how the interactions between each of these choices can result in significant variability in joint loading estimates over the entire range of a given dynamic task. The results provide some evidence that inclusion of translational joint motion could lead to reduced compressive and shear JRF during flexion of the lumbar spine. However, a more "accurate" dataset for one of the inputs (e.g. segmental kinematics) might heighten the demand for accuracy of the accompanying input variables such as passive stiffness properties and presumed neutral state of the joint.

4.3.6 Limitations

While much effort was put into incorporating accurate *in vivo* data, there remain a few limitations within the musculoskeletal models used in this study. First, the current study focuses data from three subjects. While the results from this study cannot be considered representative of a population, they were useful in laying out the study's methodology and demonstrating the effects of and interactions between the studied parameters. Second, intra-abdominal pressure, which has been shown to affect load estimates in the lumbar spine, was not included in this study. It is our hypothesis that while introduction of intra-abdominal pressure would likely alter the magnitude of JRF and muscle loads, the overall effects due to changes in input kinematics, bushing stiffness, and joint neutral state would remain the same. However, to better represent in vivo conditions, intra-abdominal should be included in future modeling studies. Another limitation is that ligaments were not explicitly modeled; instead, the passive stiffness properties included in the model were meant to represent the entire passive joint structure, as commonly done in literature. The lumped representation of the passive joints structures also aligns with the representation of the FE-derived NLBS passive stiffness properties utilized in this work. Lastly, as the focus of the current study was on the portion of the lumbar spine measured by DSX, motion above the L2 and between the sacrum and pelvis was neglected.

A considerable issue is that the large translational stiffnesses may not accurately represent the instantaneous physiological translational stiffnesses at the disc. A better approach may be to minimize the *net* joint reaction forces at each time frame of motion. The reason for this is as such: OpenSim Joint Reactions Analysis solves for the loads carried by the un-modeled structures. If it is desired to include the major load-bearing passive tissue structures (disc and ligaments) in the model, there are no remaining un-modeled structures which should bear significant loads in the joint. Thus, the values reported by JRA should, in theory, be small in magnitude. However, as evidenced by the current work, this was not the case. During the lifting motion, values of the *net* joint reaction forces reported by JRA – which did not include the prescribed stiffness reaction forces – were often over 1000 N, indicating that even after accounting for the disc and ligament forces, there remained 1000 N unaccounted for by the joint's un-modeled structures (Figure 25). The degree to which these errors effect the resulting net JRF and muscle loads is unclear, however the current study does show that with translational motion included within musuloskeletal models, these translational stiffness values do affect the net joint moments required to solve the classical equations of motion, and thus the associated muscle forces and JRF.

4.3.7 Correlations with Intervertebral Disc Deformation

The current work looked to compare the joint reaction force estimates from a musculoskeletal model to the observed disc deformation trend. Establishing a relationship between disc deformation and estimated JRF would provide valuable insight, and could potentially improve methods of incorporating passive stiffness properties in subject-specific musculoskeletal models, which have been shown by the current work to be inadequate when prescribed based on average force-displacement relationships from literature. In general, it would be expected that larger loads on the internal joint structure should results in greater disc deformation. However, results show that while estimated compressive JRF via musculoskeletal simulation may be larger due to added external load, it doesn't necessarily correspond to further anterior compression of the disc. The intervertebral disc is a complex load-bearing structure, consisting of an incompressible nucleus surrounded by several layers of annulus. Thus, the relationship between deformation of the disc and the resulting compressive, shear, and radial loads is not as straightforward as it might be for a more simplistic structure. It's plausible that the deformation data reported in the current study correlate with the estimated JRF in a more complex manner, such as the combined compression and shear at multiple regions of the disc, which may be extracted using a more involved method such as multiple linear regression. Improved accuracy of in vivo imaging techniques might also help uncover potential correlations between the two quantities. For example, imaging techniques capable of detecting compression of the nucleus pulposus with superb accuracy during in vivo activities may help establish a relationship between loading conditions on the spine and compression of the nucleus pulposus.

5.0 Conclusion

5.1 Summary of Results

5.1.1 Disc Height and Deformation

Analysis of disc height and deformation of the intervertebral disc resulted in several important conclusions. Overall, results showed that normal strains at the anterior and posterior regions of the L2L3, L3L4, and L4L5, reached approximately -40% and 60%, respectively, while shear strains reached approximately 30% and 60% at each region. However, L5S1 normal and shear strains were significantly less. Furthermore, deformation from L2L3 to L4L5 was relatively linear with respect to lumbar spine flexion during the functional lifting task, while the L5S1 displayed much less linear correlation. The study provides evidence that bi-plane DSX imaging is a sufficient means to quantifying accurate changes in disc morphometry and generalized disc strains (not internal strains). Furthermore, it is accurate enough to detect differences in such characteristics between segment levels of the lumbar spine. The general disc height and deformation characteristics quantified in this work are valuable to understanding the basic science of intervertebral discs; more specifically, their in vivo mechanical and biochemical relationships. The current work also provides data which can contribute to the development of artificial disc implants that have otherwise been unsuccessful due to inadequate information regarding dynamic lumbar disc mechanics. Furthermore, the data shows that L51 disc height and deformation characteristics are markedly different than those from L23 to L45 during functional lifting tasks, offering convincing evidence for segment-specific artificial disc implant designs, particularly at the L51.

5.1.2 Facet Joint Kinematics

The dynamic characterization of facet joint kinematics provides valuable insight on the functional mechanics of the facet joint in healthy subjects. Translations from L2L3 to L4L5 reached approximately 5-6mm during a functional lifting task, with the majority of motion occurring in the superior-inferior direction (or long axis) of the facet joint. Magnitudes of translation were approximately 45% less at the L5S1. Facet gap and sideways sliding translations ranged approximately 0-1mm and -0.5 to -2mm, respectively, from the flexed to upright position. At the upright position, SI spacing between facet surfaces was larger at L5S1, while the facet gap was much smaller. Overall, the study offers an in vivo dataset of functional facet joint kinematics in healthy subjects, with which future studies can used to identify pathological conditions. By providing normal ranges of translation motion at the facet joints, the dataset helps put into perspective the deviations from normal motion that may be necessary to induce facet-based pain during functional activity. Similar to the disc deformation analysis, the detection of significant differences at the L5S1 suggests that surgical interventions or implants should be implemented on a segment-specific basis, particularly at the L5S1.

5.1.3 Musculoskeletal Modeling

Modeling approaches to quantifying lumbar loads commonly consist of several key assumptions regarding input parameters, such as intervertebral kinematics and stiffness properties.

Building on past studies, the current study demonstrated how input kinematics, intervertebral disc stiffness, and joint neutral state configuration affected net joint reaction loads and muscle forces in the lumbar spine during a functional, dynamic task, as estimated by a subject-specific musculoskeletal model. In particular, the study not only highlights the effects of choices made regarding these parameters separately, but also how the interactions between each of these choices can result in significant variability in joint loading estimates. The current study provides evidence that inclusion of accurate 6-DOF joint motion leads to reduced estimates in compressive and shear JRF during flexion of the lumbar spine. Furthermore, inclusion of translations may provide a better understanding of the muscle force distribution between the abdominal and extensor muscles of the lower back. Lastly, the inclusion of the DSX kinematics shows significant interaction with other, and may heighten the demand on the accuracy of such parameters. The study also suggests that defining passive translational stiffness properties as a force-kinematic relationship should be excluded in musculoskeletal modeling simulations of the lumbar spine, as the introduction of such properties can place substantial spurious moments on the joints and can lead to large variations of load estimates at certain instances of the lifting motion. The only reason passive translational stiffnesses should be included within a model is if it represents accurately measured in vivo data on the same individual whose data is being implemented within the musculoskeletal model.

5.2 Future Work

5.2.1 Future of Current Work

The two motion analyses performed using the vertebral kinematics dataset can be further improved to provide additional information on soft tissue motion of the lumbar spine. For the disc deformation analysis, a valuable modification would be to measure deformation of the disc with respect to the supine position of the lumbar spine. This would provide additional insight on the total disc deformation occurring during functional activity. With respect to facet joint kinematics, it would be interesting to model the facet joint capsules to estimate its deformation during the lifting tasks. Further, contact deformation between facet surfaces could be simulated as well by observing the overlap between surfaces of adjacent CT-derived bone models. However, DSX imaging likely isn't accurate enough to support such an analysis.

The current musculoskeletal modeling work will be extended to include data from all ten subjects which participated in the DSX imaging study. This will help establish a more concrete baseline and variation of vertebral joint reaction and muscle forces during functional activity. Furthermore, it will provide a better understanding of the sensitivity of such estimates to input kinematics, passive stiffness properties, and joint configurations defined during musculoskeletal simulations.

While literature shows that including passive stiffness affects lumbar spine load estimates derived from musculoskeletal models, the stiffness properties implemented are typically representative of in vitro data. As previously discussed, these stiffness properties do not replicate in vivo motion of the lumbar spine. In the case of subject-specific modeling, this could be increasingly true, given the variability in vertebral kinematics between subjects. The resulting JRF derived from Joint Reactions Analysis – which describe the loads carried by un-modeled joint structures – should be very low, as the objective of including passive joint stiffness within a subject-specific model is to replicate in vivo passive forces and moments of all joint structures (no un-modeled joint structures). The current work shows that the stiffness values prescribed to the joint did not satisfactorily replicate disc translational forces that would have reduced JRF to approximately zero. A viable strategy to better replicate in vivo stiffness of the joints during the lifting task may be to find the passive stiffness properties which minimize or greatly reduce JRF during simulation. This may valuable in providing insight into the in vivo nonlinear stiffness properties of the lumbar joints.

5.2.2 Objectives of Future Studies

The current work serves as a preliminary baseline dataset for functional mechanics of the lumbar joints and its soft tissue during a lifting activity from which future studies can either build on or compare data against. From a methodological perspective, results from both the motion analysis and musculoskeletal simulation studies support the future acquisition of subject-specific vertebral kinematics via DSX imaging techniques to study disc deformation, facet joint kinematics, and lumbar spine loading patterns during various functional activities. Such studies can advance our knowledge of *in vivo* lumbar spine mechanics which can later be used as guidelines to identify pathological conditions and to design surgical interventions aimed at restoring normal *in vivo* mechanics. To advance the current state of knowledge of these quantities, future studies should utilize these methods to investigate lumbar mechanics during other functional tasks, such as asymmetric lifting or even more dynamic and demanding tasks such as heavy weightlifting. This will provide a more complete assessment of healthy, in vivo lumbar kinematic and loading patterns.

Results from the current work show that prescribing 6-DOF passive stiffness properties via uncoupled force-kinematic relationships may not accurately represent passive forces within the joint. Future studies should look towards other methodologies of representing the passive structures of the joint within a musculoskeletal framework. To date, some studies have elevated this representation by introducing coupled stiffness properties or have integrated data from finite element model simulations. While obtaining these data on a subject-specific basis is difficult, they may allow for more physiologically accurate approaches in subject-specific musculoskeletal simulation of the lumbar spine.

Appendix

Joint Reaction Force and Muscle Force Supplementary Material

Table 6: SI compressive forces for all subject #1 model variations.

			DSX - SUP			RHY - SUP			DSX - UP			RHY - UP		
		%MC	LBS	NLBS	NBS	LBS	NLBS	NBS	LBS	NLBS	NBS	LBS	NLBS	NBS
L2L3	10 LB	0	-2578	-2653	-2806	-3102	-2949	-3395	-2683	-2739	-2917	-3078	-2978	-3333
		25	-2649	-2714	-2791	-2735	-2651	-2964	-2673	-2673	-2745	-2702	-2674	-2895
		50	-2277	-2346	-2385	-2400	-2388	-2569	-2311	-2336	-2379	-2363	-2384	-2494
		75	-2005	-2177	-2101	-2210	-2231	-2262	-1865	-2107	-2104	-2170	-2200	-2184
		100	-1929	-1972	-1827	-1907	-1937	-1807	-2213	-2100	-1884	-1808	-1834	-1691
	30 LB	0	-2742	-3121	-3297	-3951	-3781	-4246	-2916	-3240	-3447	-3880	-3767	-4135
		25	-3296	-3384	-3496	-3548	-3467	-3778	-3315	-3418	-3520	-3475	-3444	-3663
		50	-2683	-2865	-2855	-3282	-3285	-3403	-2781	-2879	-2837	-3207	-3237	-3284
		75	-2738	-2921	-2659	-2900	-2927	-2761	-2928	-3017	-2698	-2849	-2883	-2648
		100	-2650	-2649	-2228	-2639	-2665	-2280	-2644	-2637	-2200	-2522	-2546	-2102
L3L4	10 LB	0	-2107	-2186	-2370	-3232	-3241	-3519	-2242	-2286	-2481	-3197	-3239	-3441
		25	-2785	-2876	-2979	-2789	-2833	-3010	-2804	-2857	-2958	-2750	-2829	-2931
		50	-2406	-2539	-2604	-2393	-2463	-2557	-2411	-2537	-2603	-2351	-2429	-2472
		75	-2109	-2180	-2101	-2172	-2232	-2208	-2045	-2139	-2103	-2126	-2184	-2121
		100	-1980	-2152	-2030	-1847	-1897	-1724	-2304	-2335	-2133	-1756	-1796	-1622
	30 LB	0	-3016	-2985	-3088	-4063	-4062	-4336	-3195	-3112	-3241	-3988	-4021	-4220
		25	-3355	-3397	-3524	-3537	-3582	-3738	-3384	-3440	-3565	-3464	-3538	-3624
		50	-3143	-3291	-3290	-3214	-3286	-3309	-3210	-3324	-3288	-3133	-3212	-3181
		75	-2770	-2934	-2665	-2806	-2861	-2634	-2966	-3043	-2715	-2742	-2796	-2510
		100	-2651	-2669	-2263	-2536	-2575	-2146	-2677	-2668	-2244	-2411	-2438	-1967
L4L5	10 LB	0	-3054	-3138	-3513	-3157	-3287	-3381	-3333	-3455	-3691	-3221	-3374	-3402
		25	-2700	-2744	-2916	-2712	-2823	-2885	-2719	-2845	-2911	-2749	-2880	-2883
		50	-2267	-2396	-2525	-2314	-2412	-2443	-2383	-2485	-2525	-2328	-2428	-2417
		75	-1954	-2008	-1956	-2101	-2172	-2100	-1916	-2005	-1959	-2097	-2166	-2059
		100	-1683	-1917	-1829	-1797	-1853	-1626	-2108	-2130	-1919	-1737	-1781	-1565
	30 LB	0	-3787	-3727	-4010	-3942	-4070	-4125	-4049	-4065	-4200	-3985	-4139	-4120
		25	-3256	-3279	-3473	-3406	-3516	-3534	-3343	-3457	-3523	-3419	-3544	-3498
		50	-2951	-3033	-3040	-3078	-3174	-3124	-2999	-3101	-3046	-3061	-3159	-3062
		75	-2704	-2900	-2664	-2718	-2781	-2472	-2972	-3075	-2717	-2685	-2747	-2390
		100	-2427	-2531	-2109	-2470	-2510	-2004	-2609	-2594	-2091	-2362	-2388	-1856
L5S1	10 LB	0	-3200	-3291	-3502	-3098	-3245	-3145	-3498	-3626	-3714	-3322	-3481	-3324
		25	-2783	-2826	-2830	-2650	-2770	-2652	-2811	-2937	-2835	-2847	-2979	-2802
		50	-2331	-2460	-2428	-2242	-2341	-2213	-2446	-2549	-2425	-2412	-2511	-2331
		75	-1983	-2019	-1819	-2013	-2081	-1872	-1961	-2035	-1827	-2170	-2237	-1969
		100	-1700	-1921	-1761	-1688	-1739	-1427	-2091	-2121	-1815	-1769	-1810	-1461
	30 LB	0	-3860	-3799	-3995	-3771	-3918	-3843	-4137	-4159	-4195	-4004	-4165	-4029
		25	-3325	-3345	-3406	-3258	-3375	-3247	-3411	-3521	-3453	-3460	-3586	-3397
		50	-2967	-3043	-2950	-2874	-2969	-2822	-3008	-3106	-2952	-3050	-3147	-2945
		75	-2709	-2896	-2562	-2530	-2589	-2195	-2957	-3054	-2583	-2698	-2758	-2279
		100	-2386	-2484	-1969	-2250	-2286	-1738	-2548	-2534	-1941	-2353	-2377	-1745

Table 7: AP shear forces for all subject #1 model variations.

			DSX - SUP			RHY - SUP			DSX - UP			RHY - UP		
		%MC	LBS	NLBS	NBS	LBS	NLBS	NBS	LBS	NLBS	NBS	LBS	NLBS	NBS
L2L3	10 LB	0	340	346	358	258	244	269	388	398	405	338	323	355
		25	276	288	300	193	181	213	321	315	323	258	249	280
		50	160	162	182	129	121	158	178	167	186	180	176	208
		75	115	124	129	82	74	105	102	108	129	124	120	145
		100	-4	-18	9	17	13	42	61	23	36	66	64	88
	30 LB	0	263	292	313	266	253	281	299	333	353	369	354	391
		25	223	228	251	167	156	188	248	250	271	248	240	273
		50	134	169	186	104	98	131	179	188	204	169	167	196
		75	41	53	78	33	27	62	74	78	97	88	86	104
		100	0	-19	21	-25	-27	27	-5	-12	34	26	27	54

			DSX - SUP			RHY - SUP			DSX - UP			RHY - UP		
		%MC	LBS	NLBS	NBS	LBS	NLBS	NBS	LBS	NLBS	NBS	LBS	NLBS	NBS
L3L4	10 LB	0	202	200	184	-30	-57	-69	233	241	220	181	159	154
		25	141	151	124	1	-24	-18	181	168	147	186	169	176
		50	114	109	104	19	0	22	128	108	108	177	169	185
		75	170	184	164	39	27	46	150	161	164	183	179	185
		100	71	41	46	39	33	48	146	93	86	179	179	171
	30 LB	0	56	85	77	-115	-140	-146	69	104	104	152	130	130
		25	72	77	51	-73	-99	-92	92	91	69	161	145	148
		50	101	142	129	-20	-36	-21	148	154	146	193	187	187
		75	91	100	101	18	9	28	130	132	126	210	208	185
		100	172	137	124	53	50	72	148	141	138	231	234	191

			DSX - SUP			RHY - SUP			DSX - UP			RHY - UP		
		%MC	LBS	NLBS	NBS	LBS	NLBS	NBS	LBS	NLBS	NBS	LBS	NLBS	NBS
L4L5	10 LB	0	477	487	532	614	581	643	537	554	582	761	744	785
		25	527	549	548	583	566	619	567	560	567	716	715	745
		50	495	510	527	547	546	594	505	506	531	663	672	700
		75	526	549	538	557	561	570	498	528	538	662	672	658
		100	389	414	414	531	539	483	574	522	477	636	646	567
	30 LB	0	401	448	468	711	677	728	417	476	510	885	866	895
		25	552	565	556	686	672	697	573	580	579	847	848	848
		50	576	637	637	705	708	724	631	655	654	851	864	852
		75	634	672	632	733	740	663	727	746	670	876	888	753
		100	791	788	647	775	784	631	828	820	663	896	905	676

			DSX - SUP			RHY - SUP			DSX - UP			RHY - UP		
		%MC	LBS	NLBS	NBS	LBS	NLBS	NBS	LBS	NLBS	NBS	LBS	NLBS	NBS
L5S1	10 LB	0	817	827	609	1411	1404	1202	874	891	662	1114	1100	858
		25	1018	1042	769	1356	1363	1157	1059	1062	787	1115	1120	873
		50	1009	1039	811	1269	1292	1102	1034	1046	815	1076	1093	862
		75	1028	1052	790	1265	1286	1049	1000	1038	794	1099	1116	844
		100	768	815	673	1160	1183	889	1051	998	748	1029	1045	742
	30 LB	0	630	674	512	1513	1504	1405	647	703	554	1134	1119	977
		25	988	1002	765	1543	1553	1361	1015	1027	790	1232	1239	1009
		50	1052	1121	939	1507	1535	1385	1112	1147	958	1235	1257	1070
		75	1177	1224	952	1582	1605	1251	1320	1351	996	1365	1384	991
		100	1424	1435	1001	1614	1634	1163	1494	1482	1020	1410	1423	917

Table 8: SI compressive forces for all subject #2 model variations.

			DSX - SUP			RHY - SUP			DSX - UP			RHY - UP		
		%MC	LBS	NLBS	NBS	LBS	NLBS	NBS	LBS	NLBS	NBS	LBS	NLBS	NBS
L2L3	10 LB	0	-1874	-1901	-1897	-2150	-2169	-2146	-1656	-1827	-1945	-2388	-2408	-2362
		25	-2110	-2263	-2234	-1977	-2005	-1898	-1819	-1866	-1868	-2154	-2180	-1922
		50	-1471	-1400	-1423	-1854	-1879	-1646	-1422	-1397	-1440	-2175	-2201	-1791
		75	-1356	-1280	-1226	-1481	-1483	-1188	-1081	-1212	-1177	-1664	-1661	-1246
		100	-1518	-1241	-929.6	-1126	-1107	-740.2	-1530	-1235	-860.3	-1246	-1220	-788.9
	30 LB	0	-2410	-2311	-2362	-3257	-3274	-3279	-1781	-2116	-2215	-3132	-3150	-3104
		25	-2430	-2437	-2481	-2703	-2731	-2617	-2346	-2427	-2404	-2854	-2879	-2732
		50	-2341	-2207	-2157	-2489	-2517	-2333	-1874	-2029	-2029	-2789	-2817	-2445
		75	-2524	-2655	-2339	-2327	-2350	-2047	-2777	-2720	-2256	-2660	-2680	-2199
		100	-2249	-2302	-1991	-2136	-2135	-1749	-2114	-1990	-1765	-2332	-2327	-1856

			DSX - SUP			RHY - SUP			DSX - UP			RHY - UP		
		%MC	LBS	NLBS	NBS	LBS	NLBS	NBS	LBS	NLBS	NBS	LBS	NLBS	NBS
L3L4	10 LB	0	-2160	-2202	-2192	-2294	-2353	-2287	-2078	-2188	-2218	-2551	-2610	-2523
		25	-2090	-2205	-2174	-2074	-2125	-2001	-1727	-1761	-1780	-2263	-2311	-2035
		50	-1432	-1132	-1098	-1919	-1955	-1703	-1090	-1061	-1109	-2246	-2280	-1851
		75	-1285	-1316	-1285	-1497	-1499	-1196	-1328	-1306	-1244	-1663	-1660	-1238
		100	-1406	-1249	-903	-1097	-1072	-711.2	-1423	-1216	-835.5	-1200	-1167	-745.6
	30 LB	0	-2202	-2075	-2132	-3459	-3519	-3487	-1855	-1978	-2005	-3319	-3380	-3275
		25	-2196	-2084	-2091	-2819	-2873	-2718	-1956	-2052	-2024	-2965	-3017	-2815
		50	-2482	-2455	-2427	-2572	-2617	-2391	-2284	-2302	-2250	-2890	-2935	-2518
		75	-2479	-2565	-2204	-2369	-2397	-2059	-2619	-2582	-2132	-2702	-2726	-2207
		100	-2313	-2414	-2071	-2140	-2139	-1730	-2280	-2072	-1818	-2308	-2303	-1811

			DSX - SUP			RHY - SUP			DSX - UP			RHY - UP		
		%MC	LBS	NLBS	NBS	LBS	NLBS	NBS	LBS	NLBS	NBS	LBS	NLBS	NBS
L4L5	10 LB	0	-2297	-2392	-2417	-2287	-2354	-2220	-2310	-2357	-2375	-2537	-2604	-2461
		25	-1877	-1923	-1875	-2055	-2111	-1937	-1591	-1574	-1602	-2236	-2288	-1990
		50	-1508	-1451	-1474	-1885	-1918	-1637	-1330	-1384	-1439	-2197	-2228	-1799
		75	-1044	-909	-851.9	-1462	-1464	-1135	-1050	-905.9	-830.8	-1616	-1613	-1185
		100	-1407	-1195	-696.4	-1077	-1055	-667.2	-1253	-1124	-656.8	-1183	-1154	-703.1
	30 LB	0	-2673	-2771	-2874	-3396	-3466	-3386	-2620	-2715	-2738	-3242	-3313	-3168
		25	-2493	-2551	-2601	-2762	-2823	-2611	-2446	-2570	-2549	-2896	-2954	-2704
		50	-2121	-2014	-1950	-2518	-2565	-2283	-1939	-1885	-1819	-2817	-2863	-2434
		75	-2322	-2383	-2032	-2290	-2316	-1948	-2426	-2368	-1976	-2607	-2629	-2117
		100	-2196	-2242	-1892	-2043	-2042	-1631	-2115	-1888	-1661	-2205	-2201	-1718

			DSX - SUP			RHY - SUP			DSX - UP			RHY - UP		
		%MC	LBS	NLBS	NBS	LBS	NLBS	NBS	LBS	NLBS	NBS	LBS	NLBS	NBS
L5S1	10 LB	0	-2074	-2149	-2137	-1881	-1942	-1802	-2033	-1975	-1888	-2223	-2286	-2149
		25	-1678	-1727	-1642	-1613	-1661	-1517	-1575	-1640	-1698	-1873	-1918	-1657
		50	-1298	-1290	-1295	-1447	-1473	-1242	-1107	-1126	-1138	-1815	-1840	-1459
		75	-962.7	-900.1	-780.5	-1150	-1152	-854.6	-1008	-887.7	-762.4	-1402	-1399	-985.9
		100	-1186	-1017	-576.7	-853.3	-836.4	-513	-1042	-975.1	-580	-1059	-1034	-619.4
	30 LB	0	-2546	-2716	-2773	-2838	-2901	-2762	-2600	-2722	-2703	-2884	-2950	-2778
		25	-2321	-2442	-2480	-2244	-2297	-2085	-2381	-2528	-2496	-2526	-2579	-2342
		50	-1912	-1863	-1773	-1986	-2025	-1778	-1860	-1843	-1753	-2361	-2400	-2013
		75	-2039	-2097	-1740	-1786	-1807	-1489	-2162	-2133	-1734	-2183	-2201	-1734
		100	-1916	-1960	-1593	-1607	-1606	-1238	-1893	-1742	-1506	-1920	-1916	-1443

Table 9: AP shear forces for all subject #2 model variations.

			DSX - SUP			RHY - SUP			DSX - UP			RHY - UP		
		%MC	LBS	NLBS	NBS	LBS	NLBS	NBS	LBS	NLBS	NBS	LBS	NLBS	NBS
L2L3	10 LB	0	182	162	171	213	205	225	186	171	164	268	262	272
		25	231	246	261	195	191	203	104	93	100	237	234	231
		50	68	34	66	147	147	152	76	66	92	187	188	182
		75	59	31	32	61	61	71	36	59	65	61	61	64
		100	-49	-27	3	-41	-42	-20	-8	-37	-10	-45	-46	-28
	30 LB	0	185	155	173	317	309	332	154	151	163	330	325	322
		25	122	86	101	217	213	219	103	91	83	244	241	230
		50	198	168	171	174	172	174	113	116	114	226	226	227
		75	160	174	152	123	124	118	170	159	155	150	152	146
		100	68	76	81	58	58	67	45	40	42	43	43	54

			DSX - SUP			RHY - SUP			DSX - UP			RHY - UP		
		%MC	LBS	NLBS	NBS	LBS	NLBS	NBS	LBS	NLBS	NBS	LBS	NLBS	NBS
L3L4	10 LB	0	171	144	143	232	220	231	189	158	146	192	181	186
		25	314	332	339	255	249	249	137	127	127	227	223	211
		50	102	64	77	260	262	227	94	83	93	252	253	209
		75	172	138	128	190	190	150	111	167	159	157	156	111
		100	132	127	114	109	108	60	157	95	77	65	64	23
	30 LB	0	167	130	138	320	309	327	122	127	132	213	202	199
		25	123	81	90	281	275	270	103	88	74	202	195	180
		50	299	252	239	289	286	261	150	167	162	255	254	231
		75	345	364	282	287	289	229	352	334	271	253	254	199
		100	262	278	220	244	244	185	204	165	132	171	171	126

			DSX - SUP			RHY - SUP			DSX - UP			RHY - UP		
		%MC	LBS	NLBS	NBS	LBS	NLBS	NBS	LBS	NLBS	NBS	LBS	NLBS	NBS
L4L5	10 LB	0	576	551	534	822	825	774	572	561	547	761	763	712
		25	713	733	713	830	838	760	428	394	385	776	782	683
		50	472	333	311	833	844	691	352	321	330	840	849	676
		75	455	342	308	664	665	487	393	389	339	616	615	428
		100	615	527	292	500	494	277	536	438	235	432	425	215
	30 LB	0	611	549	552	1153	1157	1147	480	499	511	904	906	870
		25	608	534	522	1019	1027	940	520	516	481	874	879	785
		50	807	722	680	1013	1023	879	596	593	564	962	970	830
		75	968	999	790	986	994	782	968	931	764	952	958	753
		100	889	919	726	888	888	667	776	657	550	777	776	582

			DSX - SUP			RHY - SUP			DSX - UP			RHY - UP		
		%MC	LBS	NLBS	NBS	LBS	NLBS	NBS	LBS	NLBS	NBS	LBS	NLBS	NBS
L5S1	10 LB	0	1107	1101	1014	1571	1595	1434	1108	1072	963	1435	1454	1317
		25	1176	1210	1131	1520	1546	1366	799	759	749	1391	1411	1195
		50	888	757	655	1532	1553	1229	696	657	606	1515	1531	1169
		75	884	750	549	1308	1309	886	822	771	573	1240	1239	792
		100	1158	999	503	1026	1012	540	1000	877	443	937	921	464
	30 LB	0	1230	1210	1114	2288	2313	2146	1128	1163	1053	1806	1826	1641
		25	1207	1163	1086	1952	1979	1745	1133	1159	1030	1685	1705	1483
		50	1366	1281	1149	1887	1911	1609	1145	1132	1011	1752	1772	1470
		75	1624	1671	1266	1867	1884	1430	1637	1589	1240	1783	1795	1345
		100	1595	1640	1203	1762	1761	1238	1449	1258	1006	1602	1599	1111

Table 10: SI compressive forces for all subject #3 model variations.

			DSX - SUP			RHY - SUP			DSX - UP			RHY - UP		
		%MC	LBS	NLBS	NBS	LBS	NLBS	NBS	LBS	NLBS	NBS	LBS	NLBS	NBS
L2L3	10 LB	0	-1941	-2095	-2073	-2323	-2281	-2460	-2021	-2100	-2062	-2320	-2320	-2409
		25	-1551	-1631	-1629	-1810	-1807	-1871	-1581	-1640	-1639	-1792	-1821	-1811
		50	-1475	-1529	-1437	-1632	-1647	-1572	-1423	-1499	-1432	-1563	-1600	-1500
		75	-1531	-1670	-1411	-1567	-1595	-1416	-1515	-1591	-1356	-1435	-1464	-1288
		100	-830.8	-964.7	-720.4	-1444	-1469	-1188	-943.1	-940.6	-676.6	-1334	-1361	-1058
	30 LB	0	-2565	-2689	-2719	-3170	-3090	-3329	-2626	-2661	-2698	-3130	-3100	-3237
		25	-2693	-2798	-2743	-2943	-2923	-3015	-2775	-2799	-2713	-2914	-2934	-2938
		50	-2487	-2558	-2445	-2565	-2588	-2498	-2453	-2540	-2422	-2455	-2489	-2367
		75	-2088	-2126	-1899	-2355	-2384	-2094	-2023	-2073	-1863	-2100	-2130	-1888
		100	-2136	-2145	-1765	-2249	-2277	-1750	-1920	-1943	-1632	-1989	-2009	-1548
L3L4	10 LB	0	-2344	-2521	-2499	-2473	-2542	-2648	-2380	-2550	-2490	-2456	-2542	-2576
		25	-1543	-1667	-1691	-1879	-1954	-1972	-1616	-1703	-1705	-1853	-1936	-1900
		50	-1343	-1437	-1377	-1669	-1729	-1615	-1357	-1433	-1375	-1586	-1657	-1534
		75	-1359	-1527	-1303	-1591	-1648	-1428	-1401	-1465	-1250	-1451	-1501	-1302
		100	-1286	-1315	-1064	-1447	-1490	-1171	-1216	-1248	-1003	-1299	-1334	-1035
	30 LB	0	-2767	-2969	-3022	-3406	-3456	-3608	-2848	-2975	-2997	-3345	-3427	-3489
		25	-2963	-3080	-3001	-3089	-3163	-3190	-3035	-3103	-2969	-3042	-3127	-3089
		50	-2437	-2555	-2423	-2645	-2720	-2583	-2470	-2567	-2401	-2515	-2585	-2433
		75	-2260	-2270	-2018	-2387	-2444	-2108	-2181	-2230	-1980	-2129	-2179	-1907
		100	-1765	-1808	-1438	-2256	-2299	-1724	-1713	-1691	-1347	-1950	-1975	-1497
L4L5	10 LB	0	-2490	-2730	-2770	-2579	-2699	-2698	-2522	-2809	-2764	-2628	-2751	-2696
		25	-1818	-1983	-2014	-1966	-2069	-1998	-1863	-2048	-2031	-1986	-2090	-1975
		50	-1574	-1698	-1597	-1751	-1824	-1623	-1563	-1709	-1593	-1699	-1782	-1578
		75	-1623	-1831	-1538	-1668	-1732	-1424	-1576	-1733	-1481	-1557	-1614	-1332
		100	-1305	-1366	-1125	-1505	-1552	-1158	-1232	-1316	-1082	-1358	-1393	-1040
	30 LB	0	-3516	-3776	-3893	-3525	-3649	-3676	-3525	-3812	-3858	-3560	-3697	-3657
		25	-3269	-3492	-3442	-3188	-3297	-3226	-3352	-3544	-3407	-3220	-3330	-3208
		50	-2657	-2784	-2634	-2720	-2811	-2594	-2732	-2827	-2611	-2647	-2730	-2502
		75	-2389	-2474	-2195	-2449	-2512	-2096	-2316	-2441	-2149	-2230	-2286	-1943
		100	-1881	-1961	-1611	-2305	-2350	-1699	-1856	-1895	-1566	-1991	-2015	-1504
L5S1	10 LB	0	-2413	-2683	-2589	-2376	-2489	-2384	-2486	-2767	-2584	-2571	-2688	-2520
		25	-1780	-1938	-1864	-1799	-1894	-1744	-1845	-2018	-1872	-1948	-2045	-1839
		50	-1529	-1644	-1467	-1577	-1642	-1401	-1528	-1654	-1451	-1668	-1746	-1474
		75	-1598	-1796	-1461	-1467	-1523	-1210	-1599	-1754	-1439	-1482	-1533	-1200
		100	-1345	-1441	-1131	-1300	-1340	-971.3	-1371	-1495	-1142	-1323	-1353	-956.2
	30 LB	0	-3327	-3611	-3591	-3246	-3365	-3275	-3378	-3655	-3536	-3463	-3595	-3433
		25	-3164	-3388	-3255	-2885	-2985	-2825	-3261	-3445	-3218	-3108	-3213	-2987
		50	-2555	-2675	-2453	-2407	-2488	-2225	-2642	-2729	-2441	-2550	-2628	-2325
		75	-2224	-2308	-1985	-2121	-2176	-1759	-2178	-2281	-1932	-2079	-2129	-1726
		100	-1849	-1929	-1576	-1951	-1988	-1391	-1851	-1916	-1612	-1985	-2007	-1453

Table 11: AP shear forces for all subject #3 model variations.

			DSX - SUP			RHY - SUP			DSX - UP			RHY - UP		
		%MC	LBS	NLBS	NBS	LBS	NLBS	NBS	LBS	NLBS	NBS	LBS	NLBS	NBS
L2L3	10 LB	0	173	165	210	253	233	290	181	170	211	262	252	300
		25	105	101	152	148	137	203	113	98	156	154	150	209
		50	86	79	119	99	89	136	80	77	123	93	91	138
		75	50	48	81	69	64	97	23	16	69	68	65	107
		100	-12	-18	13	31	27	51	-21	-23	9	-8	-8	41
	30 LB	0	232	222	252	371	347	407	236	218	256	387	373	424
		25	180	170	202	282	267	328	185	164	202	293	287	339
		50	157	153	174	205	198	234	147	148	173	204	202	232
		75	71	62	78	128	124	146	70	59	81	139	138	161
		100	-7	-19	15	48	47	83	-37	-29	-10	-3	-2	44
L3L4	10 LB	0	144	125	155	127	103	153	147	128	155	195	182	221
		25	118	109	140	93	77	135	126	104	142	147	140	185
		50	146	135	137	100	86	113	143	131	140	139	135	151
		75	144	139	110	123	114	107	111	94	92	172	168	150
		100	114	82	49	126	120	85	73	62	40	127	128	101
	30 LB	0	137	117	136	155	128	185	139	113	138	251	234	281
		25	204	187	198	162	143	198	210	181	198	249	240	279
		50	305	300	268	188	178	190	289	291	265	255	250	244
		75	267	246	179	203	195	166	264	239	180	280	277	226
		100	176	157	79	208	206	147	125	122	44	168	169	108
L4L5	10 LB	0	537	520	533	626	619	640	516	522	532	716	722	715
		25	428	441	434	505	508	519	439	440	441	576	588	571
		50	449	462	398	499	501	447	450	462	402	538	551	479
		75	470	498	370	532	537	419	405	406	337	571	580	450
		100	387	342	242	521	526	355	277	267	215	486	496	344
	30 LB	0	576	563	569	792	779	824	566	555	584	908	908	923
		25	709	710	676	793	793	802	713	704	673	902	912	890
		50	795	812	716	778	786	716	789	808	710	843	855	758
		75	798	791	614	787	794	631	779	778	608	838	849	673
		100	577	568	400	816	824	557	513	508	341	671	678	456
L5S1	10 LB	0	1272	1291	1011	1582	1607	1336	1256	1306	1008	1431	1454	1134
		25	1057	1097	805	1320	1352	1069	1080	1111	815	1216	1244	917
		50	1023	1058	703	1265	1286	920	1027	1062	704	1141	1168	787
		75	1048	1114	673	1273	1296	854	967	996	626	1141	1159	724
		100	893	856	460	1215	1234	724	754	737	426	1029	1045	582
	30 LB	0	1431	1462	1230	1960	1980	1737	1431	1461	1263	1732	1752	1454
		25	1568	1608	1281	1919	1948	1663	1590	1613	1273	1727	1754	1423
		50	1565	1604	1218	1805	1839	1457	1576	1611	1209	1610	1636	1233
		75	1541	1550	1043	1791	1817	1266	1513	1533	1026	1573	1593	1068
		100	1223	1204	751	1786	1808	1099	1075	1054	698	1408	1420	828

Table 12: Muscle forces for all subject #1 model variations.

			DSX - SUP			RHY - SUP			DSX - UP			RHY - UP		
		%MC	LBS	NLBS	NBS	LBS	NLBS	NBS	LBS	NLBS	NBS	LBS	NLBS	NBS
MF	10 LB	0	671	712	845	562	609	615	753	843	898	572	614	619
		25	465	492	519	485	523	523	461	487	516	490	522	520
		50	428	455	494	413	438	437	416	453	493	414	435	429
		75	318	330	318	353	372	357	318	319	318	348	365	346
		100	370	407	395	267	282	265	381	424	409	251	263	247
	30 LB	0	890	765	870	728	772	780	929	854	889	737	779	775
		25	538	548	585	594	626	621	552	581	596	596	625	608
		50	591	616	637	537	559	545	585	606	632	532	553	532
		75	445	494	497	420	437	411	480	503	481	400	415	391
		100	379	388	395	342	354	333	391	391	381	308	314	300
		%MC	LBS	NLBS	NBS	LBS	NLBS	NBS	LBS	NLBS	NBS	LBS	NLBS	NBS
LT	10 LB	0	1165	1199	1377	1381	1313	1555	1254	1291	1431	1315	1275	1451
		25	1064	1099	1150	1149	1123	1275	1056	1060	1125	1096	1092	1191
		50	873	911	939	944	952	1038	837	876	938	907	920	967
		75	703	785	799	774	793	840	618	754	798	744	761	780
		100	868	887	879	585	604	628	859	890	875	535	549	551
	30 LB	0	1159	1286	1463	1828	1749	2024	1199	1330	1486	1712	1666	1879
		25	1273	1321	1401	1437	1411	1581	1274	1326	1413	1346	1343	1461
		50	1039	1103	1156	1248	1261	1352	1042	1086	1142	1176	1194	1257
		75	921	1017	1043	942	962	1019	973	1012	1011	849	864	898
		100	782	819	819	760	776	809	800	806	802	711	721	727
		%MC	LBS	NLBS	NBS	LBS	NLBS	NBS	LBS	NLBS	NBS	LBS	NLBS	NBS
IL	10 LB	0	1251	1288	1342	1033	1087	1124	1301	1303	1367	1144	1203	1218
		25	921	919	1000	909	940	996	919	953	987	989	1030	1059
		50	712	750	820	771	798	849	798	800	826	830	866	892
		75	610	634	667	655	672	708	596	627	668	695	719	732
		100	237	298	338	515	529	539	418	349	345	516	531	538
	30 LB	0	1416	1543	1675	1314	1378	1383	1572	1648	1722	1457	1521	1508
		25	1114	1139	1233	1130	1163	1203	1145	1221	1253	1210	1252	1262
		50	943	987	1015	1037	1064	1111	953	995	1004	1089	1121	1143
		75	799	847	850	847	864	878	867	898	876	841	859	861
		100	702	708	711	710	723	703	690	703	699	702	712	684
		%MC	LBS	NLBS	NBS	LBS	NLBS	NBS	LBS	NLBS	NBS	LBS	NLBS	NBS
ABD	10 LB	0	317	358	387	123	149	91	211	236	184	157	196	135
		25	188	206	213	114	127	81	295	318	257	118	142	102
		50	97	86	102	107	114	79	91	83	93	102	111	83
		75	68	117	44	102	108	69	37	75	47	92	97	64
		100	89	119	117	80	84	53	239	209	171	30	32	19
	30 LB	0	403	455	420	132	151	106	484	439	361	170	211	148
		25	208	212	238	114	125	83	240	256	221	114	135	92
		50	89	99	108	107	113	91	181	189	146	105	115	92
		75	132	174	145	89	94	67	288	304	224	36	42	19
		100	80	72	45	92	93	63	152	113	65	49	50	16

Table 13: Muscle forces for all subject #2 model variations.

			DSX - SUP			RHY - SUP			DSX - UP			RHY - UP		
		%MC	LBS	NLBS	NBS	LBS	NLBS	NBS	LBS	NLBS	NBS	LBS	NLBS	NBS
MF	10 LB	0	774	838	856	446	472	477	1058	983	854	472	495	496
		25	329	344	354	389	409	418	384	410	373	398	416	401
		50	376	478	410	345	355	350	478	498	367	364	372	345
		75	220	273	267	233	232	216	368	311	250	229	227	201
		100	230	183	165	132	124	81	292	218	126	162	153	94
	30 LB	0	605	683	734	660	687	682	745	730	728	624	648	635
		25	593	705	766	541	562	555	724	756	749	531	550	536
		50	477	555	580	475	491	476	622	583	520	500	515	478
		75	369	381	373	413	420	407	379	373	356	413	419	387
		100	395	428	420	359	358	340	460	414	389	334	333	307
LT	10 LB	0	713	778	922	822	845	882	439	716	948	901	920	947
		25	788	860	865	744	767	774	1139	1217	1263	766	783	744
		50	636	695	841	642	655	664	653	709	854	682	692	647
		75	410	484	517	463	462	445	451	472	528	514	511	464
		100	504	369	330	248	231	213	699	475	401	341	321	285
	30 LB	0	1103	1161	1249	1210	1230	1280	991	1137	1247	1179	1197	1243
		25	1211	1368	1426	1009	1031	1062	1282	1370	1448	1030	1049	1076
		50	820	889	939	871	889	919	863	943	1037	900	915	896
		75	801	874	893	781	792	811	1008	1032	959	813	820	796
		100	726	749	760	724	723	711	832	869	875	765	763	725
IL	10 LB	0	490	539	524	639	649	683	431	414	404	767	785	821
		25	600	637	686	493	500	535	275	254	280	612	625	621
		50	211	114	140	366	375	394	33	17	33	526	536	508
		75	255	135	136	211	210	219	131	164	176	302	300	290
		100	196	129	160	87	80	81	182	107	114	100	91	109
	30 LB	0	835	775	797	954	964	1007	845	844	747	1024	1044	1082
		25	507	400	421	766	776	802	421	448	451	867	882	905
		50	619	528	507	633	641	648	428	433	420	761	773	732
		75	679	730	727	517	523	528	719	673	660	688	695	658
		100	496	505	506	375	375	384	407	322	338	498	497	492
ABD	10 LB	0	202	314	373	170	172	97	102	293	358	191	191	100
		25	219	264	204	186	188	116	42	47	48	259	257	95
		50	384	668	770	183	183	97	509	704	740	305	306	125
		75	112	62	73	159	159	62	1	1	1	195	195	50
		100	189	129	54	137	141	41	49	36	5	155	159	38
	30 LB	0	213	205	159	214	217	151	383	473	436	207	208	132
		25	94	59	68	200	202	119	109	139	178	202	202	111
		50	132	95	86	203	205	108	31	9	7	311	312	136
		75	208	235	134	205	205	105	220	196	46	311	312	145
		100	194	216	122	190	190	88	101	41	1	221	221	79

Table 14: Muscle forces for all subject #3 model variations.

Muscle	Load	%MC	DSX - SUP LBS	DSX - SUP NLBS	DSX - SUP NBS	RHY - SUP LBS	RHY - SUP NLBS	RHY - SUP NBS	DSX - UP LBS	DSX - UP NLBS	DSX - UP NBS	RHY - UP LBS	RHY - UP NLBS	RHY - UP NBS
MF	10 LB	0	619	672	714	578	622	606	593	683	702	581	618	594
		25	337	382	415	353	389	367	338	399	420	361	390	359
		50	319	346	346	313	341	304	302	353	347	321	343	297
		75	359	412	366	279	301	254	365	420	355	266	284	240
		100	344	314	294	230	247	196	271	301	280	195	205	167
	30 LB	0	869	923	990	721	769	761	826	936	993	718	761	744
		25	655	718	737	623	663	648	676	742	737	625	658	635
		50	473	502	499	505	534	513	518	526	500	515	539	501
		75	467	507	489	423	445	396	451	507	487	401	418	373
		100	459	455	408	361	376	312	452	518	430	402	409	325

Muscle	Load	%MC	DSX - SUP LBS	DSX - SUP NLBS	DSX - SUP NBS	RHY - SUP LBS	RHY - SUP NLBS	RHY - SUP NBS	DSX - UP LBS	DSX - UP NLBS	DSX - UP NBS	RHY - UP LBS	RHY - UP NLBS	RHY - UP NBS
LT	10 LB	0	817	874	1003	948	950	1091	791	869	990	919	933	1038
		25	471	524	648	547	564	675	460	530	655	540	561	644
		50	419	463	584	439	462	574	398	462	585	449	470	552
		75	499	590	676	352	375	482	559	642	716	333	350	425
		100	155	295	355	284	303	390	323	391	373	310	322	362
	30 LB	0	1073	1130	1296	1234	1223	1383	1043	1127	1310	1178	1180	1306
		25	966	1046	1194	1041	1054	1173	982	1059	1195	1008	1029	1120
		50	685	726	864	801	824	928	700	740	870	796	819	901
		75	539	596	748	600	623	735	515	592	748	532	551	641
		100	686	767	899	471	488	593	707	785	896	606	616	697

Muscle	Load	%MC	DSX - SUP LBS	DSX - SUP NLBS	DSX - SUP NBS	RHY - SUP LBS	RHY - SUP NLBS	RHY - SUP NBS	DSX - UP LBS	DSX - UP NLBS	DSX - UP NBS	RHY - UP LBS	RHY - UP NLBS	RHY - UP NBS
IL	10 LB	0	914	1017	1016	945	949	987	955	1026	1001	1012	1036	1050
		25	527	572	592	585	594	606	550	582	592	609	632	637
		50	483	504	484	519	528	508	467	489	472	504	523	516
		75	418	429	377	450	460	421	268	301	297	431	448	407
		100	185	177	179	356	366	332	185	201	189	305	318	301
	30 LB	0	1077	1195	1226	1200	1209	1262	1153	1216	1178	1288	1316	1341
		25	1094	1151	1131	1038	1046	1070	1140	1169	1130	1107	1131	1135
		50	930	963	945	837	849	838	933	964	939	840	860	854
		75	614	603	567	680	692	653	605	583	550	638	653	628
		100	224	248	217	545	555	505	227	212	199	307	315	327

Muscle	Load	%MC	DSX - SUP LBS	DSX - SUP NLBS	DSX - SUP NBS	RHY - SUP LBS	RHY - SUP NLBS	RHY - SUP NBS	DSX - UP LBS	DSX - UP NLBS	DSX - UP NBS	RHY - UP LBS	RHY - UP NLBS	RHY - UP NBS
ABD	10 LB	0	159	135	92	90	103	105	133	157	96	118	135	129
		25	109	93	123	66	70	74	20	38	126	67	78	75
		50	141	98	121	64	66	58	8	39	123	51	56	56
		75	52	87	57	60	62	48	61	67	38	42	45	23
		100	16	21	13	49	50	32	5	7	2	34	34	5
	30 LB	0	360	255	279	101	112	120	171	180	230	142	164	160
		25	101	129	120	106	112	122	151	153	119	107	120	118
		50	68	78	94	97	100	106	86	90	87	69	73	85
		75	325	266	331	83	84	76	123	216	348	9	13	38
		100	63	67	66	76	76	59	18	19	18	16	16	12

Table 15: Differences in SI JRF due to input kinematics (DSX-RHY) – Subject #1.

SUPINE

		LBS				NLBS				NBS			
	%MC	L23	L34	L45	L51	L23	L34	L45	L51	L23	L34	L45	L51
10 LB	0	524.0	1125.8	102.4	-102.4	296.0	1054.6	148.3	-46.3	589.4	1149.3	-132.2	-356.8
	25	86.0	4.8	11.6	-132.6	-63.0	-42.8	78.9	-56.4	172.3	31.6	-31.1	-178.5
	50	123.6	-12.8	46.6	-89.6	41.6	-75.3	15.5	-118.9	183.6	-47.0	-82.3	-214.4
	75	205.1	63.1	146.4	29.2	54.6	51.9	163.6	62.0	161.0	107.3	143.6	52.7
	100	-22.0	-132.6	113.9	-12.5	-35.6	-255.1	-64.0	-182.0	-20.0	-306.2	-202.8	-333.5
30 LB	0	1209.0	1047.7	155.1	-88.6	659.4	1077.0	342.7	119.4	948.8	1247.6	114.5	-151.2
	25	252.1	182.1	150.5	-67.7	82.7	184.9	237.4	30.2	282.1	214.0	61.2	-159.6
	50	599.1	71.9	126.5	-93.0	420.1	-4.6	140.5	-74.2	548.4	18.9	84.3	-127.4
	75	162.0	36.4	14.3	-178.9	5.8	-72.7	-119.2	-306.4	102.0	-30.4	-191.9	-367.5
	100	-11.6	-114.7	43.2	-135.7	16.0	-93.8	-20.2	-198.4	51.8	-117.1	-105.9	-231.4

UPRIGHT

		LBS				NLBS				NBS			
	%MC	L23	L34	L45	L51	L23	L34	L45	L51	L23	L34	L45	L51
10 LB	0	395.1	955.4	-111.9	-175.6	239.2	953.5	-80.5	-145.0	415.5	959.9	-288.9	-389.9
	25	28.8	-53.5	30.2	35.9	0.4	-28.2	34.5	41.4	150.3	-27.4	-28.0	-32.7
	50	51.8	-60.8	-54.9	-34.2	47.4	-107.9	-57.2	-37.2	115.0	-130.9	-108.4	-93.6
	75	304.8	80.6	181.2	209.5	92.1	44.7	161.0	202.4	79.7	17.2	99.5	142.1
	100	-404.5	-548.4	-370.7	-322.1	-265.4	-538.8	-348.6	-310.4	-192.6	-511.3	-354.4	-353.3
30 LB	0	963.9	793.0	-64.9	-133.2	526.8	909.0	73.5	6.1	687.6	979.1	-80.0	-166.0
	25	160.3	80.2	76.0	48.2	25.2	98.5	87.1	65.5	143.3	59.1	-24.6	-55.8
	50	426.5	-76.5	61.8	41.9	357.9	-112.1	57.9	41.0	447.5	-106.4	16.1	-6.3
	75	-79.3	-223.9	-286.3	-259.0	-134.4	-247.1	-327.6	-296.5	-49.7	-204.5	-327.4	-303.9
	100	-121.7	-266.2	-246.9	-195.8	-91.6	-230.1	-205.4	-157.0	-97.9	-277.2	-234.4	-196.2

Table 16: Differences in AP JRF due to input kinematics (DSX-RHY) – Subject #1.

SUPINE

		LBS				NLBS				NBS			
	%MC	L23	L34	L45	L51	L23	L34	L45	L51	L23	L34	L45	L51
10 LB	0	81.4	231.9	-137.5	-594.4	101.7	256.9	-93.7	-577.0	89.0	252.9	-111.7	-592.6
	25	83.0	140.4	-56.2	-337.6	106.5	174.5	-17.8	-321.3	87.8	141.8	-70.4	-388.1
	50	30.7	95.4	-52.4	-259.9	40.7	108.7	-36.6	-253.3	24.8	82.1	-67.3	-290.3
	75	33.1	131.6	-30.2	-236.5	49.7	157.0	-11.7	-234.7	24.4	118.7	-32.2	-259.2
	100	-21.7	31.9	-141.6	-392.4	-31.2	8.0	-124.8	-367.9	-33.6	-2.5	-69.2	-216.8
30 LB	0	-2.5	170.8	-310.4	-882.9	38.7	225.5	-229.4	-829.9	31.6	223.0	-260.2	-892.5
	25	56.3	145.2	-133.8	-555.1	72.7	176.2	-106.7	-550.6	63.3	143.1	-141.0	-595.3
	50	30.4	121.1	-128.7	-455.3	70.7	178.2	-71.3	-414.3	55.5	150.0	-87.3	-445.7
	75	7.5	73.7	-99.3	-405.0	26.0	91.3	-68.2	-381.1	15.5	73.6	-31.3	-299.1
	100	24.7	119.3	15.9	-190.3	8.0	87.4	4.4	-198.7	-5.6	52.3	16.1	-162.0

UPRIGHT

		LBS				NLBS				NBS			
	%MC	L23	L34	L45	L51	L23	L34	L45	L51	L23	L34	L45	L51
10 LB	0	49.7	51.9	-224.4	-239.3	75.0	81.4	-190.4	-209.4	50.2	65.4	-203.2	-196.1
	25	63.6	-4.8	-149.5	-56.8	66.3	-1.3	-154.8	-58.5	43.1	-28.5	-178.4	-85.8
	50	-1.9	-49.6	-157.3	-42.1	-9.0	-60.3	-166.0	-47.1	-22.6	-77.5	-168.9	-46.6
	75	-22.0	-33.1	-163.6	-98.5	-12.2	-17.5	-144.2	-78.0	-15.5	-21.5	-120.1	-49.5
	100	-4.5	-33.1	-62.0	21.6	-41.2	-85.2	-124.1	-46.8	-52.3	-85.5	-90.1	6.1
30 LB	0	-69.2	-82.9	-468.1	-487.3	-21.3	-26.5	-389.9	-415.3	-38.2	-26.3	-384.8	-423.0
	25	0.7	-69.0	-274.0	-217.1	10.5	-53.7	-267.2	-211.6	-1.8	-79.3	-269.1	-218.6
	50	10.5	-45.1	-219.9	-123.0	21.0	-32.6	-209.1	-110.5	7.3	-41.6	-197.5	-112.2
	75	-14.7	-79.6	-149.3	-45.6	-7.6	-75.4	-142.1	-33.6	-6.3	-59.3	-83.1	4.9
	100	-30.3	-83.7	-67.3	84.1	-38.4	-92.5	-85.1	59.9	-20.4	-53.2	-13.6	103.5

Table 17: Differences in SI JRF due to input kinematics (DSX-RHY) – Subject #2.

SUPINE

		LBS				NLBS				NBS			
	%MC	L23	L34	L45	L51	L23	L34	L45	L51	L23	L34	L45	L51
10 LB	0	276.0	134.6	-10.6	-192.6	267.8	151.5	-38.0	-206.3	249.1	95.7	-196.5	-335.1
	25	-132.8	-15.5	178.7	-65.0	-258.0	-79.6	188.3	-65.8	-335.1	-172.7	62.9	-124.7
	50	382.6	486.6	377.3	149.0	479.1	822.6	467.5	183.2	223.5	604.4	163.3	-53.2
	75	125.8	211.6	417.9	187.6	203.4	182.9	555.0	251.8	-37.2	-89.7	282.6	74.1
	100	-391.8	-308.7	-330.1	-333.1	-134.7	-177.1	-140.4	-180.7	-189.4	-191.8	-29.1	-63.7
30 LB	0	846.6	1257.0	722.5	291.4	962.9	1443.4	694.9	185.1	916.4	1355.0	512.8	-10.9
	25	272.8	622.8	269.0	-77.8	293.7	789.0	272.2	-145.7	135.9	626.9	9.9	-395.0
	50	148.6	89.7	396.8	73.1	310.3	161.9	551.0	162.0	175.7	-36.0	332.0	4.5
	75	-197.4	-109.9	-32.2	-253.0	-304.5	-167.9	-67.1	-290.6	-292.1	-144.1	-84.4	-251.0
	100	-113.1	-172.3	-152.9	-309.3	-167.1	-274.5	-200.3	-353.8	-242.1	-340.9	-260.9	-355.6

UPRIGHT

		LBS				NLBS				NBS			
	%MC	L23	L34	L45	L51	L23	L34	L45	L51	L23	L34	L45	L51
10 LB	0	731.8	473.1	226.9	190.8	581.2	422.1	247.7	310.7	417.0	304.6	85.9	261.1
	25	335.9	536.0	645.0	297.6	313.9	550.0	714.3	278.1	54.1	255.0	388.4	-40.3
	50	753.4	1156.2	867.1	707.8	804.0	1219.3	844.3	713.4	351.0	741.7	360.6	321.0
	75	583.2	334.7	565.4	393.2	449.1	353.5	706.8	511.6	68.8	-5.9	353.8	223.6
	100	-283.5	-222.7	-70.3	17.1	-15.0	-48.4	29.6	58.9	-71.4	-90.0	46.2	39.4
30 LB	0	1351.4	1464.7	622.9	283.5	1034.3	1401.2	597.7	227.1	889.3	1269.9	430.8	75.0
	25	507.2	1009.1	450.1	145.6	452.4	965.0	383.8	50.9	327.4	791.8	155.0	-153.9
	50	914.2	605.5	878.4	501.1	787.8	632.2	978.1	557.4	415.3	268.5	615.2	259.6
	75	-117.0	83.2	181.1	21.0	-40.5	144.2	260.8	67.7	-57.2	74.8	140.4	-0.3
	100	217.2	28.1	90.6	27.2	337.8	230.8	313.1	174.2	90.4	-6.8	57.1	-62.9

Table 18: Differences in AP JRF due to input kinematics (DSX-RHY) – Subject #2.

SUPINE

		LBS				NLBS				NBS			
	%MC	L23	L34	L45	L51	L23	L34	L45	L51	L23	L34	L45	L51
10 LB	0	-30.9	-60.3	-246.2	-463.9	-43.3	-76.0	-274.7	-493.9	-54.5	-87.9	-240.4	-420.2
	25	36.6	58.9	-117.6	-343.9	55.4	83.2	-104.6	-335.4	58.2	90.1	-47.2	-235.6
	50	-78.7	-158.2	-361.8	-644.4	-113.4	-198.1	-510.6	-796.5	-86.2	-150.3	-380.3	-573.9
	75	-1.9	-17.7	-209.6	-424.1	-29.8	-52.4	-322.9	-559.4	-39.6	-21.6	-179.4	-337.2
	100	-7.6	23.1	114.5	131.8	15.3	19.6	33.1	-13.2	23.7	54.0	14.3	-36.8
30 LB	0	-131.2	-153.5	-542.5	-1057.7	-154.0	-178.5	-607.8	-1103.3	-159.1	-188.8	-594.1	-1032.1
	25	-95.2	-157.6	-410.3	-745.5	-127.0	-194.0	-492.4	-816.1	-117.2	-179.7	-417.4	-659.4
	50	24.9	10.1	-206.5	-520.8	-3.5	-34.6	-300.3	-630.2	-2.9	-22.6	-199.7	-460.5
	75	37.0	57.7	-17.6	-243.3	50.2	74.8	4.9	-212.9	34.9	53.4	8.2	-163.5
	100	10.5	17.8	1.2	-167.2	18.6	34.0	31.3	-121.4	13.4	35.4	58.7	-35.1

UPRIGHT

		LBS				NLBS				NBS			
	%MC	L23	L34	L45	L51	L23	L34	L45	L51	L23	L34	L45	L51
10 LB	0	-82.1	-3.4	-189.0	-327.8	-90.8	-23.6	-202.2	-381.3	-107.7	-40.1	-164.8	-354.7
	25	-132.8	-90.7	-347.6	-592.0	-141.9	-96.0	-388.0	-652.1	-130.7	-84.2	-298.5	-445.9
	50	-110.5	-157.4	-487.7	-818.4	-122.0	-169.9	-527.9	-874.7	-89.4	-116.4	-346.3	-563.1
	75	-25.3	-45.3	-223.3	-418.5	-2.0	10.5	-226.2	-467.3	0.6	47.9	-89.2	-218.7
	100	37.0	92.5	104.3	62.6	9.4	31.6	13.6	-43.7	18.6	54.3	20.3	-21.4
30 LB	0	-176.2	-90.9	-423.7	-678.6	-173.8	-75.4	-407.1	-663.0	-158.9	-67.0	-359.2	-588.1
	25	-141.0	-98.7	-353.3	-552.0	-150.0	-107.3	-362.9	-546.0	-147.0	-105.7	-303.6	-452.7
	50	-113.8	-105.4	-365.0	-606.4	-110.1	-86.4	-377.2	-640.3	-112.8	-69.4	-266.0	-458.7
	75	19.8	98.5	16.4	-145.6	7.2	79.4	-27.7	-205.9	8.8	72.2	11.7	-105.3
	100	2.0	33.0	-1.4	-152.4	-2.8	-5.3	-118.4	-341.1	-12.3	5.7	-32.0	-104.4

Table 19: Differences in SI JRF due to input kinematics (DSX-RHY) – Subject #3.

SUPINE		LBS				NLBS				NBS			
	%MC	L23	L34	L45	L51	L23	L34	L45	L51	L23	L34	L45	L51
10 LB	0	381.6	129.0	89.0	-37.4	185.9	21.9	-31.2	-194.4	386.0	148.8	-72.2	-205.5
	25	259.0	335.7	147.7	19.3	176.0	287.4	85.9	-44.1	241.5	281.0	-15.5	-119.8
	50	157.3	325.3	176.8	47.6	118.3	292.4	126.4	-2.1	135.3	237.6	25.5	-66.0
	75	35.5	232.6	45.1	-131.2	-74.9	120.8	-99.0	-273.4	4.7	124.9	-113.5	-250.3
	100	613.3	161.0	200.5	-45.2	504.2	174.6	186.0	-100.9	467.9	106.9	33.6	-159.8
30 LB	0	605.3	639.2	9.2	-81.0	400.7	486.3	-127.4	-246.3	609.9	586.1	-217.1	-315.9
	25	249.9	126.2	-81.3	-278.6	124.4	82.7	-195.6	-403.0	272.0	189.0	-216.0	-430.7
	50	77.6	207.6	63.5	-148.5	30.2	164.3	26.5	-187.0	53.7	160.7	-39.6	-227.7
	75	267.1	127.9	59.1	-103.2	258.4	173.6	38.5	-132.0	194.6	89.7	-98.1	-226.3
	100	113.3	491.2	424.6	101.4	131.9	491.5	389.2	59.0	-15.8	286.2	87.9	-184.9

UPRIGHT		LBS				NLBS				NBS			
	%MC	L23	L34	L45	L51	L23	L34	L45	L51	L23	L34	L45	L51
10 LB	0	298.8	76.5	105.8	84.6	219.7	-7.9	-58.3	-79.1	347.1	86.1	-67.9	-64.2
	25	210.9	237.4	123.2	102.8	181.3	233.0	41.5	26.8	171.6	194.9	-56.6	-33.5
	50	140.8	228.9	136.0	140.4	100.7	224.2	72.9	91.5	68.0	158.7	-14.7	22.3
	75	-79.9	49.4	-18.7	-116.9	-127.6	36.5	-119.2	-220.7	-68.5	52.5	-148.4	-238.3
	100	391.0	82.8	125.2	-48.2	420.3	86.2	77.3	-142.0	381.1	32.1	-42.1	-185.6
30 LB	0	503.8	496.7	35.6	85.5	439.2	452.1	-115.7	-60.3	539.2	491.8	-201.8	-102.9
	25	138.4	7.9	-131.8	-152.6	135.5	24.6	-213.5	-232.7	224.7	120.2	-199.2	-231.0
	50	2.6	45.2	-84.6	-91.3	-50.5	18.3	-96.6	-100.8	-54.6	32.0	-109.3	-115.5
	75	76.6	-52.4	-86.3	-99.4	56.4	-51.0	-155.2	-152.0	24.9	-73.1	-205.6	-205.8
	100	69.1	237.1	134.8	134.2	65.8	284.0	119.9	91.2	-84.1	149.8	-61.4	-158.5

Table 20: Differences in AP JRF due to input kinematics (DSX-RHY) – Subject #3.

SUPINE		LBS				NLBS				NBS			
	%MC	L23	L34	L45	L51	L23	L34	L45	L51	L23	L34	L45	L51
10 LB	0	-79.9	16.7	-88.8	-309.5	-67.9	22.3	-98.8	-316.1	-80.5	1.4	-107.1	-325.0
	25	-43.6	25.1	-76.4	-263.4	-35.2	32.8	-66.3	-254.5	-50.2	4.5	-85.2	-263.7
	50	-12.8	45.6	-50.3	-241.9	-10.0	48.4	-38.8	-228.4	-17.5	23.7	-48.7	-216.8
	75	-19.1	21.4	-62.2	-224.7	-16.1	25.7	-39.0	-181.8	-16.6	3.3	-48.7	-180.4
	100	-43.0	-11.8	-134.3	-322.2	-45.0	-38.0	-184.0	-378.2	-37.2	-36.4	-112.8	-264.3
30 LB	0	-138.9	-18.0	-216.2	-528.5	-125.6	-10.7	-216.0	-518.0	-155.2	-50.0	-255.4	-507.2
	25	-101.5	42.0	-83.8	-351.0	-97.5	43.9	-82.2	-339.8	-125.7	0.5	-125.7	-382.0
	50	-47.9	117.2	16.7	-240.7	-45.3	122.2	26.2	-234.9	-59.9	77.5	0.0	-239.2
	75	-57.6	64.9	11.4	-250.9	-62.0	50.7	-3.4	-266.6	-67.7	13.6	-17.2	-222.9
	100	-54.9	-32.3	-238.6	-563.6	-66.0	-48.4	-256.1	-603.9	-68.5	-68.4	-156.6	-348.1

UPRIGHT		LBS				NLBS				NBS			
	%MC	L23	L34	L45	L51	L23	L34	L45	L51	L23	L34	L45	L51
10 LB	0	-81.4	-48.0	-200.2	-174.4	-81.9	-54.6	-200.0	-148.2	-89.0	-65.6	-182.5	-125.8
	25	-40.6	-20.7	-137.0	-135.4	-51.1	-35.5	-147.4	-132.4	-52.3	-43.0	-129.7	-101.5
	50	-13.0	3.5	-88.6	-114.1	-14.3	-3.6	-88.8	-106.2	-15.2	-11.1	-76.7	-83.3
	75	-44.8	-61.2	-166.3	-173.4	-49.4	-73.7	-173.8	-162.9	-38.6	-57.9	-113.3	-97.8
	100	-13.3	-53.6	-208.7	-275.1	-15.0	-65.9	-229.1	-307.7	-32.1	-61.4	-129.2	-155.3
30 LB	0	-151.8	-112.6	-342.0	-300.8	-155.4	-121.8	-353.5	-290.6	-168.5	-142.8	-339.0	-190.3
	25	-107.6	-39.1	-189.4	-136.7	-122.7	-59.7	-207.7	-140.6	-136.7	-81.0	-216.0	-149.8
	50	-57.7	34.2	-54.7	-33.9	-54.6	40.2	-47.5	-25.8	-59.1	20.9	-48.2	-23.7
	75	-68.9	-15.6	-59.3	-59.3	-78.7	-38.0	-70.4	-59.9	-80.1	-46.8	-65.0	-41.9
	100	-33.8	-43.6	-158.4	-333.6	-26.6	-46.7	-169.3	-365.5	-53.6	-63.8	-115.1	-130.6

Table 21: Differences in SI JRF due to stiffness properties (LBS-NBS) – Subject #1.

SUPINE

		DSX				RHY			
	%MC	L23	L34	L45	L51	L23	L34	L45	L51
10 LB	0	228.2	263.2	458.8	301.5	293.6	286.7	224.1	47.1
	25	142.3	194.2	215.5	47.6	228.6	220.9	172.8	1.7
	50	108.5	197.9	258.2	96.5	168.5	163.7	129.4	-28.3
	75	96.2	-8.3	1.9	-164.4	52.1	36.0	-0.9	-140.8
	100	-102.0	50.3	145.8	60.4	-100.0	-123.2	-170.9	-260.5
30 LB	0	555.4	72.7	223.9	134.5	295.2	272.6	183.2	71.9
	25	200.6	169.8	216.7	80.9	230.6	201.6	127.4	-11.1
	50	171.4	147.3	88.7	-17.3	120.7	94.2	46.4	-51.8
	75	-78.6	-104.9	-39.9	-146.9	-138.5	-171.8	-246.1	-335.4
	100	-422.2	-388.1	-317.7	-417.0	-358.8	-390.6	-466.8	-512.8

UPRIGHT

		DSX				RHY			
	%MC	L23	L34	L45	L51	L23	L34	L45	L51
10 LB	0	234.3	239.5	358.0	216.3	254.7	244.0	181.1	2.0
	25	71.6	154.9	192.1	24.2	193.0	181.0	133.8	-44.4
	50	67.6	191.4	142.1	-21.2	130.7	121.3	88.6	-80.7
	75	239.3	58.4	43.2	-133.5	14.2	-5.1	-38.5	-200.8
	100	-328.9	-170.8	-188.9	-276.0	-117.0	-133.7	-172.5	-307.3
30 LB	0	531.0	46.6	150.2	57.6	254.8	232.7	135.1	24.8
	25	204.9	180.6	180.0	41.2	187.8	159.5	79.4	-62.9
	50	55.8	77.9	46.7	-56.5	76.8	47.9	1.0	-104.7
	75	-230.5	-251.3	-254.0	-373.7	-200.8	-231.9	-295.0	-418.6
	100	-443.5	-433.3	-518.5	-607.1	-419.8	-444.4	-506.0	-607.6

Table 22: Differences in AP JRF due to stiffness properties (LBS-NBS) – Subject #1.

SUPINE

		DSX				RHY			
	%MC	L23	L34	L45	L51	L23	L34	L45	L51
10 LB	0	-18.8	18.3	-55.0	207.8	-11.2	39.3	-29.3	209.6
	25	-24.2	17.3	-21.5	249.3	-19.5	18.8	-35.7	198.8
	50	-22.7	9.8	-31.8	197.7	-28.7	-3.4	-46.7	167.3
	75	-14.4	6.1	-11.3	237.8	-23.1	-6.8	-13.3	215.1
	100	-13.2	25.4	-24.5	95.3	-25.1	-9.0	47.9	270.8
30 LB	0	-49.3	-21.2	-66.6	117.7	-15.2	31.0	-16.5	108.1
	25	-27.7	20.8	-3.8	222.6	-20.7	18.7	-11.0	182.3
	50	-52.0	-27.8	-61.0	113.3	-26.9	1.0	-19.6	122.8
	75	-37.3	-9.9	2.5	224.8	-29.2	-10.0	70.5	330.7
	100	-21.2	47.6	144.0	422.7	-51.6	-19.3	144.1	451.1

UPRIGHT

		DSX				RHY			
	%MC	L23	L34	L45	L51	L23	L34	L45	L51
10 LB	0	-17.0	13.2	-45.3	212.7	-16.5	26.7	-24.0	255.9
	25	-1.5	34.0	-0.4	271.4	-22.0	10.4	-29.4	242.4
	50	-7.9	20.1	-25.5	218.6	-28.5	-7.8	-37.1	214.0
	75	-27.5	-13.7	-40.0	206.5	-21.0	-2.1	3.5	255.4
	100	25.3	60.6	96.4	302.8	-22.5	8.2	68.3	287.3
30 LB	0	-53.5	-35.0	-92.5	92.4	-22.5	21.5	-9.2	156.7
	25	-22.9	22.5	-5.3	224.4	-25.4	12.3	-0.4	222.9
	50	-24.1	2.0	-23.3	154.5	-27.3	5.6	-1.0	165.3
	75	-23.4	4.3	56.8	324.0	-15.0	24.6	122.9	374.5
	100	-38.2	10.0	165.5	473.7	-28.3	40.5	219.2	493.1

Table 23: Differences in SI JRF due to stiffness properties (LBS-NBS) – Subject #2.

SUPINE

		DSX				RHY			
	%MC	L23	L34	L45	L51	L23	L34	L45	L51
10 LB	0	22.4	31.9	119.3	63.2	-4.5	-7.0	-66.6	-79.2
	25	124.0	83.8	-2.0	-36.2	-78.3	-73.4	-117.9	-95.9
	50	-48.4	-333.7	-33.4	-2.9	-207.5	-215.9	-247.4	-205.1
	75	-130.0	-0.2	-192.2	-182.2	-293.1	-301.5	-327.5	-295.7
	100	-588.2	-502.9	-711.1	-609.7	-385.9	-386.0	-410.1	-340.3
30 LB	0	-47.6	-70.3	200.6	227.1	22.2	27.7	-9.1	-75.1
	25	51.0	-105.2	107.9	158.6	-86.0	-101.1	-151.3	-158.7
	50	-183.1	-55.3	-170.3	-139.2	-156.0	-181.0	-235.1	-207.8
	75	-185.5	-275.5	-289.6	-299.4	-280.2	-309.7	-341.9	-297.3
	100	-258.7	-241.7	-304.2	-323.0	-387.7	-410.3	-412.1	-369.3

UPRIGHT

		DSX				RHY			
	%MC	L23	L34	L45	L51	L23	L34	L45	L51
10 LB	0	288.1	140.2	65.3	-144.5	-26.6	-28.3	-75.6	-74.2
	25	49.7	53.0	10.8	122.9	-232.1	-228.0	-245.8	-215.1
	50	18.5	19.4	108.5	31.2	-383.9	-395.1	-398.0	-355.6
	75	96.2	-84.7	-219.4	-246.1	-418.2	-425.3	-431.1	-415.7
	100	-669.4	-587.4	-596.6	-461.8	-457.3	-454.7	-480.0	-439.5
30 LB	0	434.4	150.2	118.2	102.9	-27.7	-44.5	-73.9	-105.6
	25	58.0	67.8	102.7	115.3	-121.8	-149.4	-192.4	-184.2
	50	154.9	-34.5	-120.2	-106.7	-344.0	-371.5	-383.5	-348.2
	75	-521.1	-486.8	-449.3	-427.9	-461.2	-495.2	-490.0	-449.2
	100	-349.1	-462.0	-453.7	-386.9	-475.9	-496.8	-487.2	-476.9

Table 24: Differences in AP JRF due to stiffness properties (LBS-NBS) – Subject #2.

SUPINE

		DSX				RHY			
	%MC	L23	L34	L45	L51	L23	L34	L45	L51
10 LB	0	11.4	28.3	42.5	93.4	-12.2	0.8	48.2	137.1
	25	-29.5	-25.3	-0.3	45.4	-7.9	5.9	70.1	153.7
	50	1.7	25.3	160.9	233.3	-5.7	33.1	142.4	303.8
	75	27.1	44.5	147.1	335.0	-10.6	40.6	177.3	421.9
	100	-51.9	17.7	323.2	654.7	-20.6	48.5	223.0	486.1
30 LB	0	12.9	28.8	58.2	116.5	-15.0	-6.4	6.5	142.1
	25	20.6	33.2	86.3	121.2	-1.4	11.1	79.2	207.3
	50	27.8	60.1	127.0	217.6	0.0	27.3	133.8	277.9
	75	7.6	62.3	177.7	357.2	5.6	58.0	203.6	437.1
	100	-12.3	42.0	163.6	391.8	-9.4	59.6	221.1	523.9

UPRIGHT

		DSX				RHY			
	%MC	L23	L34	L45	L51	L23	L34	L45	L51
10 LB	0	21.9	42.2	24.6	144.8	-3.7	5.6	48.9	117.9
	25	3.7	9.5	43.8	49.4	5.9	16.0	92.9	195.6
	50	-16.4	1.5	22.4	90.1	4.7	42.4	163.8	345.4
	75	-28.8	-48.2	53.9	248.9	-2.9	45.1	188.0	448.7
	100	1.6	79.8	300.6	556.9	-16.7	41.6	216.6	472.9
30 LB	0	-8.6	-9.3	-31.0	74.7	8.6	14.6	33.6	165.1
	25	19.8	29.5	39.3	102.8	13.8	22.5	89.0	202.1
	50	-1.8	-11.5	32.8	134.3	-0.8	24.5	131.9	282.0
	75	15.3	80.7	204.0	397.1	4.3	54.4	199.3	437.3
	100	3.4	71.9	225.7	443.3	-10.9	44.6	195.1	491.3

Table 25: Differences in SI JRF due to stiffness properties (LBS-NBS) – Subject #3.

SUPINE

		DSX				RHY			
	%MC	L23	L34	L45	L51	L23	L34	L45	L51
10 LB	0	132.2	155.4	279.8	176.2	136.7	175.2	118.6	8.1
	25	78.1	148.3	196.0	84.2	60.6	93.6	32.9	-54.9
	50	-37.8	34.0	22.6	-62.4	-59.7	-53.7	-128.7	-176.0
	75	-120.0	-55.6	-84.9	-137.5	-150.8	-163.3	-243.6	-256.5
	100	-110.4	-221.2	-180.0	-214.0	-255.8	-275.3	-346.9	-328.6
30 LB	0	154.7	255.2	376.3	264.3	159.3	202.1	150.1	29.4
	25	50.3	37.9	172.7	91.7	72.4	100.8	38.0	-60.4
	50	-42.5	-14.4	-23.0	-102.7	-66.4	-61.2	-126.1	-181.8
	75	-188.6	-241.4	-195.0	-238.8	-261.1	-279.6	-352.1	-361.8
	100	-370.3	-327.2	-270.0	-273.5	-499.4	-532.2	-606.6	-559.8

UPRIGHT

		DSX				RHY			
	%MC	L23	L34	L45	L51	L23	L34	L45	L51
10 LB	0	40.8	110.5	241.9	98.1	89.0	120.0	68.2	-50.8
	25	58.1	88.8	168.3	27.5	18.8	46.3	-11.5	-108.8
	50	9.1	18.0	29.5	-76.5	-63.7	-52.2	-121.2	-194.5
	75	-158.4	-151.2	-95.2	-160.6	-147.1	-148.1	-225.0	-282.0
	100	-266.5	-213.1	-150.6	-229.1	-276.4	-263.8	-317.8	-366.6
30 LB	0	72.0	148.4	333.7	157.8	107.4	143.6	96.4	-30.6
	25	-62.5	-65.7	55.6	-43.0	23.8	46.7	-11.8	-121.4
	50	-31.1	-68.9	-120.8	-200.6	-88.4	-82.2	-145.4	-224.8
	75	-160.4	-201.0	-167.2	-246.1	-212.1	-221.6	-286.5	-352.5
	100	-288.0	-365.5	-290.6	-239.5	-441.2	-452.8	-486.7	-532.2

Table 26: Differences in AP JRF due to stiffness properties (LBS-NBS) – Subject #3.

SUPINE

		DSX				RHY			
	%MC	L23	L34	L45	L51	L23	L34	L45	L51
10 LB	0	-36.6	-10.6	3.9	261.2	-37.2	-25.9	-14.3	245.7
	25	-47.4	-21.6	-5.1	252.1	-54.0	-42.2	-14.0	251.7
	50	-33.2	9.0	51.2	319.5	-37.9	-12.9	52.7	344.6
	75	-30.7	33.6	100.0	374.7	-28.2	15.6	113.5	419.0
	100	-25.1	65.5	145.0	433.5	-19.2	40.9	166.5	491.4
30 LB	0	-20.0	1.9	7.2	201.0	-36.4	-30.0	-32.1	222.3
	25	-21.9	5.8	33.0	286.2	-46.1	-35.6	-8.9	255.3
	50	-17.6	37.6	78.5	347.2	-29.6	-2.1	61.7	348.7
	75	-7.5	88.3	184.1	497.1	-17.6	37.0	155.5	525.2
	100	-21.1	97.0	176.9	471.8	-34.7	60.8	259.0	687.3

UPRIGHT

		DSX				RHY			
	%MC	L23	L34	L45	L51	L23	L34	L45	L51
10 LB	0	-30.6	-8.0	-16.6	248.0	-38.2	-25.6	1.2	296.6
	25	-42.9	-16.0	-2.3	265.1	-54.6	-38.4	5.0	299.0
	50	-42.8	2.7	47.5	323.7	-45.0	-11.9	59.4	354.5
	75	-45.5	18.6	68.0	341.3	-39.3	22.0	121.1	417.0
	100	-30.5	33.3	62.8	327.4	-49.3	25.5	142.2	447.2
30 LB	0	-20.1	0.4	-17.9	167.8	-36.8	-29.8	-14.9	278.4
	25	-16.9	11.9	39.5	317.5	-46.0	-30.0	12.9	304.3
	50	-26.1	24.6	78.9	367.0	-27.5	11.3	85.4	377.3
	75	-10.8	84.3	170.7	486.8	-22.0	53.1	164.9	504.2
	100	-26.6	80.6	171.9	377.1	-46.5	60.3	215.2	580.1

Table 27: Differences in SI JRF due to neutral state (SUP-UP) – Subject #1.

DSX

		LBS				NLBS				NBS			
	%MC	L23	L34	L45	L51	L23	L34	L45	L51	L23	L34	L45	L51
10 LB	0	105.2	135.4	278.5	297.8	112.0	119.6	290.8	310.8	85.8	99.2	316.1	334.6
	25	23.9	19.0	19.0	28.1	-3.5	36.9	121.5	130.8	-40.2	-18.6	100.5	111.0
	50	34.7	5.1	115.8	114.7	27.9	59.6	116.8	116.2	-10.0	-1.3	89.0	89.1
	75	-139.9	-64.0	-38.5	-22.7	-70.3	-59.0	-4.6	25.2	-69.1	-40.9	-3.7	16.0
	100	284.0	324.2	424.6	390.4	127.0	216.7	247.3	232.3	127.4	182.9	213.0	199.9
30 LB	0	174.3	179.1	262.9	277.1	159.9	158.9	322.0	338.7	118.8	127.2	338.2	359.8
	25	19.1	29.5	87.1	85.9	70.3	97.3	185.8	183.2	34.0	42.7	177.7	175.8
	50	97.4	67.2	48.1	41.1	26.0	65.4	114.1	108.7	13.6	33.6	67.6	62.6
	75	190.6	196.5	268.0	247.7	106.0	136.0	230.4	213.3	95.6	109.7	174.4	158.5
	100	-6.4	26.0	182.1	162.3	6.9	26.7	98.8	86.2	-11.9	-0.5	63.2	49.3

RHY

		LBS				NLBS				NBS			
	%MC	L23	L34	L45	L51	L23	L34	L45	L51	L23	L34	L45	L51
10 LB	0	-23.7	-35.0	64.1	224.6	29.1	-1.9	87.3	235.9	-62.6	-77.7	21.0	179.5
	25	-33.2	-39.3	37.7	196.7	23.1	-4.0	56.1	208.9	-68.8	-79.2	-1.3	150.6
	50	-37.1	-42.8	14.4	170.2	-4.2	-33.8	16.3	170.8	-74.9	-85.3	-26.4	117.8
	75	-40.2	-46.5	-3.6	157.5	-31.6	-48.1	-6.3	156.4	-78.1	-87.5	-41.2	97.6
	100	-98.5	-91.6	-60.0	80.9	-102.4	-100.7	-71.5	71.5	-115.5	-102.1	-61.6	34.1
30 LB	0	-70.8	-75.7	42.9	232.4	-13.8	-40.7	69.0	246.6	-111.2	-115.6	-5.2	185.3
	25	-72.6	-72.4	12.5	201.8	-23.5	-43.7	27.4	211.1	-115.4	-114.6	-35.5	150.0
	50	-75.1	-81.2	-16.7	176.0	-48.6	-73.8	-15.1	177.7	-118.9	-127.5	-62.1	123.1
	75	-50.8	-63.8	-32.7	167.6	-44.6	-64.7	-34.0	168.3	-113.1	-123.9	-81.6	84.4
	100	-116.4	-125.4	-108.0	102.2	-119.5	-136.8	-122.1	90.7	-177.3	-179.2	-147.2	7.4

Table 28: Differences in AP JRF due to neutral state (SUP-UP) – Subject #1.

DSX

		LBS				NLBS				NBS			
	%MC	L23	L34	L45	L51	L23	L34	L45	L51	L23	L34	L45	L51
10 LB	0	-48.4	-30.4	-60.1	-57.5	-55.8	-42.8	-66.3	-63.1	-52.2	-40.2	-66.5	-64.3
	25	-45.4	-39.9	-39.7	-40.5	-31.7	-17.6	-18.2	-28.6	-27.0	-17.2	-11.1	-19.8
	50	-18.3	-13.9	-10.1	-24.5	-11.1	-2.1	-5.4	-19.0	-4.9	0.6	4.2	-6.9
	75	13.4	20.4	28.4	27.6	27.1	35.7	32.6	20.2	16.4	22.6	21.2	13.3
	100	-65.5	-75.1	-184.5	-283.0	-36.4	-43.2	-104.5	-178.0	-40.9	-52.3	-107.8	-182.9
30 LB	0	-36.1	-12.8	-16.3	-16.8	-45.9	-24.5	-30.1	-30.3	-40.8	-18.4	-28.3	-28.9
	25	-24.9	-19.7	-21.0	-26.7	-25.2	-12.5	-23.5	-34.3	-22.2	-13.4	-15.6	-25.5
	50	-45.2	-47.0	-54.9	-59.8	-19.0	-7.4	-18.0	-31.8	-19.0	-12.1	-17.8	-26.1
	75	-33.2	-38.8	-92.7	-142.5	-24.1	-29.2	-79.3	-136.8	-24.8	-32.3	-74.1	-126.5
	100	4.2	24.1	-37.2	-69.8	-7.5	-0.6	-34.7	-56.5	-7.3	-4.0	-31.6	-47.0

RHY

		LBS				NLBS				NBS			
	%MC	L23	L34	L45	L51	L23	L34	L45	L51	L23	L34	L45	L51
10 LB	0	-80.1	-210.5	-147.0	297.6	-79.0	-215.7	-163.2	303.3	-85.4	-223.0	-141.8	344.0
	25	-64.9	-185.1	-133.0	240.4	-67.2	-193.1	-148.1	243.1	-67.3	-193.5	-126.6	284.1
	50	-50.9	-158.8	-115.1	193.3	-54.5	-168.4	-125.3	199.2	-50.8	-163.2	-105.4	240.0
	75	-41.7	-144.3	-105.0	165.6	-45.5	-152.0	-111.3	170.1	-39.7	-139.6	-88.2	205.9
	100	-48.3	-140.1	-104.9	130.9	-51.0	-145.5	-107.1	138.2	-45.7	-123.0	-84.5	147.4
30 LB	0	-102.8	-266.5	-174.0	378.8	-100.7	-270.4	-188.8	385.7	-110.1	-276.0	-166.7	427.4
	25	-80.5	-233.9	-161.2	311.2	-84.4	-243.3	-176.0	313.5	-85.2	-240.4	-150.6	351.8
	50	-65.0	-213.2	-146.2	272.4	-68.7	-222.9	-155.5	277.8	-65.5	-208.7	-127.6	314.9
	75	-55.4	-192.2	-142.7	216.9	-58.4	-198.9	-148.0	221.0	-41.2	-157.6	-90.3	260.6
	100	-50.8	-178.9	-120.4	204.6	-53.7	-184.0	-121.1	211.6	-27.6	-119.1	-45.4	246.6

Table 29: Differences in SI JRF due to neutral state (SUP-UP) – Subject #2.

DSX

		LBS				NLBS				NBS			
	%MC	L23	L34	L45	L51	L23	L34	L45	L51	L23	L34	L45	L51
10 LB	0	-217.9	-81.8	12.5	-41.5	-0.8	1.2	-52.3	-218.8	-73.7	-13.2	-35.7	-173.6
	25	-291.1	-362.8	-285.9	-102.9	-372.5	-390.5	-308.9	-61.1	-396.6	-444.2	-348.8	-86.5
	50	-49.8	-342.5	-177.3	-191.4	28.0	25.4	-25.2	-154.5	-2.6	-71.4	-66.9	-163.3
	75	-274.6	42.8	6.1	45.7	36.0	46.4	39.3	20.0	-67.2	-10.1	-3.1	-12.4
	100	11.9	17.1	-154.1	-144.7	-41.6	-28.2	-28.7	-7.5	-6.5	-32.9	-70.8	-42.0
30 LB	0	-629.2	-347.7	-53.5	54.1	-57.4	-25.3	-23.5	28.3	-195.4	-97.0	-55.6	6.3
	25	-83.5	-240.1	-47.4	59.2	13.7	26.0	50.8	109.9	-9.8	-32.1	19.4	85.7
	50	-466.2	-198.1	-182.0	-52.5	-70.6	-97.5	-83.6	15.1	-177.7	-152.3	-128.4	-19.6
	75	253.1	139.9	103.8	122.5	128.9	127.2	84.5	110.6	65.6	16.8	-14.7	35.8
	100	-135.0	-32.9	-81.0	-23.4	-227.6	-254.5	-274.5	-163.7	-312.8	-341.7	-354.4	-218.0

RHY

		LBS				NLBS				NBS			
	%MC	L23	L34	L45	L51	L23	L34	L45	L51	L23	L34	L45	L51
10 LB	0	237.9	256.7	250.0	342.0	239.8	257.4	250.0	343.4	215.8	235.4	241.0	346.9
	25	177.6	188.7	180.4	259.7	175.3	185.5	177.3	257.4	23.9	34.0	52.5	140.6
	50	321.0	327.1	312.6	367.5	322.2	325.3	309.9	366.9	144.6	147.9	162.0	216.9
	75	182.8	165.9	153.7	251.3	178.5	160.6	148.7	247.4	57.6	42.2	50.1	131.3
	100	120.1	103.0	105.8	205.6	113.3	95.8	99.3	197.6	48.7	34.4	35.9	106.4
30 LB	0	-124.4	-140.1	-153.1	46.3	-124.0	-139.1	-152.8	48.2	-174.3	-212.3	-217.9	15.8
	25	150.9	146.1	133.7	282.6	148.9	143.9	131.0	282.3	115.0	97.9	92.6	257.1
	50	299.4	317.6	299.6	375.6	299.8	318.0	298.7	375.7	111.4	127.2	151.2	235.2
	75	333.5	333.0	317.1	396.5	329.6	328.9	313.2	394.2	152.5	147.6	169.0	244.6
	100	195.3	167.5	162.5	313.0	192.1	163.6	159.0	310.0	107.1	80.9	87.5	205.4

Table 30: Differences in AP JRF due to neutral state (SUP-UP) – Subject #2.

DSX

		LBS				NLBS				NBS			
	%MC	L23	L34	L45	L51	L23	L34	L45	L51	L23	L34	L45	L51
10 LB	0	-4.1	-17.1	4.3	-0.2	-9.7	-11.0	-14.8	39.5	-9.8	-13.5	-9.9	28.6
	25	127.7	177.0	284.2	377.1	155.6	205.1	322.2	430.1	153.9	205.8	338.7	451.1
	50	-8.1	7.6	119.5	191.8	-28.4	-17.6	-9.6	87.0	-31.8	-19.7	12.4	100.0
	75	22.8	61.2	61.8	61.9	-33.1	-40.8	-64.7	-49.8	-28.1	-29.0	-47.1	-21.5
	100	-40.5	-25.0	78.7	157.9	15.5	41.1	72.8	96.7	10.0	32.1	88.7	122.0
30 LB	0	31.1	44.5	130.5	102.5	-3.5	-8.3	18.5	13.6	4.0	3.2	49.7	47.0
	25	19.0	19.9	88.3	74.0	-1.1	-2.6	12.1	-5.7	-4.6	-7.4	18.5	4.7
	50	85.8	148.8	210.1	220.8	41.0	66.8	100.9	110.4	52.1	84.6	129.3	149.3
	75	-10.1	-7.0	-0.2	-13.4	7.0	12.6	22.0	11.1	15.4	29.8	68.5	82.2
	100	23.1	58.0	113.6	145.4	29.4	95.5	219.9	320.3	36.1	112.7	261.6	382.0

RHY

		LBS				NLBS				NBS			
	%MC	L23	L34	L45	L51	L23	L34	L45	L51	L23	L34	L45	L51
10 LB	0	-55.3	39.8	61.4	135.8	-57.3	38.9	62.5	141.2	-46.8	44.6	62.1	116.6
	25	-41.8	27.4	54.2	128.9	-43.4	26.6	55.3	134.4	-28.0	37.5	77.1	170.8
	50	-39.9	8.4	-6.5	17.8	-40.5	8.6	-4.8	21.8	-29.4	17.7	14.9	59.5
	75	-0.6	33.6	48.0	67.5	-0.4	33.9	49.6	70.6	7.1	38.0	58.7	94.3
	100	4.2	44.4	68.5	88.6	4.1	44.0	69.2	91.4	8.1	37.4	62.1	75.4
30 LB	0	-13.8	107.1	249.2	481.6	-15.8	106.3	250.5	487.3	9.8	128.1	276.3	504.6
	25	-26.9	78.9	145.2	267.5	-27.6	79.3	148.0	274.7	-11.7	90.2	155.0	262.3
	50	-52.8	33.3	51.6	135.1	-54.4	32.7	52.4	139.2	-53.7	30.5	49.7	139.3
	75	-27.3	33.8	33.8	84.4	-27.6	34.4	35.9	89.2	-28.6	30.2	29.5	84.6
	100	14.6	73.2	110.9	160.3	14.7	73.4	111.9	162.3	13.0	58.2	84.9	127.7

Table 31: Differences in SI JRF due to neutral state (SUP-UP) – Subject #3.

DSX

		LBS				NLBS				NBS			
	%MC	L23	L34	L45	L51	L23	L34	L45	L51	L23	L34	L45	L51
10 LB	0	105.2	135.4	278.5	297.8	112.0	119.6	290.8	310.8	85.8	99.2	316.1	334.6
	25	23.9	19.0	19.0	28.1	-3.5	36.9	121.5	130.8	-40.2	-18.6	100.5	111.0
	50	34.7	5.1	115.8	114.7	27.9	59.6	116.8	116.2	-10.0	-1.3	89.0	89.1
	75	-139.9	-64.0	-38.5	-22.7	-70.3	-59.0	-4.6	25.2	-69.1	-40.9	-3.7	16.0
	100	284.0	324.2	424.6	390.4	127.0	216.7	247.3	232.3	127.4	182.9	213.0	199.9
30 LB	0	174.3	179.1	262.9	277.1	159.9	158.9	322.0	338.7	118.8	127.2	338.2	359.8
	25	19.1	29.5	87.1	85.9	70.3	97.3	185.8	183.2	34.0	42.7	177.7	175.8
	50	97.4	67.2	48.1	41.1	26.0	65.4	114.1	108.7	13.6	33.6	67.6	62.6
	75	190.6	196.5	268.0	247.7	106.0	136.0	230.4	213.3	95.6	109.7	174.4	158.5
	100	-6.4	26.0	182.1	162.3	6.9	26.7	98.8	86.2	-11.9	-0.5	63.2	49.3

RHY

		LBS				NLBS				NBS			
	%MC	L23	L34	L45	L51	L23	L34	L45	L51	L23	L34	L45	L51
10 LB	0	-23.7	-35.0	64.1	224.6	29.1	-1.9	87.3	235.9	-62.6	-77.7	21.0	179.5
	25	-33.2	-39.3	37.7	196.7	23.1	-4.0	56.1	208.9	-68.8	-79.2	-1.3	150.6
	50	-37.1	-42.8	14.4	170.2	-4.2	-33.8	16.3	170.8	-74.9	-85.3	-26.4	117.8
	75	-40.2	-46.5	-3.6	157.5	-31.6	-48.1	-6.3	156.4	-78.1	-87.5	-41.2	97.6
	100	-98.5	-91.6	-60.0	80.9	-102.4	-100.7	-71.5	71.5	-115.5	-102.1	-61.6	34.1
30 LB	0	-70.8	-75.7	42.9	232.4	-13.8	-40.7	69.0	246.6	-111.2	-115.6	-5.2	185.3
	25	-72.6	-72.4	12.5	201.8	-23.5	-43.7	27.4	211.1	-115.4	-114.6	-35.5	150.0
	50	-75.1	-81.2	-16.7	176.0	-48.6	-73.8	-15.1	177.7	-118.9	-127.5	-62.1	123.1
	75	-50.8	-63.8	-32.7	167.6	-44.6	-64.7	-34.0	168.3	-113.1	-123.9	-81.6	84.4
	100	-116.4	-125.4	-108.0	102.2	-119.5	-136.8	-122.1	90.7	-177.3	-179.2	-147.2	7.4

Table 32: Differences in AP JRF due to neutral state (SUP-UP) – Subject #3.

DSX

		LBS				NLBS				NBS			
	%MC	L23	L34	L45	L51	L23	L34	L45	L51	L23	L34	L45	L51
10 LB	0	-48.4	-30.4	-60.1	-57.5	-55.8	-42.8	-66.3	-63.1	-52.2	-40.2	-66.5	-64.3
	25	-45.4	-39.9	-39.7	-40.5	-31.7	-17.6	-18.2	-28.6	-27.0	-17.2	-11.1	-19.8
	50	-18.3	-13.9	-10.1	-24.5	-11.1	-2.1	-5.4	-19.0	-4.9	0.6	4.2	-6.9
	75	13.4	20.4	28.4	27.6	27.1	35.7	32.6	20.2	16.4	22.6	21.2	13.3
	100	-65.5	-75.1	-184.5	-283.0	-36.4	-43.2	-104.5	-178.0	-40.9	-52.3	-107.8	-182.9
30 LB	0	-36.1	-12.8	-16.3	-16.8	-45.9	-24.5	-30.1	-30.3	-40.8	-18.4	-28.3	-28.9
	25	-24.9	-19.7	-21.0	-26.7	-25.2	-12.5	-23.5	-34.3	-22.2	-13.4	-15.6	-25.5
	50	-45.2	-47.0	-54.9	-59.8	-19.0	-7.4	-18.0	-31.8	-19.0	-12.1	-17.8	-26.1
	75	-33.2	-38.8	-92.7	-142.5	-24.1	-29.2	-79.3	-136.8	-24.8	-32.3	-74.1	-126.5
	100	4.2	24.1	-37.2	-69.8	-7.5	-0.6	-34.7	-56.5	-7.3	-4.0	-31.6	-47.0

RHY

		LBS				NLBS				NBS			
	%MC	L23	L34	L45	L51	L23	L34	L45	L51	L23	L34	L45	L51
10 LB	0	-80.1	-210.5	-147.0	297.6	-79.0	-215.7	-163.2	303.3	-85.4	-223.0	-141.8	344.0
	25	-64.9	-185.1	-133.0	240.4	-67.2	-193.1	-148.1	243.1	-67.3	-193.5	-126.6	284.1
	50	-50.9	-158.8	-115.1	193.3	-54.5	-168.4	-125.3	199.2	-50.8	-163.2	-105.4	240.0
	75	-41.7	-144.3	-105.0	165.6	-45.5	-152.0	-111.3	170.1	-39.7	-139.6	-88.2	205.9
	100	-48.3	-140.1	-104.9	130.9	-51.0	-145.5	-107.1	138.2	-45.7	-123.0	-84.5	147.4
30 LB	0	-102.8	-266.5	-174.0	378.8	-100.7	-270.4	-188.8	385.7	-110.1	-276.0	-166.7	427.4
	25	-80.5	-233.9	-161.2	311.2	-84.4	-243.3	-176.0	313.5	-85.2	-240.4	-150.6	351.8
	50	-65.0	-213.2	-146.2	272.4	-68.7	-222.9	-155.5	277.8	-65.5	-208.7	-127.6	314.9
	75	-55.4	-192.2	-142.7	216.9	-58.4	-198.9	-148.0	221.0	-41.2	-157.6	-90.3	260.6
	100	-50.8	-178.9	-120.4	204.6	-53.7	-184.0	-121.1	211.6	-27.6	-119.1	-45.4	246.6

Table 33: Differences in muscle force due to kinematic input (DSX-RHY) – Subject #1.

SUPINE

	%MC	LBS				NLBS				NBS			
		MF	LT	IL	ABD	MF	LT	IL	ABD	MF	LT	IL	ABD
10 LB	0	108.2	-216.1	218.4	194.0	102.8	-114.2	201.4	208.9	229.7	-178.0	217.1	295.3
	25	-20.2	-85.1	11.9	73.9	-31.0	-24.9	-20.7	78.7	-3.5	-124.8	3.8	132.2
	50	14.8	-70.7	-59.6	-10.1	17.3	-41.4	-48.4	-27.8	56.4	-98.9	-28.7	22.7
	75	-34.9	-70.8	-44.5	-34.6	-42.6	-8.9	-38.6	8.8	-39.4	-41.2	-40.8	-25.0
	100	103.1	282.3	-278.2	9.0	124.5	283.4	-230.8	35.5	130.4	251.3	-200.6	63.6
30 LB	0	162.3	-668.9	102.3	271.0	-7.2	-463.2	165.1	303.8	90.8	-561.2	292.5	313.7
	25	-55.7	-164.0	-15.5	94.9	-78.7	-90.3	-23.7	86.9	-36.4	-179.9	29.7	154.9
	50	54.2	-208.8	-94.6	-18.3	56.6	-158.1	-76.6	-14.1	91.2	-196.7	-96.2	17.1
	75	25.1	-21.0	-48.5	43.1	56.7	55.0	-16.1	79.7	85.7	23.2	-27.4	77.8
	100	36.6	22.4	-7.7	-12.1	34.5	43.4	-14.5	-21.6	61.5	9.6	8.2	-18.5

UPRIGHT

	%MC	LBS				NLBS				NBS			
		MF	LT	IL	ABD	MF	LT	IL	ABD	MF	LT	IL	ABD
10 LB	0	180.5	-61.5	157.4	54.1	229.6	15.7	99.7	40.1	279.6	-20.9	148.7	49.2
	25	-29.3	-40.3	-70.1	177.1	-34.8	-32.2	-77.1	175.6	-3.9	-65.8	-72.8	154.8
	50	1.1	-69.4	-32.8	-11.0	17.6	-44.0	-66.2	-28.3	63.7	-29.1	-65.9	9.8
	75	-30.4	-126.2	-99.0	-55.4	-46.3	-6.5	-91.9	-21.6	-27.9	17.8	-63.7	-17.2
	100	130.4	323.6	-98.1	209.2	160.8	340.7	-182.8	177.3	161.7	324.5	-192.7	152.7
30 LB	0	191.6	-512.8	115.0	314.6	75.3	-336.0	126.8	227.9	114.1	-393.0	213.9	213.6
	25	-44.5	-71.6	-64.4	126.7	-44.3	-17.0	-31.4	120.6	-11.2	-48.0	-9.8	129.4
	50	52.9	-134.2	-136.5	76.0	53.1	-107.9	-125.7	74.3	100.2	-114.7	-139.1	54.2
	75	79.6	123.7	26.1	252.6	87.3	148.0	38.8	261.6	89.9	113.6	14.4	204.4
	100	82.8	89.1	-11.9	103.1	76.9	85.0	-9.8	63.2	80.1	75.3	15.5	48.2

Table 34: Differences in muscle force due to kinematic input (DSX-RHY) – Subject #2.

SUPINE

	%MC	LBS				NLBS				NBS			
		MF	LT	IL	ABD	MF	LT	IL	ABD	MF	LT	IL	ABD
10 LB	0	327.9	-109.3	-149.7	32.5	365.6	-67.3	-109.5	142.6	379.0	40.2	-158.9	276.1
	25	-60.1	44.6	107.7	33.0	-65.0	93.1	137.5	75.9	-63.8	90.3	150.4	88.3
	50	30.1	-5.8	-155.2	200.7	122.6	40.0	-261.4	484.4	59.9	177.1	-254.0	673.4
	75	-13.0	-53.3	44.4	-47.3	40.8	21.4	-74.9	-97.3	50.6	72.1	-83.1	11.0
	100	98.9	256.0	109.2	52.4	59.5	137.8	49.0	-12.4	84.6	116.8	79.1	13.1
30 LB	0	-55.0	-107.0	-119.3	-0.4	-3.9	-69.7	-189.1	-12.4	52.4	-30.6	-210.2	8.3
	25	52.2	201.8	-259.2	-106.0	143.3	337.5	-375.5	-143.3	211.8	363.4	-381.0	-50.5
	50	2.2	-50.4	-14.2	-71.9	64.1	-0.7	-113.3	-109.6	103.6	20.1	-140.6	-21.5
	75	-43.4	19.3	162.2	3.9	-39.8	81.7	206.4	30.3	-33.5	81.2	199.0	29.5
	100	36.5	2.7	121.2	3.6	70.4	26.0	130.9	25.7	80.5	49.1	121.7	33.3

UPRIGHT

	%MC	LBS				NLBS				NBS			
		MF	LT	IL	ABD	MF	LT	IL	ABD	MF	LT	IL	ABD
10 LB	0	586.4	-462.1	-335.2	-88.7	488.1	-203.6	-371.0	101.5	357.4	0.2	-417.4	258.0
	25	-14.2	373.2	-336.9	-216.9	-5.8	434.1	-371.2	-210.7	-28.1	518.7	-341.0	-47.2
	50	113.9	-29.3	-493.0	204.0	126.1	16.2	-519.0	398.7	21.7	207.1	-474.9	615.2
	75	138.7	-63.0	-171.5	-194.3	83.2	-39.3	-135.8	-194.1	49.1	63.9	-113.6	-49.0
	100	130.1	358.5	82.2	-106.8	64.1	154.4	16.3	-122.7	32.8	115.6	4.8	-33.6
30 LB	0	121.7	-188.4	-178.9	176.4	82.0	-60.4	-200.5	265.0	93.5	4.4	-335.3	304.2
	25	193.1	251.8	-445.3	-93.1	205.5	321.1	-434.2	-63.0	213.4	372.2	-453.5	67.1
	50	122.4	-36.3	-332.7	-280.1	68.5	27.6	-339.4	-302.9	41.9	140.3	-311.5	-128.2
	75	-34.9	195.3	30.5	-91.1	-46.6	211.7	-22.2	-115.4	-31.3	162.6	2.3	-99.3
	100	125.3	67.3	-91.3	-120.0	81.0	106.7	-174.1	-179.7	82.1	149.3	-153.5	-77.5

Table 35: Differences in muscle force due to kinematics input (DSX-RHY) – Subject #3.

SUPINE

	%MC	LBS MF	LBS LT	LBS IL	LBS ABD	NLBS MF	NLBS LT	NLBS IL	NLBS ABD	NBS MF	NBS LT	NBS IL	NBS ABD
10 LB	0	41.6	-131.3	-30.7	68.6	49.6	-75.6	67.9	32.4	108.0	-88.3	29.7	-12.7
	25	-15.8	-75.2	-57.7	43.0	-6.9	-39.3	-21.7	23.1	48.3	-27.2	-14.5	49.2
	50	6.7	-19.6	-35.4	77.7	5.6	0.4	-24.8	32.0	41.6	9.0	-24.8	62.4
	75	80.0	146.9	-31.6	-8.1	110.7	214.3	-30.7	25.2	112.5	193.5	-43.6	8.9
	100	113.9	-128.5	-170.7	-32.5	67.3	-7.7	-188.8	-28.5	97.7	-35.4	-153.2	-18.8
30 LB	0	148.0	-161.4	-122.9	258.7	154.7	-93.4	-14.3	142.7	228.9	-87.2	-36.3	159.2
	25	31.4	-74.7	56.1	-5.8	54.7	-7.6	104.4	16.2	88.6	21.1	61.1	-2.1
	50	-32.1	-115.9	93.7	-29.0	-32.9	-98.0	114.5	-22.1	-14.0	-63.9	107.0	-12.7
	75	44.0	-60.8	-66.6	242.3	62.4	-27.2	-88.3	181.8	92.5	13.2	-85.7	254.7
	100	97.5	214.8	-320.3	-12.7	79.6	278.5	-307.0	-9.5	96.3	306.7	-288.8	7.9

UPRIGHT

	%MC	LBS MF	LBS LT	LBS IL	LBS ABD	NLBS MF	NLBS LT	NLBS IL	NLBS ABD	NBS MF	NBS LT	NBS IL	NBS ABD
10 LB	0	11.9	-128.5	-56.8	14.5	65.1	-64.2	-10.2	21.8	108.4	-48.1	-48.7	-33.4
	25	-22.2	-80.3	-59.0	-46.8	8.9	-30.5	-49.6	-39.5	61.4	10.5	-44.8	51.5
	50	-19.2	-51.4	-37.6	-42.6	9.7	-8.2	-34.4	-16.9	50.2	32.6	-43.5	67.2
	75	99.2	225.2	-162.8	19.7	135.7	291.9	-146.2	21.5	115.5	290.9	-109.5	15.2
	100	75.7	13.7	-120.7	-29.2	96.0	68.9	-117.0	-27.3	113.3	11.5	-112.0	-3.0
30 LB	0	108.0	-134.2	-134.8	29.2	175.0	-53.1	-100.1	15.7	249.3	4.3	-163.0	70.7
	25	50.5	-26.2	32.3	43.5	84.3	30.3	38.1	33.3	101.9	74.7	-5.1	1.0
	50	3.5	-96.1	93.2	16.9	-12.3	-78.4	103.9	16.7	-1.1	-30.3	85.1	1.7
	75	50.0	-17.2	-33.4	113.1	88.6	41.2	-69.3	203.3	114.3	106.6	-78.1	310.0
	100	49.4	101.4	-80.4	1.6	108.6	169.0	-103.0	2.9	105.1	199.2	-127.8	6.0

Table 36: Differences in muscle force due to stiffness properties (LBS-NBS) – Subject #1.

SUPINE

	%MC	DSX MF	DSX LT	DSX IL	DSX ABD	RHY MF	RHY LT	RHY IL	RHY ABD
10 LB	0	-174.3	-211.5	-90.5	-69.6	-52.8	-173.3	-91.8	31.7
	25	-54.3	-86.4	-79.5	-25.9	-37.7	-126.0	-87.6	32.4
	50	-65.7	-65.7	-108.4	-5.1	-24.1	-93.9	-77.4	27.7
	75	0.0	-95.3	-57.0	23.4	-4.5	-65.7	-53.3	33.0
	100	-25.3	-11.6	-101.8	-27.9	2.0	-42.7	-24.2	26.7
30 LB	0	19.8	-303.4	-259.2	-16.5	-51.6	-195.7	-69.0	26.2
	25	-46.5	-127.9	-118.1	-29.1	-27.2	-143.8	-72.9	30.9
	50	-45.1	-116.4	-72.0	-19.0	-8.0	-104.3	-73.6	16.4
	75	-51.8	-121.5	-51.6	-12.2	8.8	-77.2	-30.6	22.5
	100	-15.5	-36.4	-8.9	34.9	9.4	-49.3	7.1	28.5

UPRIGHT

	%MC	DSX MF	DSX LT	DSX IL	DSX ABD	RHY MF	RHY LT	RHY IL	RHY ABD
10 LB	0	-145.5	-176.8	-65.2	26.5	-46.5	-136.2	-73.9	21.5
	25	-55.6	-69.3	-67.8	38.4	-30.2	-94.7	-70.5	16.1
	50	-77.4	-100.4	-28.6	-1.9	-14.8	-60.0	-61.7	18.9
	75	-0.9	-180.3	-72.0	-10.3	1.6	-36.3	-36.7	27.9
	100	-27.6	-16.1	73.4	67.6	3.6	-15.2	-21.3	11.1
30 LB	0	39.2	-286.7	-149.8	122.7	-38.3	-166.9	-50.9	21.7
	25	-44.7	-138.8	-107.5	18.8	-11.4	-115.2	-52.9	21.5
	50	-47.1	-99.6	-51.4	35.0	0.2	-80.2	-54.0	13.2
	75	-0.6	-38.5	-8.2	64.9	9.7	-48.6	-20.0	16.6
	100	10.5	-2.1	-9.4	86.9	7.8	-15.9	18.0	32.0

Table 37: Differences in muscle force due to stiffness properties (LBS-NBS) – Subject #2.

SUPINE

		DSX				RHY			
	%MC	MF	LT	IL	ABD	MF	LT	IL	ABD
10 LB	0	-174.3	-211.5	-90.5	-69.6	-52.8	-173.3	-91.8	31.7
	25	-54.3	-86.4	-79.5	-25.9	-37.7	-126.0	-87.6	32.4
	50	-65.7	-65.7	-108.4	-5.1	-24.1	-93.9	-77.4	27.7
	75	0.0	-95.3	-57.0	23.4	-4.5	-65.7	-53.3	33.0
	100	-25.3	-11.6	-101.8	-27.9	2.0	-42.7	-24.2	26.7
30 LB	0	19.8	-303.4	-259.2	-16.5	-51.6	-195.7	-69.0	26.2
	25	-46.5	-127.9	-118.1	-29.1	-27.2	-143.8	-72.9	30.9
	50	-45.1	-116.4	-72.0	-19.0	-8.0	-104.3	-73.6	16.4
	75	-51.8	-121.5	-51.6	-12.2	8.8	-77.2	-30.6	22.5
	100	-15.5	-36.4	-8.9	34.9	9.4	-49.3	7.1	28.5

UPRIGHT

		DSX				RHY			
	%MC	MF	LT	IL	ABD	MF	LT	IL	ABD
10 LB	0	-145.5	-176.8	-65.2	26.5	-46.5	-136.2	-73.9	21.5
	25	-55.6	-69.3	-67.8	38.4	-30.2	-94.7	-70.5	16.1
	50	-77.4	-100.4	-28.6	-1.9	-14.8	-60.0	-61.7	18.9
	75	-0.9	-180.3	-72.0	-10.3	1.6	-36.3	-36.7	27.9
	100	-27.6	-16.1	73.4	67.6	3.6	-15.2	-21.3	11.1
30 LB	0	39.2	-286.7	-149.8	122.7	-38.3	-166.9	-50.9	21.7
	25	-44.7	-138.8	-107.5	18.8	-11.4	-115.2	-52.9	21.5
	50	-47.1	-99.6	-51.4	35.0	0.2	-80.2	-54.0	13.2
	75	-0.6	-38.5	-8.2	64.9	9.7	-48.6	-20.0	16.6
	100	10.5	-2.1	-9.4	86.9	7.8	-15.9	18.0	32.0

Table 38: Differences in muscle force due to stiffness properties (LBS-NBS) – Subject #3.

SUPINE

		DSX				RHY			
	%MC	MF	LT	IL	ABD	MF	LT	IL	ABD
10 LB	0	-94.5	-186.1	-102.0	66.6	-28.1	-143.1	-41.6	-14.7
	25	-77.9	-176.6	-64.6	-14.6	-13.8	-128.6	-21.4	-8.3
	50	-26.6	-164.0	-0.4	20.5	8.3	-135.4	10.2	5.1
	75	-7.0	-177.4	41.6	-4.8	25.5	-130.8	29.5	12.2
	100	50.2	-199.6	6.4	2.8	34.0	-106.4	23.9	16.5
30 LB	0	-121.2	-223.1	-149.2	81.0	-40.2	-148.9	-62.6	-18.6
	25	-82.2	-228.2	-36.4	-19.5	-25.0	-132.4	-31.3	-15.9
	50	-25.8	-178.5	-15.1	-25.9	-7.7	-126.6	-1.8	-9.7
	75	-21.6	-208.6	46.9	-6.1	26.9	-134.6	27.8	6.4
	100	50.9	-213.4	7.8	-3.4	49.6	-121.6	39.3	17.2

UPRIGHT

		DSX				RHY			
	%MC	MF	LT	IL	ABD	MF	LT	IL	ABD
10 LB	0	-109.5	-199.3	-46.1	37.0	-13.0	-118.9	-38.0	-10.9
	25	-81.9	-195.0	-41.5	-106.4	1.7	-104.1	-27.3	-8.1
	50	-45.7	-187.2	-5.6	-115.4	23.7	-103.2	-11.5	-5.6
	75	10.1	-157.7	-29.2	23.4	26.4	-91.9	24.2	18.9
	100	-9.6	-50.0	-4.6	2.5	28.1	-52.1	4.0	28.7
30 LB	0	-166.8	-266.5	-25.7	-59.0	-25.6	-128.0	-53.9	-17.5
	25	-60.7	-212.9	9.3	31.5	-9.4	-112.0	-28.0	-11.0
	50	18.8	-170.3	-5.5	-1.0	14.2	-104.5	-13.6	-16.3
	75	-35.9	-232.5	55.1	-225.5	28.4	-108.7	10.4	-28.5
	100	21.4	-188.9	28.1	-0.6	77.2	-91.1	-19.4	3.7

Table 39: Differences in muscle force due to neutral state (SUP-UP) – Subject #1.

		DSX											
		LBS				NLBS				NBS			
	%MC	MF	LT	IL	ABD	MF	LT	IL	ABD	MF	LT	IL	ABD
10 LB	0	-82.3	-88.5	-50.3	106.0	-131.7	-92.3	-14.9	121.9	-53.5	-53.8	-25.1	202.1
	25	4.1	8.2	1.7	-107.4	4.5	39.0	-34.1	-112.1	2.9	25.2	13.4	-43.0
	50	12.3	35.8	-85.9	5.3	2.6	34.4	-49.6	3.5	0.6	1.2	-6.1	8.6
	75	0.1	85.8	13.7	31.0	10.7	30.2	7.0	41.9	-0.7	0.8	-1.3	-2.7
	100	-11.1	8.6	-181.6	-149.8	-17.0	-2.5	-50.4	-90.4	-13.4	4.0	-6.4	-54.3
30 LB	0	-38.2	-40.0	-156.0	-80.8	-88.9	-44.1	-105.3	15.7	-18.8	-23.4	-46.5	58.5
	25	-13.2	-1.4	-30.7	-31.8	-33.1	-4.8	-81.9	-43.8	-11.4	-12.3	-20.1	16.2
	50	6.3	-2.8	-10.3	-92.4	10.0	16.1	-7.5	-89.8	4.3	13.9	10.4	-38.3
	75	-35.2	-51.5	-68.6	-155.9	-9.1	4.6	-50.8	-129.5	16.0	31.6	-25.2	-78.8
	100	-12.0	-17.7	12.4	-72.0	-2.7	13.5	5.7	-41.3	14.0	16.6	11.9	-20.0

		RHY											
		LBS				NLBS				NBS			
	%MC	MF	LT	IL	ABD	MF	LT	IL	ABD	MF	LT	IL	ABD
10 LB	0	-9.9	66.1	-111.3	-33.9	-5.0	37.6	-116.6	-46.9	-3.6	103.3	-93.4	-44.0
	25	-5.0	53.0	-80.3	-4.2	0.7	31.7	-90.5	-15.2	2.5	84.2	-63.2	-20.4
	50	-1.4	37.1	-59.0	4.5	2.9	31.8	-67.5	3.0	7.9	71.0	-43.3	-4.3
	75	4.7	30.4	-40.8	10.2	7.0	32.6	-46.3	11.5	10.8	59.8	-24.1	5.1
	100	16.3	49.8	-1.5	50.5	19.3	54.9	-2.4	51.4	17.9	77.3	1.5	34.9
30 LB	0	-8.9	116.0	-143.2	-37.1	-6.4	83.1	-143.5	-60.1	4.4	144.8	-125.1	-41.6
	25	-2.0	91.0	-79.6	0.0	1.3	68.5	-89.6	-10.1	13.9	119.6	-59.6	-9.4
	50	5.0	71.7	-52.2	2.0	6.5	66.3	-56.6	-1.4	13.3	95.9	-32.5	-1.2
	75	19.3	93.3	6.0	53.6	21.4	97.7	4.2	52.4	20.2	121.9	16.6	47.7
	100	34.2	48.9	8.2	43.2	39.7	55.1	10.4	43.4	32.7	82.3	19.2	46.7

Table 40: Differences in muscle force due to neutral state (SUP-UP) – Subject #2.

		DSX											
		LBS				NLBS				NBS			
	%MC	MF	LT	IL	ABD	MF	LT	IL	ABD	MF	LT	IL	ABD
10 LB	0	-284.0	274.3	58.3	99.9	-145.3	61.8	125.2	21.8	1.6	-25.4	120.7	15.4
	25	-54.8	-350.8	324.8	177.7	-65.6	-357.1	383.1	216.7	-19.2	-398.1	405.5	156.0
	50	-102.1	-16.6	177.5	-125.8	-20.1	-14.0	96.9	-36.9	43.7	-13.2	106.7	30.3
	75	-147.8	-40.6	124.1	111.4	-37.5	11.9	-29.5	61.1	17.0	-10.3	-40.5	72.1
	100	-61.7	-195.1	13.8	140.4	-34.3	-106.6	22.1	92.7	39.0	-70.4	45.8	48.8
30 LB	0	-140.4	111.6	-10.0	-170.1	-47.2	23.8	-68.2	-268.4	6.4	2.2	49.7	-276.6
	25	-130.6	-71.6	85.7	-15.4	-50.1	-2.4	-47.8	-80.3	16.9	-22.8	-30.0	-110.0
	50	-145.0	-42.9	190.9	101.0	-28.4	-54.5	94.6	86.5	60.1	-98.0	87.2	78.8
	75	-9.1	-207.1	-39.9	-11.8	7.9	-158.4	56.9	39.0	17.5	-66.2	66.8	88.7
	100	-64.7	-105.9	89.3	92.9	14.5	-120.5	183.0	174.7	30.9	-114.1	167.6	120.3

		RHY											
		LBS				NLBS				NBS			
	%MC	MF	LT	IL	ABD	MF	LT	IL	ABD	MF	LT	IL	ABD
10 LB	0	-25.5	-78.5	-127.2	-21.3	-22.8	-74.5	-136.4	-19.2	-19.9	-65.4	-137.8	-2.7
	25	-9.0	-22.1	-119.8	-72.2	-6.3	-16.1	-125.6	-69.9	16.5	30.3	-85.9	20.6
	50	-18.2	-40.0	-160.3	-122.5	-16.7	-37.8	-160.7	-122.6	5.5	16.8	-114.2	-27.9
	75	4.0	-50.3	-91.8	-35.6	4.9	-48.8	-90.4	-35.7	15.4	-18.5	-71.0	12.1
	100	-30.4	-92.5	-13.3	-18.8	-29.7	-90.1	-10.6	-17.6	-12.8	-71.5	-28.4	2.2
30 LB	0	36.4	30.2	-69.6	6.7	38.7	33.1	-79.6	9.0	47.6	37.3	-75.4	19.3
	25	10.2	-21.6	-100.4	-2.5	12.1	-18.9	-106.4	0.0	18.5	-14.0	-102.5	7.6
	50	-24.8	-28.8	-127.6	-107.3	-24.0	-26.1	-131.4	-106.7	-1.6	22.2	-83.7	-27.9
	75	-0.6	-31.2	-171.6	-106.8	1.0	-28.5	-171.7	-106.7	19.7	15.2	-129.9	-40.1
	100	24.1	-41.3	-123.3	-30.7	25.2	-39.8	-122.0	-30.7	32.4	-13.9	-107.6	9.5

Table 41: Differences in muscle force due to neutral state (SUP-UP) – Subject #3.

	DSX												
		LBS				NLBS				NBS			
	%MC	MF	LT	IL	ABD	MF	LT	IL	ABD	MF	LT	IL	ABD
10 LB	0	26.5	26.1	-40.4	25.7	-11.8	4.9	-8.2	-21.9	11.5	12.9	15.5	-3.9
	25	-1.3	11.6	-22.9	88.6	-17.0	-5.9	-9.8	54.7	-5.3	-6.8	0.2	-3.3
	50	17.6	21.6	16.7	133.3	-6.9	0.9	14.7	58.9	-1.6	-1.6	11.5	-2.6
	75	-6.3	-60.1	150.3	-9.6	-7.5	-52.5	127.8	20.4	10.8	-40.3	79.6	18.5
	100	73.2	-168.0	0.5	11.4	12.6	-96.1	-24.2	14.6	13.3	-18.5	-10.5	11.2
30 LB	0	42.4	29.4	-75.9	188.9	-13.0	3.1	-21.4	75.0	-3.2	-14.0	47.6	48.9
	25	-21.2	-15.8	-45.1	-50.3	-24.5	-13.2	-18.7	-24.6	0.2	-0.6	0.5	0.8
	50	-45.2	-14.9	-3.1	-18.1	-24.8	-14.0	-0.4	-11.8	-0.6	-6.7	6.5	6.8
	75	16.0	24.1	8.8	202.3	0.0	4.2	20.0	49.5	1.7	0.3	17.0	-17.1
	100	6.9	-21.1	-2.4	45.4	-62.5	-18.5	35.7	47.8	-22.5	3.4	17.8	48.2

	RHY												
		LBS				NLBS				NBS			
	%MC	MF	LT	IL	ABD	MF	LT	IL	ABD	MF	LT	IL	ABD
10 LB	0	-3.1	28.9	-66.6	-28.4	3.7	16.4	-86.3	-32.6	11.9	53.1	-62.9	-24.6
	25	-7.7	6.4	-24.2	-1.2	-1.3	2.9	-37.7	-7.8	7.8	30.9	-30.1	-1.0
	50	-8.4	-10.2	14.5	13.0	-2.7	-7.7	5.1	10.0	7.0	22.0	-7.2	2.3
	75	12.9	18.3	19.1	18.2	17.4	25.1	12.3	16.7	13.8	57.1	13.7	24.9
	100	34.9	-25.8	50.5	14.8	41.3	-19.5	47.6	15.8	29.0	28.5	30.6	27.0
30 LB	0	2.5	56.5	-87.8	-40.7	7.3	43.4	-107.1	-52.0	17.1	77.4	-79.1	-39.6
	25	-2.1	32.7	-69.0	-1.0	5.2	24.7	-85.0	-7.5	13.5	53.1	-65.7	3.8
	50	-9.6	4.9	-3.6	27.8	-4.3	5.5	-11.0	26.9	12.3	27.0	-15.4	21.2
	75	22.0	67.8	42.0	73.1	26.2	72.6	39.0	71.1	23.4	93.7	24.7	38.1
	100	-41.2	-134.5	237.5	59.8	-33.4	-128.0	239.8	60.2	-13.7	-104.0	178.8	46.3

Bibliography

1 Disease, G. B. D., Injury, I. & Prevalence, C. Global, regional, and national incidence, prevalence, and years lived with disability for 354 diseases and injuries for 195 countries and territories, 1990-2017: a systematic analysis for the Global Burden of Disease Study 2017. *Lancet* **392**, 1789-1858, doi:10.1016/S0140-6736(18)32279-7 (2018).

2 Adams, M. A., Freeman, B. J., Morrison, H. P., Nelson, I. W. & Dolan, P. Mechanical initiation of intervertebral disc degeneration. *Spine (Phila Pa 1976)* **25**, 1625-1636 (2000).

3 Smith, L. J., Nerurkar, N. L., Choi, K. S., Harfe, B. D. & Elliott, D. M. Degeneration and regeneration of the intervertebral disc: lessons from development. *Disease models & mechanisms* **4**, 31-41, doi:10.1242/dmm.006403 (2011).

4 Rohlmann, A., Zander, T., Schmidt, H., Wilke, H. J. & Bergmann, G. Analysis of the influence of disc degeneration on the mechanical behaviour of a lumbar motion segment using the finite element method. *J Biomech* **39**, 2484-2490, doi:10.1016/j.jbiomech.2005.07.026 (2006).

5 Li, W. *et al.* Lumbar facet joint motion in patients with degenerative disc disease at affected and adjacent levels: an in vivo biomechanical study. *Spine (Phila Pa 1976)* **36**, E629-637, doi:10.1097/BRS.0b013e3181faaef7 (2011).

6 Fujiwara, A. *et al.* The effect of disc degeneration and facet joint osteoarthritis on the segmental flexibility of the lumbar spine. *Spine (Phila Pa 1976)* **25**, 3036-3044 (2000).

7 Mimura, M. *et al.* Disc degeneration affects the multidirectional flexibility of the lumbar spine. *Spine (Phila Pa 1976)* **19**, 1371-1380 (1994).

8 Wang, S. *et al.* How does lumbar degenerative disc disease affect the disc deformation at the cephalic levels in vivo? *Spine (Phila Pa 1976)* **36**, E574-581, doi:10.1097/BRS.0b013e3181f79e93 (2011).

9 Allegri, M. *et al.* Mechanisms of low back pain: a guide for diagnosis and therapy. *F1000Research* **5**, doi:10.12688/f1000research.8105.2 (2016).

10 Stokes, I. A. Mechanical function of facet joints in the lumbar spine. *Clin Biomech (Bristol, Avon)* **3**, 101-105, doi:10.1016/0268-0033(88)90052-6 (1988).

11 Arshad, R., Zander, T., Dreischarf, M. & Schmidt, H. Influence of lumbar spine rhythms and intra-abdominal pressure on spinal loads and trunk muscle forces during upper body inclination. *Med Eng Phys* **38**, 333-338, doi:10.1016/j.medengphy.2016.01.013 (2016).

12 Bassani, T., Stucovitz, E., Qian, Z., Briguglio, M. & Galbusera, F. Validation of the AnyBody full body musculoskeletal model in computing lumbar spine loads at L4L5 level. *J Biomech* **58**, 89-96, doi:10.1016/j.jbiomech.2017.04.025 (2017).

13 Cholewicki, J., Simons, A. P. & Radebold, A. Effects of external trunk loads on lumbar spine stability. *J Biomech* **33**, 1377-1385 (2000).

14 Christophy, M., Faruk Senan, N. A., Lotz, J. C. & O'Reilly, O. M. A musculoskeletal model for the lumbar spine. *Biomechanics and modeling in mechanobiology* **11**, 19-34, doi:10.1007/s10237-011-0290-6 (2012).

15 de Zee, M., Hansen, L., Wong, C., Rasmussen, J. & Simonsen, E. B. A generic detailed rigid-body lumbar spine model. *J Biomech* **40**, 1219-1227, doi:10.1016/j.jbiomech.2006.05.030 (2007).

16 Dreischarf, M. *et al.* Comparison of eight published static finite element models of the intact lumbar spine: predictive power of models improves when combined together. *J Biomech* **47**, 1757-1766, doi:10.1016/j.jbiomech.2014.04.002 (2014).

17 Han, K. S., Zander, T., Taylor, W. R. & Rohlmann, A. An enhanced and validated generic thoraco-lumbar spine model for prediction of muscle forces. *Med Eng Phys* **34**, 709-716, doi:10.1016/j.medengphy.2011.09.014 (2012).

18 Park, S. C. In vivo evaluation of lamina cribrosa deformation in glaucoma. *Journal of glaucoma* **22 Suppl 5**, S29-31, doi:10.1097/IJG.0b013e3182934a7b (2013).

19 Raabe, M. E. & Chaudhari, A. M. W. An investigation of jogging biomechanics using the full-body lumbar spine model: Model development and validation. *J Biomech* **49**, 1238-1243, doi:10.1016/j.jbiomech.2016.02.046 (2016).

20 Schmidt, H., Galbusera, F., Rohlmann, A., Zander, T. & Wilke, H. J. Effect of multilevel lumbar disc arthroplasty on spine kinematics and facet joint loads in flexion and extension: a finite element analysis. *Eur Spine J* **21 Suppl 5**, S663-674, doi:10.1007/s00586-010-1382-1 (2012).

21 Schmidt, H., Heuer, F., Claes, L. & Wilke, H. J. The relation between the instantaneous center of rotation and facet joint forces - A finite element analysis. *Clin Biomech (Bristol, Avon)* **23**, 270-278, doi:10.1016/j.clinbiomech.2007.10.001 (2008).

22 Senteler, M., Weisse, B., Rothenfluh, D. A. & Snedeker, J. G. Intervertebral reaction force prediction using an enhanced assembly of OpenSim models. *Computer methods in biomechanics and biomedical engineering* **19**, 538-548, doi:10.1080/10255842.2015.1043906 (2016).

23 Shirazi-Adl, A. Biomechanics of the lumbar spine in sagittal/lateral moments. *Spine (Phila Pa 1976)* **19**, 2407-2414 (1994).

24 Zander, T., Rohlmann, A. & Bergmann, G. Influence of different artificial disc kinematics on spine biomechanics. *Clin Biomech (Bristol, Avon)* **24**, 135-142, doi:10.1016/j.clinbiomech.2008.11.008 (2009).

25 Fagan, M. J., Julian, S., Siddall, D. J. & Mohsen, A. M. Patient-specific spine models. Part 1: Finite element analysis of the lumbar intervertebral disc--a material sensitivity study. *Proceedings of the Institution of Mechanical Engineers. Part H, Journal of engineering in medicine* **216**, 299-314 (2002).

26 Adams, M. A. & Hutton, W. C. The effect of posture on the role of the apophysial joints in resisting intervertebral compressive forces. *J Bone Joint Surg Br* **62**, 358-362 (1980).

27 Pal, G. P. & Routal, R. V. A study of weight transmission through the cervical and upper thoracic regions of the vertebral column in man. *Journal of anatomy* **148**, 245-261 (1986).

28 Yang, K. H. K., A.I. Mechanism of Facet Load Transmission as a Hypothesis for Low-Back Pain. *Spine (Phila Pa 1976)* (1984).

29 Adams, M. A. & Dolan, P. Intervertebral disc degeneration: evidence for two distinct phenotypes. *Journal of anatomy* **221**, 497-506, doi:10.1111/j.1469-7580.2012.01551.x (2012).

30 Vergroesen, P. P. *et al.* Mechanics and biology in intervertebral disc degeneration: a vicious circle. *Osteoarthritis Cartilage* **23**, 1057-1070, doi:10.1016/j.joca.2015.03.028 (2015).

31 Gillet, P. The fate of the adjacent motion segments after lumbar fusion. *J Spinal Disord Tech* **16**, 338-345 (2003).

32 Goel, V. K. *et al.* Effects of charite artificial disc on the implanted and adjacent spinal segments mechanics using a hybrid testing protocol. *Spine (Phila Pa 1976)* **30**, 2755-2764 (2005).

33 Lee, J. C. & Choi, S. W. Adjacent Segment Pathology after Lumbar Spinal Fusion. *Asian Spine J* **9**, 807-817, doi:10.4184/asj.2015.9.5.807 (2015).

34 Ren, C., Song, Y., Liu, L. & Xue, Y. Adjacent segment degeneration and disease after lumbar fusion compared with motion-preserving procedures: a meta-analysis. *European journal of orthopaedic surgery & traumatology : orthopedie traumatologie* **24 Suppl 1**, S245-253, doi:10.1007/s00590-014-1445-9 (2014).

35 Benzel, E. C. *et al.* Mechanical Characterization of a Viscoelastic Disc for Lumbar Total Disc Replacement. *J Med Devices* **5**, doi:10.1115/1.4003536 (2011).

36 Park, P., Garton, H. J., Gala, V. C., Hoff, J. T. & McGillicuddy, J. E. Adjacent segment disease after lumbar or lumbosacral fusion: review of the literature. *Spine (Phila Pa 1976)* **29**, 1938-1944, doi:10.1097/01.brs.0000137069.88904.03 (2004).

37 Xia, X. P., Chen, H. L. & Cheng, H. B. Prevalence of adjacent segment degeneration after spine surgery: a systematic review and meta-analysis. *Spine (Phila Pa 1976)* **38**, 597-608, doi:10.1097/BRS.0b013e318273a2ea (2013).

38 Cortes, D. H., Jacobs, N. T., DeLucca, J. F. & Elliott, D. M. Elastic, permeability and swelling properties of human intervertebral disc tissues: A benchmark for tissue engineering. *J Biomech* **47**, 2088-2094, doi:10.1016/j.jbiomech.2013.12.021 (2014).

39 Hudson, K. D., Alimi, M., Grunert, P., Hartl, R. & Bonassar, L. J. Recent advances in biological therapies for disc degeneration: tissue engineering of the annulus fibrosus, nucleus pulposus and whole intervertebral discs. *Current opinion in biotechnology* **24**, 872-879, doi:10.1016/j.copbio.2013.04.012 (2013).

40 Nerurkar, N. L., Elliott, D. M. & Mauck, R. L. Mechanical design criteria for intervertebral disc tissue engineering. *J Biomech* **43**, 1017-1030, doi:10.1016/j.jbiomech.2009.12.001 (2010).

41 Neidlinger-Wilke, C. *et al.* Mechanical loading of the intervertebral disc: from the macroscopic to the cellular level. *Eur Spine J* **23 Suppl 3**, S333-343, doi:10.1007/s00586-013-2855-9 (2014).

42 Chan, S. C., Ferguson, S. J. & Gantenbein-Ritter, B. The effects of dynamic loading on the intervertebral disc. *Eur Spine J* **20**, 1796-1812, doi:10.1007/s00586-011-1827-1 (2011).

43 Gawri, R. *et al.* High mechanical strain of primary intervertebral disc cells promotes secretion of inflammatory factors associated with disc degeneration and pain. *Arthritis research & therapy* **16**, R21, doi:10.1186/ar4449 (2014).

44 Paul, C. P. *et al.* Dynamic and static overloading induce early degenerative processes in caprine lumbar intervertebral discs. *PloS one* **8**, e62411, doi:10.1371/journal.pone.0062411 (2013).

45 Setton, L. A. & Chen, J. Cell mechanics and mechanobiology in the intervertebral disc. *Spine (Phila Pa 1976)* **29**, 2710-2723 (2004).

46 Wuertz, K. *et al.* In vivo remodeling of intervertebral discs in response to short- and long-term dynamic compression. *Journal of orthopaedic research : official publication of the Orthopaedic Research Society* **27**, 1235-1242, doi:10.1002/jor.20867 (2009).

47 Nachemson, A. & Morris, J. M. In Vivo Measurements of Intradiscal Pressure. Discometry, a Method for the Determination of Pressure in the Lower Lumbar Discs. *The Journal of bone and joint surgery. American volume* **46**, 1077-1092 (1964).

48 Wilke, H. J., Neef, P., Caimi, M., Hoogland, T. & Claes, L. E. New in vivo measurements of pressures in the intervertebral disc in daily life. *Spine (Phila Pa 1976)* **24**, 755-762 (1999).

49 Sato, K., Kikuchi, S. & Yonezawa, T. In vivo intradiscal pressure measurement in healthy individuals and in patients with ongoing back problems. *Spine (Phila Pa 1976)* **24**, 2468-2474, doi:10.1097/00007632-199912010-00008 (1999).

50 Smith, R. L., Carter, D. R. & Schurman, D. J. Pressure and shear differentially alter human articular chondrocyte metabolism: a review. *Clinical orthopaedics and related research*, S89-95 (2004).

51 Carragee, E. J. *et al.* 2009 ISSLS Prize Winner: Does discography cause accelerated progression of degeneration changes in the lumbar disc: a ten-year matched cohort study. *Spine (Phila Pa 1976)* **34**, 2338-2345, doi:10.1097/BRS.0b013e3181ab5432 (2009).

52 Arjmand, N. & Shirazi-Adl, A. Sensitivity of kinematics-based model predictions to optimization criteria in static lifting tasks. *Med Eng Phys* **28**, 504-514, doi:10.1016/j.medengphy.2005.10.001 (2006).

53 Arjmand, N., Plamondon, A., Shirazi-Adl, A., Lariviere, C. & Parnianpour, M. Predictive equations to estimate spinal loads in symmetric lifting tasks. *J Biomech* **44**, 84-91, doi:10.1016/j.jbiomech.2010.08.028 (2011).

54 Bruno, A. G., Bouxsein, M. L. & Anderson, D. E. Development and Validation of a Musculoskeletal Model of the Fully Articulated Thoracolumbar Spine and Rib Cage. *J Biomech Eng* **137**, 081003, doi:10.1115/1.4030408 (2015).

55 Chaffin, D. B. A computerized biomechanical model-development of and use in studying gross body actions. *J Biomech* **2**, 429-441, doi:10.1016/0021-9290(69)90018-9 (1969).

56 Granata, K. P. & Marras, W. S. An EMG-assisted model of trunk loading during free-dynamic lifting. *J Biomech* **28**, 1309-1317, doi:10.1016/0021-9290(95)00003-z (1995).

57 Schultz, A., Andersson, G., Ortengren, R., Haderspeck, K. & Nachemson, A. Loads on the lumbar spine. Validation of a biomechanical analysis by measurements of intradiscal pressures and myoelectric signals. *The Journal of bone and joint surgery. American volume* **64**, 713-720 (1982).

58 Costi, J. J. *et al.* Direct measurement of intervertebral disc maximum shear strain in six degrees of freedom: Motions that place disc tissue at risk of injury. *Journal of biomechanics* **40**, 2457-2466, doi:10.1016/j.jbiomech.2006.11.006 (2007).

59 O'Connell, G. D., Vresilovic, E. J. & Elliott, D. M. Human intervertebral disc internal strain in compression: the effect of disc region, loading position, and degeneration. *Journal of orthopaedic research : official publication of the Orthopaedic Research Society* **29**, 547-555, doi:10.1002/jor.21232 (2011).

60 Seroussi, R. E., Krag, M. H., Muller, D. L. & Pope, M. H. Internal deformations of intact and denucleated human lumbar discs subjected to compression, flexion, and extension loads. *Journal of orthopaedic research : official publication of the Orthopaedic Research Society* **7**, 122-131, doi:10.1002/jor.1100070117 (1989).

61 Jacobs, N. T., Cortes, D. H., Peloquin, J. M., Vresilovic, E. J. & Elliott, D. M. Validation and application of an intervertebral disc finite element model utilizing independently constructed tissue-level constitutive formulations that are nonlinear, anisotropic, and time-dependent. *J Biomech* **47**, 2540-2546, doi:10.1016/j.jbiomech.2014.06.008 (2014).

62 Li, H. & Wang, Z. Intervertebral disc biomechanical analysis using the finite element modeling based on medical images. *Computerized medical imaging and graphics : the official journal of the Computerized Medical Imaging Society* **30**, 363-370, doi:10.1016/j.compmedimag.2006.09.004 (2006).

63 Schroeder, Y., Wilson, W., Huyghe, J. M. & Baaijens, F. P. Osmoviscoelastic finite element model of the intervertebral disc. *Eur Spine J* **15 Suppl 3**, S361-371, doi:10.1007/s00586-006-0110-3 (2006).

64 Showalter, B. L. *et al.* Novel human intervertebral disc strain template to quantify regional three-dimensional strains in a population and compare to internal strains predicted by a finite element model. *Journal of orthopaedic research : official publication of the Orthopaedic Research Society* **34**, 1264-1273, doi:10.1002/jor.23137 (2016).

65 Pearcy, M. J. & Tibrewal, S. B. Lumbar intervertebral disc and ligament deformations measured in vivo. *Clinical orthopaedics and related research*, 281-286 (1984).

66 Edmondston, S. J. *et al.* MRI evaluation of lumbar spine flexion and extension in asymptomatic individuals. *Manual therapy* **5**, 158-164, doi:10.1054/math.2000.0356 (2000).

67 Fu, M. *et al.* The segment-dependent changes in lumbar intervertebral space height during flexion-extension motion. *Bone & joint research* **6**, 245-252, doi:10.1302/2046-3758.64.BJR-2016-0245.R1 (2017).

68 Kourtis, D., Magnusson, M. L., Smith, F., Hadjipavlou, A. & Pope, M. H. Spine height and disc height changes as the effect of hyperextension using stadiometry and MRI. *The Iowa orthopaedic journal* **24**, 65-71 (2004).

69 Suthar, P., Patel, R., Mehta, C. & Patel, N. MRI evaluation of lumbar disc degenerative disease. *Journal of clinical and diagnostic research : JCDR* **9**, TC04-09, doi:10.7860/JCDR/2015/11927.5761 (2015).

70 Kanayama, M. *et al.* A cineradiographic study on the lumbar disc deformation during flexion and extension of the trunk. *Clin Biomech (Bristol, Avon)* **10**, 193-199 (1995).

71 Wang, S., Xia, Q., Passias, P., Wood, K. & Li, G. Measurement of geometric deformation of lumbar intervertebral discs under in-vivo weightbearing condition. *J Biomech* **42**, 705-711, doi:10.1016/j.jbiomech.2009.01.004 (2009).

72 Martin, J. T. *et al.* A magnetic resonance imaging framework for quantifying intervertebral disc deformation in vivo: Reliability and application to diurnal variations in lumbar disc shape. *J Biomech* **71**, 291-295, doi:10.1016/j.jbiomech.2018.01.045 (2018).

73 Espinoza Orias, A. A. *et al.* Effects of Axial Torsion on Disc Height Distribution: An In Vivo Study. *J Manipulative Physiol Ther* **39**, 294-303, doi:10.1016/j.jmpt.2016.03.002 (2016).

74 Friedrich, K. M. *et al.* The prevalence of lumbar facet joint edema in patients with low back pain. *Skeletal Radiol* **36**, 755-760, doi:10.1007/s00256-007-0293-7 (2007).

75 Manchukonda, R., Manchikanti, K. N., Cash, K. A., Pampati, V. & Manchikanti, L. Facet joint pain in chronic spinal pain: an evaluation of prevalence and false-positive rate of diagnostic blocks. *J Spinal Disord Tech* **20**, 539-545, doi:10.1097/BSD.0b013e3180577812 (2007).

76 Simon, P., Espinoza Orias, A. A., Andersson, G. B., An, H. S. & Inoue, N. In vivo topographic analysis of lumbar facet joint space width distribution in healthy and symptomatic subjects. *Spine (Phila Pa 1976)* **37**, 1058-1064, doi:10.1097/BRS.0b013e3182552ec9 (2012).

77 Boswell, M. V., Singh, V., Staats, P. S. & Hirsch, J. A. Accuracy of precision diagnostic blocks in the diagnosis of chronic spinal pain of facet or zygapophysial joint origin. *Pain physician* **6**, 449-456 (2003).

78 Vernon-Roberts, B. & Pirie, C. J. Degenerative changes in the intervertebral discs of the lumbar spine and their sequelae. *Rheumatology and rehabilitation* **16**, 13-21 (1977).

79 Yamashita, T., Minaki, Y., Ozaktay, A. C., Cavanaugh, J. M. & King, A. I. A morphological study of the fibrous capsule of the human lumbar facet joint. *Spine (Phila Pa 1976)* **21**, 538-543, doi:10.1097/00007632-199603010-00002 (1996).

80 Cavanaugh, J. M., Ozaktay, A. C., Yamashita, H. T. & King, A. I. Lumbar facet pain: biomechanics, neuroanatomy and neurophysiology. *J Biomech* **29**, 1117-1129, doi:10.1016/0021-9290(96)00023-1 (1996).

81 Lu, Y., Chen, C., Kallakuri, S., Patwardhan, A. & Cavanaugh, J. M. Development of an in vivo method to investigate biomechanical and neurophysiological properties of spine facet joint capsules. *Eur Spine J* **14**, 565-572, doi:10.1007/s00586-004-0835-9 (2005).

82 Igarashi, A., Kikuchi, S. & Konno, S. Correlation between inflammatory cytokines released from the lumbar facet joint tissue and symptoms in degenerative lumbar spinal disorders. *J Orthop Sci* **12**, 154-160, doi:10.1007/s00776-006-1105-y (2007).

83 Pathria, M., Sartoris, D. J. & Resnick, D. Osteoarthritis of the facet joints: accuracy of oblique radiographic assessment. *Radiology* **164**, 227-230, doi:10.1148/radiology.164.1.3588910 (1987).

84 Buckland-Wright, C. Subchondral bone changes in hand and knee osteoarthritis detected by radiography. *Osteoarthritis Cartilage* **12 Suppl A**, S10-19 (2004).

85 Otsuka, Y. *et al.* In vivo measurement of lumbar facet joint area in asymptomatic and chronic low back pain subjects. *Spine (Phila Pa 1976)* **35**, 924-928, doi:10.1097/BRS.0b013e3181c9fc04 (2010).

86 Adams, M. A. & Hutton, W. C. The mechanical function of the lumbar apophyseal joints. *Spine (Phila Pa 1976)* **8**, 327-330 (1983).

87 Videman, T. *et al.* Magnetic resonance imaging findings and their relationships in the thoracic and lumbar spine. Insights into the etiopathogenesis of spinal degeneration. *Spine (Phila Pa 1976)* **20**, 928-935, doi:10.1097/00007632-199504150-00009 (1995).

88 Swanepoel, M. W., Adams, L. M. & Smeathers, J. E. Human lumbar apophyseal joint damage and intervertebral disc degeneration. *Annals of the rheumatic diseases* **54**, 182-188, doi:10.1136/ard.54.3.182 (1995).

89 Lewin, T. Osteoarthritis in Lumbar Synovial Joints. A Morphologic Study. *Acta orthopaedica Scandinavica. Supplementum*, SUPPL 73:71-112 (1964).

90 Kalichman, L. & Hunter, D. J. Lumbar facet joint osteoarthritis: a review. *Seminars in arthritis and rheumatism* **37**, 69-80, doi:10.1016/j.semarthrit.2007.01.007 (2007).

91 Svedmark, P. *et al.* Three-dimensional movements of the lumbar spine facet joints and segmental movements: in vivo examinations of normal subjects with a new non-invasive method. *Eur Spine J* **21**, 599-605, doi:10.1007/s00586-011-1988-y (2012).

92 Svedmark, P. *et al.* A New CT Method for Assessing 3D Movements in Lumbar Facet Joints and Vertebrae in Patients before and after TDR. *BioMed research international* **2015**, 260703, doi:10.1155/2015/260703 (2015).

93 Kozanek, M. *et al.* Range of motion and orientation of the lumbar facet joints in vivo. *Spine (Phila Pa 1976)* **34**, E689-696, doi:10.1097/BRS.0b013e3181ab4456 (2009).

94 Yao, Q., Wang, S., Shin, J. H., Li, G. & Wood, K. B. Lumbar facet joint motion in patients with degenerative spondylolisthesis. *J Spinal Disord Tech* **26**, E19-27, doi:10.1097/BSD.0b013e31827a254f (2013).

95 Park, W. M., Kim, K. & Kim, Y. H. Effects of degenerated intervertebral discs on intersegmental rotations, intradiscal pressures, and facet joint forces of the whole lumbar spine. *Computers in biology and medicine* **43**, 1234-1240, doi:10.1016/j.compbiomed.2013.06.011 (2013).

96 Arjmand, N. & Shirazi-Adl, A. Model and in vivo studies on human trunk load partitioning and stability in isometric forward flexions. *J Biomech* **39**, 510-521, doi:10.1016/j.jbiomech.2004.11.030 (2006).

97 Zanjani-Pour, S., Winlove, C. P., Smith, C. W. & Meakin, J. R. Image driven subject-specific finite element models of spinal biomechanics. *J Biomech* **49**, 919-925, doi:10.1016/j.jbiomech.2016.02.025 (2016).

98 Xu, M., Yang, J., Lieberman, I. H. & Haddas, R. Lumbar spine finite element model for healthy subjects: development and validation. *Computer methods in biomechanics and biomedical engineering* **20**, 1-15, doi:10.1080/10255842.2016.1193596 (2017).

99 Rohlmann, A., Zander, T., Rao, M. & Bergmann, G. Realistic loading conditions for upper body bending. *J Biomech* **42**, 884-890, doi:10.1016/j.jbiomech.2009.01.017 (2009).

100 Zhu, R. *et al.* Considerations when loading spinal finite element models with predicted muscle forces from inverse static analyses. *J Biomech* **46**, 1376-1378, doi:10.1016/j.jbiomech.2013.03.003 (2013).

101 Monteiro, N. T. d. S. M. P., Folgado, J.; Melancia, J. Structural analysis of the intervertebral discs adjacent to an interbody fusion using multibody dynamics and finite element cosimulation. *Multibody Syst Dyn*, 245-270, doi:10.1007/s11044-010-9226-7 (2011).

102 Brown, M. D., Holmes, D. C. & Heiner, A. D. Measurement of cadaver lumbar spine motion segment stiffness. *Spine (Phila Pa 1976)* **27**, 918-922 (2002).

103 Heuer, F., Schmidt, H., Claes, L. & Wilke, H. J. Stepwise reduction of functional spinal structures increase vertebral translation and intradiscal pressure. *J Biomech* **40**, 795-803, doi:10.1016/j.jbiomech.2006.03.016 (2007).

104 Wong, K. W., Luk, K. D., Leong, J. C., Wong, S. F. & Wong, K. K. Continuous dynamic spinal motion analysis. *Spine (Phila Pa 1976)* **31**, 414-419, doi:10.1097/01.brs.0000199955.87517.82 (2006).

105 Akhavanfar, M. H., Kazemi, H., Eskandari, A. H. & Arjmand, N. Obesity and spinal loads; a combined MR imaging and subject-specific modeling investigation. *J Biomech* **70**, 102-112, doi:10.1016/j.jbiomech.2017.08.009 (2018).

106 Toumanidou, T. & Noailly, J. Musculoskeletal Modeling of the Lumbar Spine to Explore Functional Interactions between Back Muscle Loads and Intervertebral Disk Multiphysics. *Frontiers in bioengineering and biotechnology* **3**, 111, doi:10.3389/fbioe.2015.00111 (2015).

107 Abouhossein, A., Weisse, B. & Ferguson, S. J. A multibody modelling approach to determine load sharing between passive elements of the lumbar spine. *Computer methods in biomechanics and biomedical engineering* **14**, 527-537, doi:10.1080/10255842.2010.485568 (2011).

108 Arshad, R., Zander, T., Bashkuev, M. & Schmidt, H. Influence of spinal disc translational stiffness on the lumbar spinal loads, ligament forces and trunk muscle forces during upper body inclination. *Med Eng Phys* **46**, 54-62, doi:10.1016/j.medengphy.2017.05.006 (2017).

109 Eskandari, A. H., Arjmand, N., Shirazi-Adl, A. & Farahmand, F. Subject-specific 2D/3D image registration and kinematics-driven musculoskeletal model of the spine. *J Biomech* **57**, 18-26, doi:10.1016/j.jbiomech.2017.03.011 (2017).

110 Kim, H. K. & Zhang, Y. Estimation of lumbar spinal loading and trunk muscle forces during asymmetric lifting tasks: application of whole-body musculoskeletal modelling in OpenSim. *Ergonomics* **60**, 563-576, doi:10.1080/00140139.2016.1191679 (2017).

111 Malakoutian, M. *et al.* A musculoskeletal model of the lumbar spine using ArtiSynth – development and validation. *Computer Methods in Biomechanics and Biomedical Engineering: Imaging & Visualization*, 1-8, doi:10.1080/21681163.2016.1187087 (2016).

112 Arjmand, N. & Shirazi-Adl, A. Biomechanics of changes in lumbar posture in static lifting. *Spine (Phila Pa 1976)* **30**, 2637-2648, doi:10.1097/01.brs.0000187907.02910.4f (2005).

113 Bazrgari, B., Shirazi-Adl, A., Trottier, M. & Mathieu, P. Computation of trunk equilibrium and stability in free flexion-extension movements at different velocities. *J Biomech* **41**, 412-421, doi:10.1016/j.jbiomech.2007.08.010 (2008).

114 Tafazzol, A., Arjmand, N., Shirazi-Adl, A. & Parnianpour, M. Lumbopelvic rhythm during forward and backward sagittal trunk rotations: combined in vivo measurement with inertial tracking device and biomechanical modeling. *Clin Biomech (Bristol, Avon)* **29**, 7-13, doi:10.1016/j.clinbiomech.2013.10.021 (2014).

115 Aiyangar, A., Zheng, L., Anderst, W. & Zhang, X. Apportionment of lumbar L2-S1 rotation across individual motion segments during a dynamic lifting task. *J Biomech* **48**, 3709-3715, doi:10.1016/j.jbiomech.2015.08.022 (2015).

116 Aiyangar, A. K., Zheng, L., Tashman, S., Anderst, W. J. & Zhang, X. Capturing three-dimensional in vivo lumbar intervertebral joint kinematics using dynamic stereo-X-ray imaging. *J Biomech Eng* **136**, 011004, doi:10.1115/1.4025793 (2014).

117 Breen, A. & Breen, A. Uneven intervertebral motion sharing is related to disc degeneration and is greater in patients with chronic, non-specific low back pain: an in vivo, cross-sectional cohort comparison of intervertebral dynamics using quantitative fluoroscopy. *Eur Spine J* **27**, 145-153, doi:10.1007/s00586-017-5155-y (2018).

118 Dehghan-Hamani, I., Arjmand, N. & Shirazi-Adl, A. Subject-specific loads on the lumbar spine in detailed finite element models scaled geometrically and kinematic-driven by radiography images. *International journal for numerical methods in biomedical engineering* **35**, e3182, doi:10.1002/cnm.3182 (2019).

119 Zanjani-Pour, S., Meakin, J. R., Breen, A. & Breen, A. Estimation of in vivo inter-vertebral loading during motion using fluoroscopic and magnetic resonance image informed finite element models. *J Biomech* **70**, 134-139, doi:10.1016/j.jbiomech.2017.09.025 (2018).

120 Eskandari, A. H., Arjmand, N., Shirazi-Adl, A. & Farahmand, F. Hypersensitivity of trunk biomechanical model predictions to errors in image-based kinematics when using fully displacement-control techniques. *J Biomech* **84**, 161-171, doi:10.1016/j.jbiomech.2018.12.043 (2019).

121 Gardner-Morse, M. G. & Stokes, I. A. Structural behavior of human lumbar spinal motion segments. *J Biomech* **37**, 205-212, doi:10.1016/j.jbiomech.2003.10.003 (2004).

122 Meng, X. *et al.* Incorporating Six Degree-of-Freedom Intervertebral Joint Stiffness in a Lumbar Spine Musculoskeletal Model-Method and Performance in Flexed Postures. *J Biomech Eng* **137**, 101008, doi:10.1115/1.4031417 (2015).

123 Senteler, M., Aiyangar, A., Weisse, B., Farshad, M. & Snedeker, J. G. Sensitivity of intervertebral joint forces to center of rotation location and trends along its migration path. *J Biomech* **70**, 140-148, doi:10.1016/j.jbiomech.2017.10.027 (2018).

124 Epstein, N. E. Adjacent level disease following lumbar spine surgery: A review. *Surgical neurology international* **6**, S591-599, doi:10.4103/2152-7806.170432 (2015).

125 van den Eerenbeemt, K. D., Ostelo, R. W., van Royen, B. J., Peul, W. C. & van Tulder, M. W. Total disc replacement surgery for symptomatic degenerative lumbar disc disease: a systematic review of the literature. *Eur Spine J* **19**, 1262-1280, doi:10.1007/s00586-010-1445-3 (2010).

126 Dombrowski, M. E. *et al.* ISSLS PRIZE IN BIOENGINEERING SCIENCE 2018: dynamic imaging of degenerative spondylolisthesis reveals mid-range dynamic lumbar instability not evident on static clinical radiographs. *Eur Spine J* **27**, 752-762, doi:10.1007/s00586-018-5489-0 (2018).

127 Anderst, W., Donaldson, W., Lee, J. & Kang, J. Cervical disc deformation during flexion-extension in asymptomatic controls and single-level arthrodesis patients. *Journal of orthopaedic research : official publication of the Orthopaedic Research Society* **31**, 1881-1889, doi:10.1002/jor.22437 (2013).

128 Schmidt, H. *et al.* Application of a new calibration method for a three-dimensional finite element model of a human lumbar annulus fibrosus. *Clin Biomech (Bristol, Avon)* **21**, 337-344, doi:10.1016/j.clinbiomech.2005.12.001 (2006).

129 Team, R. C. R. A Language and Environment for Statistical Computing. *R Foundation for Statistical Computing* (2015).

130 Delp, S. L. *et al.* OpenSim: open-source software to create and analyze dynamic simulations of movement. *IEEE transactions on bio-medical engineering* **54**, 1940-1950, doi:10.1109/TBME.2007.901024 (2007).

131 Seth, A. *et al.* OpenSim: Simulating musculoskeletal dynamics and neuromuscular control to study human and animal movement. *PLoS computational biology* **14**, e1006223, doi:10.1371/journal.pcbi.1006223 (2018).

132 Seth, A., Sherman, M., Reinbolt, J. A. & Delp, S. L. OpenSim: a musculoskeletal modeling and simulation framework for in silico investigations and exchange. *Procedia IUTAM* **2**, 212-232, doi:10.1016/j.piutam.2011.04.021 (2011).

133 Sherman, M. A., Seth, A. & Delp, S. L. What Is a Moment Arm? Calculating Muscle Effectiveness in Biomechanical Models Using Generalized Coordinates. *Proceedings of the ... ASME Design Engineering Technical Conferences. ASME Design Engineering Technical Conferences* **2013**, doi:10.1115/DETC2013-13633 (2013).

134 Arnold, E. M., Ward, S. R., Lieber, R. L. & Delp, S. L. A model of the lower limb for analysis of human movement. *Annals of biomedical engineering* **38**, 269-279, doi:10.1007/s10439-009-9852-5 (2010).

135 Thelen, D. G. Adjustment of muscle mechanics model parameters to simulate dynamic contractions in older adults. *J Biomech Eng* **125**, 70-77, doi:10.1115/1.1531112 (2003).

136 Kadaba, M. P., Ramakrishnan, H. K. & Wootten, M. E. Measurement of Lower-Extremity Kinematics during Level Walking. *Journal of Orthopaedic Research* **8**, 383-392, doi:DOI 10.1002/jor.1100080310 (1990).

137 Woltring, H. J. A Fortran Package for Generalized, Cross-Validatory Spline Smoothing and Differentiation. *Adv Eng Softw Workst* **8**, 104-113, doi:Doi 10.1016/0141-1195(86)90098-7 (1986).

138 Bruno, A. G. *et al.* Incorporation of CT-based measurements of trunk anatomy into subject-specific musculoskeletal models of the spine influences vertebral loading predictions. *Journal of orthopaedic research : official publication of the Orthopaedic Research Society* **35**, 2164-2173, doi:10.1002/jor.23524 (2017).

139 Affolter, C., Kedzierska, J., Vielma, T. & Aiyangar, A. in *3rd International Workshop on Spine Loading and Deformation.*

140 van der Houwen, E. B. *et al.* Geometry of the intervertebral volume and vertebral endplates of the human spine. *Annals of biomedical engineering* **38**, 33-40, doi:10.1007/s10439-009-9827-6 (2010).

141 Wang, Y., Battie, M. C. & Videman, T. A morphological study of lumbar vertebral endplates: radiographic, visual and digital measurements. *Eur Spine J* **21**, 2316-2323, doi:10.1007/s00586-012-2415-8 (2012).

142 O'Connell, G. D., Vresilovic, E. J. & Elliott, D. M. Comparison of animals used in disc research to human lumbar disc geometry. *Spine (Phila Pa 1976)* **32**, 328-333, doi:10.1097/01.brs.0000253961.40910.c1 (2007).

143 White, A. A. P., M. M. *Clinical biomechanics of the spine.* 2nd edn, (Lippincott, 1990).

144 Tsantrizos, A., Ito, K., Aebi, M. & Steffen, T. Internal strains in healthy and degenerated lumbar intervertebral discs. *Spine (Phila Pa 1976)* **30**, 2129-2137, doi:10.1097/01.brs.0000181052.56604.30 (2005).

145 Nagel, T. M., Zitnay, J. L., Barocas, V. H. & Nuckley, D. J. Quantification of continuous in vivo flexion-extension kinematics and intervertebral strains. *Eur Spine J* **23**, 754-761, doi:10.1007/s00586-014-3195-0 (2014).

146 Amin, D. B., Moawad, C. M. & Costi, J. J. New Findings Confirm Regional Internal Disc Strain Changes During Simulation of Repetitive Lifting Motions. *Annals of biomedical engineering* **47**, 1378-1390, doi:10.1007/s10439-019-02250-z (2019).

147 Ghezelbash, F. *et al.* Effects of motion segment simulation and joint positioning on spinal loads in trunk musculoskeletal models. *J Biomech* **70**, 149-156, doi:10.1016/j.jbiomech.2017.07.014 (2018).

148 Beaucage-Gauvreau, E. *et al.* Validation of an OpenSim full-body model with detailed lumbar spine for estimating lower lumbar spine loads during symmetric and asymmetric lifting tasks. *Computer methods in biomechanics and biomedical engineering* **22**, 451-464, doi:10.1080/10255842.2018.1564819 (2019).

149 Meijer, G. J., Homminga, J., Veldhuizen, A. G. & Verkerke, G. J. Influence of interpersonal geometrical variation on spinal motion segment stiffness: implications for patient-specific modeling. *Spine (Phila Pa 1976)* **36**, E929-935, doi:10.1097/BRS.0b013e3181fd7f7f (2011).

150 Natarajan, R. N. & Andersson, G. B. The influence of lumbar disc height and cross-sectional area on the mechanical response of the disc to physiologic loading. *Spine (Phila Pa 1976)* **24**, 1873-1881 (1999).

151 Niemeyer, F., Wilke, H. J. & Schmidt, H. Geometry strongly influences the response of numerical models of the lumbar spine--a probabilistic finite element analysis. *J Biomech* **45**, 1414-1423, doi:10.1016/j.jbiomech.2012.02.021 (2012).

152 DeLucca, J. F. *et al.* Off-axis response due to mechanical coupling across all six degrees of freedom in the human disc. *JOR spine* **2**, e1047, doi:10.1002/jsp2.1047 (2019).

153 Sabnis, A. B., Chamoli, U. & Diwan, A. D. Is L5-S1 motion segment different from the rest? A radiographic kinematic assessment of 72 patients with chronic low back pain. *Eur Spine J* **27**, 1127-1135, doi:10.1007/s00586-017-5400-4 (2018).

154 Jacobs, W. *et al.* Total disc replacement for chronic back pain in the presence of disc degeneration. *The Cochrane database of systematic reviews*, CD008326, doi:10.1002/14651858.CD008326.pub2 (2012).

155 Salzmann, S. N., Plais, N., Shue, J. & Girardi, F. P. Lumbar disc replacement surgery-successes and obstacles to widespread adoption. *Current reviews in musculoskeletal medicine* **10**, 153-159, doi:10.1007/s12178-017-9397-4 (2017).

156 Yoder, J. H. *et al.* Internal three-dimensional strains in human intervertebral discs under axial compression quantified noninvasively by magnetic resonance imaging and image registration. *J Biomech Eng* **136**, doi:10.1115/1.4028250 (2014).

157 Shirazi-Adl, A. Finite-element evaluation of contact loads on facets of an L2-L3 lumbar segment in complex loads. *Spine (Phila Pa 1976)* **16**, 533-541, doi:10.1097/00007632-199105000-00009 (1991).

158 Du, C. F., Yang, N., Guo, J. C., Huang, Y. P. & Zhang, C. Biomechanical response of lumbar facet joints under follower preload: a finite element study. *BMC Musculoskelet Disord* **17**, 126, doi:10.1186/s12891-016-0980-4 (2016).

159 Masharawi, Y. *et al.* Facet orientation in the thoracolumbar spine: three-dimensional anatomic and biomechanical analysis. *Spine (Phila Pa 1976)* **29**, 1755-1763 (2004).

160 Aiyangar, A., Zheng, L., Anderst, W. & Zhang, X. Instantaneous centers of rotation for lumbar segmental extension in vivo. *J Biomech* **52**, 113-121, doi:10.1016/j.jbiomech.2016.12.021 (2017).

161 Ianuzzi, A., Pickar, J. G. & Khalsa, P. S. Relationships between joint motion and facet joint capsule strain during cat and human lumbar spinal motions. *J Manipulative Physiol Ther* **34**, 420-431, doi:10.1016/j.jmpt.2011.05.005 (2011).

162 Dong, L., Odeleye, A. O., Jordan-Sciutto, K. L. & Winkelstein, B. A. Painful facet joint injury induces neuronal stress activation in the DRG: implications for cellular mechanisms of pain. *Neurosci Lett* **443**, 90-94, doi:10.1016/j.neulet.2008.07.059 (2008).

163 Dong, L. & Winkelstein, B. A. Simulated whiplash modulates expression of the glutamatergic system in the spinal cord suggesting spinal plasticity is associated with painful dynamic cervical facet loading. *J Neurotrauma* **27**, 163-174, doi:10.1089/neu.2009.0999 (2010).

164 Jaumard, N. V., Welch, W. C. & Winkelstein, B. A. Spinal facet joint biomechanics and mechanotransduction in normal, injury and degenerative conditions. *J Biomech Eng* **133**, 071010, doi:10.1115/1.4004493 (2011).

165 Lee, K. E., Davis, M. B., Mejilla, R. M. & Winkelstein, B. A. In vivo cervical facet capsule distraction: mechanical implications for whiplash and neck pain. *Stapp Car Crash J* **48**, 373-395 (2004).

166 Lu, Y., Chen, C., Kallakuri, S., Patwardhan, A. & Cavanaugh, J. M. Neural response of cervical facet joint capsule to stretch: a study of whiplash pain mechanism. *Stapp Car Crash J* **49**, 49-65 (2005).

167 Kingma, I., Faber, G. S. & van Dieen, J. H. Supporting the upper body with the hand on the thigh reduces back loading during lifting. *J Biomech* **49**, 881-889, doi:10.1016/j.jbiomech.2015.09.035 (2016).

168 MacDonald, D. A., Moseley, G. L. & Hodges, P. W. The lumbar multifidus: does the evidence support clinical beliefs? *Manual therapy* **11**, 254-263, doi:10.1016/j.math.2006.02.004 (2006).

169 Ghezelbash, F., Arjmand, N. & Shirazi-Adl, A. Effect of intervertebral translational flexibilities on estimations of trunk muscle forces, kinematics, loads, and stability. *Computer methods in biomechanics and biomedical engineering* **18**, 1760-1767, doi:10.1080/10255842.2014.961440 (2015).